

DISS. ETH NO. 17575

**A THREE-DIMENSIONAL ANALYSIS OF
EXCAVATION-INDUCED PERTURBATIONS IN
THE OPALINUS CLAY AT THE MONT TERRI
ROCK LABORATORY**

A dissertation submitted to

ETH ZURICH

for the degree of

Doctor of Sciences

presented by

SALINA YONG

Masters of Science in Geotechnical Engineering
University of Alberta

01November1973

citizen of Canada

accepted on the recommendation of

Prof. Dr. Simon Loew
Dr. Corrado Fidelibus
Prof. Dr. Peter K. Kaiser

2007

Copyright © 2007 Salina Yong
All Rights Reserved

A Three-Dimensional Analysis of Excavation-Induced Perturbations in the Opalinus Clay at the Mont Terri Rock Laboratory

Doctoral Exam: 13Dec2007
Final Manuscript: 30May2008

Published and distributed by:
Engineering Geology
Geological Institute
ETH Zurich (Swiss Federal Institute of Technology, Zurich)
ETH Hoenggerberg
Wolfgang-Pauli-Strasse 15
8093 Zurich
Switzerland
www.engineeringgeology.ethz.ch

In loving memory of Rita Chang

Extended Abstract

In Switzerland, the Opalinus Clay is under consideration as a potential host rock for the deep geological disposal of nuclear waste. The construction of an underground opening perturbs the surrounding rock mass and leads to the creation of an Excavation Damaged/disturbed Zone (EDZ/EdZ), which may in turn lead to significant changes in hydraulic properties. Consideration of an overconsolidated argillaceous host rock adds mechanical complexities as these materials are inherently transitional and rarely isotropic. The Opalinus Clay at the Mont Terri Rock Laboratory in Switzerland is anisotropic and heterogeneous as bedding is thin and pronounced (thereby leading to intact rock anisotropy) while small-scale tectonic shears are prevalent (thereby leading to rock mass heterogeneity). Understanding the response of rock to excavation requires consideration of the structure of both the intact rock and the rock mass as failure can be structurally-controlled and/or stress-driven. While past and present investigations focus on the intact rock anisotropy caused by the bedding, none have considered the rock mass heterogeneity caused by the tectonic shears. This thesis examines the role of geological heterogeneity and its three-dimensional effect on the rock damage incurred by the construction of the EZ-B Niche at the Mont Terri Rock Laboratory.

The EZ-B Niche was excavated sequentially during a recent expansion of the Rock Laboratory, which resulted in the excavation of the adjoining Gallery04. Construction of the niche (6-7m long) was completed with a pneumatic hammer and involved eight excavation steps: one for the full-face excavation of the niche entrance, six for the excavation of the main body, and one for the excavation of the invert. A number of boreholes were also drilled from and around the niche. Three observation boreholes were drilled after the niche entrance was excavated but before the niche body was excavated. After the niche was completed, a remaining 12 boreholes were drilled in three planes with two vertical planes near the middle of the niche and one horizontal plane at the springline that included two additional boreholes in the final face of the niche. The rock mass surrounding the niche was monitored before, during, and after the niche excavation. This thesis considers geological mapping, drillcore mapping, digital optical televiewer imaging, single-hole seismic measurements, and geodetic displacement measurements.

Analysis and interpretation of the field data was carried out in two parts. The first focused on the EDZ/EdZ around Gallery04 as inferred from the induced fractures mapped in the entrance of the EZ-B Niche. Geological mapping of the niche entrance provided evidence that the tectonic shears influenced induced fracturing. Two sets of tectonic shears were intersected by the EZ-B Niche: one sub-parallel with bedding and one that is sub-horizontal. The stress redistribution in the surrounding rock mass was provided by two- and three-dimensional continuum and discontinuum numerical modelling to account for the tectonic shears and the intact rock anisotropy. Two-dimensional numerical modelling showed that induced fracturing mapped in the west entrance wall was most likely affected only by mobilisation of the bedding-parallel shears whereas induced fracturing in the east entrance wall was affected by mobilisation of both the bedding-parallel and sub-horizontal shears. As a result, induced fractures propagated sub-perpendicular to the bedding-parallel shears in the west wall and sub-perpendicular to the sub-horizontal shears in the east wall. In the surrounding intact rock, three-dimensional numerical modelling showed that mobilisation of the tectonic shears resulted in stress levels conducive for extensional (i.e. spalling) failure. Results from numerical simulations showed that when the tectonic shears are accounted for (i.e. more deformable than the surrounding intact rock), the stress field was influenced in a similar manner whether or not the intact rock was isotropic or anisotropic. This suggested that rock mass heterogeneity (i.e. due to the tectonic shears), rather than intact rock anisotropy (i.e. due to the bedding), played a key role in inducing the fractures mapped in the EZ-B Niche entrance.

In the second part of the analysis and interpretation, perturbations around the EZ-B Niche were assessed. Geological mapping of drillcore and digital optical televiewer imaging identified only a limited number of visible induced fractures. However, rock mass perturbations were clearly seen in the borehole seismic measurements and intensity changes in borehole instabilities. As a result, field data (drillcore mapping, digital optical televiewer imaging, and single-hole seismic measurements) were integrated to define the extent of the EDZ/EdZ around the niche. The EDZ/EdZ around the EZ-B Niche consisted of a thin zone of macroscopic fracturing (averaging 20cm) and a thicker zone of seismic wave amplitude

disturbance (ranging 50-100cm), which also coincided roughly with the depth where borehole instabilities commenced. Three-dimensional continuum numerical modelling showed that damage in the niche EDZ/EdZ could be attributed to spalling type failure in regions of high deviatoric stress and low confinement. In this case, damage increased and coincided with a decreasing spalling limit (i.e. ratio between the minimum and maximum principal stresses) as the excavation boundary was approached. Hence, damage around the EZ-B Niche in regions of high deviatoric stress and low confinement is related to micro-cracking resulting from redistributed stress levels in excess of the crack initiation threshold but below macroscopic failure.

Pertaining to nuclear waste storage, the relevance of the findings in this thesis is in the scale of the field experiment, which considers an excavation size that may be comparable to a repository scale. Although induced fractures in argillaceous rocks are expected to seal hydraulically due to physical and chemical alterations, design of tunnel support and engineered barriers necessitate determination of the EDZ/EdZ extent and associated failure mechanisms with confidence. With few macroscopic extensional fractures identified, this thesis demonstrated that the degree of rock damage can be correlated to changes in the spalling limit. In addition and most importantly, this study showed that excavation-induced perturbations in anisotropic rock mass can be strongly influenced by elastic and plastic shear on discrete tectonic discontinuities. Hence, determination of relevant mechanical properties for the tectonic discontinuities encountered in the Opalinus Clay at the Mont Terri Rock Laboratory needs to be carried out in future work.

Zusammenfassung

Seit dem Projekt Entsorgungsnachweis wird in der Schweiz der Opalinuston als bevorzugtes Wirtsgestein zur geologischen Tiefenlagerung hochradiokativer Abfälle detailliert untersucht. Durch den Bau eines Tiefenlagers im Opalinuston (und anderen Gesteinstypen) werden mechanische Risse um den Hohlraum induziert und es bildet sich eine hohlraumnahe Auflockerungszone (Excavation Damaged/disturbed Zone, EDZ/EdZ), welche einen signifikanten Einfluss auf die anfänglichen hydraulischen Gebirgseigenschaften zur Folge hat. Überkonsolidierte Tonschiefer bringen zusätzlich eine mechanische Komplexität mit sich, da diese Materialien sowohl spröde wie duktile Verformungseigenschaften haben und selten isotrop sind. Der intakte Opalinuston ist aufgrund seiner sedimentären marinen Genese sehr feinkörnig und schichtartig aufgebaut und verhält sich im Labormassstab mechanisch anisotrop. Zusätzlich treten im Massstab der Untertagebauwerke im Felslabor Mont Terri viele tektonische Scherflächen auf, die zu einer markanten grossskaligen Heterogenität des Gebirges führen. Um die Reaktion des Gebirges auf die Ausbrucharbeiten um ein zukünftiges Endlager verstehen zu können, muss darum sowohl die Struktur des intakten Gesteins als auch des Gebirges berücksichtigt werden, da das Gebirge sowohl strukturbedingt als spannungsbedingt versagen (d.h. den elastischen Verformungsbereich überschreiten) kann. Während sich die bisherigen Untersuchungen zum mechanischen Verhalten des Opalinustons auf die sedimentär angelegte Anisotropie des intakten Gesteins konzentrierten, gab es bisher keine Untersuchung zu den Auswirkungen der aus den tektonischen Trennflächen resultierenden Gebirgheterogenität. Die vorliegende Arbeit untersucht die Rolle aller geologischen Heterogenitäten auf das dreidimensionale Bruchverhalten des Opalinustons während des Ausbruchs der EZ-B Nische im Felslabor Mont Terri, welche eine ähnlichen kreisförmigen Querschnitt wie die geplanten Endlagerstollen (Durchmesser von rund 4 Meter) hat.

Die 6-7 Meter lange EZ-B Nische wurde während einer im Jahr 2004 durchgeführten Erweiterung des Felslabors („Gallery04“) mit einem pneumatischen Hammer ausgebrochen. Der Bauvorgang der Nische bestand aus acht Schritten: Dem Vollausbuch des Nischeneingangs, sechs je eintägigen Abschlägen des kreisförmigen Nischenkörpers und einem Ausbruch einer horizontalen 30 cm tiefen Sohle. Zusätzlich wurden vier Piezometerbohrungen und zahlreiche Kernbohrung aus dem Inneren der Nische sowie um die Nische herum erstellt: Vier Piezometerbohrungen und drei lange horizontale Kernbohrungen wurden nach Ausbruch des Nischeneingangs, jedoch vor jenem des Hauptkörpers der Nische ausgebrochen. Nach der Fertigstellung der Nische wurden 12 weitere Kernbohrungen in drei Ebenen erstellt: in zwei vertikalen Ebenen nahe der Mitte der Nische und einer horizontalen Ebene mittig durch die endgültige Tunnelbrust. Die Reaktionen des die Nische umgebenden Gebirgskörpers wurden an den Ausbruchsoberflächen sowie in den Bohrungen systematisch vor, während und nach dem Ausbruch der Nische detailliert erfasst. Die in dieser Arbeit ausgewerteten Daten umfassen geologische Kartierungen, Bohrkernanalysen, digitale optische Bohrloch-Televierermessungen, Bohrloch-Refraktionsseismik sowie geodätische Verformungsmessungen.

Die Analyse und Interpretation dieser Felddaten wurde in zwei Schritten durchgeführt. Der erste Schritt konzentrierte sich auf die EDZ/EdZ um die Gallery04, die aus den durch die Gallery04 verursachten Rissen besteht, welche im Eingangsbereich der EZ-B Nische kartiert werden konnten. Die geologische Kartierung des Nischeneingangs deutet klar darauf hin, dass tektonische Scherflächen die Bildung von EDZ-Rissen beeinflussen. Zwei Familien mm-dünner tektonischer Scherflächen wurden in der EZ-B Nische angetroffen: die dominante Familie liegt sub-parallel zu den mit 45 Grad nach SSE einfallenden Schichtungsflächen mit einem Abstand von 0.2-1.0 Metern, die zweite Familie tritt nur lokal auf und liegt sub-horizontal. Die induzierten Spannungsumlagerungen im Opalinuston wurden durch zwei- und dreidimensionale, numerische Kontinuums- und Diskontinuums-Modellierungen berechnet, wobei die tektonische Scherflächen und die Gesteinsanisotropie berücksichtigt wurden. Zweidimensionale numerische Modellierungen zeigen, dass die induzierten Risse in der Westwand des Nischeneingangs sehr wahrscheinlich einzig durch die Mobilisierung der schichtparallelen Scherflächen beeinflusst wurden, während die induzierten Risse in der Ostwand durch die Mobilisierung sowohl von den schichtparallelen als auch sub-horizontalen Scherflächen beeinflusst wurden. Darum breiteten sich die dominierenden

induzierten Risse in der Westwand nahezu senkrecht auf die schichtparallelen Scherflächen und in der Ostwand nahezu senkrecht auf die sub-horizontalen Scherflächen aus. Für das umgebende Gebirge zeigen dreidimensionale numerische Modellrechnungen, dass die Mobilisierung tektonischer Scherflächen zu Spannungsverhältnissen führt, welche extensive Dehnungsrisse (d.h. Spalling) begünstigen. Die Ergebnisse der numerischen Modellierung zeigen auch, dass bei Berücksichtigung tektonischer Scherflächen (d.h. durch eine erhöhte Verformbarkeit verglichen mit dem intakten Umgebungsgestein) das Spannungsfeld sowohl für isotrope als auch anisotrope Gebirgseigenschaften auf ähnliche Weise beeinflusst wurde. Dies legt nahe, dass die Gebirgheterogenität auf Grund tektonischer Scherflächen eine Schlüsselrolle bei der Bildung der kartierten neuen Risse am EZ-B Nischeneingang spielte und nicht so sehr die primäre Anisotropie des intakten Gesteins auf Grund der sedimentären Schichtung.

Im zweiten Schritt der Analyse und Interpretation wurden die durch den Ausbruch induzierten Gebirgsveränderungen um die EZ-B Nische untersucht. Geologische Bohrkernaufnahmen und optische Bohrloch-Televieveraufnahmen zeigten lediglich eine geringe Anzahl von makroskopisch sichtbaren, Ausbruch-induzierten Rissen. Hingegen können aus seismischen Bohrlochmessungen und spannungsinduzierten Bohrlochrandausbrüchen klare Gebirgsstörungen identifiziert werden. Darum wurden für die Erfassung der Ausdehnung der EDZ/EdZ um die EZ-B Nische verschiedenste Felddaten integriert. Die EDZ/EdZ um die EZ-B Nische besteht aus einer geringmächtigen Zone makroskopischer Risse (im Mittel 20 cm) und einer mächtigeren Zone (50-80 cm), die sich durch Veränderungen in den Amplituden und Geschwindigkeiten seismischer Wellen auszeichnet, und auch in etwa mit der Tiefe übereinstimmt, in der Bohrlochinstabilitäten auftreten. Dreidimensionale numerische Kontinuumsmodellrechnungen zeigen, dass das Gebirgsversagen in der EDZ/EdZ der Nische auf extensive Zugrisse (Spalling) in Bereichen hoher deviatorischer Spannungen und geringer Seitendrucke zurückzuführen ist. In diesem Fall nimmt das Ausmass der Gebirgsschädigung mit sinkendem Verhältnis zwischen der minimalen und maximalen Hauptspannung, d.h. in Richtung auf die Nischenwand zu. Daher kann die dominierende Gebirgsschädigung in der Umgebung der EZ-B Nische mit der Bildung mikroskopischer Risse erklärt werden, die in Regionen entstehen, wo die Spannungsumlagerungen zu hohen sekundären Deviatorspannungen und geringer Einspannung (Seitendrucke) führen, welche aber nur selten den Grenzwert überschreiten, der zur Ausbildung makroskopischer Risse notwendig wäre.

Die hier vorgestellten Prozesse sind auch für Endlagerstollen relevant, da der Querschnitt der EZ-B Nische vergleichbare Dimensionen hat. Die kurze Länge der EZ-B Nische reduziert durch die noch wirksame Bruststützung das Ausmass der zu erwarteten Gebirgsschädigungen im Vergleich zu den langen geplanten Endlagerstollen.

Obwohl man davon ausgeht, dass sich induzierte Risse in Tonschiefern nach ihrer Bildung wieder durch chemische und physikalische Alterationen hydraulisch abdichten, ist es für die Planung der Tunnelausbruchmethoden, der Sicherungs- und Stützmittel, der Absperrbauwerke und technischen Barrieren von Bedeutung, die Ausdehnung der EDZ/EdZ sowie die damit verbundenen Bruchmechanismen mit hoher Zuverlässigkeit zu verstehen. Die um die EZ-B Nische nur in geringer Häufigkeit auftretenden makroskopischen Extensionsbrüche sowie die seismischen Gebirgsveränderungen zeigen, dass der Grad der spröden Gebirgsdeformationen mit dem Verhältnis der minimalen zur maximalen Sekundärspannung (Spalling Limit) korreliert werden kann. Ein weiteres und sehr wichtiges Ergebnis dieser Arbeit ist, dass das mechanische Gebirgsverhalten und die ausbruchsbedingten Gebirgsveränderungen in anisotropen Tonschiefern sehr stark durch elastische und plastische Scherungen von diskreten tektonischen Diskontinuitäten beeinflusst werden können. Daher bedarf es zukünftiger Untersuchungen zur Bestimmung der relevanten mechanischen Parameter dieser tektonischen Diskontinuitäten im Felslabor Mont Terri.

Acknowledgements

Completion of this thesis would not have been possible without the unwavering support of Shannon Lim, my parents, sister, and brothers. To them, I owe a tremendous amount of gratitude and respect for seeing me through the highs and lows of the challenges I faced in the last five years.

The Swiss Nuclear Safety Inspectorate (HSK) provided funding for this project and to them, (especially Erik Frank) I am thankful for this opportunity. Prof. Simon Loew and Dr. Corrado Fidelibus are graciously thanked for their encouragement and support throughout the thesis. A number of other individuals have also been involved in helping me rein in the potentially large scope of this thesis. Most notably, Prof. Peter Kaiser and Prof. Derek Martin are thanked for their time spent in numerous (and often impromptu) discussions; their enthusiasm in learning, exploring, and discovery are greatly appreciated. Dr.'s Frank Lemy and Kristof Schuster have also been great sources of encouragement and for being willing sounding boards in academic and life matters, I am grateful.

The volume of data collected in this thesis was large and the field investigation heavily constrained by time and space. I am indebted to everyone who took part and made it an adventure in cultural, academic, and technical diversity. Geological data and site support were provided by Dr. Christophe Nussbaum, Dr. Nicolas Badertscher, Olivier Meier, and Dr. Paul Bossart. Seismic data were provided by Dr. Kristof Schuster with field support from Torsten Tietz, Dieter Boeddener, Friedhelm Schulte, and Wilfried Stille. Displacement data were provided by Dr. Thorsten Schulz and Hans-Martin Zogg with field support from Dr. Frank Lemy and Jonas von Ruetten. Support in the field and office were also provided by: Dr. Keith Evans, Jonas von Ruetten, Dr. Frank Lemy, Dr. Corrado Fidelibus, Marcel Mettler, Dr. Andrew Corkum, Dr. Peter Bluemling, Dr. Tim Vietor, Dr. Benoît Valley, Prof. Mark Diederichs, Dr. David Jaeggi, Dr. Martin Herfort, Shannon Lim, Olivier Masset, Valentin Gischig, Kerry Leith, Urs Gerber, Alastair McClymont, Anna Kaiser, Dr. Bill Fry, and Dr. Alexander Stephan. Many thanks go to Juergen Hansmann for the translation of the abstract. Finally, everyone at the Chair of Engineering Geology is most gratefully thanked for their camaraderie and for providing an endless source of humour and philosophical debates...vielen Dank!

Table of Contents

Dedication	iii
Abstract.....	v
Acknowledgements	ix
Table of Contents.....	xi
List of Figures	xv
List of Tables.....	xxi
Symbols and Notation	xxiii
1 Introduction.....	1
1.1 Approach.....	2
1.2 Thesis Organisation.....	2
2 Induced Fracturing In The Opalinus Clay – An Integrated Field Experiment	3
Abstract.....	3
2.1 Introduction.....	4
2.2 Site Description.....	5
2.3 Field Investigation	5
2.3.1 Construction & Installation Activities.....	5
2.3.2 Field Measurements	7
2.4 The Experimental EDZ Model.....	8
2.5 Conclusion	9
References	10
3 Influence Of Tectonic Shears On Tunnel-Induced Fracturing.....	13
Abstract.....	13
3.1 Introduction.....	14
3.2 Site Description.....	16
3.3 Geological Setting.....	18
3.3.1 Opalinus Clay	18
3.3.2 Tectonic Structures.....	19
3.3.3 In situ Stress Field	20
3.4 Field Observations.....	20
3.4.1 Influence of the Tectonic Shears	22
3.4.2 Influence of Excavation Sequence.....	22
3.5 Mechanisms Responsible for Induced Fracturing in the North Wall of Gallery04 Near the EZ-B Niche	23
3.5.1 Modelling Rock Anisotropy.....	23
3.5.2 Estimating Properties for the Tectonic Shears	27

3.5.3 Three-dimensional Analysis	29
3.5.4 Response of the Bedding-Parallel Shears.....	29
3.5.5 Matrix Response	32
3.6 Discussion	33
3.7 Conclusions.....	34
References	35
4 Excavation Induced Perturbations Around A Short Tunnel.....	39
Abstract.....	39
4.1 Introduction.....	40
4.2 Site Description.....	41
4.3 Field Data.....	43
4.3.1 Induced Fractures.....	43
4.3.2 Borehole Instabilities.....	45
4.3.3 Seismic Measurements	48
4.3.4 Displacement Monitoring	49
4.4 Numerical Modelling.....	53
4.5 Assessing Rock Damage.....	54
4.5.1 Data Integration.....	57
4.5.2 Southern Vertical Borehole Plane.....	57
4.5.3 Northern Vertical Borehole Plane	61
4.5.4 Horizontal Borehole Plane Ahead of the Face.....	65
4.5.5 Characterising the Zone of Perturbation Around the EZ-B Niche.....	68
4.6 Conclusions.....	72
References	73
5 Rock Mass Response Ahead Of An Advancing Face.....	77
Abstract.....	77
5.1 Introduction.....	78
5.2 Site Description.....	79
5.2.1 Geological Setting.....	79
5.2.2 The EZ-B Niche.....	81
5.3 Field and Model Data Integration.....	82
5.3.1 Field Data.....	82
5.3.2 Numerical Modelling.....	83
5.3.3 Data Integration.....	84
5.4 Data Analysis and Interpretation	87
5.4.1 Before the EZ-B Niche Excavation.....	87

5.4.2 During the EZ-B Niche Excavation	88
5.4.3 After the EZ-B Niche Excavation.....	91
5.5 Conclusions.....	96
References	102
6 Summary & Recommendations	105
6.1 Summary of the Field Approach.....	106
6.2 Summary of the Interpretation Approach.....	106
6.3 Summary of Findings	106
6.4 Assessment of Field Methods.....	107
6.5 Future Work	108
Bibliography	109
Appendix A: Constraining the Geometry	115
A.1 Niche Surfaces.....	115
A.2 Boreholes and Roof Anchors	115
A.3 Integration.....	116
Appendix B: Locating the Tectonic Shears.....	119
B.1 Geological Maps.....	119
B.2 Laser Scanner.....	119
B.3 Integration into the GOCAD model.....	119
Appendix C: Drillcore Maps.....	127
Appendix D: Pore Pressure and Atmospheric Data.....	139

List of Figures

Fig. 2.1	The EZ-B experiment is located in the Mont Terri Rock Laboratory, Switzerland.....	4
Fig. 2.2	Isometric view of the EZ-B niche construction and the borehole layout.....	6
Fig. 2.3	Timeline and sequence of construction and installation activities in the field investigation.....	6
Fig. 2.4	Summary of the measurement activities in the field investigation.....	7
Fig. 2.5	Mapped EDZ fractures in the east wall of the EZ-B niche entrance.....	7
Fig. 2.6	Optical televiewer image from a borehole drilled perpendicular to bedding.....	8
Fig. 2.7	Displacements measured at discrete points with a total station and along surfaces with a panoramic laser scanner via comparing point clouds.....	9
Fig. 2.8	Seismic measurements at the midheight of the niche.....	10
Fig. 2.9	Differential elevation map of the upper region of the final niche face that compares two laser scanning sessions six days apart.....	10
Fig. 3.1	Location of the Mont Terri Rock Laboratory in northern Switzerland.....	14
Fig. 3.2	Different rock failure modes along in principal stress space.....	15
Fig. 3.3	Interference of tectonic shears on induced fracturing in the EB Niche northeast wall.....	16
Fig. 3.4	Location of the EZ-B Niche in Gallery04.....	16
Fig. 3.5	Layout of the Rock Laboratory around the EZ-B Niche and in situ stress field with cross-sections of Gallery04 and the EZ-B Niche.....	17
Fig. 3.6	Stratigraphic sequence along the Security Gallery.....	18
Fig. 3.7	Prominence of the bedding in the Opalinus Clay with interstratified sandy lenses.....	19
Fig. 3.8	In situ stress field at the Mont Terri Rock Laboratory in relation to bedding and SSE bedding-parallel shears.....	20
Fig. 3.9	Induced fracturing in the east and west walls in the EZ-B Niche entrance.....	21
Fig. 3.10	Induced fracturing mapped in the SB Niche.....	23
Fig. 3.11	Phase2 geometry and mesh of Gallery04 at the east and west walls of the EZ-B Niche.....	24
Fig. 3.12	Deviatoric stress contours of elastic isotropy compared to elastic transverse isotropy without consideration of the tectonic shears.....	25
Fig. 3.13	Deviatoric stress contours of elastic isotropy compared to elastic transverse isotropy with only the SSE shears modelled.....	26
Fig. 3.14	Deviatoric stress contours of elastic isotropy compared to elastic transverse isotropy with all mapped shears modelled.....	27
Fig. 3.15	Yielded matrix and joint elements from plastic isotropic analyses in Phase2 compared with field observations for the east and west niche entrance wall.....	30
Fig. 3.16	Graded mesh of the 3DEC model illustrated on one of SSE bedding-parallel shears with three reference excavation rounds.....	31
Fig. 3.17	Shear displacement contours along F7 and F1 at the end of the simulated Gallery04 excavation.....	32
Fig. 3.18	Stress paths of the matrix in the west and east walls of the EZ-B Niche at weakened shear properties.....	32

Fig. 3.19	Stress paths of the matrix in the west and east walls of the EZ-B Niche at glued shear properties.....	33
Fig. 3.20	Location of most critical β angles along the gallery wall with approximate intersections of the bedding-parallel shears that daylight in Gallery04.....	34
Fig. 4.1	Location of the EZ-B Niche in the Mont Terri rock laboratory in northern Switzerland and in relation to the three main facies of the Opalinus Clay.....	41
Fig. 4.2	The in situ stress field at the Mont Terri Rock Laboratory relative to the EZ-B Niche and the nearly parallel bedding planes and SSE-bedding-parallel shears	42
Fig. 4.3	SSE bedding-parallel shears mapped in the west and east walls of the niche.....	42
Fig. 4.4	Layout of the Rock Laboratory around the EZ-B Niche and in situ stress field with cross-sections of Gallery04 and the EZ-B Niche	43
Fig. 4.5	Isometric view of the EZ-B Niche	44
Fig. 4.6	The Digital Optical Televiewer used to image the borehole walls.....	44
Fig. 4.7	Fractures identified in BEZ-B15 from drillcore mapping and photo-documentation and DOPTV imaging.....	45
Fig. 4.8	Classification of the fractures mapped in the boreholes	46
Fig. 4.9	Fracture counts from the EZ-B Niche boreholes compared to boreholes drilled in older sub-parallel excavations	47
Fig. 4.10	Extent of borehole instabilities observed in the sidewalls, upper east walls, and face	47
Fig. 4.11	Different degrees of borehole instabilities observed in unwrapped DOPTV images.....	48
Fig. 4.12	The BGR mini-sonic probe used in the single-hole seismic measurements	49
Fig. 4.13	Seismic wave parameters derived from single-hole interval velocity logging in BEZ-B19.....	50
Fig. 4.14	Average P-wave and S-wave velocities from all three channels arranged from highest to lowest relative to the P-wave velocity in channel 3.....	50
Fig. 4.15	Geodetic displacement monitoring at object points installed in four circular arrays and one linear array in the face	51
Fig. 4.16	Displacement vectors of arrays 100-400.	52
Fig. 4.17	Largest total convergence determined from the geodetic measurements.	52
Fig. 4.18	Displacement vectors of array 500.....	53
Fig. 4.19	Excavations modelled in the continuum simulation.....	54
Fig. 4.20	Brittle failure modes in σ_1 - σ_3 space, normalised by σ_c	55
Fig. 4.21	Stress-strain diagram from a uniaxial compression test with the crack initiation, crack interaction, and peak strength thresholds defined.....	56
Fig. 4.22	Increasing length of stable crack propagation as the spalling limit decreases with damage distributed between the crack initiation and interaction thresholds.....	57
Fig. 4.23	Integration of the borehole data from BEZ-B11	58
Fig. 4.24a	BEZ-B14 data integration	59
Fig. 4.24b	BEZ-B15 data integration	59
Fig. 4.24c	BEZ-B16 data integration	60
Fig. 4.24d	BEZ-B17 data integration	60

Fig. 4.25a	BEZ-B8 data integration	62
Fig. 4.25b	BEZ-B9 data integration	62
Fig. 4.25c	BEZ-B10 data integration	63
Fig. 4.25d	BEZ-B11 data integration	63
Fig. 4.25e	BEZ-B12 data integration	64
Fig. 4.25f	BEZ-B13 data integration	64
Fig. 4.26a	BEZ-B18 data integration	66
Fig. 4.26b	BEZ-B3 data integration	67
Fig. 4.26c	BEZ-B19 data integration	67
Fig. 4.27	Zone of perturbation around the niche determined from borehole data integration	68
Fig. 4.28a	Bedding-parallel borehole integration of seismic data with modelled stress ratios.....	69
Fig. 4.28b	Bedding-perpendicular borehole integration of seismic data with modelled stress ratios.....	69
Fig. 4.28c	Bedding-45° borehole (upper walls and crown) integration of seismic data with modelled stress ratios.....	70
Fig. 4.28d	Bedding-45° boreholes in the face and crown integration of seismic data with modelled stress ratios.....	70
Fig. 4.29	Stress redistributions plotted along each borehole in the three borehole planes from CIE and CAE numerical simulations.....	71
Fig. 5.1	Location of the Mont Terri Rock Laboratory in northern Switzerland.....	79
Fig. 5.2	Plan view of the Mont Terri Rock Laboratory and the main facies of the Opalinus Clay	80
Fig. 5.3	The in situ stress field at the Mont Terri Rock Laboratory in relation to bedding and the SSE shear set.....	80
Fig. 5.4	Isometric view of the EZ-B Niche	81
Fig. 5.5	Step sizes of the EZ-B Niche excavation	82
Fig. 5.6	Boreholes drilled into the face of the EZ-B Niche	83
Fig. 5.7	Structures mapped in the EZ-B drillcores with corresponding photographs.....	83
Fig. 5.8	The Robertson Geologging Digital Optical Televiewer (DOPTV) used to image the borehole walls.....	84
Fig. 5.9	The BGR mini-sonic probe used in the single-hole seismic measurements	84
Fig. 5.10	Excavations simulated in the continuum model.....	85
Fig. 5.11	Pre-excavation stage integration of borehole field and model data.....	86
Fig. 5.12	Simulated stress redistributions plotted along BEZ-B3 for key steps in the excavation sequence for the CIE and CAE models.....	88
Fig. 5.13	Key excavation steps in the numerical simulations where data were analysed	89
Fig. 5.14	Excavation of the “Mini niche” in the centre of the entrance face.....	89
Fig. 5.15	Location of the steeper-dipping shear, FA, between the faces of Syn3 and Syn4	90
Fig. 5.16	Syn1 integration of field and model data from BEZ-B3.....	91
Fig. 5.17	Syn2 integration of field and model data from BEZ-B3.....	92

Fig. 5.18	Syn3 integration of field and model data from BEZ-B3.....	93
Fig. 5.19	Syn4 integration of field and model data from BEZ-B3.....	94
Fig. 5.20	Syn5 integration of field and model data from BEZ-B3.....	95
Fig. 5.21	Syn6 integration of field and model data from BEZ-B3.....	96
Fig. 5.22	Seismic parameters derived from the syn-excavation measurements taken in BEZ-B3.....	97
Fig. 5.23	BEZ-B18 PostA integration of field and model data	98
Fig. 5.24	BEZ-B3 PostA integration of field and model data.....	98
Fig. 5.25	BEZ-B19 PostA integration of field and model data	99
Fig. 5.26	Seismic parameters derived from post-excavation measurements made in BEZ-B3, B18, and B19	100
Fig. 5.27	Seismic parameters derived from post-excavation measurements made in BEZ-B3.....	101
Fig. A1	Point clouds of the EZ-B Niche acquired from the laser scanner	116
Fig. A2	Isolation of the niche face from the first syn-excavation step	116
Fig. A3	The integrated geometrical relationships between the different elements of the EZ-B Niche construction	117
Fig. B1	Geological map of the west niche wall.....	120
Fig. B2	Geological map of the east niche wall.....	121
Fig. B3	Geological map of the niche faces and invert.....	122
Fig. B4	Geological map of the niche roof.....	123
Fig. B5	Location of tectonic shears F9, F10, and F10A in the laser scanner point cloud with the geological maps as guidance.....	124
Fig. B6	Comparison of the bedding-parallel shears with the locations of shear planes mapped in the drillcore as viewed along strike.....	124
Fig. B7	Comparison of the bedding-parallel shears with the locations of shear planes mapped in the drillcore as viewed isometrically	125
Fig. C1	Layout of the boreholes drilled in the EZ-B Experiment.....	127
Fig. C2a	Drillcore map of BEZ-B1	128
Fig. C2b	Continuation of BEZ-B1 drillcore map.....	128
Fig. C2c	Continuation of BEZ-B1 drillcore map.....	129
Fig. C3a	Drillcore map of BEZ-B2	129
Fig. C3b	Continuation of BEZ-B2 drillcore map.....	130
Fig. C3c	Continuation of BEZ-B2 drillcore map.....	130
Fig. C3d	Continuation of BEZ-B2 drillcore map.....	131
Fig. C4a	Drillcore map of BEZ-B3	131
Fig. C4b	Continuation of BEZ-B3 drillcore map.....	132
Fig. C4c	Continuation of BEZ-B3 drillcore map.....	132
Fig. C5	Drillcore map of BEZ-B8	133
Fig. C6	Drillcore map of BEZ-B9	133

Fig. C7	Drillcore map of BEZ-B10	134
Fig. C8	Drillcore map of BEZ-B11	134
Fig. C9	Drillcore map of BEZ-B12	135
Fig. C10	Drillcore map of BEZ-B13	135
Fig. C11	Drillcore map of BEZ-B14	136
Fig. C12	Drillcore map of BEZ-B15	136
Fig. C13	Drillcore map of BEZ-B16	137
Fig. C14	Drillcore map of BEZ-B17	137
Fig. C15	Drillcore map of BEZ-B18	138
Fig. C16	Drillcore map of BEZ-B19	138
Fig. D1	Integration of the pore pressures with atmospheric data obtained from a nearby niche and from the EZ-B Niche.....	140
Fig. D2	Location of the boreholes (BEZ-B4 to B7) where pore pressure sensors were installed.....	140
Fig. D3	Integration of the pore pressures with atmospheric data during the niche excavation.....	141

List of Tables

Tab. 3.1: Elastic matrix properties used in the Phase2 analyses	24
Tab. 3.2: Laboratory-determined matrix properties	28
Tab. 3.3: Matrix properties estimated from Phase2.....	29
Tab. 3.4: Tectonic shear properties estimated from Phase2	29
Tab. 3.5: Summary of the properties used in the 3DEC analysis.....	31
Tab. 4.1: All fractures identified in BEZ-B8 to B19 and the last 3m of BEZ-B3.....	46
Tab. 4.2: Total displacement magnitudes determined from geodetic measurements	51
Tab. 4.3: Total convergence determined from geodetic surveys	53
Tab. 4.4: Material properties used in the elastic continuum models.....	55
Tab. 5.1: Material properties used in the elastic anisotropic continuum model.....	85

Symbols & Notation

A	Deviatoric stress criterion factor ranging from 1 to 1.5
ad	Artificial discontinuities
A_p	P-wave amplitude
A_s	S-wave amplitude
β	Angle between the plane normal and the maximum applied stress
B	Deviatoric stress criterion factor ranging from 0.3 to 0.5
c	Cohesion
CAE	Continuum, anisotropic, and elastic numerical model
CIE	Continuum, isotropic, and elastic numerical model
D	Disturbance factor
dc	Dessication cracks
DOPTV	Digital optical televiewer
E_i	Intact rock modulus
E_{rm}	Rock mass modulus
EDZ	Excavation damaged zone
EdZ	Excavation disturbed zone
ESE	East-southeast
ϕ	Frictional strength component
F	Tectonic shear
G	Shear modulus
G_i	Intact rock shear modulus
G_{rm}	Rock mass shear modulus
GSI	Geological strength index
I	Induced fracture
I1	Induced fracture with the highest level of confidence
I2	Possible induced fracture
IF1	Induced fracture oriented sub-parallel with tunnel axis
IF2	Induced fracture oriented oblique to tunnel axis
IF3	Induced fracture oriented sub-parallel with bedding
k_n	Joint normal stiffness
k_s	Joint shear stiffness
L	Spacing between joints
ν	Poisson's ratio
N-S	North to south
NAp	Normalised P-wave amplitude

NAs	Normalised S-wave amplitude
NE	Northeast
NNW	North-northwest
O	Unclassified fracture
σ_1	Maximum principal stress
σ_2	Intermediate principal stress
σ_3	Minimum principal stress
σ_c	Unconfined compressive strength or uniaxial compressive stress
σ_{cc}	Crack closure threshold
σ_{cd}	Crack interaction threshold
σ_{ci}	Crack initiation threshold
σ_{peak}	Peak strength
S-SW	South to southwest
SE	Southeast
SW	Southwest
SSE	South- southeast
sst	Bedding-parallel tectonic shears
uj	Excavation-induced unloading joints
UCS	Unconfined compressive strength or uniaxial compressive stress
V_p	P-wave velocity
V_s	S-wave velocity
WNW	West-northwest

Chapter 1

Introduction

The Opalinus Clay in Switzerland is under consideration as a potential host rock for the deep geological disposal of nuclear waste. The construction of an underground opening perturbs the surrounding rock mass and leads to the creation of an Excavation Damaged/Disturbed Zone (EDZ/EdZ). Degradation of the rock mass may or may not lead to significant changes in flow and transport properties; the EDZ in the former and the EdZ in the latter. Understanding the processes under which excavation-induced perturbations are created and their impact on the properties of the host rock is important in the context of geological waste repositories.

When a volume of rock is perturbed, damage processes depend on the location of critical geological structures and the ensuing stress redistribution. Rock mass perturbations can range in scale from microscopic (e.g. grain-scale micro-fracturing) to macroscopic (e.g. extensile fracturing around tunnels). If disturbed stresses are high enough, rock mass strength may be exceeded and lead to macro-fracturing. However, if disturbed stresses are not sufficiently high enough to reach the strength envelope, micro-damage may be nonetheless sustained.

During a recent expansion of the Mont Terri Rock Laboratory, limited macroscopic fracturing was observed around a short test tunnel (EZ-B Niche). This finding differed from past investigations around openings with the same orientation as the EZ-B Niche. The objectives of this thesis were to define the perturbation around the EZ-B Niche and to identify the mechanisms responsible for and the factors that influenced the development of the perturbation.

1.1 Approach

In this thesis, the perturbed zone around the EZ-B Niche at the Mont Terri Rock Laboratory was investigated. The field campaign consisted of three stages. In the pre-excavation stage, an entrance to the niche was excavated. Three observation boreholes were then drilled parallel to the future niche axis. The target of the pre-excavation stage was to set benchmark measurements. In the syn-excavation, the niche was excavated to its final length in seven steps. Between each excavation step, field measurements were carried out. In the post-excavation stage, an additional 12 observation boreholes were drilled in three planes: a horizontal plane near the springline and two vertical planes near the middle of the niche. The purpose of this stage was to define the zone of perturbation in three dimensions and to monitor its evolution.

Although a large volume of data was collected, this thesis considers 1) tunnel and drillcore mapping, 2) digital optical televiewer imaging, 3) single-hole seismic measurements, and 4) geodetic displacement monitoring. The field data was used to define the relative geometry of the niche and the zone of perturbation caused by the excavation of the niche. Both of these required the integration of the field data. Numerical modelling was incorporated to assess the processes responsible for the observed perturbation. Three-dimensional modelling was required as the intersection of the EZ-B Niche with the adjoining gallery is also shared by the intersection of a neighbouring niche resulting in an enlarged opening. In addition, the axis of the EZ-B Niche is not perpendicular to the adjoining gallery nor is it parallel with a principal stress axis.

1.2 Thesis Organisation

This thesis was written in a paper format so that each main chapter stands alone. As a result, the literature review is disseminated and may be repeated throughout the thesis. However, in the chapter with the greatest relevancy, the literature review was expanded. Presentation of the data analyses and discussions follow the field investigation stages: the pre-excavation stage is considered in Chapter 3, the post-excavation stage in Chapter 4, and the syn-excavation stage in Chapter 5.

Chapter 2 summarises the field investigation and is a modified reprint of a paper presented at the Fourth Asian Rock Mechanics Symposium in Singapore (Yong et al., 2006). The field investigation consisted of the niche excavation, drilling of observation boreholes, and data collection.

Chapter 3 investigates the influence of tectonic shears on fracturing induced by the excavation of a gallery with which the niche intersects. Induced fractures mapped in the entrance of the niche were examined and properties for the tectonic shears were determined from two-dimensional numerical modelling. Three-dimensional discontinuum modelling was undertaken to examine the rock matrix response to the presence of the tectonic shears.

Chapter 4 examines the perturbation to the rock mass surrounding the niche at the end of its construction. Rock mass perturbation and its extent were determined from the integration of the field data. Results from three-dimensional numerical modelling were used to examine the use of stress ratios as damage indicators.

Chapter 5 investigates the rock mass response ahead of the advancing niche face during the niche excavation. Field data were integrated to determine the extent of the perturbation and to analyse its evolution. Consideration was given to the perturbed zone of niche entrance and to the tectonic bedding-parallel shears.

Chapter 6 gives an overview of the thesis by summarising the work carried out and the major findings. An assessment of the field methods is also provided along with recommendations for future work.

Chapter 2

Induced Fracturing in the Opalinus Clay – An Integrated Field Experiment

Abstract

The Opalinus Clay is under consideration as a potential host rock for a nuclear waste repository in Switzerland. The performance of the repository may be affected by an Excavation Damaged Zone (EDZ), which is inevitably created when an underground opening is constructed. A test niche was sequentially excavated and monitored in the Mont Terri Rock Laboratory, Switzerland, to obtain a description of the induced fracturing in the EDZ during and after the excavation and to identify the mechanisms that dominate their formation. The field investigation provided essential data for an integrated development of an experimental EDZ model that described the in situ geological conditions, induced fracturing pattern, and rock mass response. The approach used in the field investigation is presented along with preliminary results.

test niche was excavated in a stepwise manner and the rock mass response monitored via surface and borehole methods. The main objectives were to describe the EDZ formation and to identify the factors and mechanisms that governed its formation. The key considerations were the geometry of the induced fractures and the network they encompassed; the timing of the formation; and the influence of the excavation process, the pre-existing heterogeneities, the in situ stress field, and the atmospheric conditions. This chapter focuses on the approach used in the field investigation and presents preliminary results.

2.2 Site Description

The field investigation was carried out in the new expansion (Gallery 04) of the rock laboratory, which is located in the Opalinus Clay (140m thickness) in the southern limb of the Mont Terri anticline. The Opalinus Clay is a Jurassic deposit consisting of a sequence of overconsolidated claystones and marls. Bedding planes at Mont Terri are highly continuous and thinly laminated with spacing less than 20mm [2]. In the EZ-B niche, the bedding has a dip of about 45° and two major sets of tectonic shears have been identified [3]. The shaly facies has an in situ water content of 6%, a plastic limit of 23% and a liquid limit of 38%. The uniaxial compressive strength is 16MPa perpendicular to bedding and 10MPa parallel to bedding while the elastic modulus is 4GPa and 10GPa [4], respectively. These values illustrate the marked mechanical anisotropy caused by the bedding.

2.3 Field Investigation

The field investigation provided essential data for the development of an experimental EDZ model that describes the in situ geological conditions, the induced fracture pattern, and the rock mass response. To facilitate detailed observations and measurements of the EZ-B niche EDZ, the field investigation was carried out in three stages: pre-, syn-, and post-excavation. The pre-excavation stage had a five-fold purpose: geological characterisation, drillcore sampling for laboratory testing, pore pressure monitoring, provision of observation boreholes, and setting benchmark measurements for borehole monitoring methods. The syn-excavation stage focused on monitoring the EDZ development and evolution as the excavation advanced and also included characterising the rock mass and documenting the influences of the experiment activities and excavation interruptions. In the post-excavation stage, the EDZ surrounding the niche was defined and its evolution monitored over timescales of weeks and months.

2.3.1 Construction & Installation Activities

Construction and installation activities consisted of borehole drilling, excavation, and the installation of instrumentation. A three-dimensional illustration of the construction is shown in Fig. 2.2 and the timeline is summarised in Fig. 2.3.

The pre-excavation stage spanned eight months and included the excavations of Gallery 04 in the vicinity of the EZ-B niche and its entrance and the installation of excavation support. Two sets of boreholes were drilled in this stage, four for pore pressure monitoring and three for geophysical observations. The pore pressure boreholes (BEZ-B4 to B7) were 20mm in diameter and located in different zones of pore pressure change. The observation boreholes (BEZ-B1 to B3) were 100mm in diameter and located in the area of greatest interest regarding the EDZ (i.e. the region immediately surrounding the excavation boundary). Thus, BEZ-B1 was located along the east wall of the niche and became the benchmark for the locations of BEZ-B2 to B3 and the alignment guide for the niche excavation. In turn, this required the partial excavation of BEZ-B1 as the niche advanced. BEZ-B2 and B3 were located no more than 2m from BEZ-B1 to be within the limits of effective seismic cross-hole measurements. In addition, the boreholes were not capped to ensure maximum borehole stability against the adverse effects of elevated humidity.

The niche (3.8m in diameter and 6.5m in length) was constructed with a pneumatic hammer in seven steps over a period of 12 days in the syn-excavation stage. The final niche face and body were created in the first six steps while the invert was excavated in its entirety in the last step. The first six excavation steps ranged from 0.3m to 1.3m. Each step except the first began with the excavation near the invert and concluded with the partial excavation of BEZ-B1. The first step was completed over a two-day period; the

not tensioned. A 300mm thick concrete floor was poured over the invert and a 10cm thick foam contraction joint was incorporated in the centre of the floor to allow for movement at the base of the niche walls.

The post-excavation stage began with the drilling of a third set of observation boreholes that radiated from the niche in three planes: two orthogonal to the niche axis and one parallel to it. The orthogonal plane closest to the face consisted of six boreholes (BEZ-B8 to B13) and provided the greatest radial coverage. The second orthogonal plane was drilled about 1m south of the first and consisted of four boreholes (BEZ-B14 to B17). The remaining boreholes (BEZ-B18 and B19) were drilled in the face at the same elevation as the pre-excavation boreholes (BEZ-B1 to B3) and located as close as possible to the sidewalls.

Borehole stability became an appreciable logging issue in this stage as four of the newly drilled boreholes (BEZ-B8, B14, B12, and B17) were oriented sub-parallel to bedding and thus, subjected to a higher propensity for collapse. Applying a vacuum was relatively effective at the beginning of this stage but over the subsequent months, an additional cleaning tool (similar to a garden spade) was incorporated.

2.3.2 Field Measurements

Several geological, geotechnical, geodetic, and geophysical measurements were carried out at each excavation stop, which ranged from 12 hours during the week to 65 hours over the weekend. Fig. 2.4 summarises the data collected in each stage and indicates the number of datasets obtained.

Stage	Niche Mapping	Digital Video Documentation	Laser Scanner	Total Station	Tunnel Seismics	Atmospheric Monitoring	Borehole					
							Drillcore Logging	Pore Pressure Monitoring	Optical Televiewer	Single-hole Seismics	Cross-hole Seismics	Spectral Gamma
Pre	wall (1) face (1)						borehole (3)	continuous	borehole (3)	(3)	(2)	
	wall, floor, roof (1) face (6)	continuous	(11)	(11)				continuous	borehole (18)	(11)	(6)	
Post			(1)	(1)	refraction (2) borehole (2)	continuous	borehole (12)	continuous	borehole (30)	(24)	(12)	borehole (15)

Fig. 2.4: A summary of the measurement activities in the field investigation with the number of datasets in brackets.

The geology of the rock mass was characterised through the integration of geological maps, drillcore logs, optical televiewer images, and seismic data. Subsequently, the spatial distribution and approximate size of significant geological heterogeneities was determined. The focus of these measurements was on the identification of significant pre-existing and induced features, such as lenses/inclusions, tectonic shears, and EDZ from Gallery 04 and the niche excavations (Figures 2.5 and 2.6).

The rock mass response was characterised by integrating geological mapping, optical televiewer images, seismic data, and displacement monitoring. Displacement and seismic data were periodically collected. The niche excavation was video-documented to provide assistance to the data interpretation should the

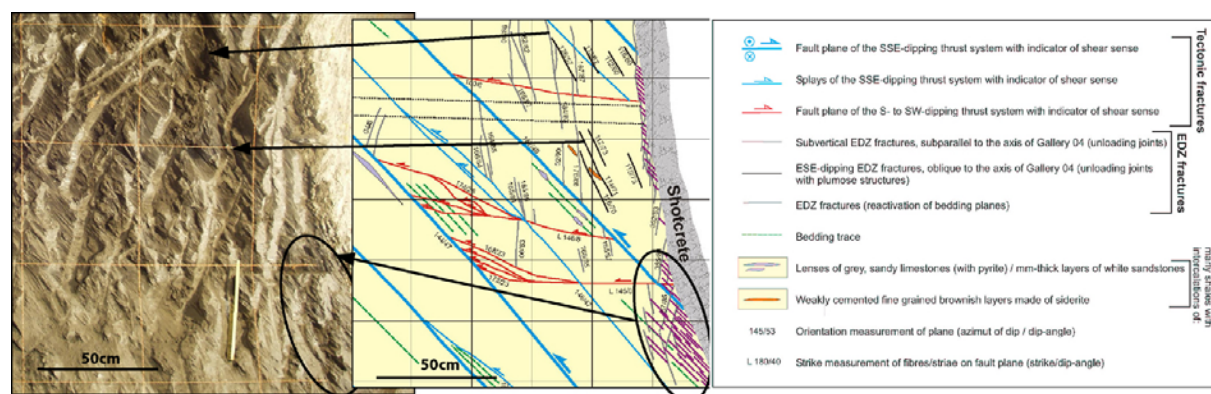


Fig. 2.5: Mapped EDZ fractures in the east wall of the EZ-B niche entrance (modified from [3]). “Faults” in this figure are referred to as “shears” in this thesis.

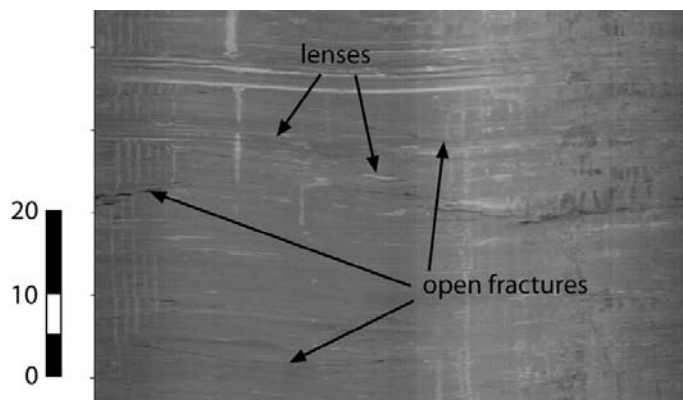


Fig. 2.6: Optical televiewer image (unwrapped) from a borehole drilled perpendicular to bedding. Sandy lenses and open fractures follow the bedding trace, which is subhorizontal. The scale is in centimetres.

need arise. Displacements were monitored with a novel approach, which incorporated point displacements measured with a total station and surficial displacements measured with a panoramic laser scanner. The total station method entailed installing and surveying discrete points as the excavation advanced. A total of 27 object points were installed over four circular arrays in the niche body and one linear array in the final niche face (Fig. 2.7a). Each circular array consisted of six points at 45° intervals that were aligned with the assumed directions of the principal stresses (Fig. 2.7a). The linear array consisted of three points distributed over the height of the final face. The laser scanner method consisted of scanning the niche surfaces and resulted in point clouds of x-, y-, z-coordinates (Fig. 2.7b). In the syn-excavation stage, 11 survey sessions were completed over a 12-day period, thereby encompassing three time-scales, hours, days, and weeks. The addition of a repeat measurement in the post-excavation expanded the time-scale to months.

Seismic measurements consisted of borehole and tunnel methods, which were carried out in 11 sessions. The seismic measurements began in the pre-excavation stage by establishing benchmarks, which consisted of seismic interval velocity in individual boreholes and cross-hole measurements between adjacent boreholes (Fig. 2.8). In the syn-excavation, the same measurements were carried out in the regions ahead of the face and those adjacent to the sidewalls. In the post-excavation, the investigation focused on completing the EDZ definition around the niche and monitoring its evolution via repeat measurements. The same single- and cross-hole measurements were made with the addition of tomography in a 1m by 1m region in the east wall and tunnel seismics in the final face (Fig. 2.8). Tunnel seismics consisted of refraction measurements and borehole seismic profiling (i.e. a horizontal version of vertical seismic profiling) along two linear profiles aligned sub-parallel and perpendicular to bedding. In addition, interval velocity measurements with probe rotation were also made in BEZ-B2 in the pre- and post-excavation stages to assess the influence of the transmitting direction.

2.4 The Experimental EDZ Model

Preliminary results from the field investigation indicated complexity in characterising the EDZ. Drillcore logs and televiewer images in the post-excavation boreholes showed little induced fracturing and few fractures cutting the bedding. Numerous EDZ fractures were identified in the niche entrance, whereas few were clearly identifiable in the niche interior. The seismic data showed a marked velocity increase about 1.5m ahead of the face and the pore pressure data showed suction in the floor and sidewall during the niche excavation. These observations indicated a need for integration of the collected data if the EDZ phenomenon in the EZ-B niche was to be understood.

Integration of the field data was necessary to develop an experimental EDZ model that defined physical, mechanical, and temporal characteristics. The dataset in this research investigation was large and its integration complex. As a result, a number of tools were developed to ease and expedite the process. For example, data from the laser scanner (with a point cloud resolution in the order of millimetres) was processed through noise reduction and subtraction of spatial values to derive maps [5] from which deformational patterns were identified (Fig. 2.9). After processing, the data was integrated to produce a 3D visualisation, thereby illustrating the spatial relationships and interactions between the datasets. For

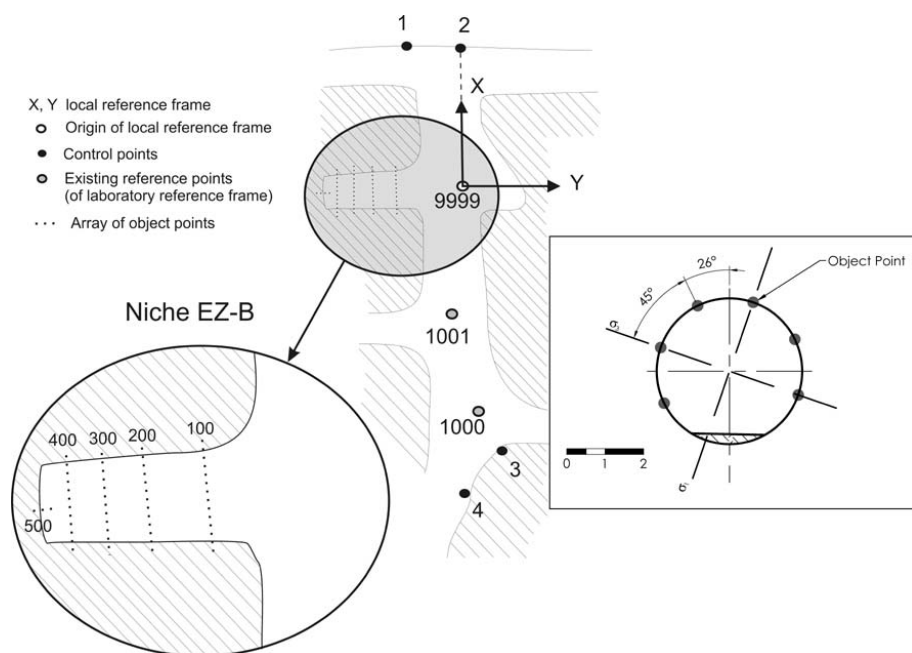
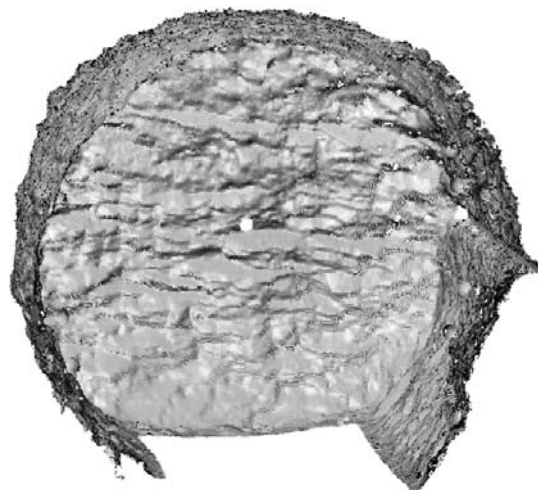


Fig. 2.7: The displacements were measured (a) at discrete points (inset) with a total station and along surfaces with a panoramic laser scanner via comparing point clouds (b) (after [5]).

(a)



(b)

example, tectonic shears and EDZ fractures were integrated with the location of the niche faces (Fig. 2.2) to define the relative geometry of the fracture network with the excavation interruptions (Appendix B). Likewise, the displacement vectors and differential elevation maps could be incorporated to correlate the fracture network with the deformational response. In this manner, the experimental EDZ model would highlight areas that may require additional field investigations and isolate areas for numerical studies. Numerical analyses focused on identifying dominating mechanisms and factors responsible for induced fracturing around the EZ–B niche and facilitated an examination of possible damage modes.

2.5 Conclusion

Induced fracturing in the EDZ constitutes an important issue in waste isolation. Describing the EDZ requires an integrated field experiment that involves the repeat use of complementary investigative methods. The EZ–B experiment utilised geological, geotechnical, geodetic, and geophysical methods to monitor the EDZ resulting from the stepwise excavation of a test niche in the Opalinus Clay at the Mont Terri Rock Laboratory. Preliminary results emphasised complexity in the EDZ: few induced fractures were clearly identified in the geological mapping while disturbance in the near-field during and after the niche construction were indicated by the pore pressure and seismic data. These observations indicated a

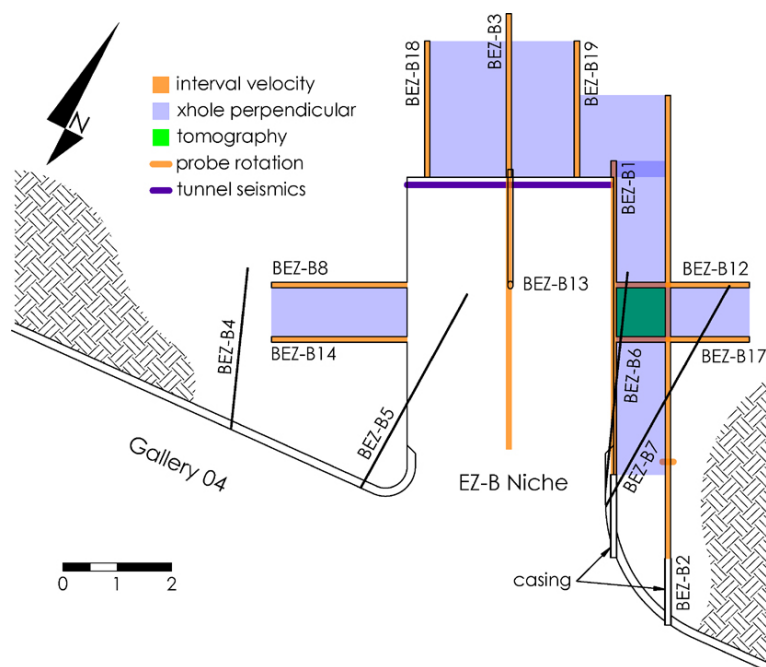


Fig. 2.8: Seismic measurements at the midheight of the niche (drawing scale in metres).

need for data integration if the complex phenomenon of the EDZ was to be understood. Data integration from the field investigation facilitated the development of an experimental EDZ model. In turn, the experimental EDZ model formed a basis for numerical analyses, which were necessary for identifying dominating EDZ mechanisms and factors.

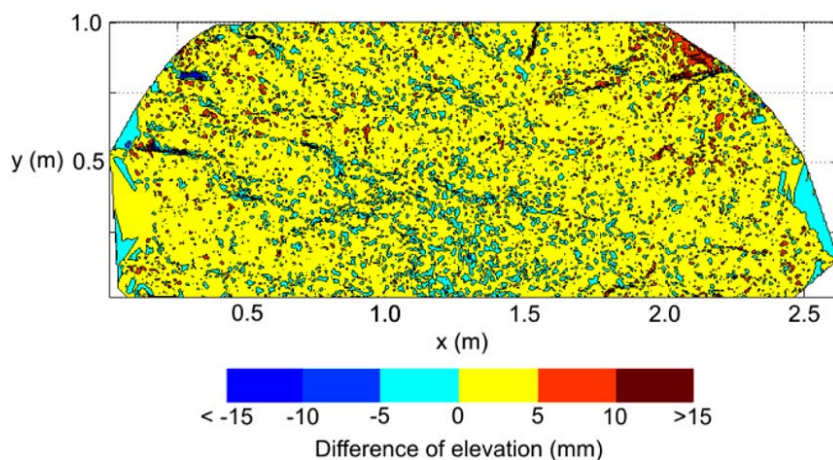


Fig. 2.9: A differential elevation map of the upper region of the final niche face that compares two laser scanning sessions six days apart (after [5]).

References

- [1] Bossart P, Trick T, Meier PM, Mayor J-C. Structural and hydrogeological characterisation of the excavation-disturbed zone in the Opalinus Clay (Mont Terri Rock Project, Switzerland). *Applied Clay Science* 2004;26:429–488.
- [2] Martin CD, Lanyon GW. Excavation Disturbed Zone (EDZ) in Clay Shale: Mont Terri, Unpublished Mont Terri Technical Report, 2004. 207pp.
- [3] Nussbaum C, Bossart P, von Ruetze J, Meier O, Badertscher N. EZ-B experiment: small-scale mapping of tectonic and artificial (EDZ) fractures of the EZ-B niche. Unpublished Mont Terri Technical Note, 2005. 23pp.
- [4] Bock H. RA experiment rock mechanics analyses and synthesis: data report on rock mechanics. Unpublished Mont Terri Technical Report, 2001. 52pp.

[5] Lemy F, Yong S, Schulz T. Assessment of laser-based displacement mapping in an underground opening. In: Eberhardt E, Stead D, Morrison T, editors. Rock Mechanics Meeting Society's Challenges and Demands. Vol. 1. Vancouver: Taylor & Francis; 2007. pp.85-92.

Chapter 3

Influence of Tectonic Shears on Tunnel-Induced Fracturing

Abstract

The Opalinus Clay as encountered at the Mont Terri Rock Laboratory is currently under investigation as a potential host rock for deep geological disposal of nuclear waste in Switzerland. Understanding the conditions under which fracturing is induced and the mechanisms involved in causing fractures due to the construction of a repository are important. The nature of an overconsolidated argillaceous host rock adds mechanical complexities as these materials are inherently transitional and rarely isotropic. In this chapter, mapped tectonic shears played a key role in the development of induced fracturing around a gallery at the Rock Laboratory. When the tectonic shears were accounted for in numerical analyses, the redistributed stress field was influenced in a similar manner whether or not the matrix was isotropic or anisotropic. This implied that in certain situations, rock mass anisotropy (i.e. due to the tectonic shears) may be a more critical factor than the rock matrix anisotropy (i.e. due to the bedding). In the west wall of the entrance to the EZ-B Niche, mobilisation of bedding-parallel shears led to induced fracturing at orientations nearly perpendicular to the bedding-parallel shears. In the east entrance wall, two sets of tectonic shears were mobilised. Induced fracturing in this case was dominated by the more critical sub-horizontal shear that interfered with the mobilisation of the bedding-parallel shears in the east niche wall. Consequently, induced fracture orientations in the east wall appeared to be parallel to the gallery wall.

3.1 Introduction

At the Mont Terri Rock Laboratory in Switzerland (Fig. 3.1), research is undertaken to investigate the potential of the Opalinus Clay as a host rock for deep geological disposal of high-level nuclear waste. The performance of a geological repository may be affected by the Excavation Damaged and/or Disturbed Zone (EDZ/EdZ) [1] that is inevitably created when an underground opening is constructed. Depending on the altered stress state, fracturing may be induced in the EDZ/EdZ. In most geological materials, fractures are the conduits through which preferential flow and transport might occur. Consequently, understanding the conditions under which fracturing in the EDZ/EdZ is induced and the corresponding mechanisms are important.

The mechanical response of a rock mass to the construction of an underground opening depends on the orientation(s) of existing geological structures and the path of the ensuing stress redistribution. Structurally-controlled failure is gravity-driven and depends on the intersection of the opening with existing geological discontinuities. Stress-driven failure depends on the rock mass strength and on the magnitudes and orientations of the in situ stress field relative to the opening. In both cases, confinement plays an important role in dictating the mode of failure and the orientation of macroscopic fracturing (Fig. 3.2). Failure in a brittle rock mass can occur in three modes: tensile failure, spalling failure, and shear failure. Tensile-driven failure dominates when the minor principal stress (σ_3) is less than zero. As σ_3 approaches zero, the predominant failure mode becomes that of spalling (where no spalling occurs to the right of this line). At this point, the in situ failure envelope deviates from that determined in the laboratory towards a lower bound coinciding with damage initiation [2, 3]. This corresponds with the onset of seismicity (acoustic emissions) and the accumulation of micro-fracture damage. With increasing confinement, the third failure mode of shear is prevalent. The zone bounded between damage initiation and the failure envelope is one of reduced rock mass strength where damage is distributed. In addition to the final stress state, the path followed needs to be considered as Martin [4], through numerical modelling, Ganne and Vervoot [5], through laboratory experiments, and Kaiser et al. [6], through field measurements, have shown the stress path can be complex involving several changes in magnitudes and directions.

Indurated argillaceous materials, such as the Opalinus Clay (with an in situ water content of 6%, liquid limit of 38%, and plastic limit of 23% [7]), exhibit both rock-like (brittle) and soil-like (ductile) behaviour; thus, complex mechanisms are involved in the development and evolution of the EDZ/EdZ in such materials. Additionally, inherent to most shales is the added complexity of sedimentary-related structures. As a result, understanding induced fracturing in indurated argillaceous media requires considerations of both stress redistribution and sedimentary structures. Examples of this can be found at the Tournemire Underground Research Laboratory [8] and the Mont Terri Rock Laboratory [9].

The laboratory at Tournemire is located adjacent to a motorway tunnel that dissects the argillaceous Toarcian formation [8]. The uniaxial compressive strength (UCS) of the Toarcian formation at

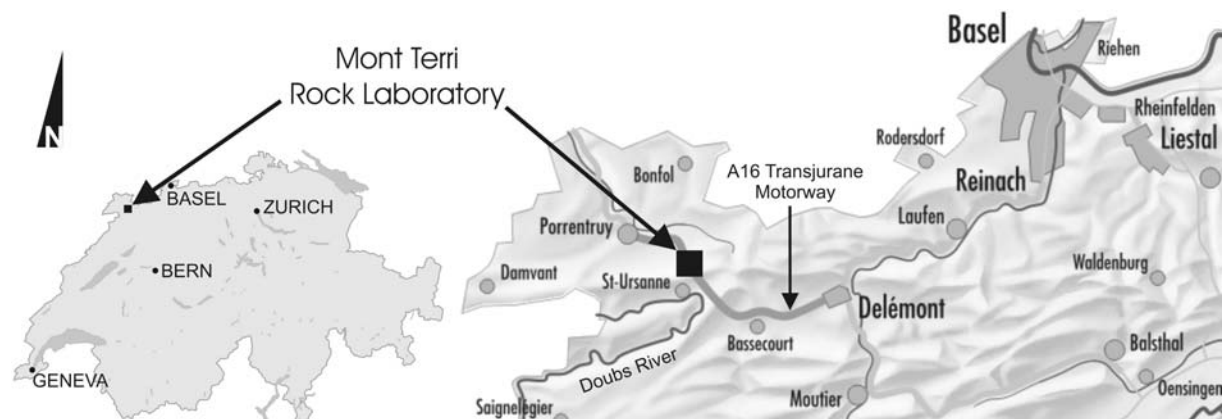


Fig. 3.1: Location of the Mont Terri Rock Laboratory in northern Switzerland (modified from www.swisstopo.ch).

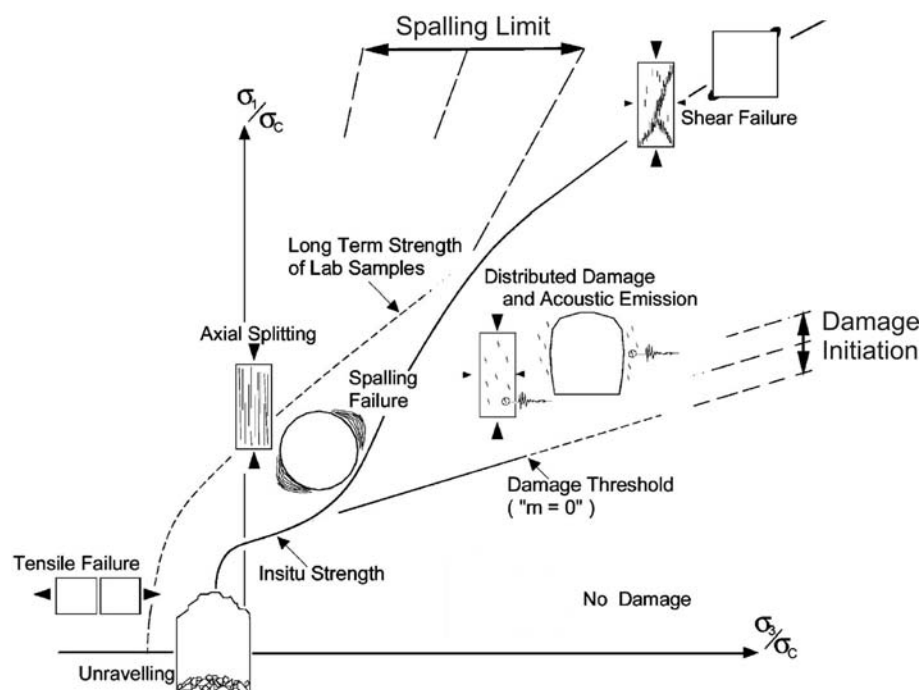


Fig. 3.2: Different rock failure modes along in principal stress space (after Diederichs [2] and Kaiser et al. [3]).

Tournemire, which dips sub-horizontally towards the north, ranges from 13MPa (perpendicular to bedding) to 32MPa (parallel with bedding). EDZ/EdZ extents of 0.16 to 0.22 tunnel radii have been determined around three openings at the laboratory from drillcore mapping (i.e. identification of induced fracturing), petrophysical measurements (i.e. changes in the degree of saturation) and pneumatic and hydraulic tests (i.e. permeability changes). Drillcore mapping have shown induced fracturing consists of two networks: one oriented sub-parallel with the opening axis and the other sub-parallel with bedding. The first has been attributed to stress redistribution resulting from tunnel construction while the second has been attributed to desaturation of the rock mass due to ventilation of exposed rock surfaces.

The Opalinus Clay formation at the Mont Terri Rock Laboratory dips towards the southeast at 22° to 55° [10]. The uniaxial compressive strength of the Opalinus Clay ranges from 10MPa at bedding-parallel loading to 16MPa at bedding-perpendicular loading [7]. The EDZ/EdZ has been investigated by means of geological mapping of tunnel surfaces, drillcore mapping, seismic measurements, and hydraulic and pneumatic testing [11, 9]. The EDZ/EdZ at Mont Terri extends for half to one tunnel radii from the excavation periphery and induced fracturing consists of sidewall fractures oriented parallel with the tunnel axis and bedding-parallel fractures above the crown and below the invert [11, 9]. Fracturing in the sidewalls has been attributed to spalling while bedding-parallel fracturing occurs in zones of extensional [11].

Bedding in the Opalinus Clay at Mont Terri is the most prominent geological feature consisting of persistent ubiquitous planes spaced at millimetres. This is consequently reflected in the anisotropic nature of the mechanical properties; the Young's modulus ranges from 4GPa, perpendicular to bedding, to 10GPa, parallel with bedding. An additional complexity at the Rock Laboratory is the consistent occurrence of two sets of tectonic shears [12]. The use of "shears" in this thesis departs from the terminology established at the Rock Laboratory, where the use of "faults" prevails. Preference is given to "shears" as the term better describes the displacement magnitude and thickness of the structures mapped at the Rock Laboratory. Geological maps of niche surfaces in older parts of the laboratory [13] provide evidence that the shears influenced both the frequency and termination of induced fracturing (Fig. 3.3). At Mont Terri, much of the analyses have focused on the bedding anisotropy owing to its prominent nature, which affects both mechanical properties and the development of the EDZ/EdZ. Consequently, little is known regarding the impact of the tectonic shears on the EDZ/EdZ. Observations made during a recent expansion of the laboratory indicated that the shears may play an important role in the development of induced fracturing. A new 80m-long gallery (Gallery04) was excavated in 2004 with four adjoining niches

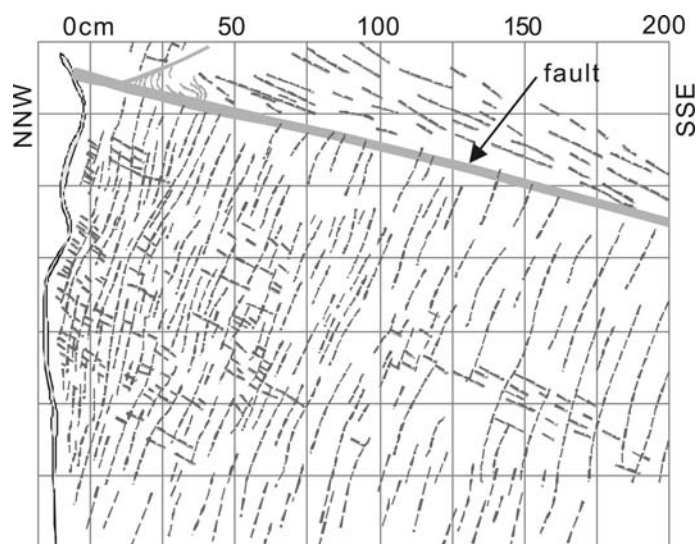


Fig. 3.3: Interference of tectonic shears on induced fracturing (dashed lines) in the northeast wall of the EB Niche (after Nussbaum et al. [13]). Refer to Fig. 3.4 for the location of the EB Niche.

that facilitated mapping of the damage caused by the gallery construction. This chapter examines the influence of the tectonic shears on the fracturing induced in one of the niches (EZ-B Niche) and the potential mechanisms involved.

3.2 Site Description

Located northwest of Saint-Ursanne (Fig. 3.1), the Mont Terri Rock Laboratory consists of two galleries and a series of niches excavated adjacent to the A16 Transjurane Motorway tunnel (Fig. 3.4). The Rock Laboratory is an international research facility (and is not under consideration as a repository site) was initiated in 1996 with the excavation of eight niches in the southwest wall of the Security Gallery. In 1998, Gallery98, with a nominal length of 175m, was excavated southwest of the NNW-SSE (332° to 152°) trending Security Gallery. More recently, the laboratory was expanded southeast of Gallery98 in 2004 with the excavation of the 80m-long Gallery04. Gallery04 trends 262° for the first 30m then curves northwards to a final azimuth of about 300° . The site of interest in this chapter is Gallery04 in the vicinity of the EZ-B Niche between tunnel metres (TM) 20 and TM25 (Fig. 3.5).

Excavation of Gallery04 and its niches involved a road header and pneumatic hammer [14, 12]. Gallery04 and the DR Niche were excavated with a road header while a pneumatic hammer was additionally used in

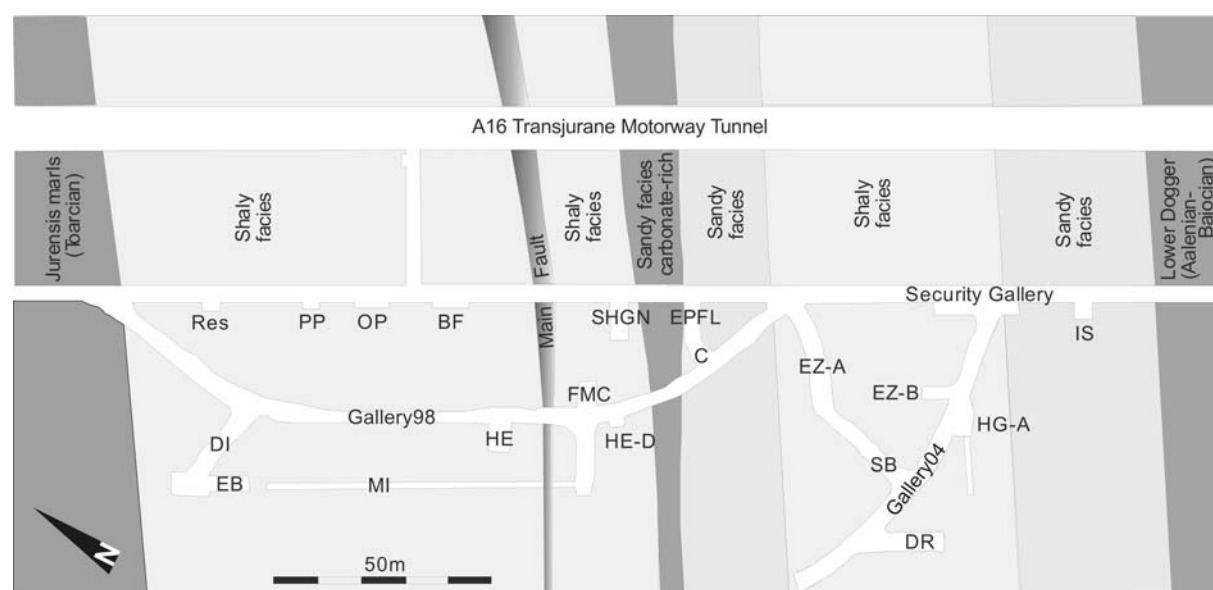


Fig. 3.4: Location of the EZ-B Niche in Gallery04 (after Nussbaum et al. [12]).

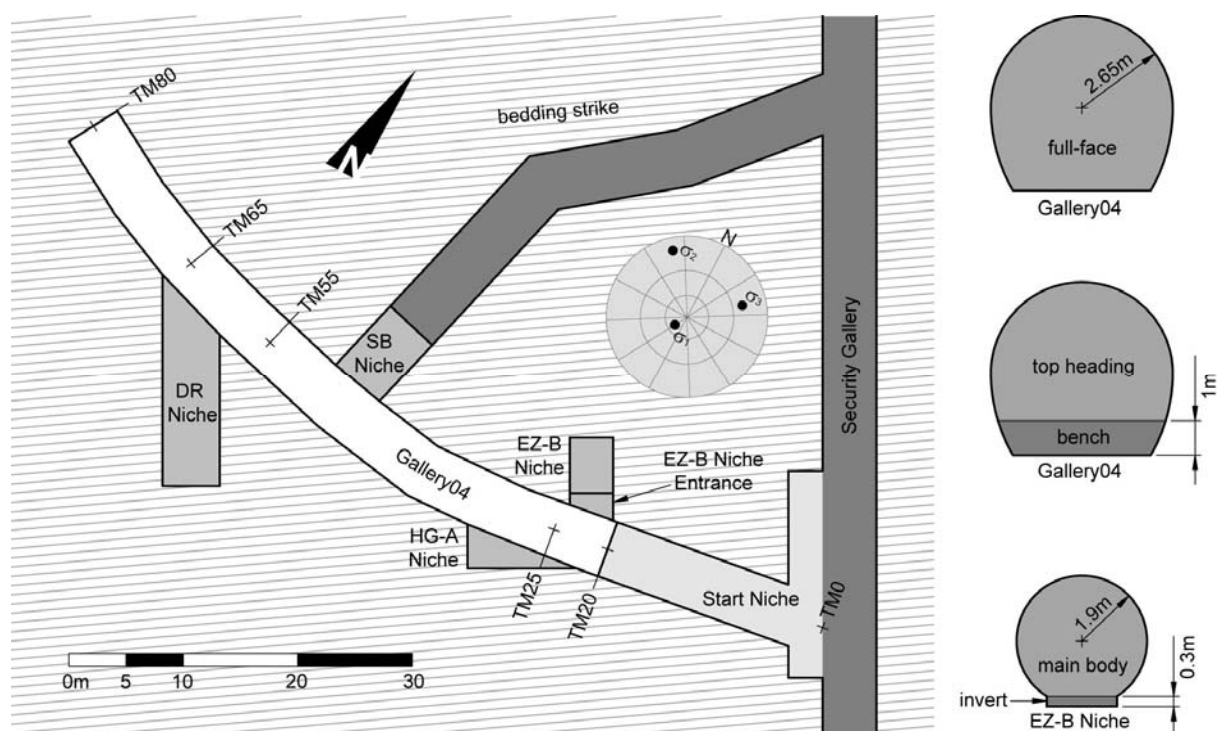


Fig. 3.5: Layout of the Rock Laboratory around the EZ-B Niche and in situ stress field (lower hemisphere) with cross-sections of Gallery04 and the EZ-B Niche to the right.

the EZ-B, SB, and HG-A Niches. In the SB Niche, the pneumatic hammer was used only in the rear to finish the profile while the hammer was used in the HG-A Niche to excavate the invert. The EZ-B Niche was excavated with the pneumatic hammer in its entirety with the exception of its entrance where the road header was used in addition to the pneumatic hammer.

Gallery04 was excavated in three stages (Fig. 3.5). A 20m-long section (Start Niche) was first excavated under full-face conditions in March 2004 over a span of 25 days [14]. The final face of the Start Niche terminated near the east wall of the EZ-B Niche (TM20). The remaining length of Gallery04 was excavated in two stages [12]: a top heading and a 1m-bench. The top heading was excavated continuously over a period of 58 days spanning August to October, 2004. The bench was excavated up to TM55 in eight days (28 October to 4 November, 2004) and stopped for the excavation of the SB and DR Niches. The bench excavation then re-commenced and was completed in an additional five days (25 to 29 November, 2004). The HG-A Niche and the entrance to the EZ-B Niche were subsequently completed over a five-day period (6 to 10 December, 2004).

Support in the gallery and the adjoining niches consisted of steel and fibreglass anchors and steel- or fibre-reinforced shotcrete. At the end of each excavation day, 3m-long anchors (25mm diameter) were installed in areas most susceptible to structurally-related instabilities and shotcrete was applied to the newly-excavated surfaces. In the first 20m, anchors were installed where bedding or the bedding-parallel shear set was tangent to the gallery profile (between 9 o'clock and 11 o'clock, looking northwest). In the next 10m, anchors were installed between 9 o'clock and 12 o'clock. Prior to the invert excavation from TM20, anchors were also installed in both lower sidewalls. At the end of each day during the bench excavation, the shotcrete layer was continued from the bench walls to the previously excavated top heading surfaces. The final shotcrete thickness was nominally 15cm. The last element of support was a 300mm-thick concrete floor slab, poured in four stages. The gallery floor was completed in the first (10 November, 2004) and third stages (2 December, 2004) with the former stretching TM20 to TM55 and the latter including the DR Niche. The SB Niche floor was completed in the second stage (19 November, 2004) while the floors of the HG-A Niche and EZ-B Niche entrance were completed in the final stage (13 December, 2004).

3.3 Geological Setting

Intersecting the Opalinus Clay formation, the Mont Terri Rock Laboratory is situated in the southern limb of the SW-NE trending Mont Terri Anticline. The Opalinus Clay is shale deposited in a basinal marine environment during the Middle Jurassic. Following deposition, the shale was subjected to two successive burial events (during the Cretaceous and Miocene) that were separated by a period of uplift [15]. More than 1km of burial and an estimated 600m of erosion have resulted from these events with the maximum burial and compaction occurring in the shorter Miocene event [15, 10]. Following this, the area of the laboratory emerged and erosion and down-cutting by the Doubs River (southwest of the laboratory, Fig. 3.1) began [16]. Glaciation during the Pleistocene did not provide additional burial as the most extensive ice cover terminated about 8km south of the laboratory [16]. Where the laboratory lies, the present overburden is 250-320m [17].

Mont Terri is the northernmost in a series of anticlines that constitute the Folded Jura in the Jura Mountains. Inherited pre-orogenic tectonic structures were crucial for the development of the Folded Jura [18, 19]. During the second burial event, the adjacent Delémont basin began to subside and with it, the Mont Terri flexure formed along with a N-S strike-slip fault system east of the laboratory [16]. A period of WNW-ESE extension followed [19]. This pre-orogenic fault pattern controlled subsequent tectonic activity by disrupting the Triassic basal décollement of the Jura Mountains and controlling the nucleation of thrusts, folds, and transfer zones; the pronounced along-strike asymmetry characteristic of the northernmost anticlines (including Mont Terri) was pre-determined by this fault pattern [18]. The Jura Mountains formed during late Miocene-early Pliocene in response to late alpine folding and thrusting, which resulted in the Folded Jura being thrust more than 1km north-westwards over the Tabular Jura [19]. The Mont Terri anticline (Fig. 3.6) was formed by fault bend folding and fault propagation folding that have resulted in a number of thrust faults [20, 12]. The N-S strike-slip system has also segmented the northern limb of the anticline into a number of pieces [17]. The laboratory is located in the weakly deformed and less tectonically disturbed southern limb [10]. A detailed description of the tectonic history of the Mont Terri area can be found in Bath and Gautschi [10], Ustaszewski and Schmid [18], and Homberg et al. [19].

3.3.1 Opalinus Clay

The Opalinus Clay is overlain by limestone and underlain by a sequence of marls, shales, and limestones (Fig. 3.6). The Opalinus Clay is dark grey shale consisting of claystone and marl with intercalated sandy and calcareous layers and lenses. At Mont Terri, the formation consists of five lithostratigraphic subunits grouped into three main facies [21]: shaly, sandy, and carbonate-rich sandy (Fig. 3.4). The major components of the shaly facies, where the Gallery04 and EZ-B Niche are located, consists of [21]: clay minerals (58-76%), carbonates (0-28%), quartz (6-24%), feldspars (0-3%), pyrite (0-2%), and organic carbon (0-2%). Clay minerals consist mostly of illite (16-40% of total weight) and kaolinite (15-33%) followed by chlorite (4-20%) and illite/smectite mixed-layers (0-20%). The carbonate fraction is

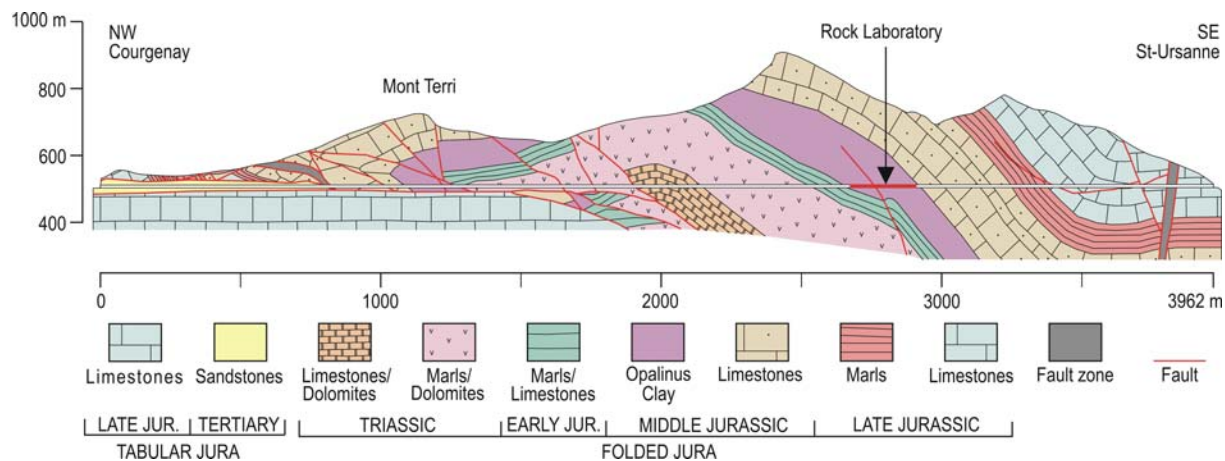


Fig. 3.6: Stratigraphic sequence along the Security Gallery (after Freivogel et al. [20]).

dominated by calcite at 5-28% (total weight), while the remaining consists of siderite (1-4%) and dolomite/ankerite (0-2%). Structurally, the fabric is dominated by bedding-parallel flocculation; bedding is well-developed and the most pronounced feature at Mont Terri (Fig. 3.7). Bedding in the laboratory dips towards the SE from 22° at the northernmost contact to 55° at the southernmost contact [10]. Bedding in the EZ-B Niche is millimetres thick (Fig. 3.7) with an average dip angle of 45° (ranging 38° to 50°) and dip direction of 147° (ranging 140° to 155°). Other structures include oxidized lenses (with siderite) and grey-white sandy lenses (with pyrite). Both are distributed throughout the niche surfaces and occur sub-parallel with bedding.

3.3.2 Tectonic Structures

At the laboratory-scale, tectonic features include shears and a single fault zone. Veins, joints, and kink bands have also been observed but only on rare occasions [10]. Three shear sets and a thrust zone (Main Fault; Fig. 3.4) are the prominent tectonic features at the Rock Laboratory [12, 22].

The most frequently occurring shear set is oriented sub-parallel with bedding and dips SSE (SSE bedding-parallel shears) [12]. This set was initiated during the early stages of Jura folding and then tilted towards the SSE during anticline folding. The bedding-parallel shears, closed and sealed with clay minerals and calcite, are splays related to the fault bend folding of the anticline. These shears are of minor tectonic importance with shear displacements in the order of millimetres (Nussbaum, pers. comm.). The second shear set (S-SW shears) consists of a sub-horizontal system dipping S to SW at a maximum of 22° [12]. The S-SW shears constitutes a minor thrust system and appears to be less developed in the older parts of the laboratory. Locally, the S-SW shears are cut and folded by the SSE bedding-parallel shears. The last and least frequently occurring shear set dips sub-vertically towards the W to WNW and has only been mapped in Gallery04 [12]. This set is associated with inherited structures related to extensional and strike-slip faults that were reactivated and tilted during folding of the anticline.

The Main Fault (Fig. 3.4) is 1-5m thick and the only larger thrust zone intersecting the laboratory. Also oriented sub-parallel with bedding but dipping slightly steeper (SE at a mean of 50°), the Main Fault shows a displacement of about 5m [22, 23]. The thrust zone consists of millimetre-thin faults (with a frequency greater than 20 per metre) with slickensided surfaces and highly deformed intervals displaying a braided network of connected micro-fractures filled with calcite [23].

In the vicinity of the EZ-B Niche, only two of the three shear sets have been mapped [24]: the SSE bedding-parallel and S-SW sub-horizontal shears. The SSE bedding-parallel shears is the dominant set with 12 to 13 thin (millimetres in thickness) shears intersecting the niche (Fig. 3.8). The extent of these shears is at least 20m as the same shear can be traced for a similar distance along Gallery04 [12]. The average shear frequency in the niche is one to two per metre. In addition to mapping, the location and orientation of these shears were also determined from laser scans undertaken as part of the field

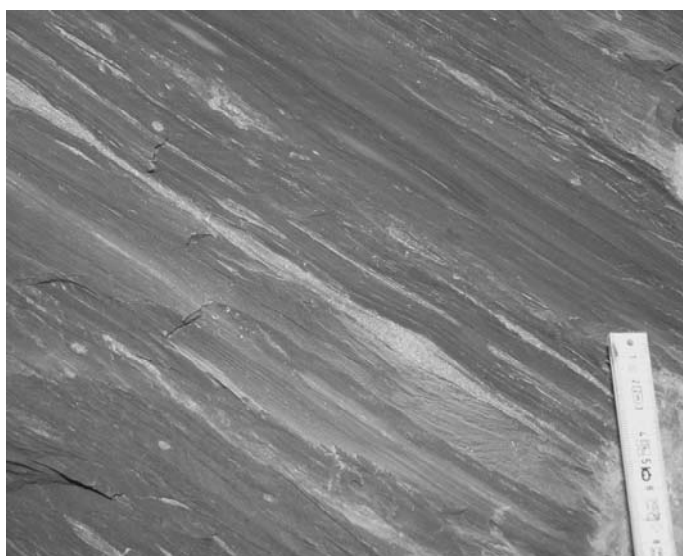


Fig. 3.7: Prominence of the bedding in the Opalinus Clay with interstratified sandy lenses.

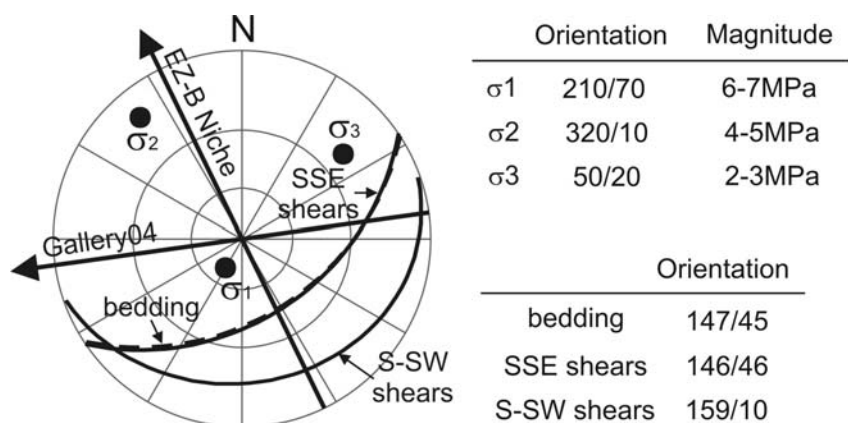


Fig. 3.8: The in situ stress field (lower hemisphere) at the Mont Terri Rock Laboratory. Bedding planes (dashed line) and SSE bedding-parallel shears (solid line) are nearly parallel.

investigation [25 or Chapter 2]. On average, the SSE shears dip 46° (ranging 45° to 50°) towards 146° (ranging 138° to 156°). In the EZ-B Niche, the S-SW shears are isolated to two areas: near the middle of the east wall and in the entrance of both walls. In both cases, these shears are bounded by the SSE shears. The S-SW set dips 0° to 20° towards 132° to 186° (Fig. 3.8). Shears of both sets are slickensided and indicate thrusting towards the northwest.

3.3.3 In situ Stress Field

A number of stress measurements utilising different techniques (borehole slotter, undercore, and hydro-fracture) have been carried out at the Rock Laboratory [28]. Due to the argillaceous nature of the material and the persistent and ubiquitous nature of the bedding planes, constraining the tensor has been a difficult task. Two different tensors have been derived from the borehole slotter and undercore methods [26, 27]. The largest difference between the two methods lies in the directions of the principal stresses. In the borehole slotter method, the maximum (σ_1) and intermediate (σ_2) principal stress lie in the bedding plane while the minimum principal stress (σ_3) is oriented normal to the bedding plane [26]. In the undercore method, σ_1 is sub-vertical while σ_2 and σ_3 are sub-horizontal [26].

Martin and Lanyon [27], through numerical modelling, found the tensor derived from the undercore method provided a better fit to the observations of borehole breakouts [27]. In addition, the normal stress acting on the bedding determined from the undercore method also agreed better with that determined from hydro-fracture measurements [27]. Martin and Lanyon [27] also reasoned that stress relief and erosion from valley formations to the southwest and northeast of the Rock Laboratory agreed better with the orientation of σ_3 determined from the undercore method. The elevation of the Laboratory, above the valley bottoms, was also used to justify the low σ_3 magnitudes (less than 2MPa) determined from both methods [27]. However, because undisturbed pore pressure at the Rock Laboratory is around 2MPa, Bossart and Wermeille [26] have recommended an equivalent minimum value for σ_3 .

The stress tensor recommended by Bossart and Wermeille [26], which accounts for the work of Martin and Lanyon [27] in addition to the other measurement campaigns, is used in this thesis (Fig. 3.8). Despite the past thrust fault regime, the maximum principal stress at the laboratory is sub-vertically inclined towards the S-SW. In this case, the maximum principal stress reflects the gravity loading of the rock mass above the Rock Laboratory. The minimum principal stress is sub-horizontal and oriented towards the northeast or approximately normal to the axis of the EZ-B Niche. The intermediate stress is sub-parallel with the niche with an offset of about 14° (Fig. 3.8).

3.4 Field Observations

Excavation of the EZ-B Niche entrance in the north wall of the gallery made it possible to map the fractures induced by the construction of Gallery04 (Fig. 3.9). Induced fractures in these maps have been distinguished based on their orientation with bedding and the gallery axis. The most commonly mapped system (IF1) is oriented sub-parallel with the gallery while features (IF2) oblique to the gallery axis are less often mapped as these were specifically sought after in the EZ-B Niche. The third system (IF3) is sub-

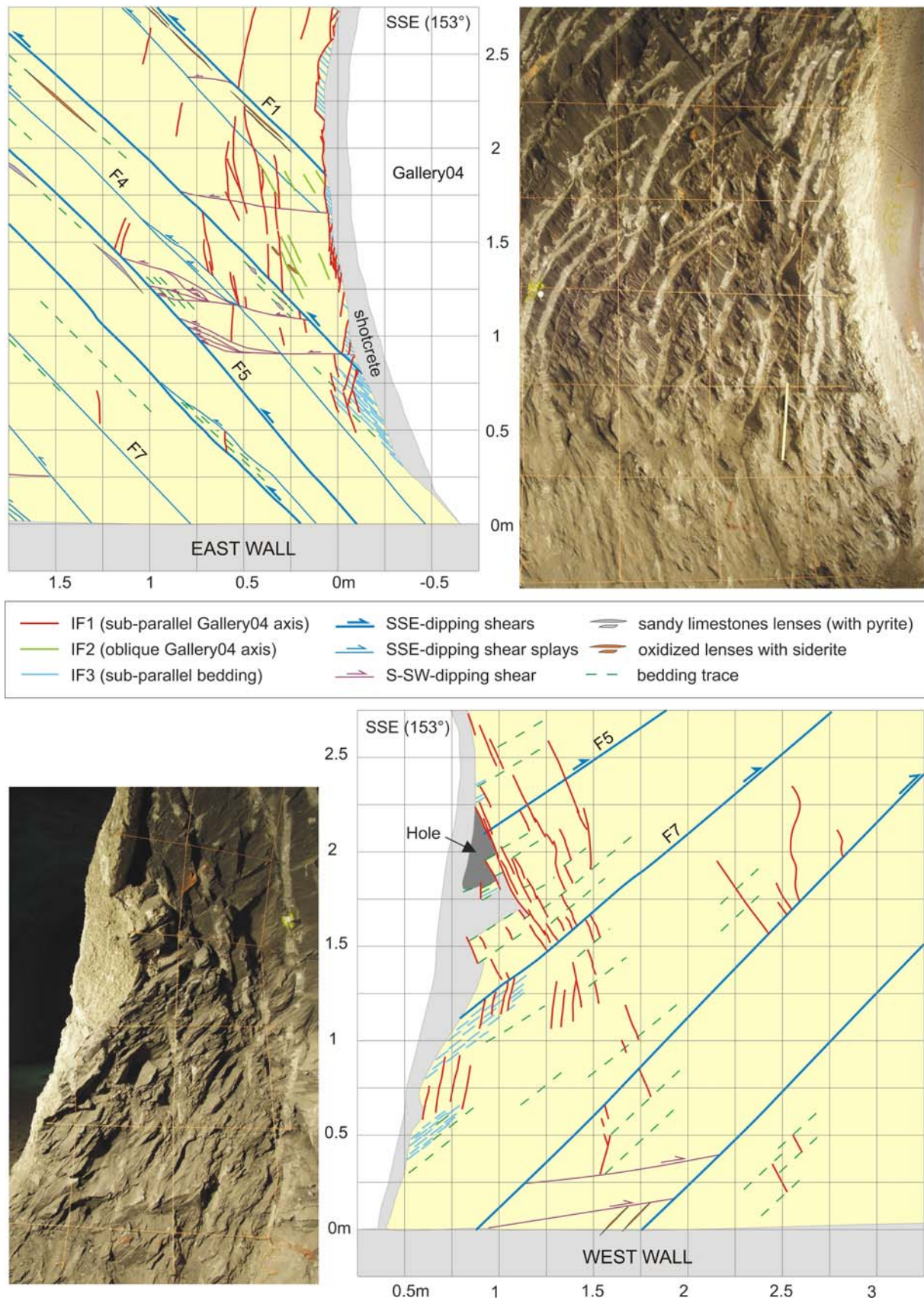


Fig. 3.9: Induced fracturing in the east (top) and west (bottom) walls in the EZ-B Niche entrance (geological maps after Nussbaum et al. [25]).

parallel with bedding and appears to be limited to the perimeter of the gallery. The first two systems are found at greater depths; IF2 fractures are found as far as 0.5m from the gallery wall and IF1 fractures are found at depths exceeding 1m.

3.4.1 Influence of the Tectonic Shears

The influence of the SSE and S-SW shear sets on IF1 fracturing in both niche walls is shown in Fig. 3.9; fracture termination occur at or near the shear planes. Also notable in the west wall is the embedment of shotcrete near the niche mid-height, which suggests IF1 fractures may have formed quite quickly as shotcrete was applied as early as one hour and as late as three hours after the excavation step was completed [12]. A distinct difference observed between the two walls is that IF1 fractures were more or less parallel with the gallery wall in the east wall and more or less bedding-perpendicular in the west wall. These field observations indicated that the tectonic shears may influence not only the location of the IF1 fractures but also their orientation.

Understanding the difference in the IF1 fracture orientation between the east and west walls requires a return to the site description and the geological setting (Fig. 3.5). For the first 30m, Gallery04 trends about 70° from the Security Gallery or 25° to 30° from the strike of the SSE shears. The SSE bedding-parallel shears in the vicinity of the EZ-B Niche have an average dip of 46° and an average dip direction of 146°. Consequently, shears that intersected Gallery04 in the west wall of the niche did not intersect the gallery in the east wall of the niche. For example, F5 and F7 daylighted in Gallery04 in the west niche wall but neither daylighted in Gallery04 in the east niche wall (Fig. 3.9). Conversely, F1, F2, and F3 shears daylighted in the east wall but were not mapped in the west wall. In addition, S-SW shears daylighted in the east wall whereas those in the west wall did not. This led to kinematic freedom of F5 and F7 in the west wall and the S-SW shears, F1, F2, and F3 in the east wall. Thus, the distinct difference between the two walls seemed to be the kinematic freedom of the S-SW shears. Consequently, the SSE shears may have displaced more readily in the west wall while displacement along the S-SW shears may have reduced displacement along the SSE shears in the east wall. In this case, IF1 fracturing would be nearly perpendicular to the most displaced shear in both walls.

This difference in the orientation of induced fracturing was also observed in the geological maps of the SB Niche shown in Fig. 3.10. Similar to the EZ-B Niche entrance, induced fractures in the SB Niche west wall were oriented perpendicular to the SSE shears while those in the east wall followed the gallery wall. Again, the S-SW shears appeared to have interfered with the displacement of the SSE shears only in the east wall as they appeared sub-parallel to the SSE shears in the west wall.

3.4.2 Influence of Excavation Sequence

The excavation sequence of Gallery04 may have also played a role in the creation of the three fracture sets mapped in the EZ-B Niche entrance. Gallery04 is a rounded horseshoe in cross-section with a nominal diameter of 5.3m and height of 5m (Fig. 3.5). Excavation of the gallery near the niche consisted of three stages. The first 20m of the gallery (Start Niche), excavated full-face, terminated near the east wall of the EZ-B Niche. The rest of the gallery was excavated five months later as a top heading and bench. The first three days of the top heading excavation near the EZ-B Niche consisted of a weekend stoppage with the advancing face terminating near the centre of the niche [14, 12]. Consequently, it is speculated that either or both of these excavation steps could be responsible for the IF2 fractures seen in the east wall since these fractures were absent in the west wall. The oblique nature of the IF2 fractures may be indicative of fracturing around an advancing face.

Following completion of the top heading over the entire length of the gallery, the bench was excavated. The area near the niche was excavated about 60 days after the top heading excavation. In both walls, the largest area of bedding-parallel fractures (IF3) correlated roughly with the top of the bench. Additionally, orientations of the IF1 fractures in the west wall deviated from shear-normal to gallery-wall-parallel near this location. Above the bench and in the absence of shotcrete or concrete floor, no kinematic constraint was provided to the daylighting shears in the west and east walls. As a result, IF1 fracturing above the

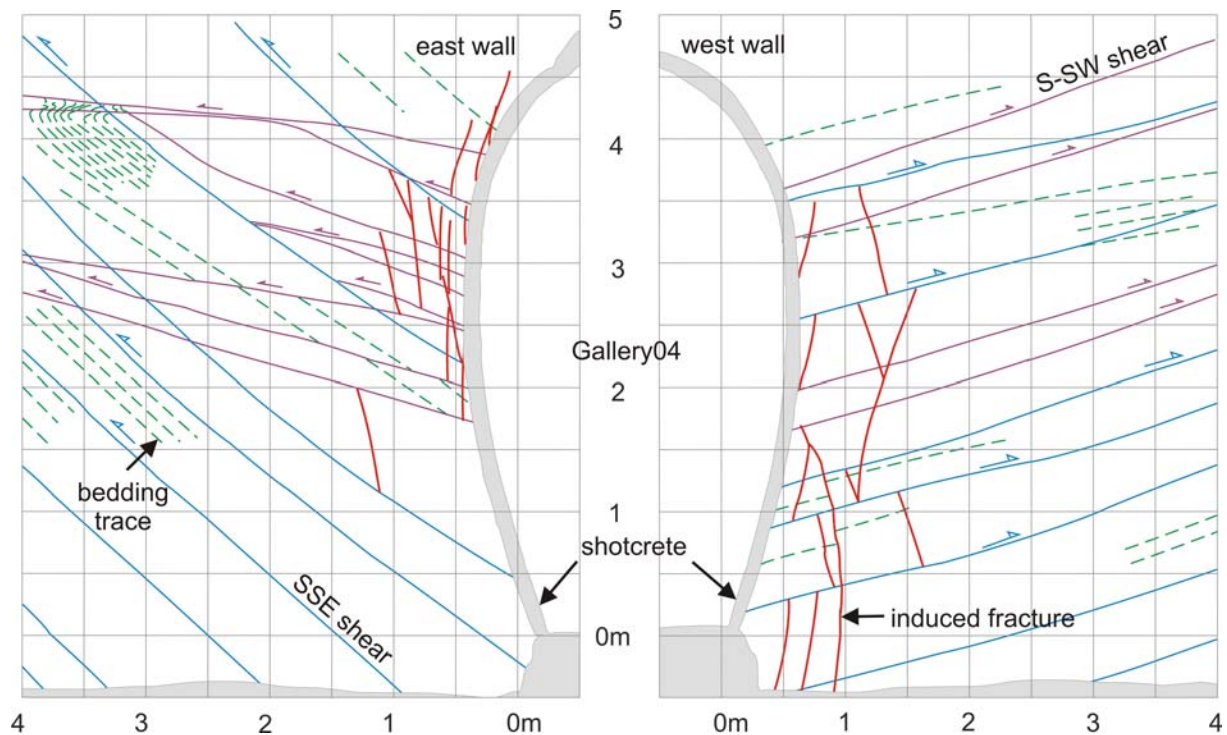


Fig. 3.10: Induced fracturing mapped in the SB Niche (after Nussbaum et al. [12]). “Faults” in this figure are referred to as “shears” in this thesis.

bench could be related to movement along the shears while the shears below the top of the bench may have had little to no affect on the mapped IF1 fracturing.

3.5 Mechanisms Responsible for Induced Fracturing in the north wall of Gallery04 near the EZ-B Niche

Simulating the observed difference in the IF1 orientations relative to bedding required a three-dimensional discontinuum model to account for the kinematic constraint of the SSE shears in a realistic manner. 3DEC (3-dimensional Distinct Element Code), version 3.00.116 DP, developed by Itasca Consulting Group Inc. [28] was used for the analyses presented here. Modelling with a three-dimensional discontinuum code required several days for one complete run, rendering parametric studies a time-consuming process. Hence, two-dimensional modelling in Phase2 [29] was first carried out to run parametric studies for determining appropriate mechanical properties for the SSE shears, which are poorly defined or even unknown.

3.5.1 Modelling Rock Anisotropy

Owing to the two-dimensional nature of Phase2, two models were built with one representing the west niche wall and one representing the east wall (Fig. 3.11). Construction of Gallery04 was simulated in two steps with excavation of the top heading in the first followed by excavation of the bench (Fig. 3.5). The external boundary was fixed in all directions and located about 40m from the gallery boundary, which was more than seven times the diameter of Gallery04. The SSE shears mapped in the EZ-B Niche and Gallery04 were modelled as continuous joints (Phase2 terminology for discontinuity elements) with a global dip angle of 46° (the average value mapped in the niche). The in-plane stress field in Gallery04 at the EZ-B Niche consisted of σ_1 at 7MPa inclined 20° from vertical (Fig. 3.11) and σ_2 as the minimum principal stress at 4MPa. The out-of-plane stress consisted of σ_3 at 2MPa. These values would result in the largest stress differentials and therefore, development of maximum deviatoric stresses.

In the elastic analyses of both walls, three scenarios were examined to assess the impact of rock anisotropy on the modelled results in comparison with field observations. The first scenario considered only the rock matrix (i.e. no joints), the second considered the SSE shears, and the third considered both the SSE and S-

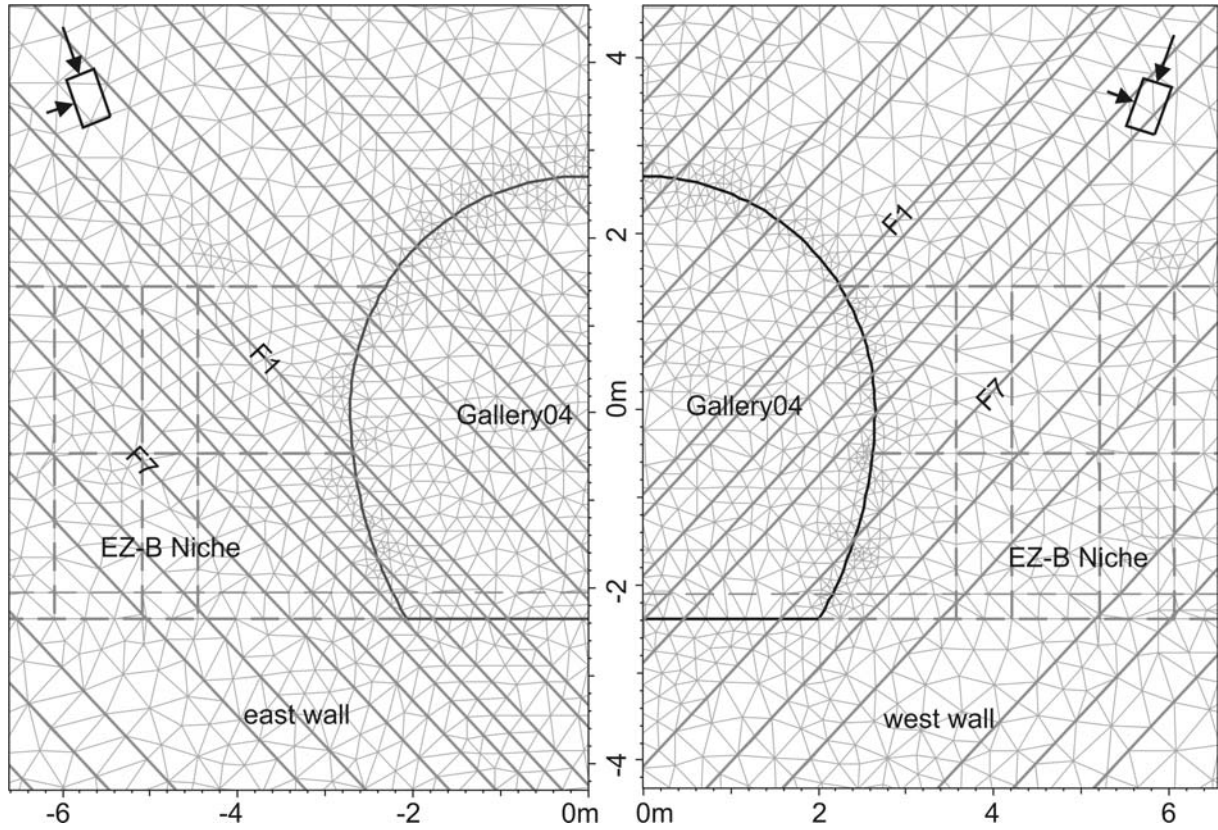


Fig. 3.11: Phase2 geometry and mesh of Gallery04 at the east and west walls of the EZ-B Niche.

SW shears mapped in the niche entrance. In this manner, model complexity increased from one scenario to the next. Additionally, two matrix conditions were compared in each scenario. The first considered an isotropic rock matrix (Tab. 3.1) while the second considered a transverse isotropic rock matrix (Tab. 3.1). In the latter case, the bedding anisotropy was represented with the isotropic plane inclined 45° from horizontal.

Iso-lines corresponding to three deviatoric stress levels are also included in the figures: 8MPa in red , 10MPa in white, and 16MPa in black. The deviatoric stress ($\sigma_1 - \sigma_3$) criterion has been shown to provide a realistic indication of the damage extent related to a compressive stress regime in several studies [30, 6, 4]. The criterion is based on compressive damage initiation (Fig. 3.2) and is expressed in relation to UCS (σ_c):

$$\sigma_1 - A\sigma_3 = B\sigma_c \quad (3.1)$$

where A and B are constants ranging from 1 to 1.5 for A and 0.3 to 0.5 for B [2]. B represents the reduction in stress levels at which in situ compressive damage has been observed. Accordingly, the deviatoric stress levels corresponding to compressive failure in tunnels in the Opalinus Clay range from 3MPa (with bedding-parallel $\sigma_c = 10$ MPa) to 8.5MPa (with bedding-perpendicular $\sigma_c = 16$ MPa) with A = 1. The 10MPa deviatoric stress iso-line then corresponds to a loading direction parallel with bedding while the 16MPa iso-line corresponds to a loading direction perpendicular to bedding [7]. Use of the deviatoric

Tab. 3.1: Elastic matrix properties used in the Phase2 analyses [5].

	Isotropic	Anisotropic
E(parallel bedding)	6 GPa	10 GPa
E(perpendicular bedding)		4 GPa
v(parallel bedding)	0.27	0.33
v (perpendicular bedding)		0.24

stress criterion as formulated above may be somewhat limited for anisotropic rock masses; however, it is used here to provide a point of reference.

Deviatoric stress contours from the first scenario, where no joints were included, are shown in Fig. 3.12. In both niche walls, matrix anisotropy (i.e. transverse isotropy) resulted in stress localisation near the invert of the niche entrance. This also coincided with where bedding was nearly tangential to the perimeter of Gallery04. In the second scenario (Fig. 3.13), the SSE shears were incorporated as elastic elements but with stiffness values equivalent to those used in the subsequent plastic analysis. Interestingly, the three deviatoric stress iso-lines differed only slightly between the isotropic matrix and transverse isotropic matrix cases. In a similar manner, deviatoric stress contours also did not differ significantly between the two matrix cases when the S-SW shears were added to the SSE shears in the last scenario (Fig. 3.14).

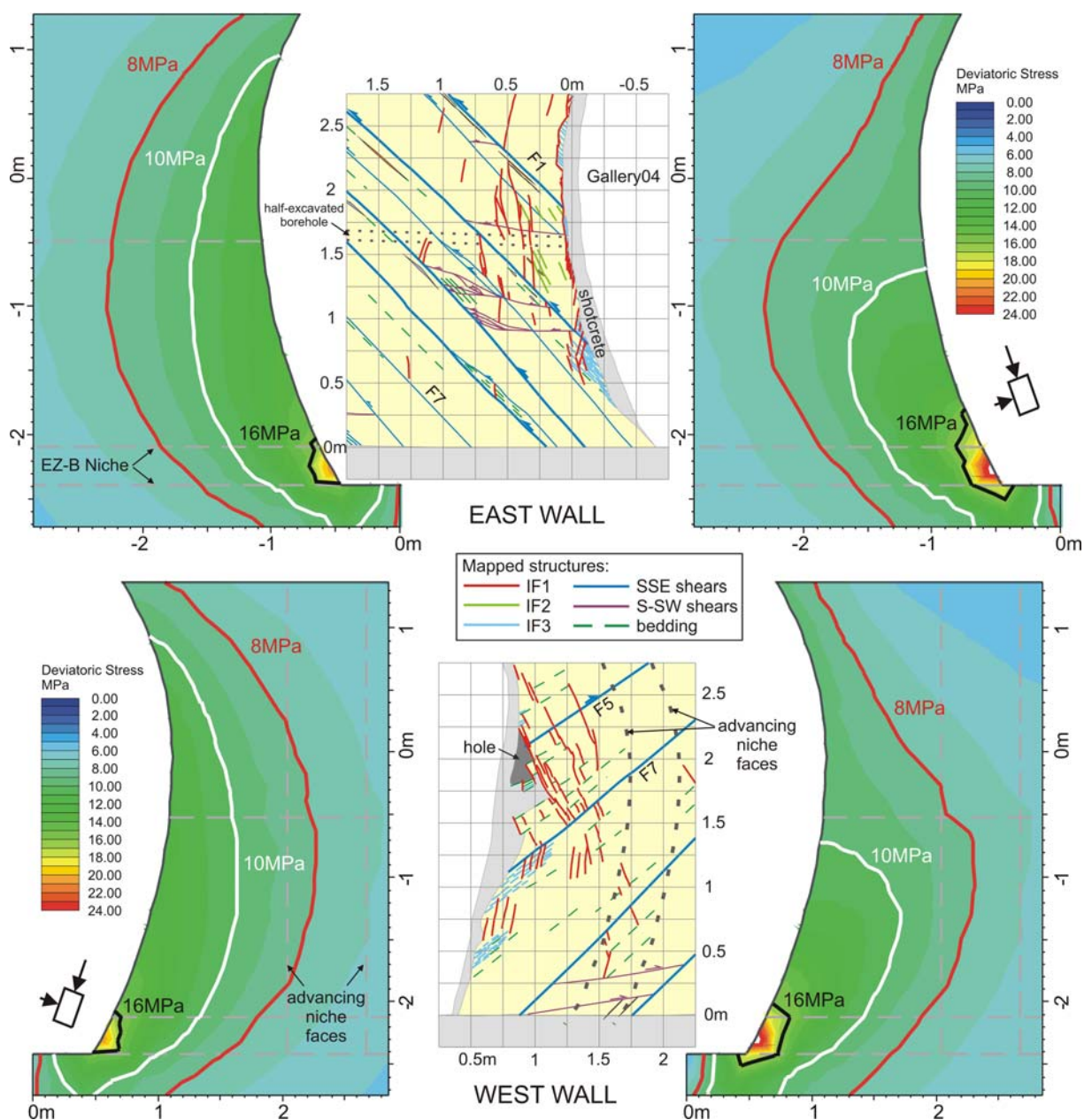


Fig. 3.12: Deviatoric stress contours of elastic isotropy (left) compared to elastic transverse isotropy (right) without consideration of the tectonic shears. East niche entrance wall in the top and west niche entrance wall in the bottom.

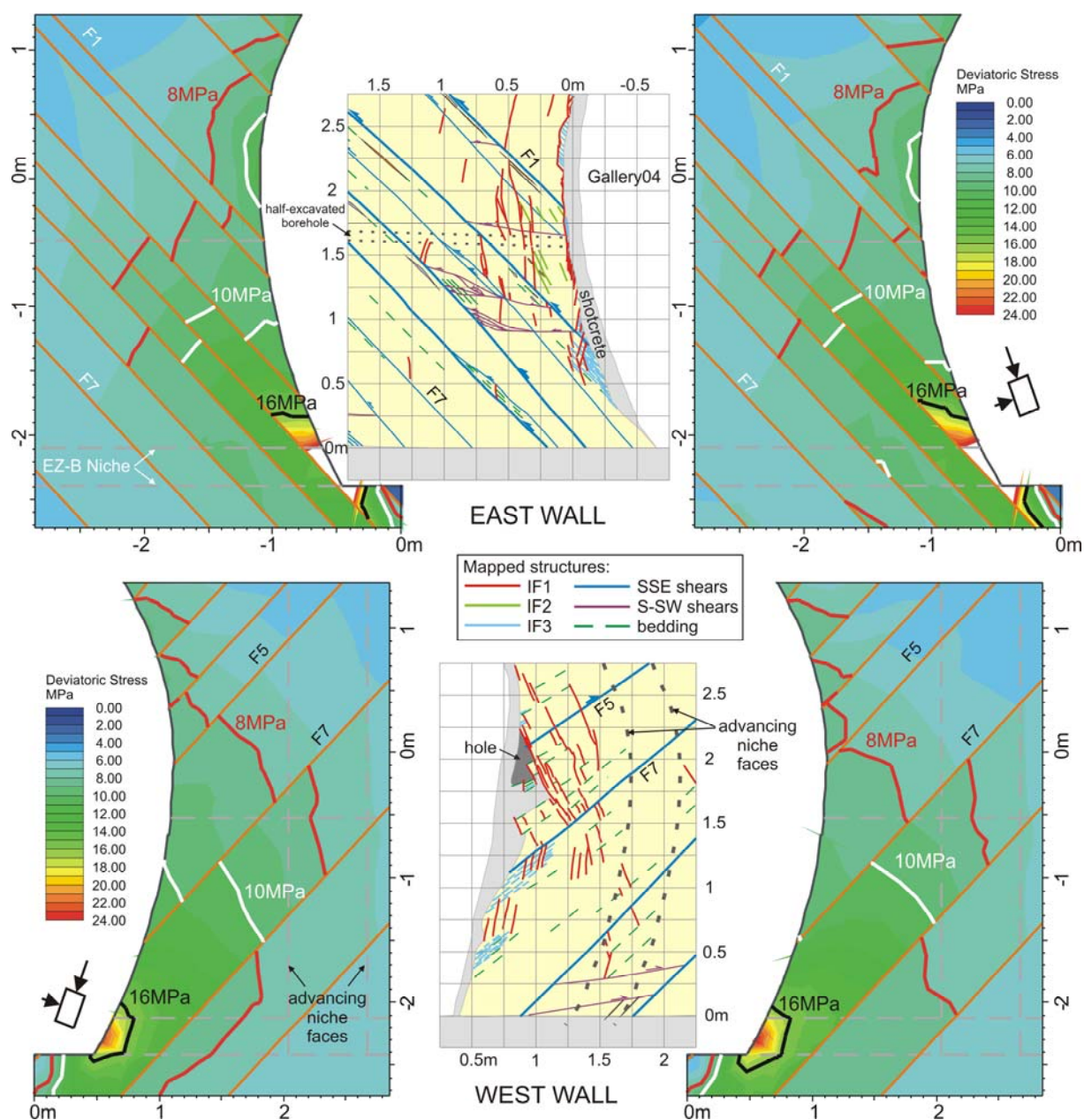


Fig. 3.13: Deviatoric stress contours of elastic isotropy (left) compared to elastic transverse isotropy (right) with only the SSE shears modelled. East niche entrance wall in the top and west niche entrance wall in the bottom.

The results from these scenarios demonstrated the importance of the tectonic shears on the stress redistribution in response to the excavation of Gallery04. When the tectonic shears were accounted for (i.e. more deformable than the surrounding matrix), the stress field was influenced in a similar manner whether or not the matrix was isotropic or anisotropic. This implied that rock mass anisotropy (i.e. due to the tectonic shears) may be a more critical factor in the EZ-B Niche entrance than the rock matrix anisotropy (i.e. due to the bedding). The last two scenarios also showed that the S-SW shears were more influential in the east wall than the west wall since the S-SW shears were much closer to the gallery in the east wall than the west wall. In particular, deviatoric stress contours between F2 and F5 became more parallel with the gallery perimeter in the east niche wall suggesting mobilisation of the S-SW shears. Conversely, the S-SW shears only had a local effect in the west wall as they were more kinematically constrained. Thus, the S-SW shears did not change the orientation of the deviatoric stress iso-lines in the west wall. These results implied that the SSE shears may have been mobilised without interference from the S-SW shears in the

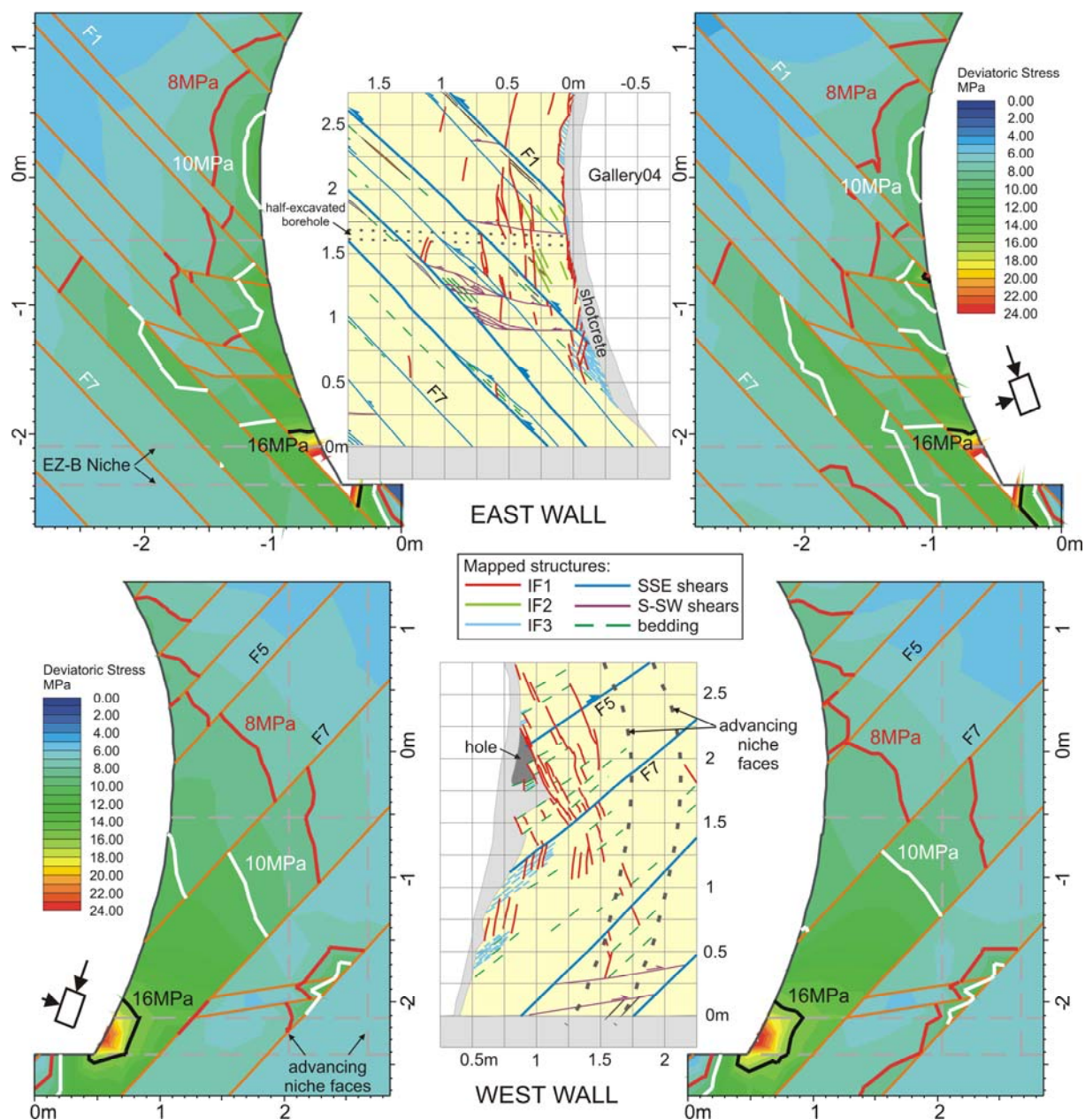


Fig. 3.14: Deviatoric stress contours of elastic isotropy (left) compared to elastic transverse isotropy (right) with all mapped shears modelled. East niche entrance wall in the top and west niche entrance wall in the bottom.

west wall. In contrast, mobilisation of the S-SW shears interfered with the mobilisation of the SSE shears in the east wall.

3.5.2 Estimating Properties for the Tectonic Shears

Mechanical properties of the Opalinus Clay at Mont Terri have been determined from laboratory testing on intact rock samples. Peak matrix properties are known but no information exists regarding the mechanical properties of the tectonic shears. Phase2 was used to estimate an appropriate range in values for the shears, specifically normal stiffness, shear stiffness, tensile strength, cohesive strength, and frictional strength. Consequently, plastic analyses of both walls were carried out under isotropic conditions for the matrix and with Mohr-Coulomb as the failure criterion for both matrix and joint elements.

Stiffness values of the tectonic shears were estimated according to Barton [31]. Given the rock mass modulus (E_{rm}) along with the intact rock modulus (E_i) and the spacing between joints (L), the normal stiffness is obtained via:

$$k_n = \frac{E_i E_{rm}}{L(E_i - E_{rm})} \quad (3.2)$$

Likewise, given the equivalent shear moduli (G) and the joint spacing, the shear stiffness is obtained via:

$$k_s = \frac{G_i G_{rm}}{L(G_i - G_{rm})} \quad (3.3)$$

The average spacing of the tectonic shears in the vicinity of the niche is about 1m. The intact rock moduli are known from Bock [7] but not the rock mass moduli. As a first approximation, the rock mass modulus was estimated based on intact UCS (σ_{ci}), GSI, and disturbance (D) according to Hoek et al. [32]:

$$E_m (GPa) = \left(1 - \frac{D}{2}\right) \sqrt{\sigma_{ci}/100} \cdot 10^{((GSI-10)/40)} \quad (3.4)$$

GSI for the Opalinus Clay at Mont Terri was estimated based on values typical of bedded, foliated, and fractured clay shale after Marinatos and Hoek [33]. This yielded a rock mass modulus of 0.8-1.3GPa for a corresponding GSI range of 25 to 30 and D = 0 (minimal disturbance). The corresponding normal and shear stiffness values were 920-1450MPa/m and 350-580MPa/m, respectively. These values represented reductions in the intact modulus greater than or equal to 75% and resulted in extensive matrix failure above the crown and below the invert when implemented in the models at maximum matrix strength (i.e. elastic, perfectly plastic). Stiffness values representing approximately 50% reduction of the intact modulus ($k_n = 4\text{GPa/m}$ and $k_s = 1.5\text{GPa/m}$) were found to produce more reasonable results in the extent of joint and matrix yielding. In turn, these values corresponded with a GSI range of 40 to 50, which coincided with a blocky structure and fair to poor surface conditions.

Estimating strength properties for the SSE and S-SW shears was an iterative process requiring parametric studies of both the matrix and joint elements. Given peak matrix strength with respect to bedding orientation [7], three peak strength scenarios were considered (Tab. 3.2): 1) values perpendicular to bedding, 2) values parallel with bedding, and 3) an average of the former and latter for cohesion and friction with a tension cut-off at the minimum tensile strength. For the tectonic shears and matrix post-peak, the parameters were constrained based on bedding plane strength (Tab. 3.2); bedding plane strength represented an upper bound in the tectonic shears and a lower bound in the matrix post-peak.

Two sets of parameters were ascertained, one for the west wall and one for the east wall (Tab. 3.3). Properties for the tectonic shears differed little between the two walls (Tab. 3.4). Cohesive strengths greater than 0MPa were required for the SSE and S-SW shears despite their slickensided nature. This may not be unrealistic as the shears have been often observed with calcite infilling [12]. Additionally, in the case of EZ-B Niche entrance, the tectonic shears displaced in the opposite direction of thrusting. As a result, asperities on the tectonic surfaces may have provided apparent strength. In both walls, smeared peak matrix properties provided the best match to the field observations in terms of extent (Fig. 3.15). In the matrix post-peak, a reduction of 0-15% was required in the east wall while a reduction of 15-45% was required in the west wall.

Tab. 3.2: Laboratory-determined matrix properties [5].

	Bedding-parallel Loading	Bedding-normal Loading	Smeared	Bedding Planes
UCS (MPa)	10	16	-	-
UTS (MPa)	2	1	1	-
c (MPa)	2.2	5.0	3.6	1
ϕ (°)	25	25	25	23
i (°)	0	0	0	-

Tab. 3.3: Matrix properties estimated from Phase2 ($E=6$ GPa, $\nu=0.27$).

	Tension (MPa)	C_{peak} (MPa)	ϕ_{peak} ($^{\circ}$)	i ($^{\circ}$)	C_{residual} (MPa)	ϕ_{residual} ($^{\circ}$)
east wall	1	3.6	25	0	3-3.6	25
west wall	1	3.6	25	0	2-3	25

3.5.3 Three-dimensional Analysis

The 3DEC model (Fig. 3.16) consisted of 2575 deformable blocks comprising a volume 52m in width, 64m in length, and 52m in height. The mesh was radially-graded from an edge length of 0.25m adjacent to the EZ-B Niche to 3.5m at the external boundaries. A minimum of 38 steps (including initial equilibrium) were required to simulate the as-built excavation advance of Gallery04, which in turn required 5 to 6 days (Intel Core 2 Duo 2.4GHz processor and 4GB RAM). Each step required 3000 to 6000 cycles to reach equilibrium, which was determined by monitoring displacements at various points and the unbalanced force.

The excavations modelled consisted of Gallery04 and the EZ-B and HG-A Niches (Fig. 3.16). Gallery04 was simulated as a straight alignment since it is straight east of the EZ-B Niche and curved at a radius of 45m to the west (Fig. 3.5). To minimize the runtime, the full cross-section of each opening was excavated at each step. Construction of Gallery04 was simulated in 1.6-2.3m steps with vertical faces; the actual advance averaged 1.8m and the faces were rounded [12]. This resulted in 13 steps from either external boundary to the niche walls with two steps required for the gallery immediately in front of the niche. The HG-A Niche was excavated in three steps with the last step including the entrance of the EZ-B Niche. Excavation the EZ-B Niche will be discussed in Chapter 4. The SSE shears were represented as parallel continuous planes of discontinuity dipping 46° towards 146° (to match the field measured average). The shears were also constrained to an extent 18m west and east of the EZ-B Niche and 19m south and 28m north of Gallery04 (Fig. 3.16). In addition to the 12 bedding-parallel shears mapped in the EZ-B Niche, bedding-parallel shears south and north of the niche were also included and located according to field mapping of the gallery [12]. External model boundaries, located four to eight tunnel diameters from Gallery04, were fixed in all three directions and the in situ stress field (Fig. 3.8) applied was the same as the Phase2 model (albeit transformed).

The model considered an isotropic and elastic matrix while the shears were allowed to fail according to the Mohr-Coulomb strength criterion (Tab. 3.5). Two sets of properties (Tab. 3.5) were considered for the tectonic shears to examine their influence. The first consisted of values estimated from Phase2 (“weakened”) while the second considered a “glued” state by assigning high values for tensile, cohesive, and frictional strengths. In the latter case, gluing the tectonic shears simulated significant kinematic constraint but did not eliminate deformation altogether as stiffness values were no different from those used in the weakened case.

3.5.4 Response of the Bedding-Parallel Shears

To understand the response of the bedding-parallel shears to the construction of Gallery04, the shear displacements along F1 and F7 were considered (Fig. 3.17). Also, both the weakened and glued cases were examined (Fig. 3.17). F1 intersected the east wall near the niche mid-height and the west wall near the crown while F7 intersected the west wall about 1m above the invert and did not intersect the east wall. The intersections of F1 with the east wall and F7 with the west wall in the numerical model were approximately where they were mapped in the field (Fig. 3.9). The five SSE shears mapped in between

Tab. 3.4: Tectonic shear properties estimated from Phase2 ($E=6$ GPa, $\nu=0.27$).

	Tension (MPa)	C_{shear} (MPa)	ϕ_{shear} ($^{\circ}$)	k_n (GPa/m)	k_s (GPa/m)
east wall	0	1-1.1	23-24	4	1.5
west wall	0	0.8-1.0	22-23	4	1.5

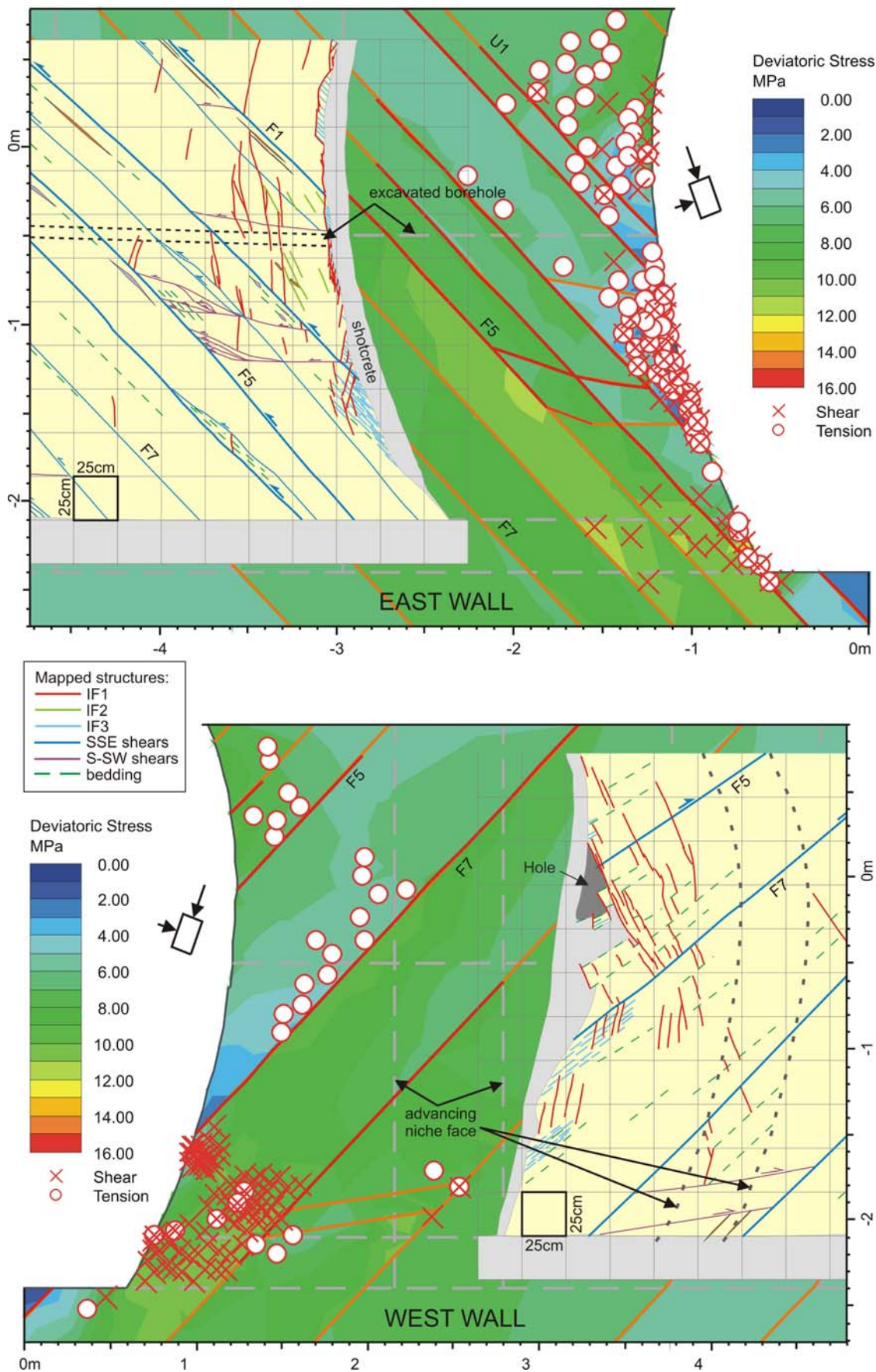


Fig. 3.15: Yielded matrix and joint elements from plastic isotropic analyses in Phase2 compared with field observations for the east niche entrance wall (top) and west niche entrance wall (bottom).

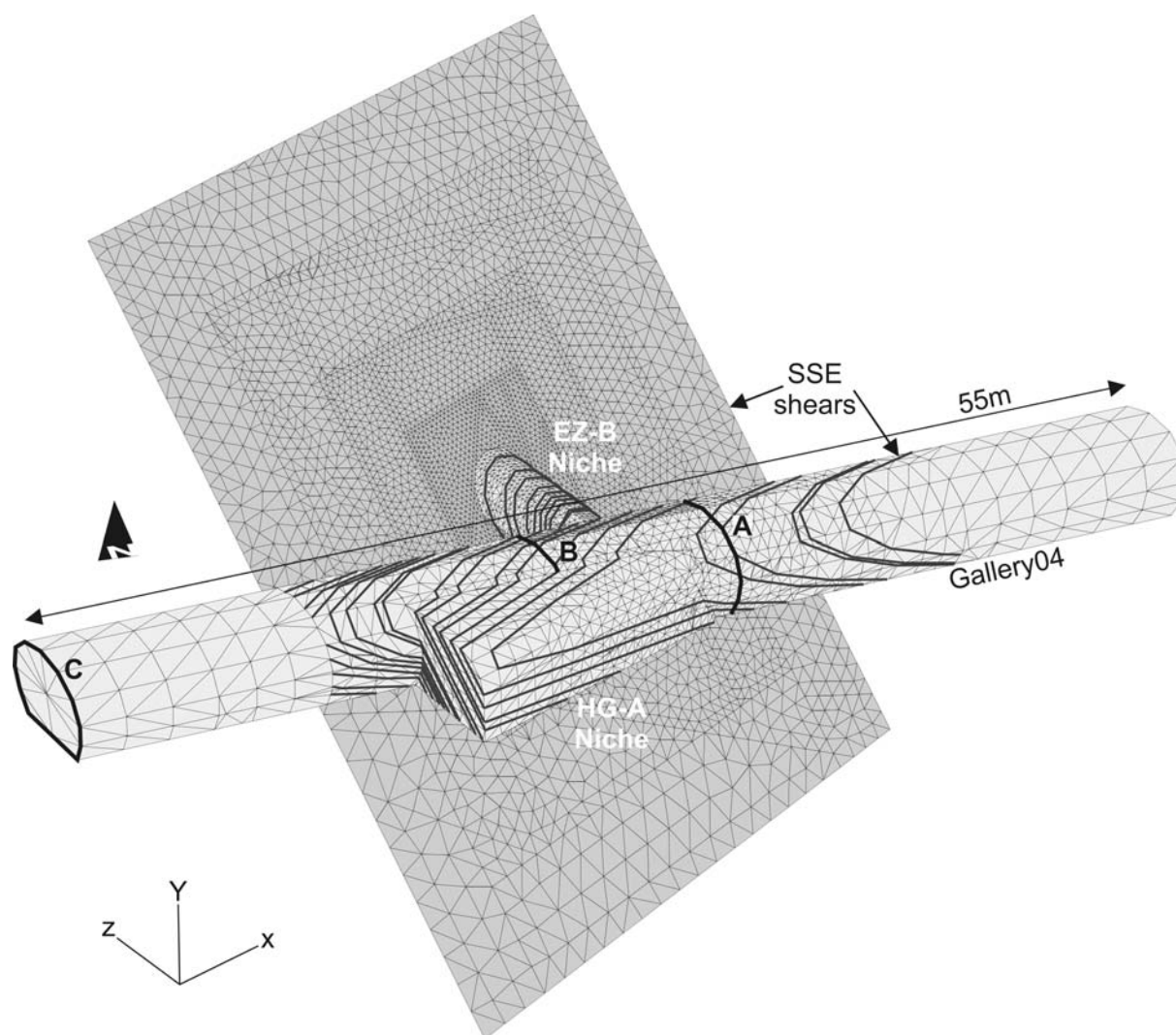


Fig. 3.16: Graded mesh of the 3DEC model illustrated on one of SSE bedding-parallel shears (looking northeast). Three reference points during the advance of Gallery04 are also indicated: A is 2m east of the east wall of the EZ-B Niche, B is 2m west of the west niche wall, and C is the end of the simulated Gallery04 excavation.

were located based on their relative locations along the east wall (Appendix B). For simplicity, the S-SW shears were not considered in the numerical model.

The numerical model showed that once Gallery04 was driven well past the west wall of the EZ-B Niche, shear displacements in the east niche wall along F1 exceeded those in the west wall (i.e. in the weakened

Tab. 3.5: Summary of the properties used in the 3DEC analysis.

Isotropic Matrix Properties		Tectonic Shear Properties					
		Weakened				Glued	
Density (kg/m ³)	2450	k_n (GPa/m)	4	Tension (MPa)	0	Tension (MPa)	100
Bulk Modulus (MPa)	4350	k_s (GPa/m)	1.5	c_{shear} (MPa)	0.8	c_{shear} (MPa)	100
Shear Modulus (MPa)	2360			ϕ_{shear} (°)	23	ϕ_{shear} (°)	100

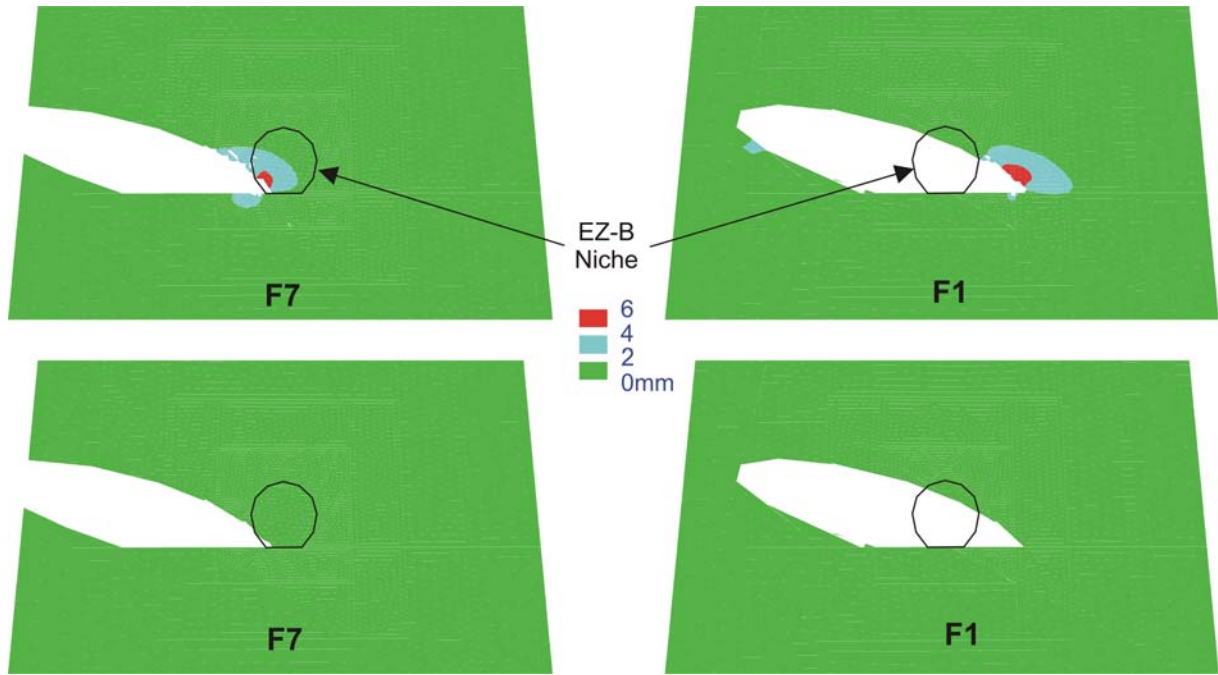


Fig. 3.17: Shear displacement contours along F7 (left) and F1 (right) at the end of the simulated Gallery04 excavation (i.e. point C in Fig. 3.16), looking towards the rear of the EZ-B Niche (northwest). Results from weakened properties are shown in the top and strengthened properties are shown in the bottom.

case in Fig. 3.17). In contrast, shear displacements along F7 were greater in the west niche wall. While gluing the tectonic shears resulted in significant reductions in shear displacement along both F1 and F7, the greatest impact was seen at F7 where shear displacements reduced by 50% (Fig. 3.17). Hence, it would seem that the SSE bedding-parallel shears were mobilised more readily in the west niche wall during the excavation of Gallery04. In the east niche wall, the Phase2 analysis demonstrated that the S-SW shears interfered with the mobilisation of the SSE bedding-parallel shears. The analysis here demonstrated that even without the S-SW shears, the SSE bedding-parallel shears were mobilised less in the east niche wall during the excavation of Gallery04.

3.5.5 Matrix Response

The matrix response was examined by following the minimum and maximum principal stress magnitudes at three points in each wall of the niche entrance as the gallery advanced (Fig. 3.18). Two points above (W1, W2) and one (W3) below F7 were considered in the west wall while one (E1) above and two (E2, E3) below F7

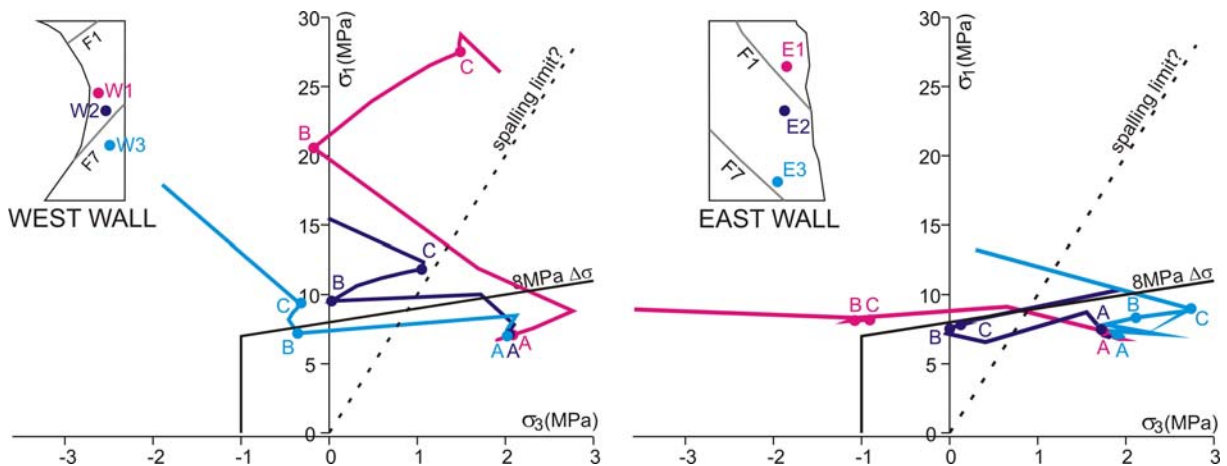


Fig. 3.18: Stress paths of the matrix in the west (left) and east (right) walls of the EZ-B Niche at weakened shears. Refer to Fig. 3.16 for the locations of the reference points: A, B, and C.

below F1 were considered in the east wall. E2 and W2 were located approximately at the niche mid-height. E1 was about 15cm from the periphery of Gallery04, E2 was around 35cm, and E3 was nearly 55cm. W1 and W2 were approximately 50cm and W3 was about 95cm from the periphery of Gallery04. The stress paths are plotted in Fig. 3.18 for the weakened case and in Fig. 3.19 for the glued case. Also plotted in both figures are the 8MPa deviatoric stress criterion and the spalling limit estimated after Dierderichs [2] and Kaiser et al. [3] at $\sigma_3:\sigma_1 = 0.1$. Point A in Figures 3.18 and 3.19 is about 0.4 tunnel diameters ahead of the east niche wall and point B is about 0.4 tunnel diameters behind the west niche wall. Point C is the end of the gallery excavation simulated in 3DEC (Fig. 3.16).

The numerical model showed that mobilisation (i.e. the weakened case) of the SSE bedding-parallel shears in the west wall resulted in stress levels well beyond the spalling limit and the deviatoric stress limit in the surrounding rock matrix (Fig. 3.18). In contrast, stress levels close to the deviatoric stress limit (i.e. the anticipated in situ damage initiation threshold) were reached when F7 was glued (Fig. 3.19). Moreover, stress changes in the east wall above and below F1 remained near the deviatoric stress limit even in the glued case. These results showed that the key to inducing the fracturing observed in the west entrance wall of the EZ-B Niche was the mobilisation of the SSE shears. Indirectly, the model showed that the induced fracturing observed in the east wall may not have been primarily caused by the SSE bedding-parallel shears. In this case, interference from the S-SW shears may be the key to the induced fracturing in the east wall.

3.6 Discussion

Failure of transversely isotropic rock mass [34, 35] depends on the inclination of weakness planes with the maximum applied stress. Fracturing occurs either along or across the planes of weakness. Failure along weakness planes is governed by the strength of the discontinuities, which reaches a minimum when:

$$\beta = \pi/4 + \phi/2 \quad (3.5)$$

where β is the angle between the plane normal and the maximum applied stress (Fig. 3.20). In contrast, failure across weakness planes additionally mobilises matrix strength. Consequently, the cohesive and frictional components of transversely isotropic rock mass strength vary with the orientation of the maximum applied stress.

In a series of uniaxial and triaxial tests on synthetic samples of transverse isotropy, Tien et al. [36] showed that fracturing along discontinuities dominated at β values of 31° to 80° under low confinement ($\sigma_3 = 0-6$ MPa). The greatest propensity for failure along discontinuities was reached when β was 50° to 60° . In the vicinity of the EZ-B Niche, the SSE shears averaged in dip around 46° (bedding dip averages about 45°). Hence, along an idealised half-section of Gallery04 in the vicinity of the EZ-B Niche, failure along the SSE bedding-parallel shears would most likely occur where β is approximately 50° to 60° (Fig. 3.20).

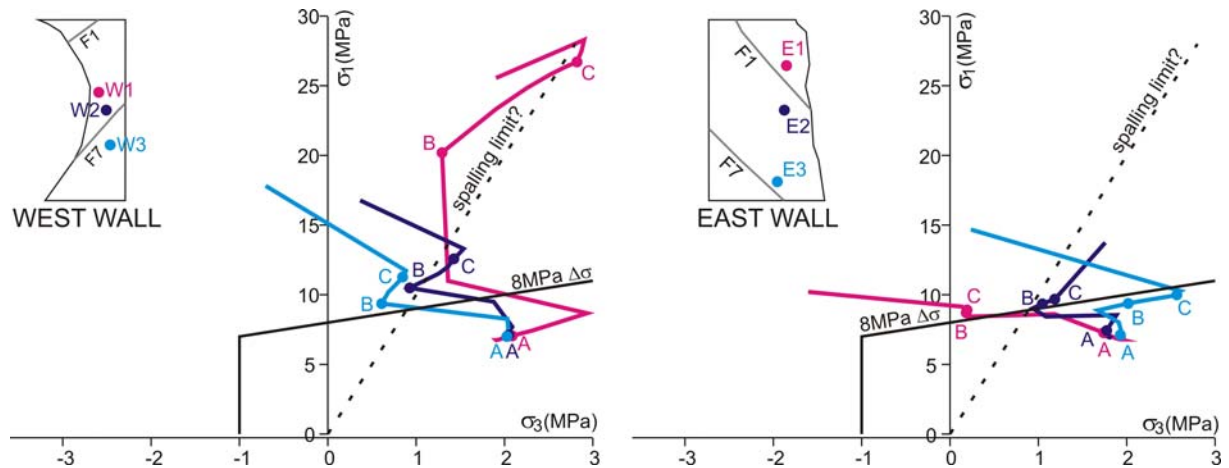


Fig. 3.19: Stress paths of the matrix in the west (left) and east (right) walls of the EZ-B Niche at glued shears. Refer to Fig. 3.16 for the locations of the reference points: A, B, and C.

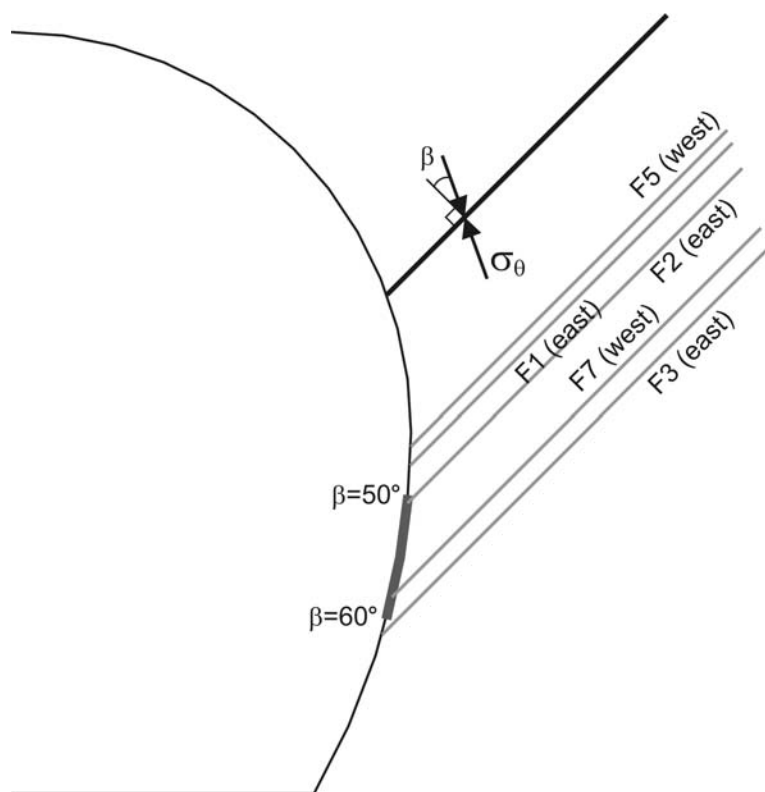


Fig. 3.20. Location of most critical β angles along the gallery wall. The approximate intersections of the bedding-parallel shears that daylight in Gallery04 are superimposed.

Additionally, with $\phi = 23^\circ$ to 25° (bedding and intact, respectively), the minimum strength for failure along weakness planes would be reached at $\beta = 56^\circ$ to 58° . This region coincided with the idealised intersections of all the mapped SSE bedding-parallel shears with Gallery04. Moreover, the largest deformations measured in the field during the gallery excavation occurred in a direction sub-parallel with bedding and/or the SSE bedding-parallel shears. Up to 65mm of convergence were measured in arrays east (18m, near the Security Gallery) and west (15m, near the SB Niche) of the niche [12].

Numerical modelling results demonstrated that SSE bedding-parallel shears were mobilised when their β values were conducive for failure along the shear and when interference from the S-SW shears were minimal or absent. This was the case for F7 in the west niche wall. Consequently, stress levels in the surrounding rock matrix exceeded both the deviatoric stress and spalling limits. In the east niche walls, mobilisation of the S-SW shears interfered with the mobilisation of the SSE bedding-parallel shears. As a result, induced fracturing in the east niche wall was most likely related to mobilisation of the S-SW shears. In particular, the S-SW shear located 1-1.5m above the top of the concrete floor (Fig. 3.15) appeared to be the more critical structure as most of the mapped induced fractures terminated near this shear, which also coincided with joint element yielding in the Phase2 analysis.

It should also be noted that the structural control of induced fracturing in the west entrance walls of the EZ-B Niche may be further exacerbated by the niche excavation itself as this resulted in the formation of a wedge in the west wall. Stress paths of the matrix in both EZ-B Niche walls changed considerably following the excavation of the entrance (Fig. 3.18). However, the impact of the entrance excavation on the fractures induced from the gallery construction is unclear as mapping necessitated the creation of a free surface intersecting the gallery.

3.7 Conclusions

Understanding the conditions under which fracturing in the EDZ/EdZ is induced and the mechanisms responsible are important in the context of geological nuclear waste disposal. Consideration of an overconsolidated argillaceous host adds mechanical complexities as these materials are inherently transitional and rarely isotropic. The Opalinus Clay at the Mont Terri Rock Laboratory exemplifies these qualities. Adding to the complexity at the research facility is the frequent and consistent occurrence of

small-scale tectonic shears. Much focus in the past has been on the rock matrix anisotropy (i.e. bedding) resulting from the ubiquitous and highly continuous bedding planes at the research facility. However, in this chapter, rock mass heterogeneity resulting from the inclusion of the mapped tectonic shears were shown to be a more dominant factor in the development of induced fracturing around Gallery04.

Geological mapping of excavation surfaces during a recent expansion of the facility provided evidence that tectonic shears influenced fracturing induced from the excavation process in both niche walls. In the west wall of the EZ-B Niche, the SSE bedding-parallel shears were mobilised without interference from the S-SW shears. In this case, the SSE bedding-parallel shears were mobilised when their β angles were conducive for failure along the shear. β represents the angle between the plane normal and the maximum stress trajectory. Consequently, as the SSE shears were mobilised, stress levels in the surrounding rock matrix exceeded both the deviatoric stress and spalling limits. In the east wall of the EZ-B Niche, mobilisation of the S-SW shears interfered with the mobilisation of the SSE shears. Furthermore, 3DEC modelling demonstrated that even without the S-SW shears, the SSE bedding-parallel shears were mobilised less in the east niche wall during the excavation of Gallery04. As a result, induced fracturing in the east niche wall was most likely related to mobilisation of the S-SW shears.

This investigation demonstrated that the tectonic shears at the Mont Terri Rock Laboratory can influence the fracturing induced by the excavation of an underground opening. However, the strength properties used in this thesis were estimated numerically as the properties of these properties are unknown. Consequently, it would be prudent to determine the strength properties of the tectonic shears encountered at the Rock Laboratory.

References

- [1] Tsang C-F, Bernier F, Davies C. Geohydromechanical processes in the Excavation Damaged Zone in crystalline rock, rock salt, and indurated and plastic clays-in the context of radioactive waste disposal. *International Journal of Rock Mechanics & Mining Sciences* 2005;42:109-125.
- [2] Diederichs MS. Rock fracture and collapse under low confinement conditions. *Rock Mechanics and Rock Engineering* 2003;36:339-381.
- [3] Kaiser PK, Diederichs MS, Martin CD, Sharp J, Steiner W. Underground works in hard rock tunnelling and mining. In: *GeoEng2000 An International Conference on Geotechnical & Geological Engineering*. Vol 1. Melbourne: Technomic Publishing Company; 2000. pp.841-926.
- [4] Martin CD. Seventeenth Canadian geotechnical colloquium: the effect of cohesion loss and stress path on brittle rock strength. *Canadian Geotechnical Journal* 1997;34:698-725.
- [5] Ganne P, Vervoort A. Characterisation of tensile damage in rock samples induced by different stress paths. *Pure Applied Geophysics* 2006;163:2153-2170.
- [6] Kaiser PK, Yazici S, Maloney S. Mining-induced stress change and consequences of stress path on excavation stability - a case study. *International Journal of Rock Mechanics & Mining Sciences* 2001;38:167-180.
- [7] Bock H. RA experiment rock mechanics analyses and synthesis: data report on rock mechanics. Unpublished Mont Terri Technical Report, 2001. 52pp.
- [8] Matry JM, Savoye S, Cabrera J. Desaturation and structure relationships around drifts excavated in the well-compacted Tournemire's argillite (Aveyron, France). *Engineering Geology* 2007;90:1-16.
- [9] Bossart P, Meier PM, Moeri A, Trick T, Mayor J-C. Geological and hydraulic characterisation of the excavation disturbed zone in the Opalinus Clay of the Mont Terri Rock Laboratory. *Engineering Geology* 2002;66:19-38.
- [10] Bath A, Gautschi A. Geological setting and sample locations. In: Pearson FJ, Arcos D, Bath A, Boisson J-Y, Fernandez AM, Gaebler H-E, Gaucher E, Gautschi A, Griffault L, Hernan P, Waber HN, editors. *Reports of the Federal Office for Water and Geology, Geology Series*. 2003. pp.30-35.

- [11] Martin CD, Lanyon GW, Bluemling P, Mayor J-C. The excavation disturbed zone around a test tunnel in the Opalinus Clay. In: Hammah R, Bawden W, Curran J, Telesnicki M, editors. Mining and Tunnelling Innovation and Opportunity. Vol 2. Toronto: University of Toronto Press; 2002. pp.1581-1588.
- [12] Nussbaum C, Bossart P, Burrus F, Badertscher N, Meier O, Nold A. Excavation of Gallery04: general documentation, deformation measurements and geological surveys. Unpublished Mont Terri Technical Note, 2005. 87pp.
- [13] Nussbaum C, Bossart P, Mayoraz J, Niederhauser B, Steiger H, Zingg A. Engineered barrier experiment structural mapping of artificial fractures and tectonic features of the EB niche. Unpublished Mont Terri Technical Note, 2002. 12pp.
- [14] Nussbaum C, Bossart P, Burrus F, Jeannin PY, Graf A. Survey and documentation of the Start Niche excavation. Unpublished Mont Terri Technical Note, 2004. 26pp.
- [15] Mazurek M, Elie M, Hurford A, Leu W, Gautschi A. Burial history of Opalinus Clay. In: Clays in Natural and Engineered Barriers for Radioactive Waste Confinement. 2002. pp.101-102.
- [16] Wermeille S, Bossart P. Paleohydrological study on the surroundings of the Mont Terri Rock Laboratory. Unpublished Mont Terri Technical Report, 1999. 22pp.
- [17] Bossart P, Wermeille S. Geological overview. In: Thury M, Bossart P, editors. Mont Terri Rock Laboratory: Results of the Hydrogeological, Geochemical and Geotechnical Experiments Performed in 1996 and 1997. Bern: Swiss National Hydrological and Geological Survey; 1999. pp.5-14.
- [18] Ustaszewski K, Schmid SM. Control of preexisting faults on geometry and kinematics in the northernmost part of the Jura fold-and-thrust belt. *Tectonics* 2006;25. 26pp.
- [19] Homberg C, Bergerat F, Philippe Y, Lacombe O, Angelier J. Structural inheritance and cenozoic stress fields in the Jura fold-and-thrust belt (France). *Tectonophysics* 2005;357:137-158.
- [20] Freivogel M, Huggenberger P. Modellierung bilanzierter Profile im Gebiet Mont Terri - La Croix (Kanton Jura). In: Heitzmann p, Tripet J-P, editors. Reports of the Federal Office for Water and Geology, Geology Series. 2003. pp.7-43.
- [21] Gaucher EC, Fernandez AM, Waber HN. Rock and mineral characterisation of the Opalinus Clay Formation. In: Pearson FJ, Arcos D, Bath A, Boisson J-Y, Fernandez AM, Gaebler H-E, Gaucher E, Gautschi A, Griffault L, Hernan P, Waber HN, editors. Reports of the Federal Office for Water and Geology, Geology Series. 2003. pp.281-303.
- [22] Nussbaum C, Bossart P, Zingg A, Inderbitzin L, Steiger H. Géométrie et cinématique d'une zone de chevauchement („Main Fault“) recoupant les Argiles à Opalinus dans le laboratoire souterrain du Mont Terri. Unpublished Mont Terri Technical Report, 2001. 28pp.
- [23] Bossart P, Adler M. Tectonic and artificial fractures. In: Thury M, Bossart P, editors. Mont Terri Rock Laboratory: Results of the Hydrogeological, Geochemical and Geotechnical Experiments Performed in 1996 and 1997. Bern: Swiss National Hydrological and Geological Survey; 1999. pp.19-26.
- [24] Nussbaum C, Bossart P, von Ruette J, Meier O, Badertscher N. EZ-B experiment: small-scale mapping of tectonic and artificial (EDZ) fractures of the EZ-B niche. Unpublished Mont Terri Technical Note, 2005. 23pp.
- [25] Yong S, Loew S, Fidelibus C, Frank E, Lemy F, Schuster K. Induced fracturing in the Opalinus Clay: an integrated field experiment. In: Leung CF, Zhou YX, editors. Rock mechanics in underground construction. Singapore: World Scientific; 2006. CD-Rom. 9pp.
- [26] Bossart P, Wermeille S. The stress field in the Mont Terri region data compilation. In: Heitzmann p, Tripet J-P, editors. Reports of the Federal Office for Water and Geology, Geology Series. 2003. pp.65-92.

- [27] Martin CD, Lanyon GW. Measurement of in-situ stress in weak rocks at Mont Terri Rock Laboratory, Switzerland. *International Journal of Rock Mechanics & Mining Sciences* 2003;40:1077-1088.
- [28] Itasca Consulting Group Inc. 3 Dimensional Distinct Element Code, version 3.0. Itasca Consulting Group Inc. 2003.
- [29] Rocscience Inc. Phase2 version 6.0 - finite element analysis for excavations and slopes. www.rocscience.com 2005.
- [30] Diederichs MS, Kaiser PK, Eberhardt E. Damage initiation and propagation in hard rock during tunnelling and the influence of near-face stress rotation. *International Journal of Rock Mechanics & Mining Sciences* 2004;41:785-812.
- [31] Barton NR. A model study of rock-joint deformation. *International Journal of Rock Mechanics & Mining Sciences* 1972;9:579-602.
- [32] Hoek E, Carranza-Torres C, Corkum B. Hoek-Brown failure criterion - 2002 edition. In: Hammah r, Bawden W, Curran J, Telesnicki M, editors. *Mining and Tunnelling Innovation and Opportunity*. Vol 1. Toronto: University of Toronto Press; 2002. pp.267-273.
- [33] Marinos P, Hoek E. GSI: a geologically friendly tool for rock mass strength estimation. In: *Proceedings of GeoEng 2000, Melbourne, 2000*. 19pp.
- [34] Jaeger JC. Shear failure of anisotropic rocks. *Geological Magazine* 1960;97:65-72.
- [35] McLamore R, Gray KE. The mechanical behavior of anisotropic sedimentary rocks. *Journal of Engineering for Industry* 1967;89:62-73.
- [36] Tien YM, Kuo MC, Juang CH. An experimental investigation of the failure mechanism of simulated transversely isotropic rocks. *International Journal of Rock Mechanics & Mining Sciences* 2006;43:1163-1181.

Chapter 4

Excavation-Induced Perturbations Around A Short Tunnel

Abstract

In Switzerland, the Opalinus Clay is under consideration as a potential host rock for deep geological disposal of nuclear waste. Past investigations indicate that the Excavation Damaged/Disturbed Zone is comprised of macroscopic fracturing. Recent excavation of the EZ-B Niche at the Mont Terri Rock Laboratory revealed only a few induced macroscopic fractures that can be associated with extensional failure. The EZ-B Niche was excavated sequentially in eight steps and the surrounding rock mass monitored before, during, and after the niche construction. Characterisation of the excavation-induced perturbations was achieved by integrating borehole data from field measurements and numerical modelling. The zone of perturbation around the niche consisted of two parts: 1) an inner macro-fractured zone coinciding with the lowest seismic wave amplitudes and velocities and 2) an outer zone absent of macro-fracturing but coinciding with increasing seismic wave amplitudes and velocities. The stress redistribution from numerical simulations indicated that spalling failure was susceptible in the sidewalls and upper west wall. In this case, stress levels exceeded the crack initiation threshold and continued to unload towards lower spalling limits, thus indicating increasing crack-induced damage from the far-field towards the near-field. Stress ratios near the borehole collars were not considerably less than a spalling limit of 0.05, suggesting the zone of macro-fracturing around the niche would not necessarily be significant. The rock mass in the crown, invert, and upper east wall were in regions of low deviatoric stress and low confinement. In this case, damage may be more readily influenced by the intact rock anisotropy resulting from the thin and pronounced bedding. In the lower portion of the niche, relatively large displacements were measured in a direction roughly perpendicular to bedding suggesting uplift of the invert. Seismic data also indicated the greatest damage in the borehole drilled in the invert.

4.1 Introduction

The Opalinus Clay is under consideration as a potential host rock for deep geological disposal of nuclear waste in Switzerland. Excavation-induced perturbations created by the construction of underground openings may affect the performance of such a repository. The zone of perturbation (i.e. hydromechanical and geochemical modifications) is comprised of an Excavation Damaged Zone (EDZ) and/or an Excavation Disturbed Zone (EdZ) [1]. The EDZ consists of significant alterations to the rock mass flow and transport properties, which may result from persistent and/or interconnected macroscopic fracturing. In contrast, less significant alteration of the rock mass occurs in the EdZ due to the infrequency in interconnected macroscopic fracturing. In indurated argillaceous media, characterising excavation-induced perturbations is challenging as these materials are inherently transitional and rarely isotropic, requiring considerations of geological heterogeneities in addition to stress redistribution [2].

At the Tournemire rock laboratory in France, perturbations around three openings of different ages in the argillaceous Toarcian formation were characterised from drillcore mapping, petrophysical measurements (to determine the degree of saturation), pneumatic and hydraulic tests, and seismic measurements [3, 4]. Excavation-induced perturbations were attributed to stress redistribution and desaturation [3, 4]. The former consisted of fracturing parallel with the tunnel wall while the latter involved bedding-parallel fractures. Bedding at Tournemire is sub-horizontal and dips 4° towards the north [4]. Fracturing was found within a zone of 0.16 to 0.22 tunnel radii whereas the desaturated zone extended as far as 0.4 to 0.6 tunnel radii [3]. The fractured zone consisted of a dense network of macroscopic fractures while the desaturated zone consisted of unsaturated macro- and micro-cracks [3, 4]. Fracturing oriented parallel with the tunnel wall was attributed to compressive failure due to unloading while bedding-parallel fracturing was attributed to natural ventilation [3, 4]. The measured permeability in the perturbed zone was up to 5 to 6 orders of magnitude higher than the undisturbed rock mass [5].

The argillaceous Callovo-Oxfordian formation at the Meuse/Haute-Marne underground research laboratory (Bure, France) is currently under investigation as a potential host rock [5, 6]. Bedding at this site is sub-horizontal and dips $1-2^\circ$ towards the southwest. Characterisation of excavation-induced perturbations at the laboratory has involved surficial geological mapping, drillcore resin impregnation, borehole seismic measurements, and pneumatic and hydraulic measurements [5]. Induced fracturing 490m below ground consists of three different sets [5, 6]: 1) v-shape with a horizontal axis of symmetry (chevron, herringbone) ahead of the face, 2) sub-vertical and oblique to the tunnel axis in the walls, and 3) sub-parallel with the tunnel wall. The extent of the v-shaped set is about 4m ahead of the face, up to 5m behind the face, 2-2.5m above the crown and below the invert, and less than 1m in the walls [5, 6]. Similar v-shaped fracturing was also observed at the face in the plastic Boom Clay at the HADES underground research facility in Mol, Belgium [7]. V-shaped and sub-vertical fracturing are slickensided with lineations oriented in the direction of excavation and have been attributed to shear failure [5, 6]. Fractures sub-parallel with the tunnel axis have been attributed to extensile failure due to unloading [5, 6]. The extent of this third fracture set is about 1m [6]. In the fractured zone, seismic wave velocities were reduced and hydraulic conductivities were 4 to 5 orders of magnitude higher where open extensional fractures have been observed [5]. In contrast, only small increases were measured in the shear fracture zone, which has been deemed mechanically-closed [5].

At the Mont Terri rock laboratory in Switzerland, the EDZ/EdZ in the Opalinus Clay has been characterised from surface and drillcore geological mapping, drillcore resin-impregnation, seismic velocity, and hydraulic and pneumatic testing [8, 9]. Induced fracturing consists of sidewall fractures oriented parallel with the tunnel wall and bedding-parallel fractures above the crown and below the invert [9, 8]. Bedding at Mont Terri dips towards the southeast at 22° to 55° [10]. Fracturing in the sidewalls has been attributed to extension while bedding-parallel fracturing has been attributed to shear with contribution from swelling and/or softening [9]. The zone of perturbation extends 0.5 to 1 tunnel radii [9] into the rock mass with the highest unloading fracture frequencies found in the first metre [8]. The interconnected induced fracture network in the first metre is unsaturated while fractures in the adjacent metre are isolated

and partially-saturated [8]. Permeability measured in the perturbed zone can be 6 to 7 orders of magnitude higher with the highest permeability measured in the first 10-20cm [8].

As illustrated above, characterisation of excavation-induced perturbations in indurated clays is not a unique process. Although, petrophysically or geomechanically, the formations above do not differ drastically, induced fracturing at each site is somewhat distinctive. Common to all the sites is open extensional fractures oriented parallel with the tunnel wall in high-deviatoric stress regions immediately adjacent to the excavation boundary [9, 4, 5]. However, the recent excavation of a short tunnel (EZ-B Niche) at the Mont Terri Rock Laboratory revealed few extensional fractures in the immediate vicinity of the test niche yet indications of induced disturbance were observed with other field measurements. In this chapter, excavation-induced perturbations were characterised through the integration of field data and results from numerical modelling.

4.2 Site Description

Located in north-western Switzerland (Fig. 4.1), the rock laboratory at Mont Terri facilitates research of nuclear waste storage in the Opalinus Clay (and is not under consideration as a potential repository site). Research at the Rock Laboratory was initiated in 1996 with the excavation of eight niches in the Security Gallery (Fig. 4.1). In 1998, a 175m-long gallery (Gallery98) along with a number of niches were excavated west of the Security Gallery. The most recent expansion occurred in 2004 with the excavation of the 80m-long Gallery04. The EZ-B Niche is located in Gallery04, which is 25m southwest of the Security Gallery.

Mont Terri is the northernmost in a series of anticlines in the Jura Mountains, which formed during late Miocene to early Pliocene in response to late alpine folding and thrusting [11]. Fault bend folding and fault propagation folding were responsible for the formation of the anticline and resulted in a number of thrust faults, such as those found in the northern limb [12]. The Rock Laboratory is located in the weakly deformed and less tectonically disturbed southern limb [10]. The in situ stress field at Mont Terri consists of a sub-vertical maximum principal stress (σ_1) inclined towards the S-SW and a sub-horizontal minimum principal stress (σ_3) inclined towards the NE [13]. Consequently, σ_3 is roughly normal to the EZ-B Niche axis while σ_2 (the intermediate principal stress) is sub-parallel with an offset of about 14° (Fig. 4.2).

At the laboratory, prominent tectonic features consist of minor tectonic shears and a larger thrust fault zone (Main Fault in Fig. 4.1) [12, 10]. Three sets of shears have been identified in Gallery04 [12] but only two intersect the EZ-B Niche [14]. The most frequently occurring set is sub-parallel with bedding and

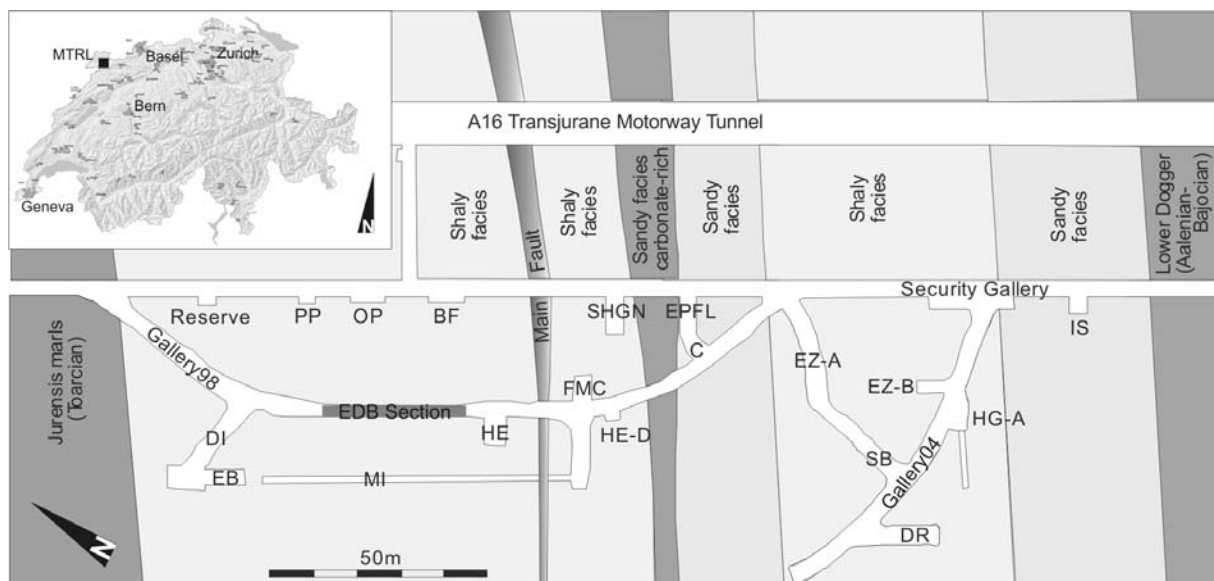


Fig. 4.1: Location of the EZ-B Niche in the Mont Terri rock laboratory (MTRL) in northern Switzerland (inset) and in relation to the three main facies of the Opalinus Clay (modified from Nussbaum et al. [12]).

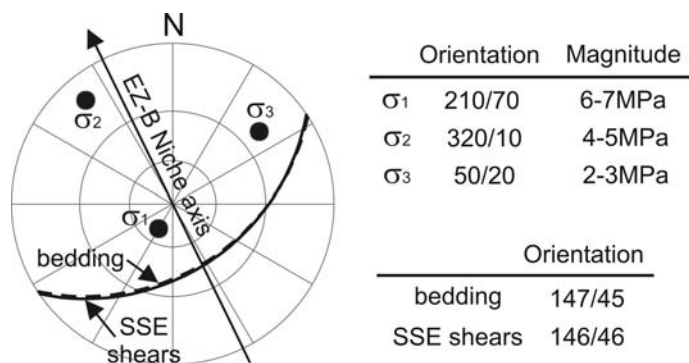


Fig. 4.2: The in situ stress field (lower hemisphere) at the Mont Terri Rock Laboratory relative to the EZ-B Niche and the nearly parallel bedding planes (dashed line) and SSE-bedding-parallel shears (solid line).

dips SSE (SSE and/or bedding-parallel shears) [12]. SSE bedding-parallel shears (Fig. 4.3), closed and sealed with calcite and clay minerals, are of minor tectonic importance with displacements in the order of millimetres (Nussbaum, pers. comm.). In the EZ-B Niche, the SSE set dips 46° (ranging 45° to 50°) towards 146° (ranging 138° to 156°) [14]; the niche trends roughly perpendicular to the SSE system. A second set mapped in isolated areas of the niche [14] consists of sub-horizontal shears that dip S to SW (with dip angles ranging 0° to 20° and dip directions ranging 132° to 186°). In the niche, the S-SW shears are bounded by the SSE shears (see Appendix B). Surfaces of both sets are slickensided and indicate thrusting towards the NW [12].

The Jurassic Opalinus Clay at Mont Terri is dark grey shale consisting of claystone and marl with intercalated sandy and calcareous layers and lenses. At Mont Terri, the formation consists of five lithostratigraphic subunits that have been grouped into three facies [15]: shaly, sandy, and carbonate-rich sandy (Fig. 4.1). The major components of the shaly facies, where the Gallery04 and EZ-B Niche are located, consist of [15]: clay minerals (58-76%), carbonates (0-28%), quartz (6-24%), feldspars (0-3%), pyrite (0-2%), and organic carbon (0-2%). Clay minerals consist mostly of illite (16-40% of total weight) and kaolinite (15-33%) followed by chlorite (4-20%) and illite/smectite mixed-layers (0-20%). The carbonate fraction is dominated by calcite at 5-28% (total weight). Structurally, the fabric is dominated by bedding-parallel flocculation; bedding is well-developed and the most pronounced feature at Mont Terri. In the EZ-B Niche, bedding is millimetres thick with an average dip angle of 45° (ranging 38° to 50°) and dip direction of 147° (ranging 140° to 155°) [13]. Consequently, the niche trends approximately normal to the strike of bedding (Fig. 4.2).

Construction of the EZ-B Niche and associated borehole drilling campaigns spanned a period of five months from December 2004 to April 2005 [16 or Chapter 2]. The EZ-B Niche is circular in cross-section with a flat floor, measuring 3.8m in diameter and 6-7m in length (Fig. 4.4). Construction of the EZ-B Niche began in December with the excavation of an entrance 1-2m in length. Fibre-reinforced shotcrete (with a nominal thickness of 150mm) was applied to the exposed rock above the invert and a 300mm-thick concrete floor slab was constructed over the invert. Four pore pressure sensors were installed near the mid-length of the niche in 20mm-diameter boreholes (BEZ-B4 to B7) in January (Fig. 4.5). Three 100mm-diameter horizontal observation boreholes (BEZ-B1 to B3), with lengths of 8-9.5m, were drilled in February. The remainder of the niche was excavated over a 12-day period in March with the main body

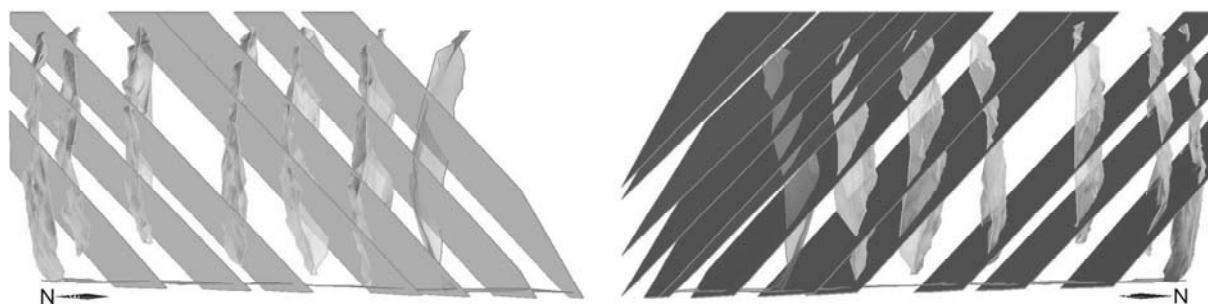


Fig. 4.3: SSE bedding-parallel shears mapped in the west (left) and east (right) walls of the niche. The entrance face is in grey and the five interim and final faces are in yellow.

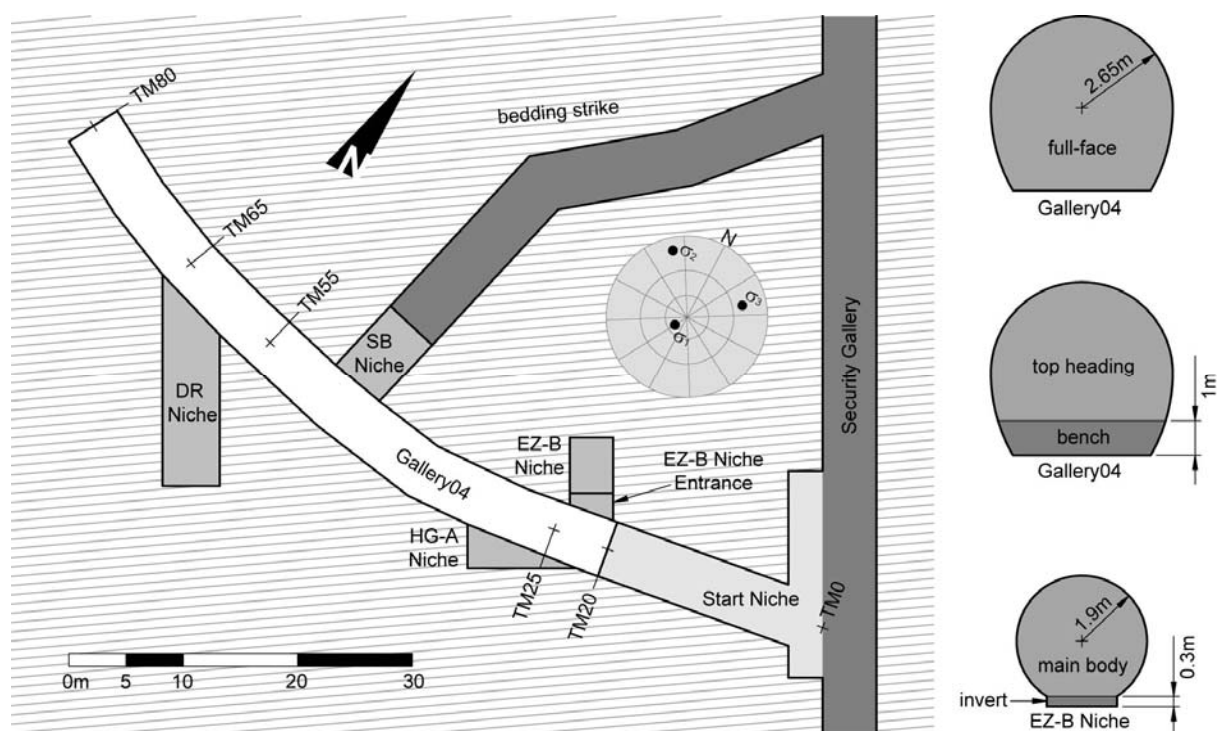


Fig. 4.4: Layout of the Rock Laboratory around the EZ-B Niche and in situ stress field (lower hemisphere) with cross-sections of Gallery04 and the EZ-B Niche to the right.

constructed in six steps and the invert in a single step (Fig. 4.5). A pneumatic hammer was used in the construction of the niche with the exception of the entrance, where a road-header was additionally employed [14]. Due to the advantageous orientation of the niche axis with the SSE bedding-parallel shears and bedding, the niche required only minimal roof support. The support system consisted of a roof mesh, aluminium nails, and un-tensioned 50cm-long steel anchors grouted in place. In April, 12 additional 100mm-diameter and 2-3m long observation boreholes (BEZ-B8 to B19) were drilled in three planes; two vertical planes near the mid-length of the niche and one horizontal plane in the niche face.

4.3 Field Data

A number of borehole and surface measurements and observations were carried out during the niche construction [16]. These included geological mapping of niche surfaces and drillcore, drillcore photo-documentation, borehole digital optical televiewer (DOPTV and shown in Fig. 4.6) imaging, spectral gamma logging, pore pressure monitoring, displacement monitoring (total station and panoramic laser scanner), borehole (single-hole, cross-hole, and tomography) and tunnel (refraction and vertical seismic profiling via a horizontal borehole) seismic measurements, and atmospheric monitoring (temperature, humidity, and barometric pressure). Due to the large volume of data collected, only a portion was available for consideration at the time this thesis was written. Characterisation of the EDZ/EdZ around the niche in this chapter focuses on borehole and drillcore data: geological mapping, DOPTV imaging, and single-hole seismic measurements.

4.3.1 Induced Fractures

Fracture mapping of an overconsolidated argillaceous material with pronounced strength anisotropy (due to the pronounced bedding) from drillcores can be challenging. Most of the structures mapped in drillcores at Mont Terri have been attributed to drilling and handling (labelled “ad” for artificial discontinuity in drillcore maps). For example, about 10% of more than 1000 discontinuities mapped in boreholes drilled from openings with the same orientation as the EZ-B Niche (e.g. Security Gallery and Gallery98) have been interpreted as unloading joints (“uj” in drillcore maps). As a result, induced fractures around the EZ-B Niche were identified by cross-referencing drillcore mapping and photo-documentation with DOPTV images (Fig. 4.7). In this way, the subjective nature of mapping was minimized. All

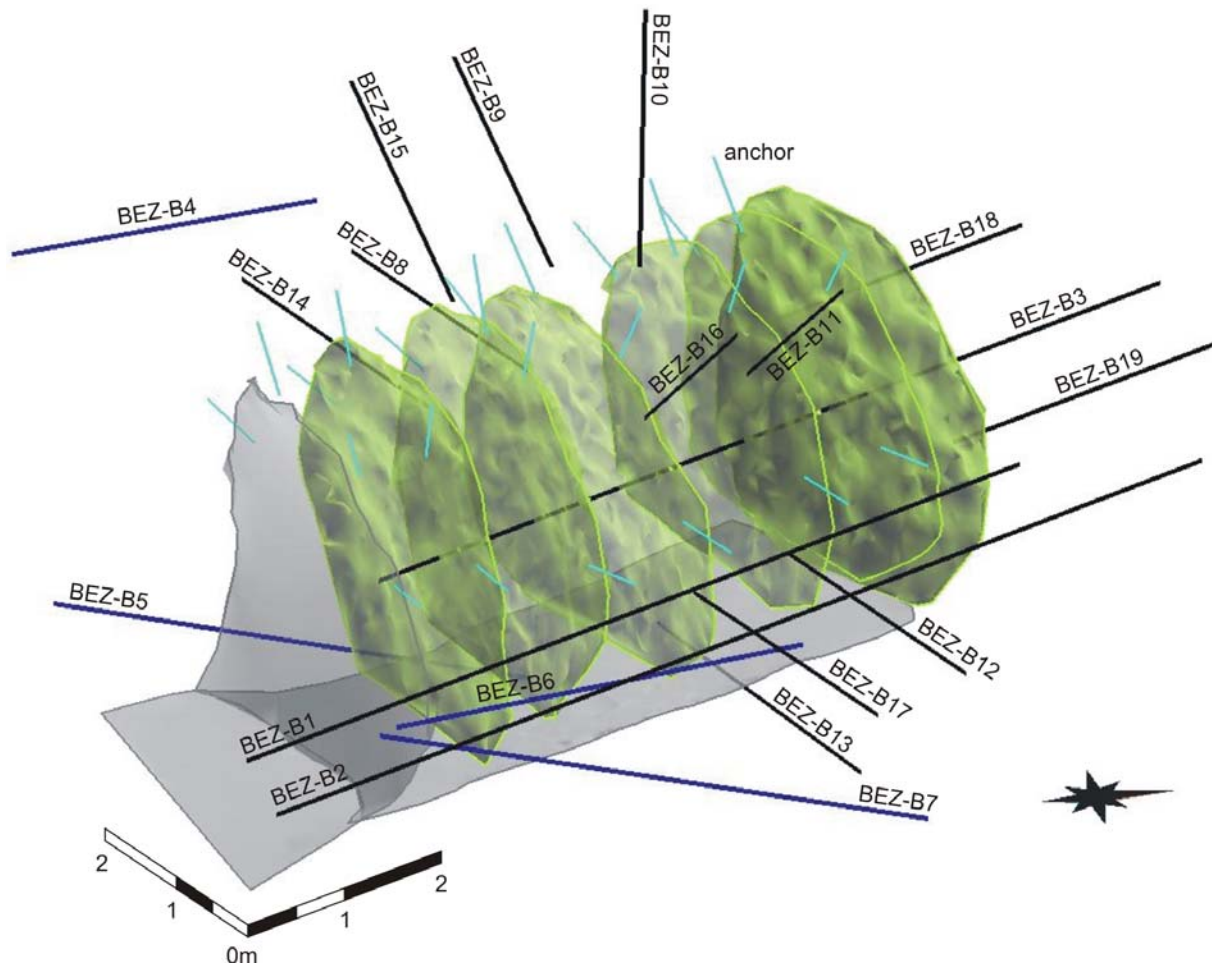


Fig. 4.5: Isometric view of the EZ-B Niche. Entrance face and the top of the concrete floor are shown in grey while the interim and final faces are shown in yellow. Observation boreholes (BEZ-B1 to B3, B8 to B19) are shown in black and pore pressure sensors were installed in BEZ-B4 to B7 (blue). The roof anchors are shown in light blue.

structures except those related to drill stem extraction were separated into three groups (Fig. 4.8): tectonic shears (F), induced fractures (I), and unclassified (O). Induced fractures were further sub-divided into two groups based on the level of confidence in interpretation. The highest level of confidence (I1) was assigned when mapped drillcore fractures were also seen in the DOPTV images. I2 represent possible induced fractures.

More than 80 fractures were mapped in the boreholes (BEZ-B8 to B19 and the last 3m of B3 or what remains of the borehole after the niche excavation) radiating from the niche (Tab. 4.1). Of these, 23%

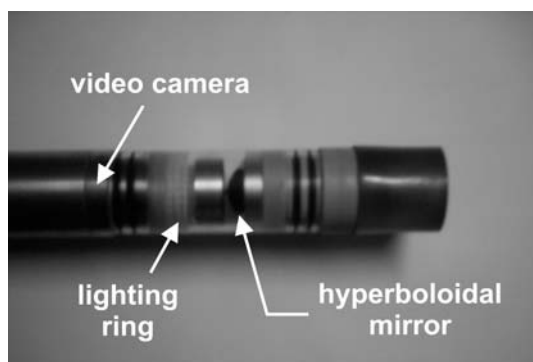


Fig. 4.6: The Digital Optical Televiewer (DOPTV) used to image the borehole walls.

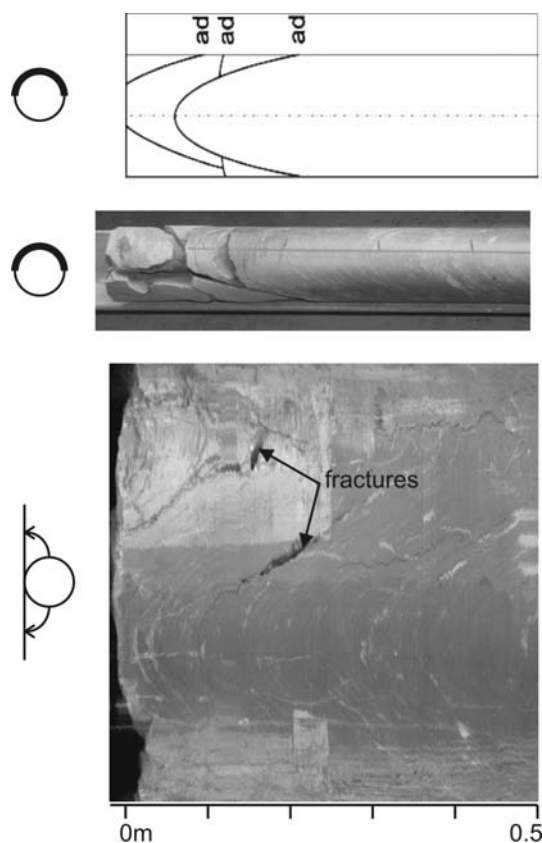


Fig. 4.7: Fractures identified in BEZ-B15 from drillcore mapping and photo-documentation and DOPTV imaging.

were tectonic shears (F) and 22% were induced fractures with the highest level of confidence (I1). Excluding tectonic-related fractures, 80% were bedding-parallel. Considering only I1 fractures, 75% were bedding-parallel and most occurred within the first 20cm with the exception of BEZ-B11, B17, and B18 where they were found as far as 55cm. I2 fractures were found from 9cm to 3m.

The fracturing mapped around the EZ-B Niche was also compared with those mapped in boreholes drilled from the Security Gallery and Gallery98 (in more than 100 boreholes). Again, all structures except those obviously related to tectonic activity and drill stem extraction were counted over intervals of 50cm and their orientation with respect to bedding accounted for. Due to an uneven distribution of borehole directions (almost 75% have been drilled in the sidewalls), the counts shown in Fig. 4.9 have been normalised by the number of boreholes drilled in each direction. Additionally, the total fracture counts from drillcore obtained in the sidewalls were also compared with sidewall fracture mapping of the niches in the Security Gallery [8]. Without classifying the fracturing, Fig. 4.9 shows that the occurrence of fracturing around the EZ-B Niche is lower than that around other galleries. Bedding-parallel fracturing was also more dominant around the niche than the galleries: 80% in the former compared to 30% in the latter.

4.3.2 Borehole Instabilities

Borehole instabilities may provide indications of the formation stress state [17] and/or may be related to strength anisotropy [18]. In anisotropic materials, such as the Opalinus Clay at Mont Terri, borehole instabilities have been attributed to both [13]. Symmetrical instabilities in the EZ-B boreholes were observed in nine out of 12 boreholes from unwrapped DOPTV images. The types of outbreaks are plotted in relation to bedding in Fig. 4.10. The sub-horizontal boreholes in the sidewalls were drilled sub-parallel with bedding and sustained the most pronounced damage (BEZ-B8 in Fig. 4.11). Bedding traces in the DOPTV images are highlighted by the lighter-coloured sandy layers, which are parallel with bedding. Generally, borehole outbreaks coincided with where bedding was tangential to the boreholes (Fig. 4.10) in all four boreholes (BEZ-B8, B12, B14, B17). The instabilities in these boreholes can be attributed to the strength anisotropy inherent to the Opalinus Clay at Mont Terri. Instabilities in the 45°-inclined boreholes in the east wall (BEZ-B11, B16 in Fig. 4.10) were also found where bedding was tangential to the borehole

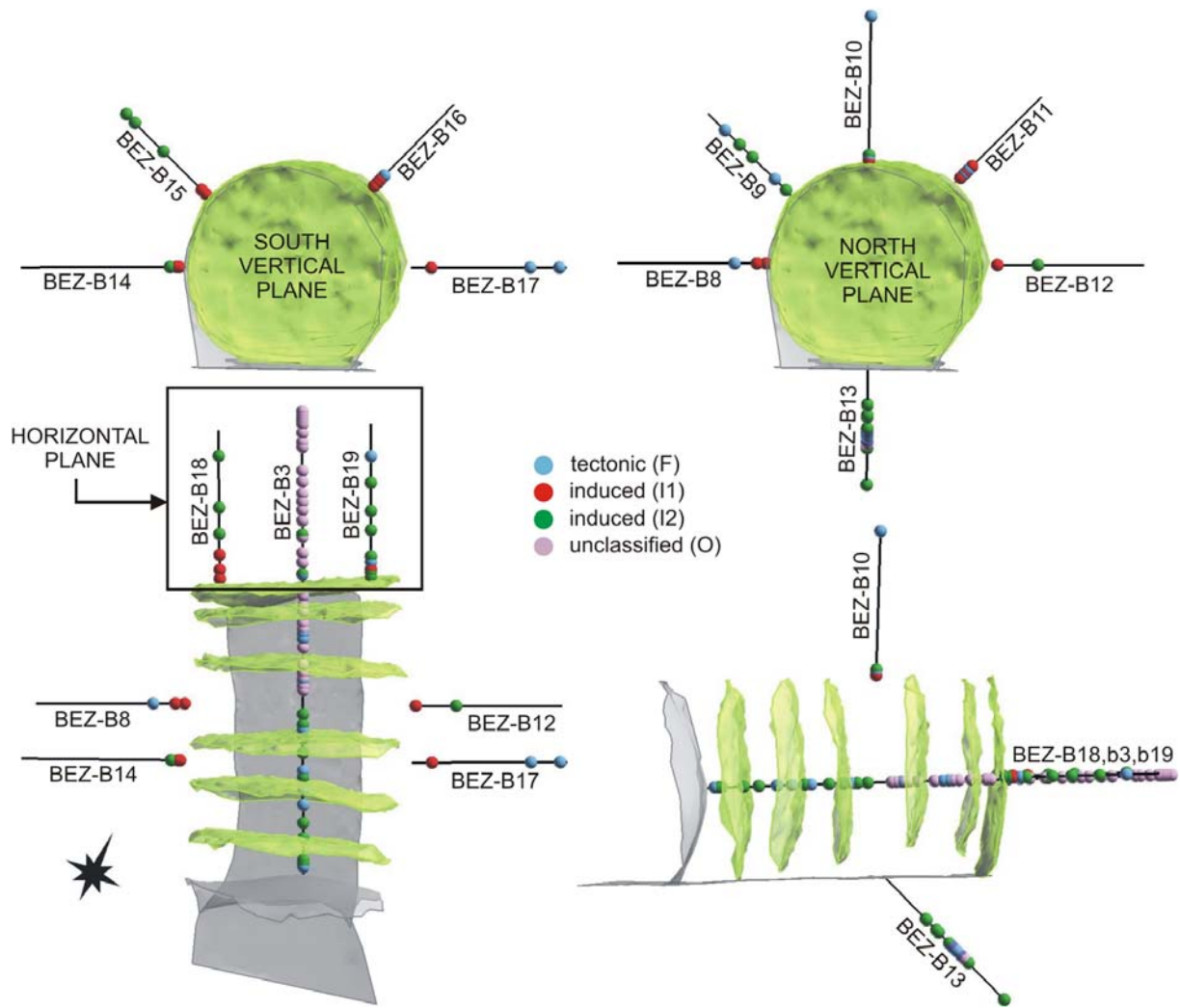


Fig. 4.8: Classification of the fractures mapped in the boreholes. The two vertical planes are shown in the top plots, looking at the face. The horizontal plane is viewed in plan in the lower left and the lower right is a longitudinal section looking southwest.

(Fig. 4.11). However, these boreholes (like their undamaged west-wall counterparts: BEZ-B9, B15) were not drilled sub-parallel with bedding but intersected bedding at angles closer to 45° (Fig. 4.11). Borehole outbreaks in the sub-horizontal boreholes in the face (BEZ-B3, B18, B19) were also symmetrical but were much smaller in extent (Fig. 4.11). These boreholes intersected bedding at roughly 45° and the observed instabilities did not coincide with where bedding became tangential. In this case, these instabilities could be indicative of the formation stress state since the orientations concur with similar observations made in past investigations at the laboratory [13]. Lack of ventilation (i.e. trapped humidity) also likely promoted degradation of the borehole walls and was most severe at depth in the longer and older boreholes (i.e. BEZ-B1 to B3).

Tab. 4.1: All fractures identified in BEZ-B8 to B19 and the last 3m of BEZ-B3.

Fracture Type	Bedding-Parallel	Others	Total
Shear (F)	20	0	20
Induced1 (I1)	14	5	19
Induced2 (I2)	24	4	28
Unclassified (O)	16	5	21
Total	74	14	88

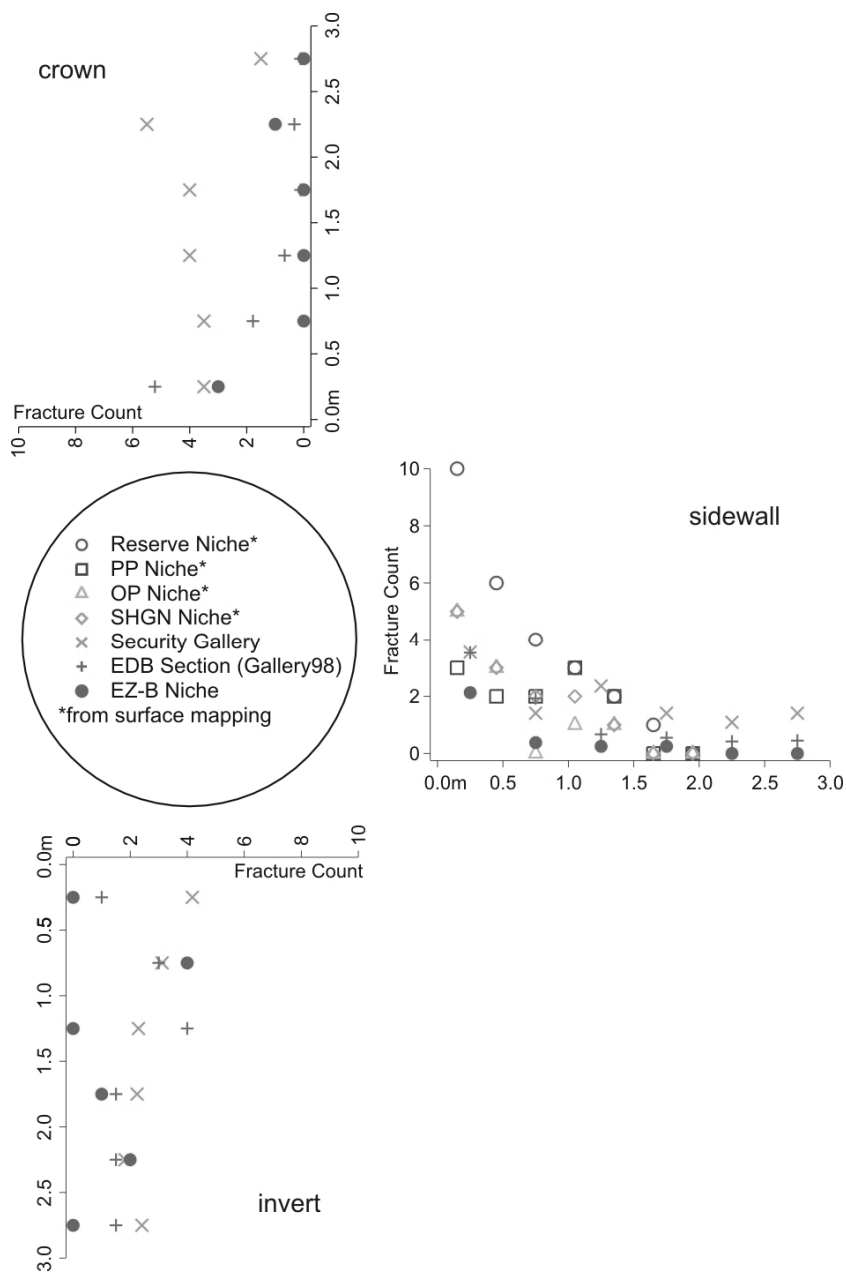


Fig. 4.9: Fracture counts (in 0.5m intervals) from the EZ-B Niche boreholes compared to boreholes drilled in older sub-parallel excavations (refer to Fig. 4.1 for excavation locations).

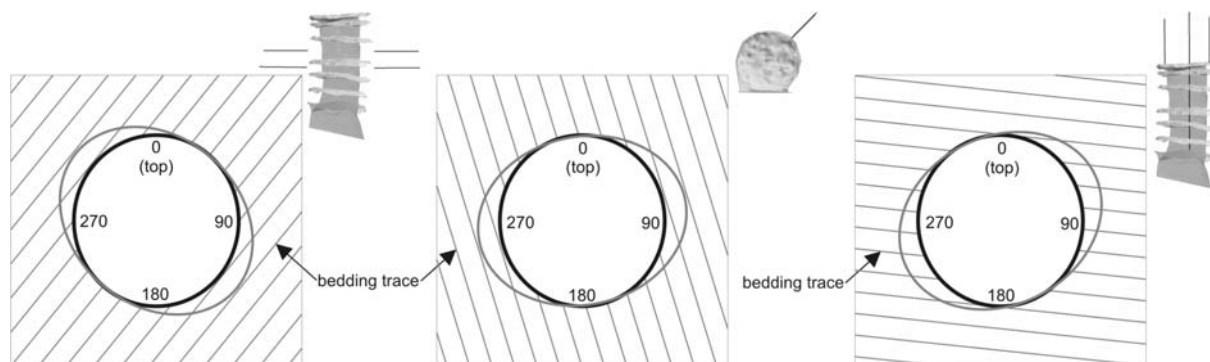


Fig. 4.10: Extent of borehole instabilities observed in the sidewalls (far left), upper east walls (middle), and face (far right). Solid blue lines represent the average of the instability extent (blue areas) while the dashed green lines represent where bedding is tangent to the boreholes.

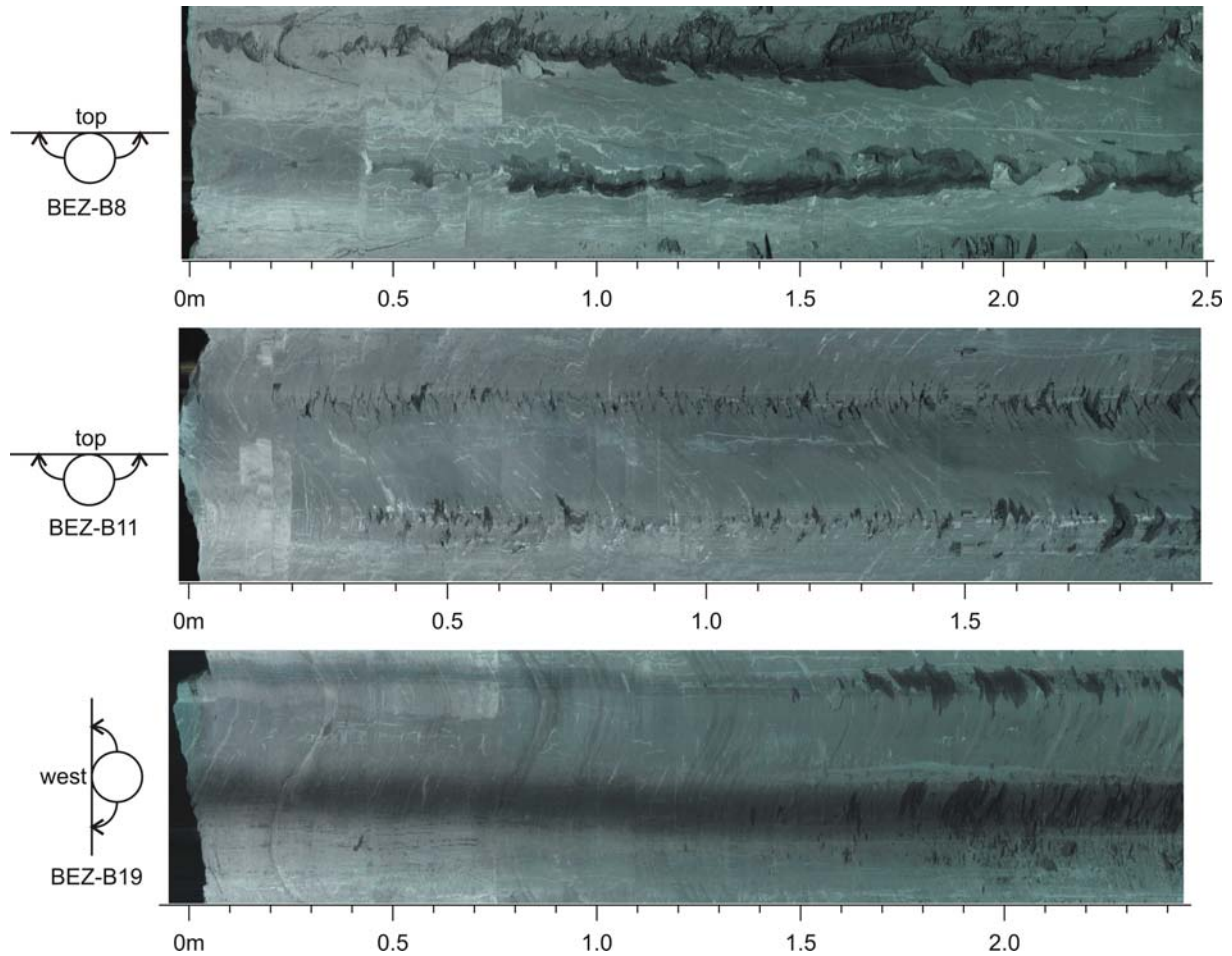


Fig. 4.11: Different degrees of borehole instabilities observed in unwrapped DOPTV images (refer to Fig. 4.5 for borehole locations).

Instabilities in boreholes occur where the hoop stress exceeds the strength of the rock. In turn, changes in the intensity of the instability may indicate changes in the formation stress state and/or strength of the rock mass. As a result, boreholes with visible instability also provide indications of excavation-induced perturbation. In these boreholes, instabilities intensified with depth (Fig. 4.11), suggesting weakening near the collar. On average, instabilities in the sidewalls intensified 0.6m from the collar. In comparison, borehole instabilities in the face started 1.5m from the collar and those in the upper east wall (BEZ-B9, B15) started 0-0.2m from the collar. Instabilities in BEZ-B3, the only borehole drilled prior to the main stage of the niche construction, were also seen starting from the collar but the damage in this case was incurred before the final niche face was reached.

4.3.3 Seismic Measurements

Seismic parameters used in the characterisation of the EDZ/EdZ included: P- and S-wave velocities (V_p and V_s , respectively), P- and S-wave amplitudes, and the ratio of the p-wave velocity to the s-wave velocity (V_p/V_s) [19, 20]. A mini-sonic probe (Fig. 4.12) from BGR (Federal Institute for Geosciences and Natural Resources) was used in the single-hole seismic measurements. The probe, with a maximum sampling frequency of 10MHz, consisted of four piezo-electric transducers spaced 10cm apart with one as a seismic source and three as receivers [21]. The larger the separation between the source and receiver, the greater the depth of seismic wave penetration. For the BGR mini-sonic probe, a penetration depth of 1-2cm was determined from finite difference modelling (Schuster, pers. comm.). As a result, channel 1 is most affected by the borehole EDZ/EdZ while channel 3 is least affected. Coupling of the probe was achieved pneumatically and travel times were measured at intervals of 5-10cm. The P-wave and S-wave (vertically-polarised only) velocities and respective amplitudes were derived from first-arrival phases.

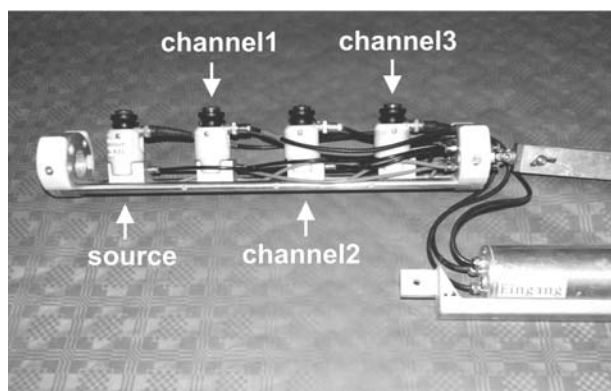


Fig. 4.12: The BGR mini-sonic probe used in the single-hole seismic measurements.

Uncertainties involved in processing the seismic measurements were roughly $\pm 9\%$ for channel 1 P-wave velocities, $\pm 3\%$ for channel 3 P-wave velocities, and 4% for channel 3 S-wave velocities: i.e. $\pm 0.5\mu\text{s}$ to $\pm 1.5\mu\text{s}$ for the onsets of P-wave first arrivals and $\pm 1\mu\text{s}$ to $\pm 4\mu\text{s}$ for the S-waves [22]. A more detailed description of the equipment, logging method, and data processing is found in [21, 22].

Investigations in indurated clays [19, 20] and hard rocks [23, 24] have shown that seismic wave velocities and amplitudes generally increase with distance from the tunnel perimeter. Changes in seismic wave velocities and amplitudes may reflect changes in rock properties thereby providing indications of damage [21, 22, 23]. Decreasing P- and S-wave velocities have been linked to both a decrease in confinement and an increase in crack density and porosity that may result from stress-relief damage [21, 23]. Low V_p/V_s ratios, typical for hard rocks at depth, have been attributed to low crack density and high rock quality (RQD) [22]. The greatest velocity and amplitude reductions are often seen immediately adjacent to the tunnel periphery. This is illustrated in Fig. 4.13 where the greatest reductions in the P-wave velocities and amplitudes were seen in the first 0.5-0.6m. In Fig. 4.13, seismic parameters derived for BEZ-B19 (Fig. 4.5) are plotted. Measurements from all three channels are plotted for P-wave velocities and amplitudes in the bottom of Fig. 4.13. However, due to difficulty in recognising the first arrival of S-waves and interference from the borehole EDZ/EdZ, only channel 3 data was considered for parameters associated with the S-waves [19]. The amplitudes plotted in Fig. 4.13 have also been normalised by the average of each respective channel to enable comparison between boreholes [19].

In transverse isotropic media such as the Opalinus Clay, seismic wave velocities also correspond with the direction of wave propagation relative to the plane of isotropy. The average velocity of each channel from all the boreholes is summarised in Fig. 4.14, which shows the largest velocities in boreholes drilled sub-parallel with bedding (BEZ-B8, B12, B14, B17) and the lowest in the borehole drilled perpendicular to bedding (BEZ-B13). Intermediate velocities were seen in boreholes that intersected bedding near 45° . Also illustrated in Fig. 4.14, are lower velocities in the east wall (BEZ-B11, B12, B16, B17) compared with their west wall counterparts (BEZ-B8, B9, B14, B15).

4.3.4 Displacement Monitoring

In addition to the borehole data collected, periodic geodetic (total station) and optical (panoramic laser scanner) monitoring was also carried out to monitor surficial displacements of the niche. Data from the geodetic method will be considered in this thesis. The optical method is examined in Lemy et al. [25]. A total of 27 object points were installed in four circular arrays and one linear array (Fig. 4.15). The object points were anchored about 5cm into the rock mass. Each circular array consisted of six points aligned with the orientations of σ_1 and σ_3 while the linear array consisted of three points distributed over the height of the face. For logistical reasons, arrays 200 to 400 were installed within a 1-2m band near the face and 18 of 27 points were installed only after the niche body was excavated but prior to the invert excavation. Anchoring was particularly problematic in the first and oldest array (100) and damage was also sustained during the excavation process: data from two out of six object points in array 100 were deemed usable. As a result, 20 out of 27 object points and three periods were considered in assessing the deformational behaviour of the niche. The three periods considered were two days (13Mar2005) after the niche body was excavated (11Mar2005), two to three days (17Mar2005) after the invert was excavated

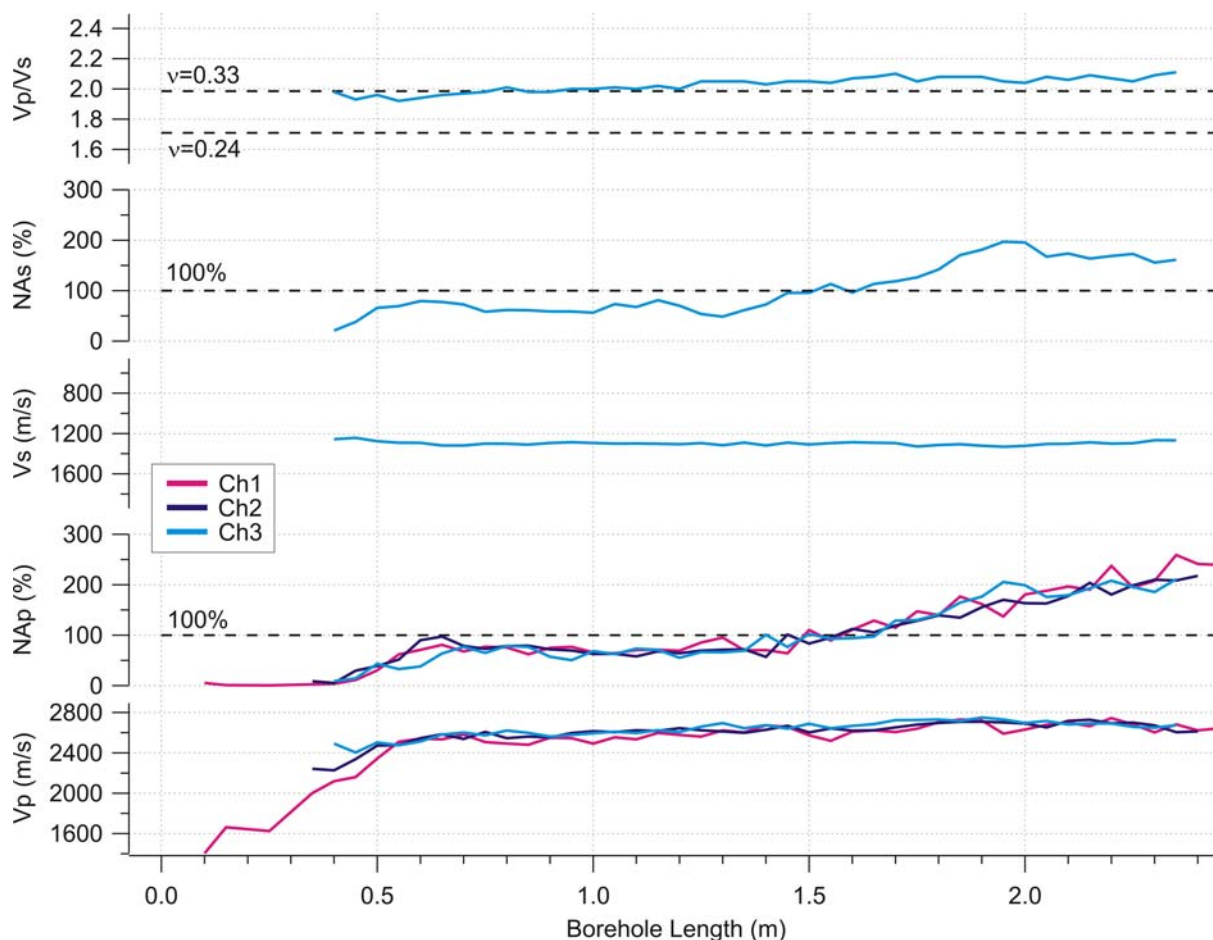


Fig. 4.13: Seismic wave parameters derived from single-hole interval velocity logging in BEZ-B19 (sensor travel along the west borehole wall).

(14Mar2005) and a concrete floor poured in place (15Mar2005), and 32 to 33 weeks (28Oct2005) after the niche was completed. During construction of the niche, displacements did not exceed 3mm (object points 101 and 106). The accuracy of the automated total station used in this investigation is less than 1mm [26].

Prior to the invert excavation (13Mar2005), the largest displacements (Tab. 4.2) occurred in the upper walls in array 400 (10-11mm at 405 and 9-10mm at 402). Similar magnitudes were measured in a survey taken the day prior indicating the greatest component of these displacement occurred within a 24-hour period. In both cases, the movement was downward and sub-parallel with bedding (Fig. 4.16). However, both were nearly orthogonal to the niche axis with dip angles of 14° to 30°. All other displacements were less than 3mm with dominantly upwards movement. At object points 201, 305, 306, displacements were nearly orthogonal to bedding but directed upwards. The largest convergence (18-19mm) occurred between 402 and 405 (Fig. 4.17 and Tab. 4.3). Convergence of 6-10mm was also seen along 402-404, 401-405, and 402-406. Along the remaining lines, convergence was less than 2mm.

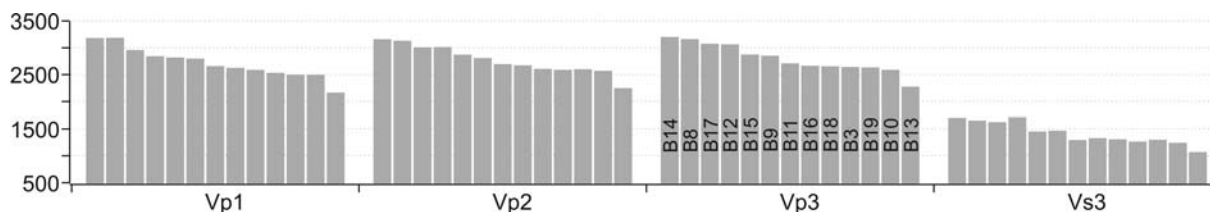


Fig. 4.14: Average P-wave (V_p) and S-wave (V_s) velocities from all three channels arranged from highest to lowest relative to the P-wave velocity in channel 3.

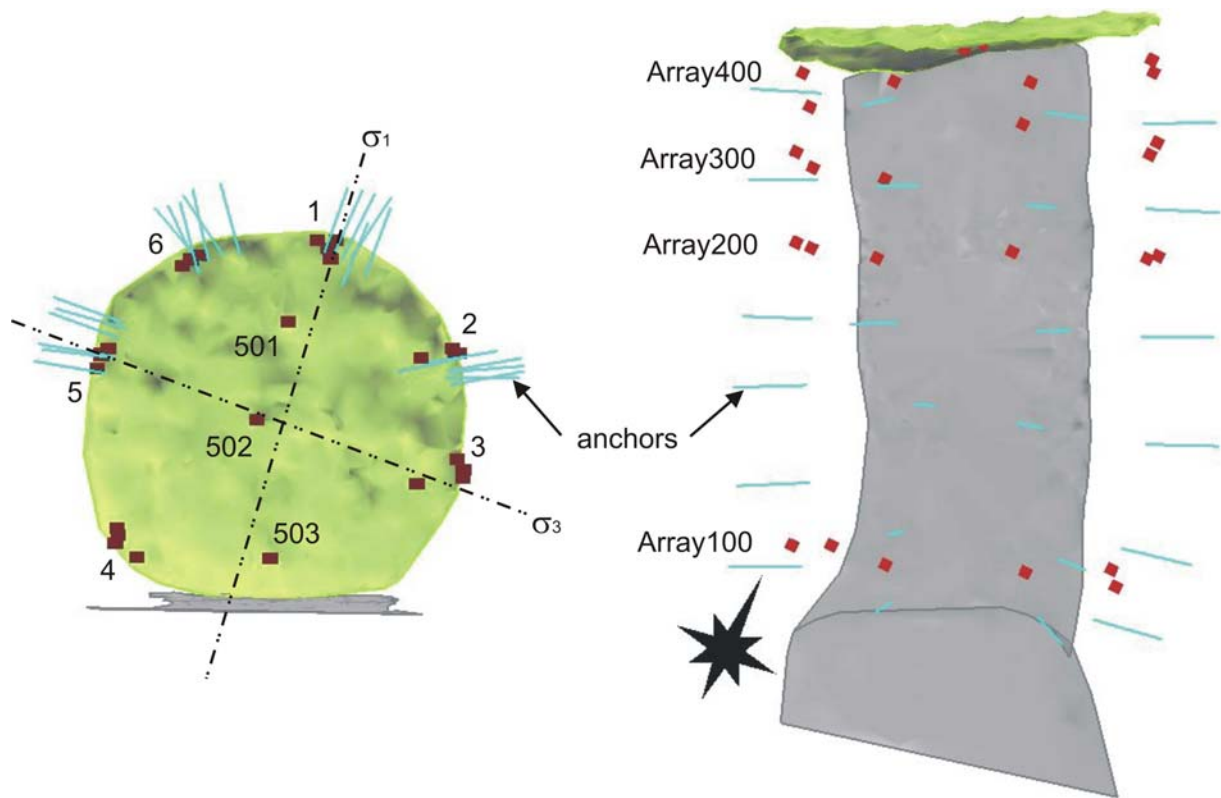


Fig. 4.15: Geodetic displacement monitoring at object points (red squares) installed in four circular arrays (100-400 in the plan view on the right). Each array consisted of six points (1-6 in the cross-sectional view on the left). Three points (501-503) were installed in a linear array in the face.

Tab. 4.2: Total displacement magnitudes (mm) determined from geodetic measurements (reference date is 11March2005). Locations of the points are given in Fig. 4.15.

	101	102	103	104	105	106
13mar2005	1.0	-	-	-	-	2.2
17mar2005	2.0	-	-	-	-	2.2
28oct2005	2.0	-	-	-	-	2.0
	201	202	203	204	205	206
13mar2005	2.5	0.6	-	1.5	-	0.4
17mar2005	2.4	11.2	-	1.2	-	1.0
28oct2005	0.9	11.6	-	4.3	-	2.8
	301	302	303	304	305	306
13mar2005	1.0	0.4	0.9	0.5	0.4	0.3
17mar2005	1.0	1.2	0.8	0.8	0.8	0.4
28oct2005	3.5	1.5	0.8	4.9	1.9	3.3
	401	402	403	404	405	406
13mar2005	0.9	9.3	-	1.0	10.9	1.0
17mar2005	0.9	1.0	-	0.9	1.5	1.8
28oct2005	4.2	1.0	-	3.8	2.8	1.8
	501	502	503			
13mar2005	0.8	1.0	1.6			
17mar2005	0.8	0.8	1.4			
28oct2005	1.8	2.4	5.9			

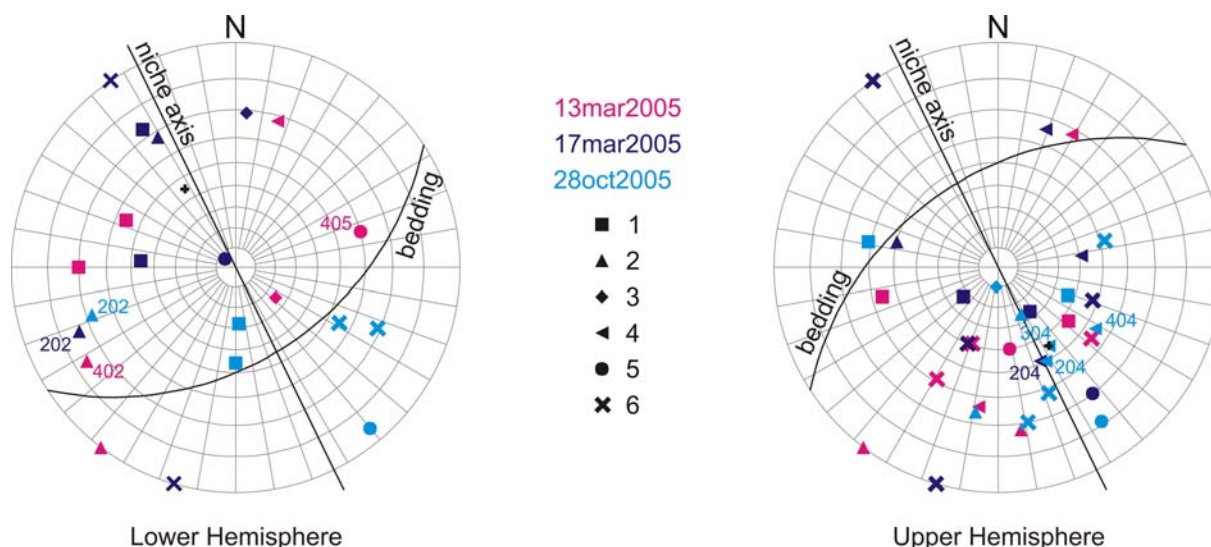


Fig. 4.16: Displacement vectors of arrays 100-400 (refer to Fig.16 for locations).

After the invert was excavated (17Mar2005), the largest displacement (Tab. 4.2) also occurred in the upper wall but only in the east wall at 202 (11-12mm). The movement was downwards with no particular relation to bedding but again nearly orthogonal to the niche axis (Fig. 4.16). At the remaining points, displacements did not exceed 3mm and were predominantly upwards. Interestingly, displacement at 204 was nearly orthogonal to bedding but directed upwards. The largest convergence (Fig. 4.17) occurred along 202-204 (11-12mm) and 202-206 (9-10mm). Convergence along other lines did not exceed 2mm (Tab. 4.3).

In a similar manner, the largest displacement (11-12mm) at the last survey (28Oct2005 in Fig. 4.16) also involved downwards movement at 202 (Tab. 4.2). Again, the vector at 202 was nearly orthogonal to the niche axis and dips 22° . Predominantly upwards displacements less than 5mm were seen at the other points. Again notable upwards displacements nearly orthogonal to bedding were seen at 106, 304, and 404. The largest convergence (Fig. 4.17) occurred along 202-204 (12-13mm) and 202-206 (9-10mm). Other notable convergence involved object point 4 and object point 6: 4-6mm along 301-304 and 401-404, 4-5mm along 204-206 and 304-306, and 3-4mm along 303-306. Convergence along the remaining four lines did not exceed 3mm (Tab. 4.3).

Displacements in the face (Fig. 4.18) for all three periods were concentrated near the floor at object point 503 (Tab. 4.2). The largest displacement of 5-6mm was measured at the last survey (28Oct2005) at an orientation nearly perpendicular to bedding and directed upwards.

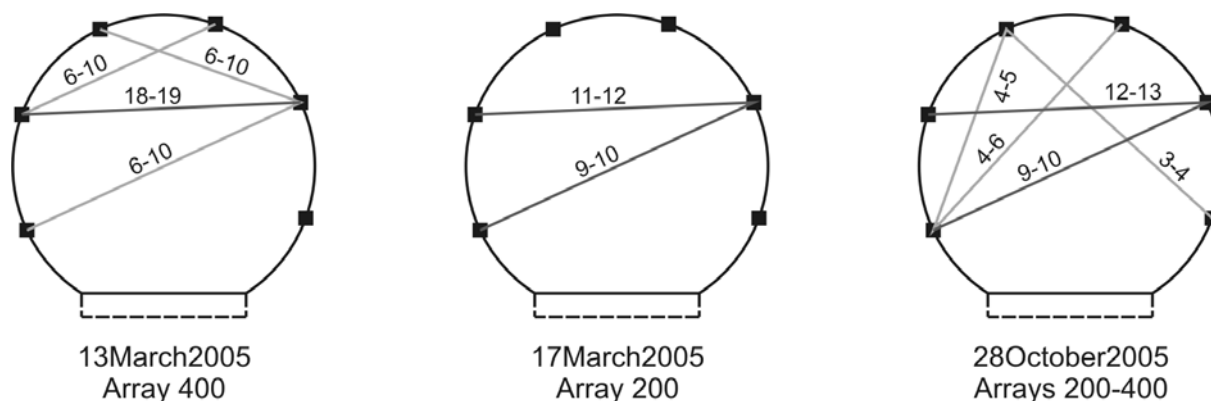


Fig. 4.17: Largest total convergence (mm) determined from the geodetic measurements.

Tab. 4.3: Total convergence (mm) determined from geodetic surveys (refer to Fig.4.15 for locations).

	1-3	1-4	1-5	2-4	2-5	2-6	3-4	3-5	3-6	4-6
Array200										
13mar2005	-	-2.0	-	0.1	-	0.5	-	-	-	0.5
17mar2005	-	-1.5	-	11.2	-	9.9	-	-	-	0.0
28oct2005	-	1.6	-	12.5	-	9.4	-	-	-	4.0
Array300										
13mar2005	-0.7	1.1	0.8	0.5	-0.1	0.2	0.5	-0.7	-0.5	0.1
17mar2005	-0.1	1.6	0.8	1.2	1.0	1.1	0.5	-0.3	-0.4	0.5
28oct2005	3.1	4.9	1.6	2.6	0.8	2.3	0.7	1.0	3.1	4.7
Array400										
13mar2005	-	0.6	6.6	9.3	18.1	6.5	-	-	-	-0.4
17mar2005	-	0.9	-0.3	0.9	0.0	-1.2	-	-	-	1.1
28oct2005	-	5.4	2.0	2.4	0.5	-0.4	-	-	-	2.5

4.4 Numerical Modelling

Three-dimensional numerical modelling was also carried out to provide an indication of the stress evolution in response to the various excavation activities. The enlarged opening near the EZ-B Niche entrance and the non-orthogonal intersection of the niche with Gallery04 (Fig. 4.4) necessitated three-dimensional considerations. FLAC3D (Fast Lagrangian Analysis of Continua in 3 Dimensions), version 3.00-308 [27], was used in the simulations, which required two to three days for an elastic model (on an Intel Pentium 4 3.2GHz processor with 3GB RAM).

The FLAC3D grid (Fig. 4.19) consisted of 391,620 zones, graded radially outwards from the EZ-B Niche and encompassed a volume 65m wide, 77m long, and 65m high (or five to eight tunnel diameters). The simulations involved the staged excavations of three openings: Gallery04 and the HG-A and EZ-B Niches. Gallery04 (69m in length) was simulated as a straight alignment and excavated full-face in 33 rounds of 1.1-3.7m (depending on the mesh gradation). In comparison, the actual advance averaged 1.8m [12]. The HG-A Niche excavation was simulated in three steps with the last step including the entrance of the EZ-B Niche to match the as-built sequence. The EZ-B Niche was excavated in seven steps with the first six consisting of the main body (Fig. 4.4) and the invert in the seventh. An additional 11 steps were also simulated to extend the EZ-B Niche to the northern external boundary.

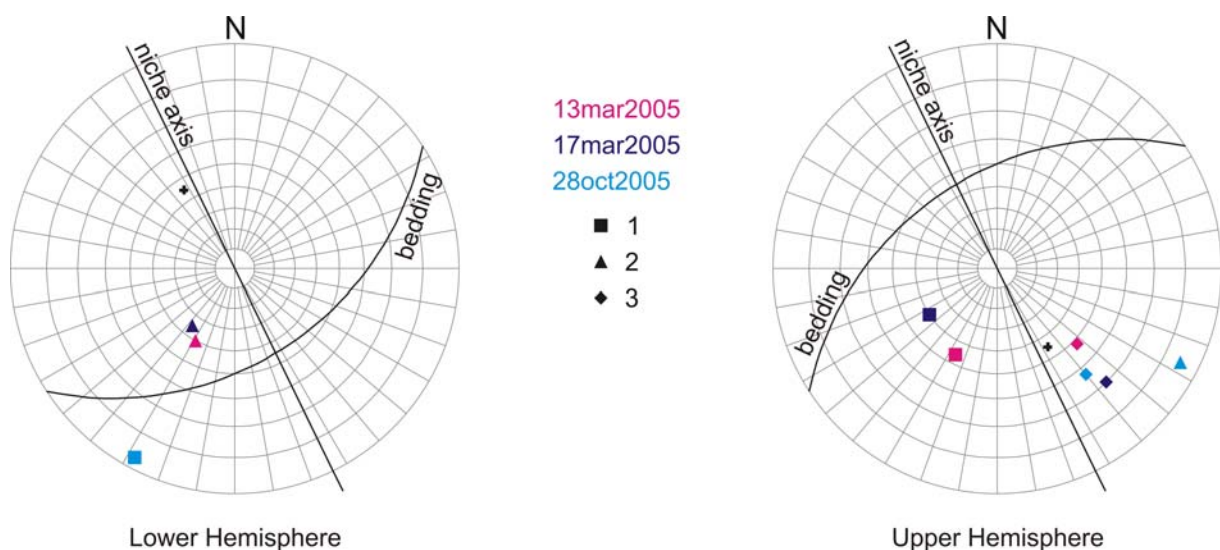


Fig. 4.18: Displacement vectors of array 500 (refer to Fig. 4.15 for locations).

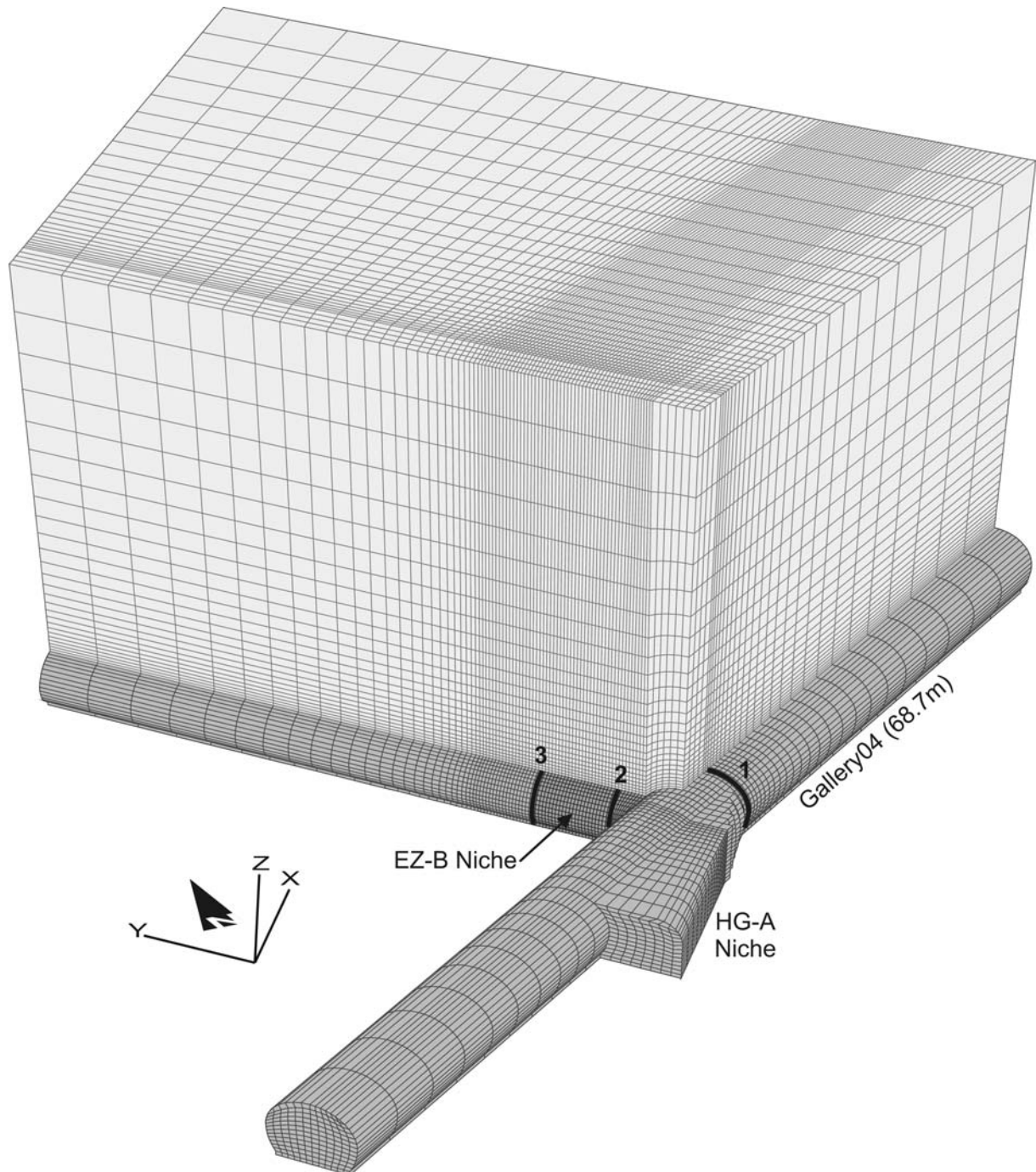


Fig. 4.19: Excavations modelled in the continuum simulation (looking northeast). Point 1 is 0.5m east of the east niche wall, point 2 represents the niche entrance, and point 3 represents the end of the niche excavation (and also after the invert excavation).

The external boundaries were fixed in all three directions and the initial stress applied is shown in Fig. 4.2. Two sets of material properties were considered in the numerical simulations. The first considered an elastic isotropic rock matrix (CIE) and the second considered an elastic anisotropic rock matrix (CAE) with the plane of transverse isotropy dipping 45° towards 147° . The respective properties were taken from a synthesis carried out by Bock [28] and are summarised in Tab. 4.4.

4.5 Assessing Rock Damage

Around the EZ-B Niche, a relatively thin zone of macroscopic fracturing was indicated by the fracture mapping completed on the drillcores and in the boreholes. However, seismic data and changes in the

Tab. 4.4: Material properties used in the elastic continuum models (after Bock [28]).

	Isotropic	Anisotropic
E(parallel bedding)	6 GPa	10 GPa
E(perpendicular bedding)	6 GPa	4 GPa
G(perpendicular bedding)	1.2 GPa	1.2 GPa
v(parallel bedding)	0.27	0.33
v (perpendicular bedding)	0.27	0.24

borehole instabilities indicated that the perturbed zone extended beyond the zone of macroscopic fracturing. To better assess the rock damage incurred, the different borehole data were integrated and compared with the simulated stress redistribution in the rock mass surrounding the EZ-B Niche. In turn, this allowed for the identification of possible failure modes (Fig. 4.20) that the rock mass may have encountered in response to the various excavation activities.

The strength of rock is often defined from laboratory testing under various deviatoric stress states to capture the full range of failure modes illustrated in Fig. 4.20. Since rocks are inherently much weaker in tension, tensile failure occurs under considerably smaller loads than compressive failure. In compression, rock failure involves a number of thresholds (Fig. 4.21): crack closure (σ_{cc}), crack initiation (σ_{ci}), crack interaction (σ_{cd}), and peak strength (σ_{peak}) [29, 30, 31, 32]. When a laboratory test sample is initially loaded, existing cracks first close. Following this, the stress-strain behaviour is linear and elastic until new damage is initiated. At crack initiation, new microscopic fracturing begins and the lateral and volumetric strain curves deviate from linearity [33]. The onset of micro-fracturing is marked by a continuous detection of acoustic emissions beyond background levels with crack orientations parallel with the greatest applied compressive load [33, 34, 30]. Subsequently, cracks propagate in a stable manner (in the direction of the greatest applied compressive load) such that crack growth is a function of and can be controlled by varying the load imposed [29, 30, 33]. With continued loading, the accumulated crack-induced tensile damage reaches a critical density at which point macroscopic failure initiates due to the interaction of cracks [35]. The crack interaction threshold is most commonly associated with a reversal in volumetric strain as shown in Fig. 4.21 and represents the yield (or long-term) strength [35]. Diederichs [36] has indicated that the use of the volumetric strain reversal may over-predict yield and instead, has suggested the use of the first significant point of non-linearity in the axial stress-strain plot as the yield point. Unstable crack growth occurs at stress levels beyond crack interaction until the rock sample can no longer

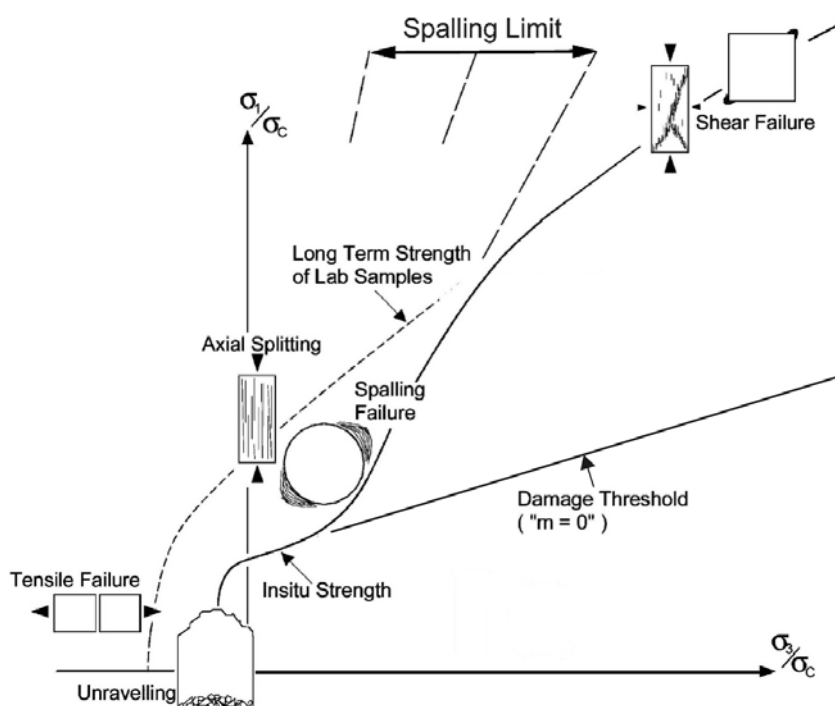


Fig. 4.20: Brittle failure modes in σ_1 - σ_3 space, normalised by σ_c (after Diederichs [38]).

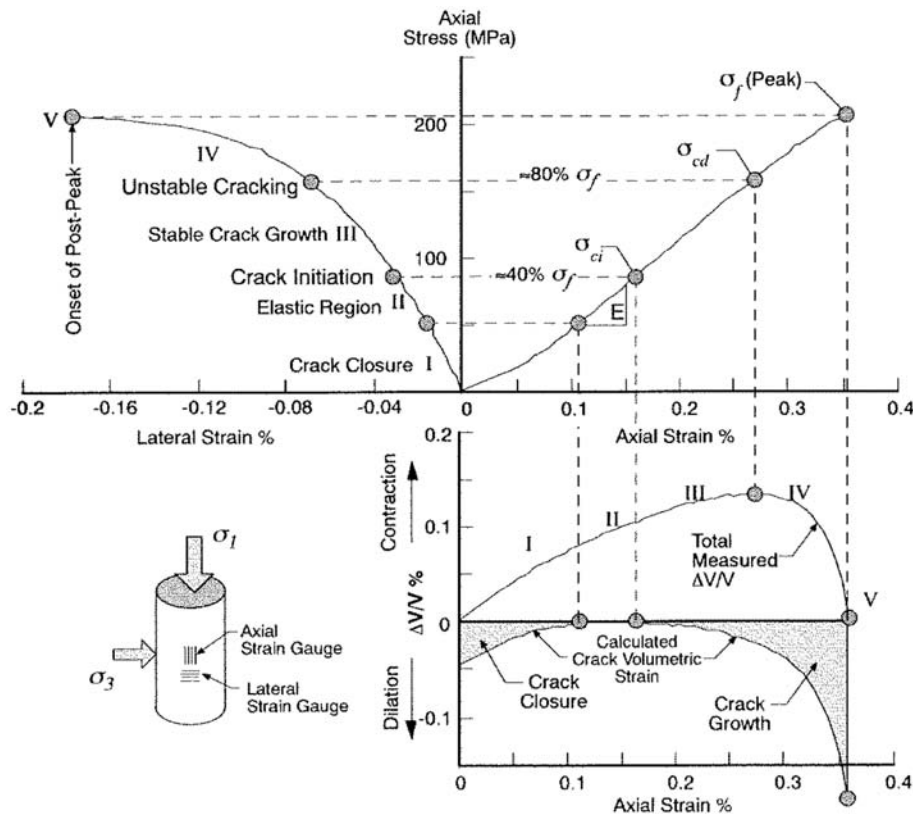


Fig. 4.21: Stress-strain diagram from a uniaxial compression test with the crack initiation, crack interaction, and peak strength thresholds defined (after Martin [30]).

sustain increased loading whereby reaching a peak in the imposed loading (or short-term strength). Macroscopic failure ensues.

The strength envelope illustrated in Fig. 4.20 is then assembled using the thresholds described above, which are typically determined from a series of laboratory tests. Depending on the stress path taken, a unit volume of rock can undergo failure in tension, spalling, or shear. In tension, failure is controlled by the first crack (i.e. crack initiation) whereas failure in compression involves damage accumulation, crack interaction, and critical extension strain [36]. Above damage initiation and at low confinement, spalling failure occurs due to the propagation of individual cracks. In regions of high confinement and above damage initiation, shear failure takes place due to the interaction of several cracks.

The crack initiation and crack interaction thresholds define the specific shape of the strength envelope in regions of low confinement as shown in Fig. 4.20; the former represents the in situ lower bound strength while the latter, the upper bound in situ strength [37, 38]. At AECL (Atomic Energy of Canada Limited), research activities have focused on the quantification of rock damage via the use of the crack initiation and crack interaction thresholds [33]. In situ, failure around underground openings in regions of high deviatoric stress and low confinement can occur at stress levels as low as $0.3-0.5\sigma_c$ (i.e. crack initiation) and as high as $0.7\sigma_c$ (i.e. crack interaction) [35, 37, 36]. The transition from the lower bound strength (i.e. crack initiation) to the upper bound strength (i.e. crack interaction or yield) is controlled by the spalling limit (the ratio between σ_3 and σ_1), which represents a critical confinement ratio [39, 37, 38]. The spalling limit deviates from the laboratory-determined strength envelope due to differences in the stress path (loading history) and geometry of the laboratory sample: i.e. fewer cracks that are free to propagate are required to reach the yield strength in situ [37, 38, 36].

In experimental studies [39, 40], it has been demonstrated that stable crack growth increases significantly when the spalling limit is less than 0.05 (Fig. 4.22). As a result, significant damage, related to crack growth and resulting in strength reduction, is relatively high where the spalling limit is less than 0.05 [37]. Diederichs [32, 38, 36] in numerical studies also demonstrated that crack length is important to strength degradation in regions of low confinement where initiating cracks are able to extend freely in length. As confinement increases, unstable crack growth is suppressed and failure occurs by damage accumulation

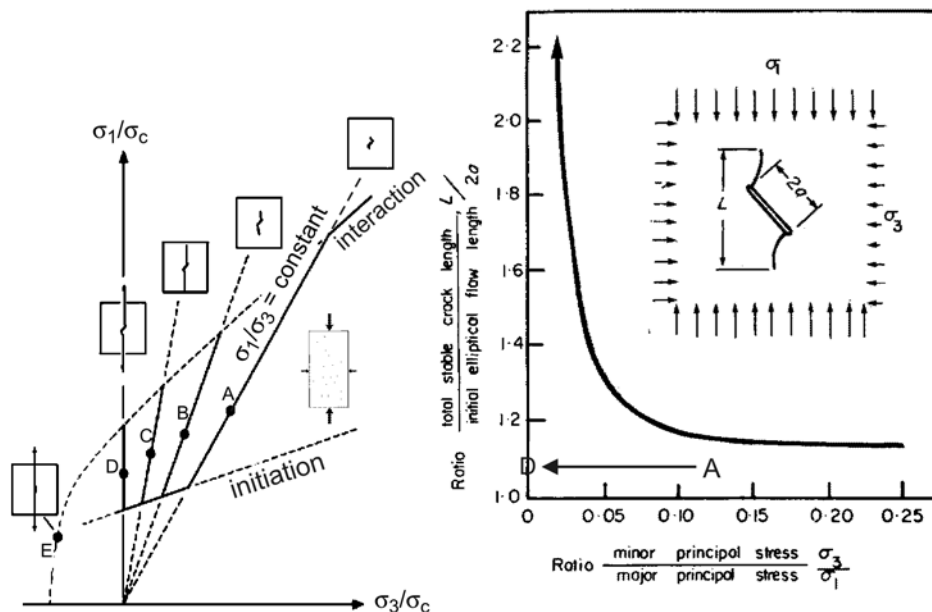


Fig. 4.22: Increasing length of stable crack propagation as the spalling limit decreases with damage distributed between the crack initiation and interaction thresholds (modified from Diederichs [38], Read et al. [37], and Hoek [39]).

and interaction [36]. Strength reduction can result from excavation damage (e.g. stress rotation), variability (e.g. scale effects), and heterogeneity (i.e. resulting in local internal tensile stress concentrations) [38, 36]. Thus, as the spalling limit decreases, the potential for damage and consequently, strength degradation along with crack length increases.

4.5.1 Data Integration

Integration of borehole data involved drillcore mapping, DOPTV imaging, derived seismic wave parameters, and stress ratios from three-dimensional numerical simulations. To provide guidance to understanding the large amount of information contained in the figures that summarise the data integration of each borehole, a brief explanation follows by using BEZ-B11 as an example (Fig. 4.23).

The background of each figure consists of the drillcore map (topmost) and unwrapped DOPTV images. With the exception of BEZ-B9, each figure contains two DOPTV images with the oldest at the bottom. The oldest DOPTV image was taken eight to 17 days after the radial boreholes (BEZ-B8 to B19) were drilled and 24 days after the niche was completed. The youngest image was taken 33 to 35 weeks after the radial boreholes were drilled and 35 to 36 weeks after the niche was completed. The borehole collars were captured only in the youngest images as modifications to the logging equipment were required. In addition, some of the older images were also distorted near the collar due to the lack of support for the sonde. The DOPTV images have also been rotated so that the centreline of each image corresponded with the travel path of the seismic probe.

Seismic wave velocities and normalised amplitudes overlay the DOPTV images while V_p/V_s ratios overlay the drillcore map. A normalised amplitude value of 100% is shown as a dashed line and V_p/V_s ratios representing the Poisson's ratios parallel with and perpendicular to bedding are also shown as dashed lines (at 2.0 and 1.7, respectively). Seismic data are from loggings carried out concurrently with the older DOPTV logging or five to 22 days after the boreholes were drilled (which spanned a period of nine days) and 21 to 29 days after completion of the niche.

Stress ratios extracted from continuum elastic isotropic (CIE) and continuum elastic anisotropic (CAE) numerical simulations are shown in the topmost plot in all the figures. Borehole drilling was not simulated in the three-dimensional numerical simulations. Consequently, the ratios represent values taken from the centreline of where each borehole is located in the numerical simulations.

4.5.2 Southern Vertical Borehole Plane

The southern vertical plane of boreholes is located about 3.2m south of the niche face (Fig. 4.8) and consists of four boreholes (BEZ-B14 to B17). Two boreholes (BEZ-B14 and B17) with nominal lengths

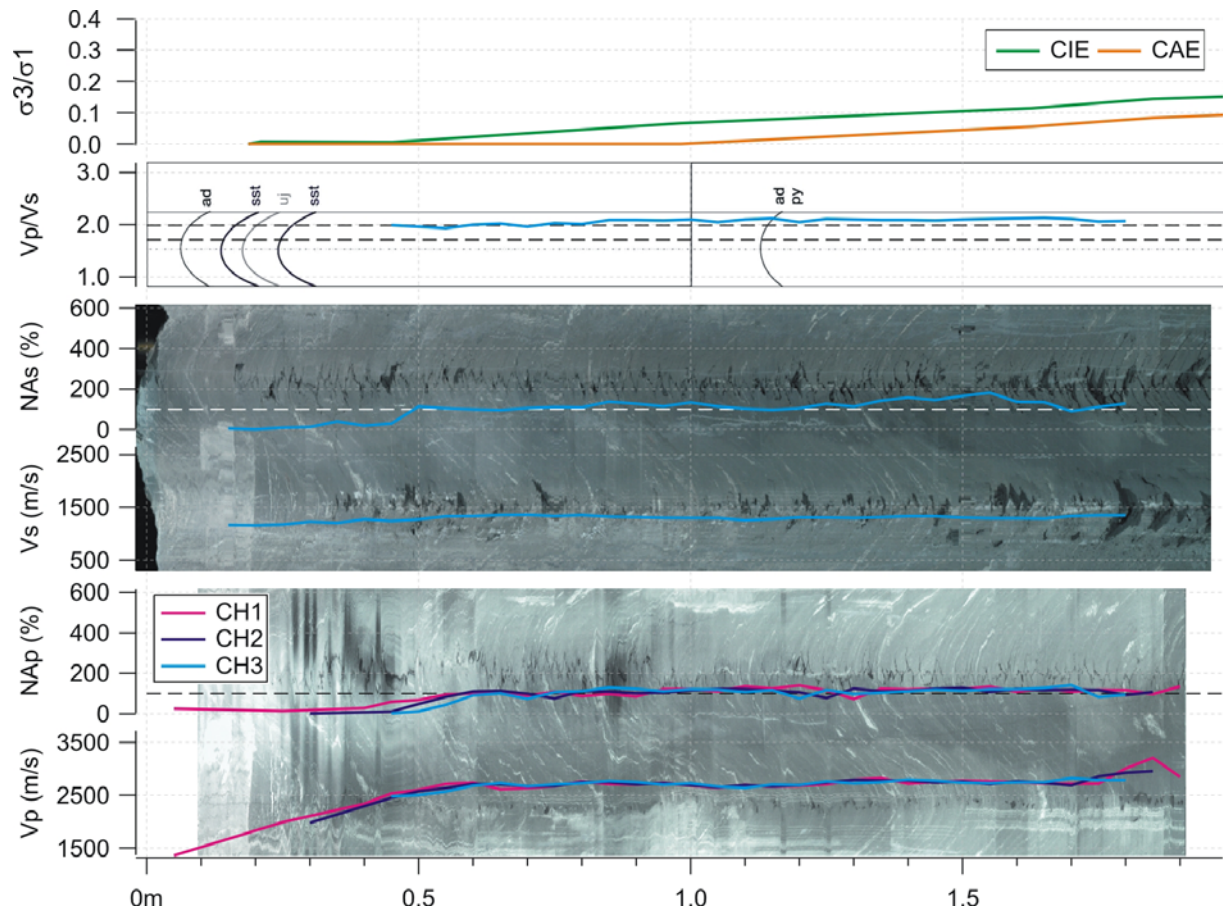


Fig. 4.23: Integration of the borehole data from BEZ-B11.

of 2.5m were drilled sub-horizontally in both sidewalls and therefore, are sub-parallel with bedding. The remaining two boreholes (BEZ-B15 and B16) with nominal lengths of 2m were drilled with an inclination of 45° into the upper walls. The inclined boreholes likewise intersect bedding at angles closer to 45° . Integration of the field and modelling data for BEZ-B14 to B17 are found in Figures 4.24a to 4.24d, respectively.

A total of 15 fractures have been identified in BEZ-B14 to B17 [41]. Three of the mapped fractures are tectonic in nature (labelled “F” in Fig. 4.8), four are possible induced fractures (labelled “IF2” in Fig. 4.8), and eight are induced fractures with the highest level of confidence (labelled “IF1” in Fig. 4.8). As Figures 4.24b and 4.24d show, some of the fractures grouped in this manner differed from those mapped in the drillcore. Fractures labelled as “ad” in these figures are clearly seen in the DOPTV images, suggesting they are not artificial in origin. Hence, they have been labelled IF1. About half of the IF1 fractures, 75% of which were bedding-parallel, occurred in the first 10cm (from the borehole collars) while 40% were found in the second 10cm.

Borehole instabilities were seen in three out of the four boreholes in the southern vertical plane: BEZ-B14 (Fig. 4.24a), B16 (Fig. 4.24c), and B17 (Fig. 4.24d). Instabilities in the sub-horizontal boreholes (BEZ-B14 and B17) were more severe than those in the inclined borehole (BEZ-B16) as notch formation was more prominent in the former while instabilities appeared to be more surficial in the latter. Regardless, both types of instabilities were diametrically-opposed and concentrated where bedding was tangential to the borehole wall. In all three boreholes, the instabilities tended to start a distance from the borehole collar and intensified with depth. The severity in the instabilities also appeared to increase with time.

In the seismic measurements, the probe travelled the length of the borehole along the top (when facing the borehole from the niche). The location of the probe around the borehole must be kept in mind when interpreting the data obtained from transverse isotropic media (such as the Opalinus Clay) as the P-waves will be most affected by structures perpendicular to the borehole axis whereas the vertically-polarised S-

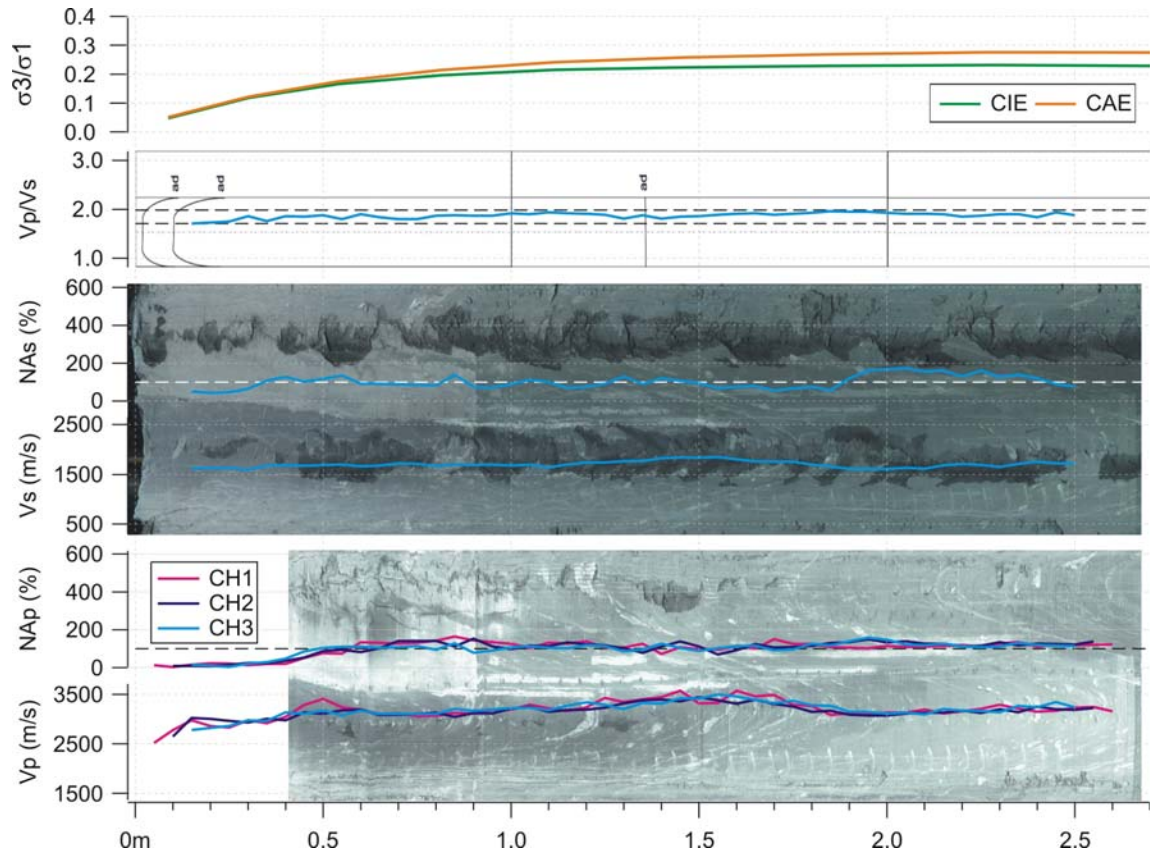


Fig. 4.24a: BEZ-B14 data integration with seismic sensors coupled to the top of the borehole. Refer to Fig. 4.5 for borehole location and Appendix C for enlarged drillcore maps.

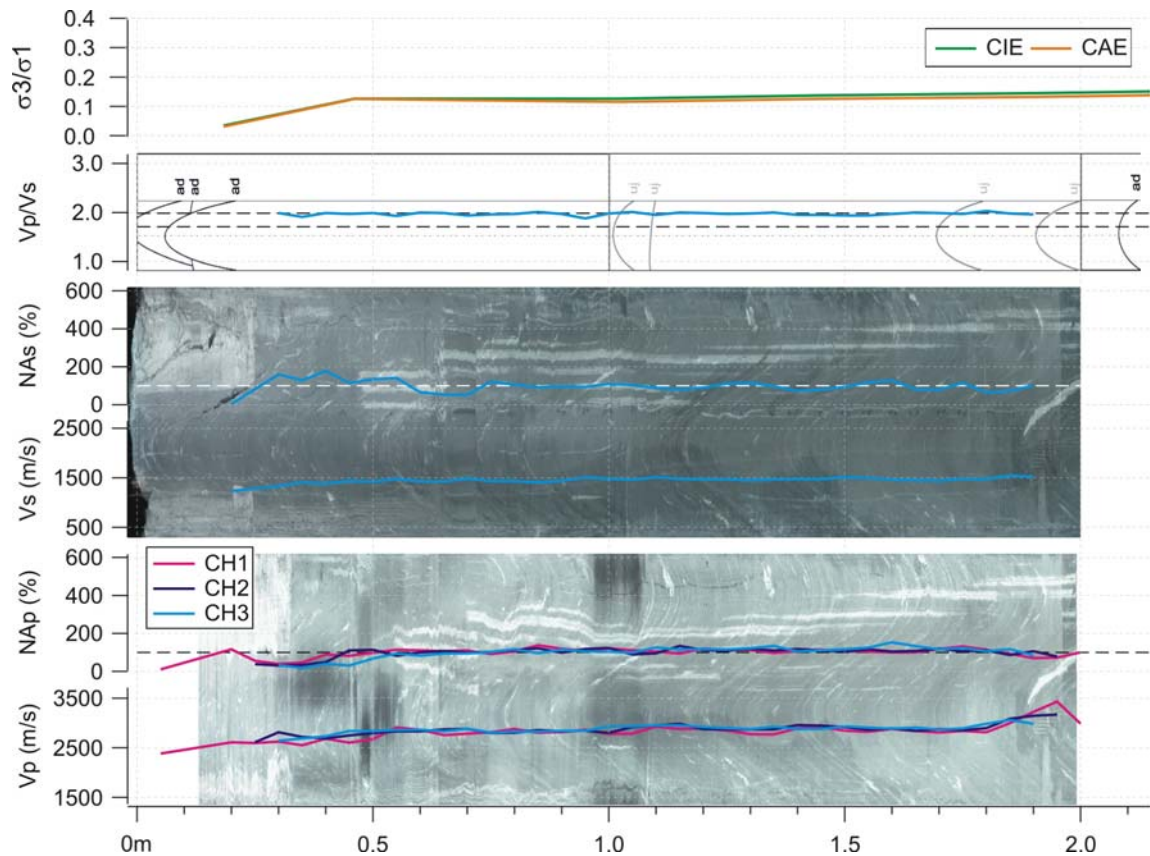


Fig. 4.24b: BEZ-B15 data integration with seismic sensors coupled to the top of the borehole. Refer to Fig. 4.5 for borehole location and Appendix C for enlarged drillcore maps.

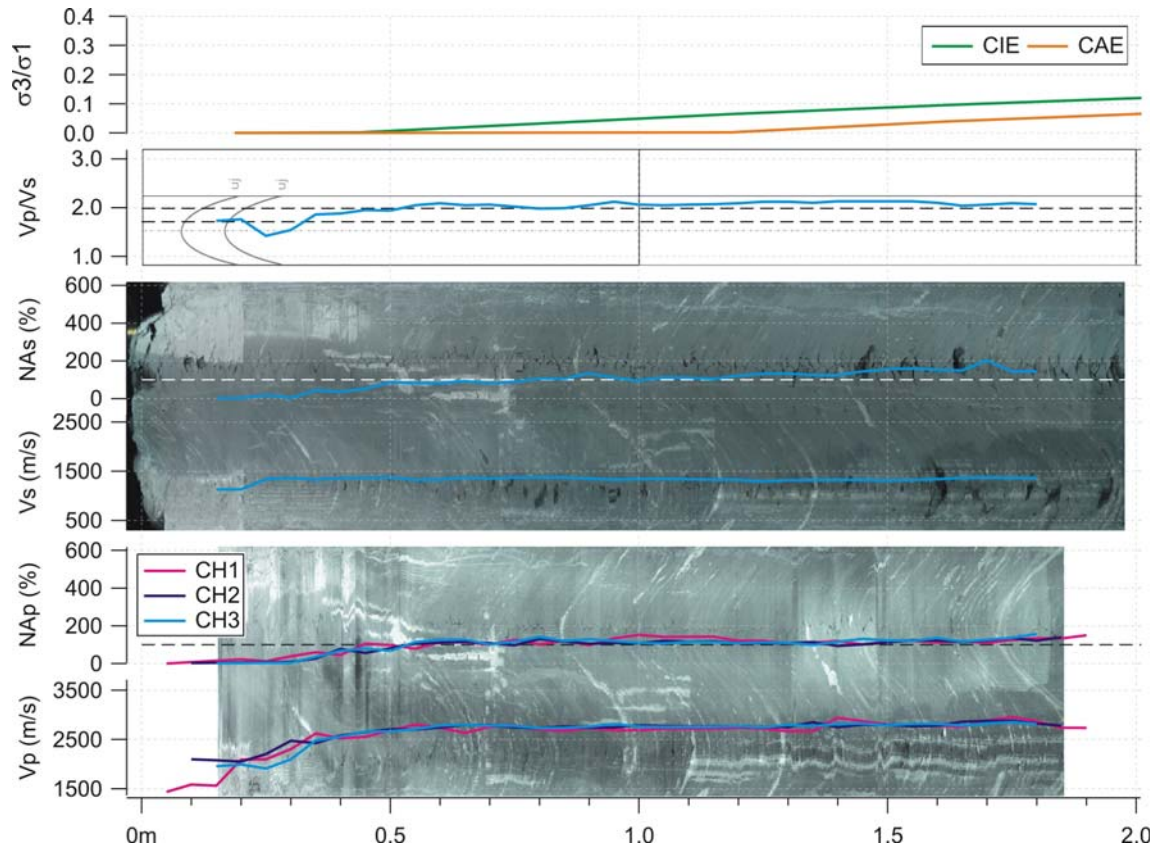


Fig. 4.24c: BEZ-B16 data integration with seismic sensors coupled to the top of the borehole. Refer to Fig. 4.5 for borehole location and Appendix C for enlarged drillcore maps.

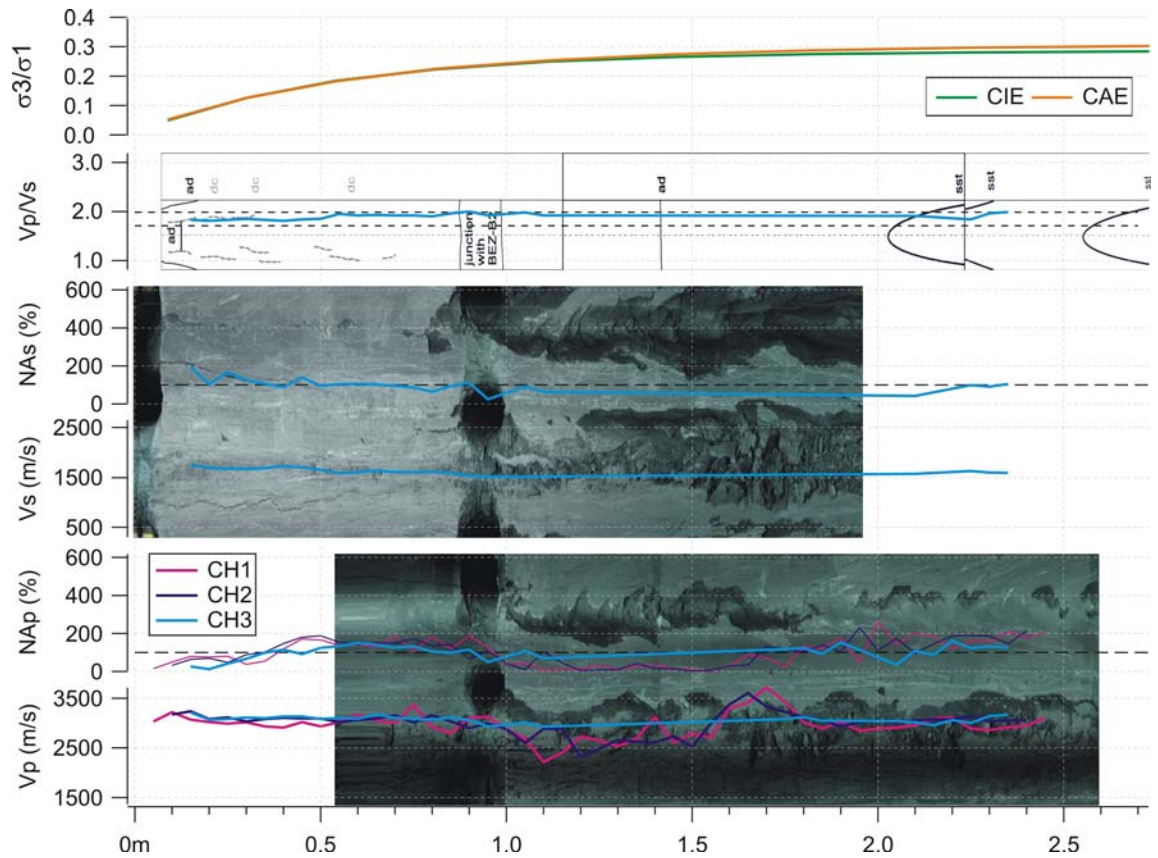


Fig. 4.24d: BEZ-B17 data integration with seismic sensors coupled to the top of the borehole. Refer to Fig. 4.5 for borehole location and Appendix C for enlarged drillcore maps.

waves will be most affected by structures parallel with the borehole axis. The directional-dependency of the P- and S-waves were illustrated in Fig. 4.14, where velocities were shown to be highest in the boreholes drilled sub-parallel with bedding and lowest in the borehole drilled perpendicular to bedding. As a result, amplitude changes may be more sensitive to overall rock damage as wave attenuation would be incurred regardless of preferred fracture and/or fabric orientation. The influence of the bedding is evident in Figures 4.24a and 4.24d as a large reduction in the velocities in BEZ-B14 and B17 did not correspond with a reduction in the normalised amplitudes; this is most probably attributed to the direction of the near bedding-parallel seismic wave propagation. In this case, velocity profiles may also not be greatly affected by the predominantly bedding-parallel fractures that have been mapped in both boreholes (Figures 4.24a and 4.24d). In comparison, the seismic wave velocities and normalised amplitudes in the inclined boreholes (where seismic waves propagate at higher angles to bedding) plateaued near the same borehole depth (or distance from the borehole collar). The normalised amplitudes in the sub-horizontal boreholes (BEZ-B14 and B17) plateaued near 0.5m from the collar. Likewise, both the velocities and normalised amplitudes in the inclined boreholes (BEZ-B15 and B16) plateaued near 0.5 to 0.6m.

Integration of the field data showed that IF1 fractures were found in regions of the lowest seismic wave amplitudes and velocities (where they were affected). The locations where borehole instabilities became diametrically-opposed also corresponded with where the seismic wave amplitudes and velocities plateaued. Hence, the perturbed zone consisted of the volume rock where induced fractures were found and where the seismic wave amplitudes and velocities had yet to plateau.

Integration of the modelling data with the field data showed that regions where IF1 fractures were found, which correspond with the lowest seismic wave amplitudes and velocities, corresponded with stress ratios ranging from zero to 0.15. Stress ratios of zero to 0.2 were attained where the seismic wave amplitudes and/or velocities plateau, which also corresponded with where borehole instabilities became diametrically-opposed. With the exception of BEZ-B16 (Fig. 4.24c), stress ratios were greater than 0.1 after some distance from the borehole collar. In BEZ-B16, stress ratios were quite low (0 to 0.05) up to 1m from the collar and remain below 0.1 until near the borehole terminus. The numerical results also showed that the isotropic and anisotropic (or transversely-isotropic) simulations were very similar in the perturbed zone defined by the field data. In the sub-horizontal boreholes, both simulations differed little to the end of the borehole. This was not the case in the inclined boreholes, most notably BEZ-B16.

The perturbed zone around the niche at this plane appeared to be fairly uniform with an extent ranging from 0.5m to 0.6m. This coincided with stress ratios of 0.15 to 0.2 in the sidewalls and less than 0.15 in the inclined boreholes. The inclined borehole in the upper east wall seemed to be more perturbed than its west wall counterpart as instabilities were apparent and low stress ratios (less than 0.1) along the entire borehole length.

4.5.3 Northern Vertical Borehole Plane

The northern vertical plane of boreholes (Fig. 4.8) consists of six boreholes (BEZ-B8 to B13) and is located about 2.2m from the niche face. The borehole configuration with respect to bedding and the niche axis is the same as the southern vertical plane with the exception of an additional two boreholes: BEZ-B10 and B13. BEZ-B10 has been drilled vertically into the crown and has a nominal length of 2.5m. BEZ-B13 has been drilled with an inclination of 45° into the floor and has a nominal length of 3m. The former intersects bedding at roughly 45° while the latter intersects bedding at about 90°. BEZ-B8 and B12 are sub-horizontal with nominal lengths of 2.5m and have been drilled nearly parallel with bedding in both sidewalls. BEZ-B9 and B11 are inclined upwards at about 45° and likewise intersect bedding at about 45°. The data integrations for this plane of boreholes are found in Figures 4.25a to 4.25f.

In the six boreholes, 37 fractures were identified [41]: 14 were tectonic, 16 were either IF2 or unclassified ("O"), and seven were IF1. Again inconsistencies between the drillcore maps and DOPTV images were seen. In BEZ-B8 (Fig. 4.25a), B10 (Fig. 4.25c), and B13 (Fig. 4.25f) "ad" fractures were clearly seen in the DOPTV images and have been consequently categorised as IF1 or F in Fig. 4.8. Of the IF1 fractures, nearly 60% were bedding-parallel and about 70% were found in the first 20cm. In BEZ-B13 alone, 18 fractures were mapped. Seven of these, which can be seen in the DOPTV images (Fig. 4.25f), were

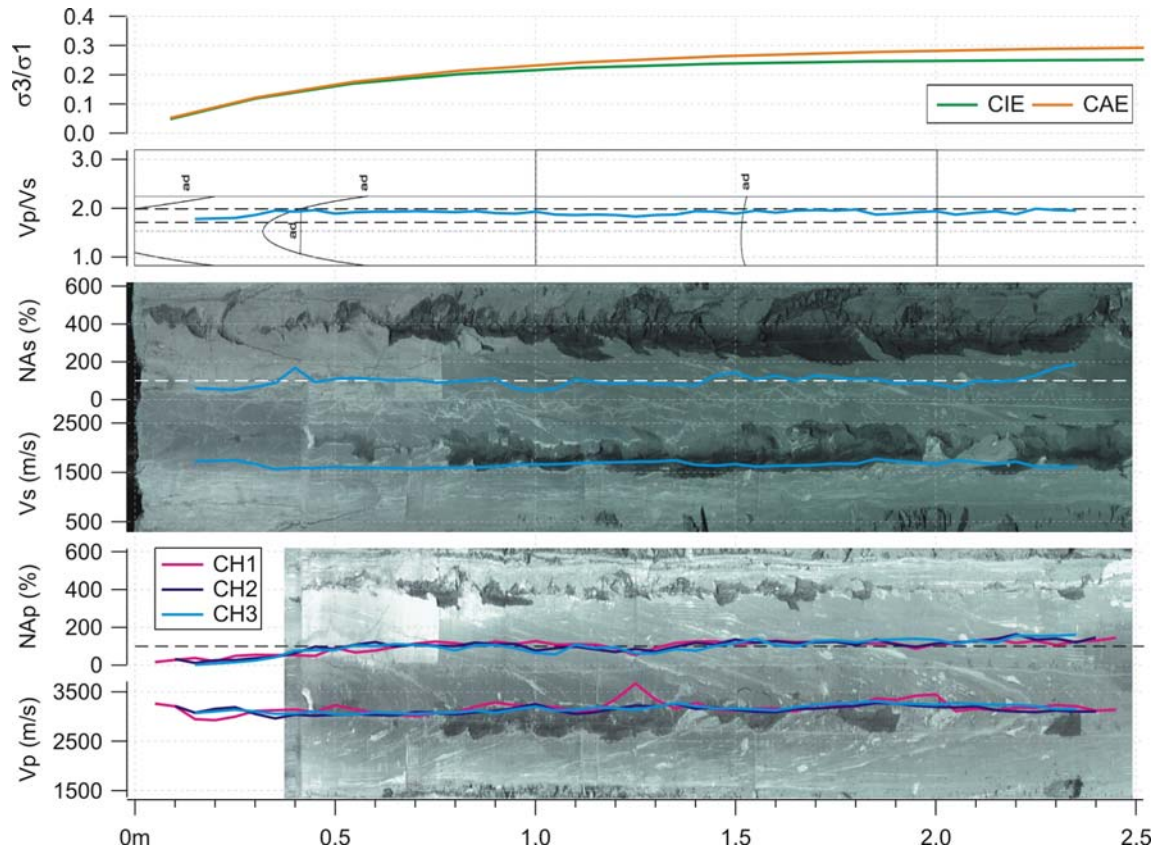


Fig. 4.25a: BEZ-B8 data integration with seismic sensors coupled to the top of the borehole. Refer to Fig. 4.5 for borehole location and Appendix C for enlarged drillcore maps.

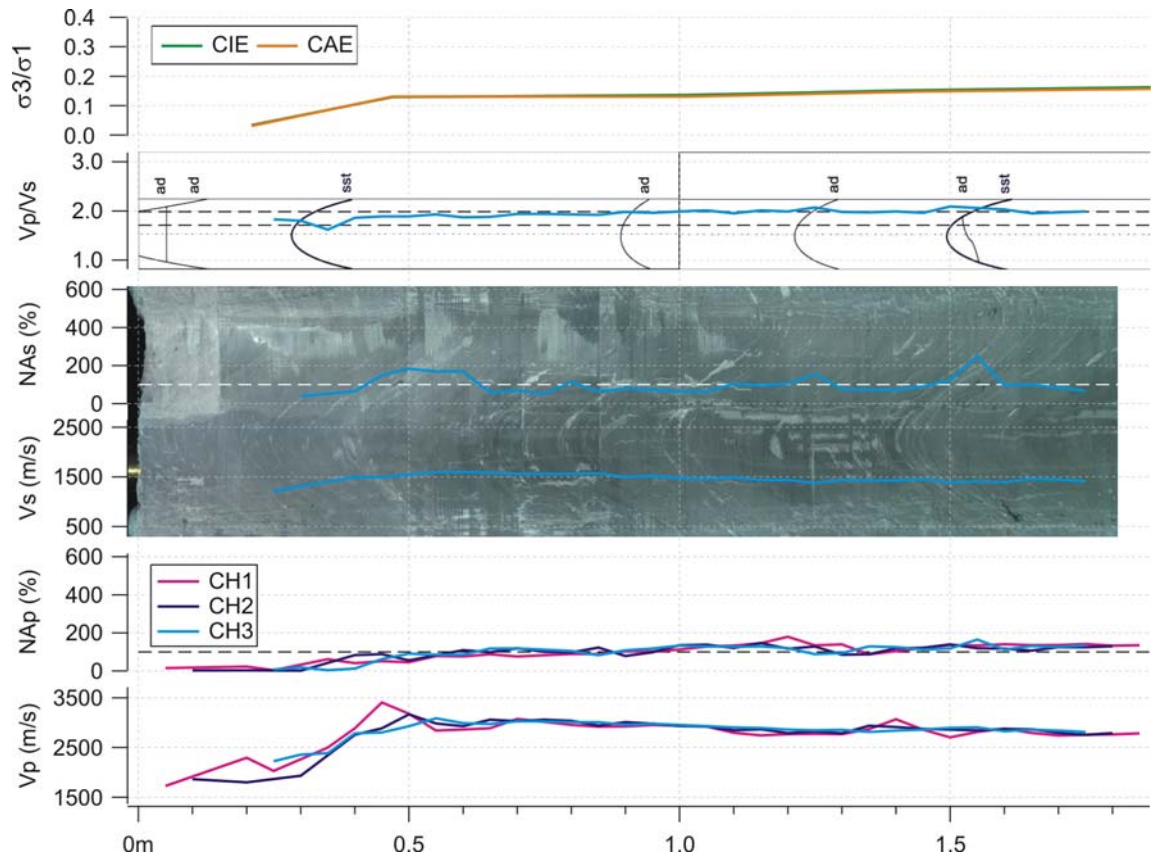


Fig. 4.25b: BEZ-B9 data integration with seismic sensors coupled to the top of the borehole. Refer to Fig. 4.5 for borehole location and Appendix C for enlarged drillcore maps.

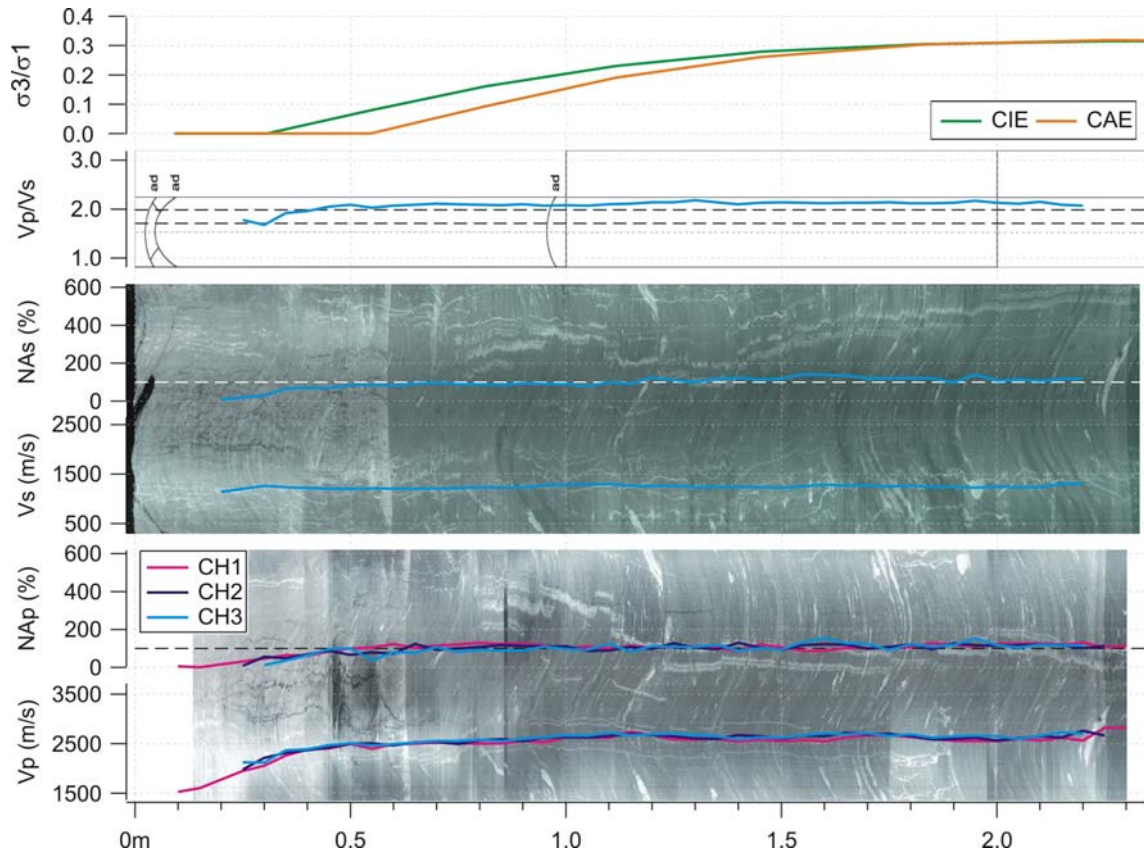


Fig. 4.25c: BEZ-B10 data integration with seismic sensors coupled to the east wall of the borehole. Refer to Fig. 4.5 for borehole location and Appendix C for enlarged drillcore maps.

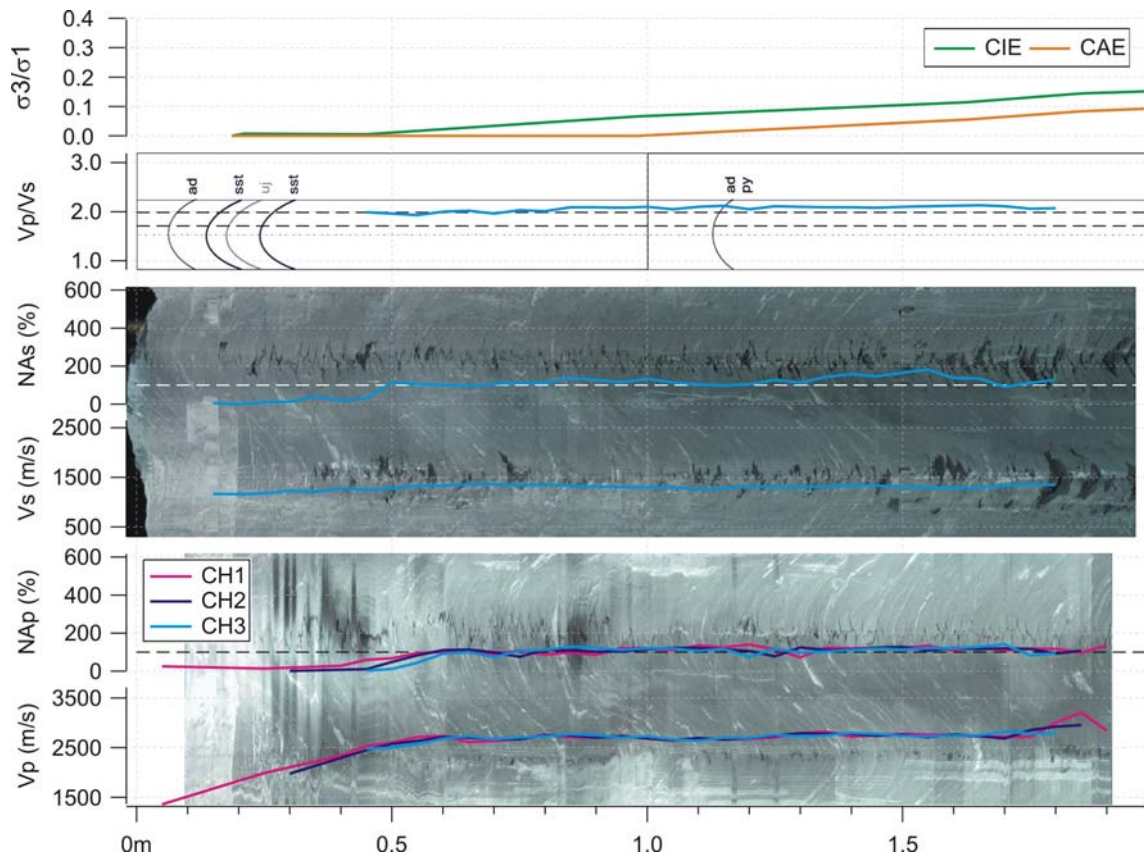


Fig. 4.25d: BEZ-B11 data integration with seismic sensors coupled to the top of the borehole. Refer to Fig. 4.5 for borehole location and Appendix C for enlarged drillcore maps.

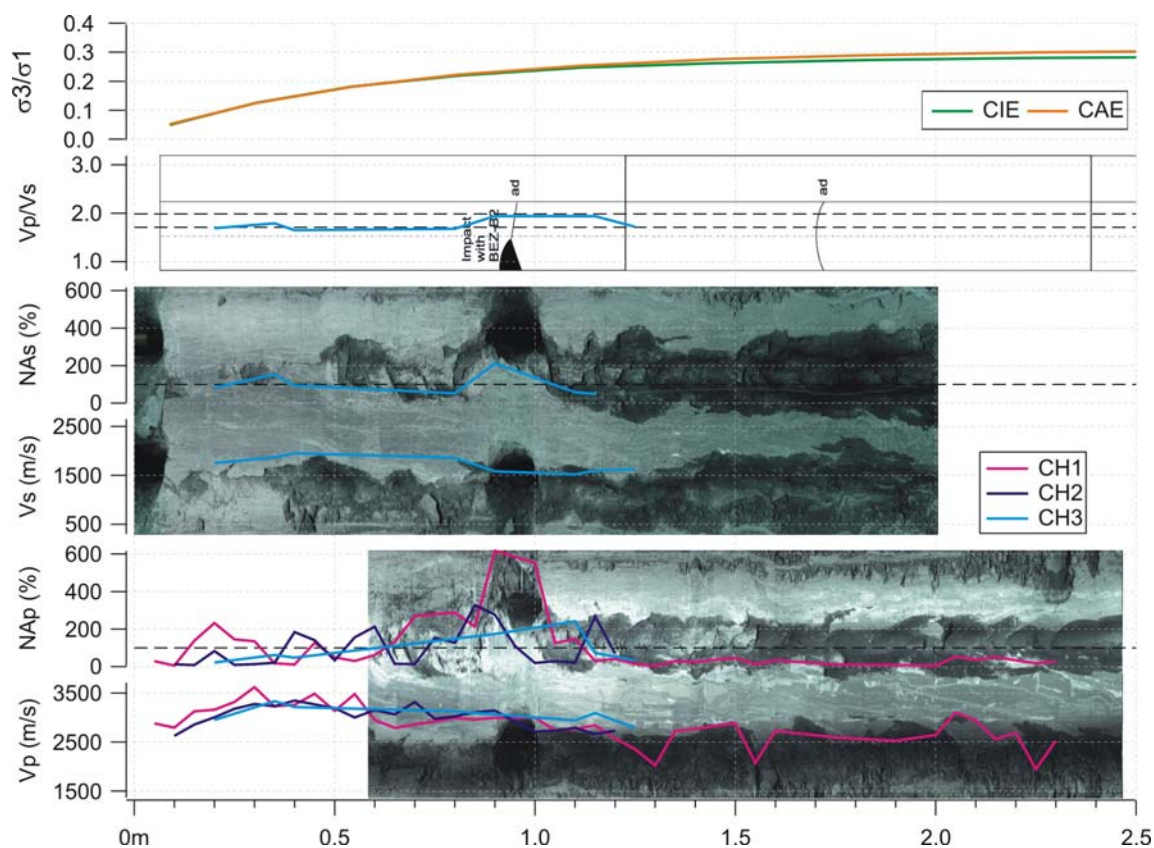


Fig. 4.25e: BEZ-B12 data integration with seismic sensors coupled to the top of the borehole. Refer to Fig. 4.5 for borehole location and Appendix C for enlarged drillcore maps.

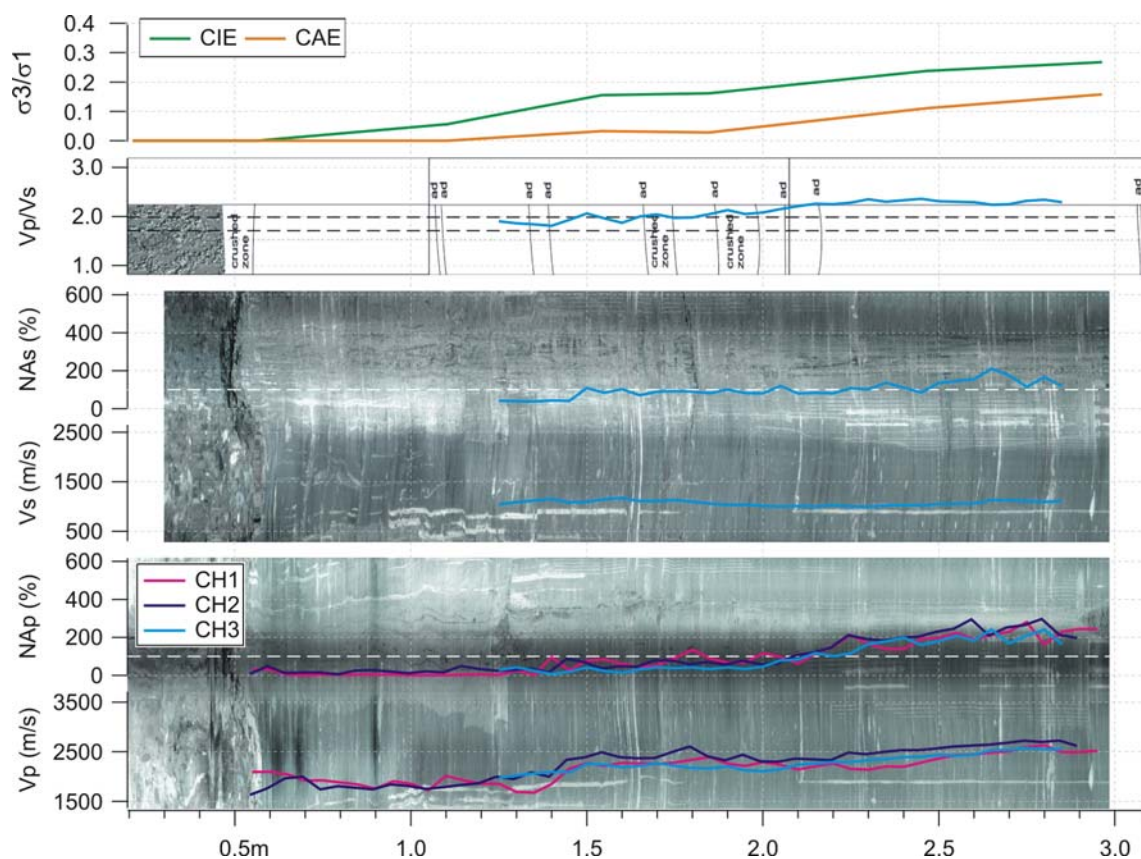


Fig. 4.25f: BEZ-B13 data integration with seismic sensors coupled to the east wall of the borehole. Refer to Fig. 4.5 for borehole location and Appendix C for enlarged drillcore maps.

attributed to a possible tectonic structure that may correspond with the tectonic structure mapped in BEZ-B19 at a distance of about 2.1m from the collar (Fig. 4.26c). Most of the fractures in BEZ-B13 were concentrated in the middle of the borehole, where two crushed zones have also been mapped, from 0.9m to 2.1m depth (Fig. 4.25f).

Similar to the southern vertical plane, instabilities were seen in three boreholes: BEZ-B8 (Fig. 4.25a), B11 (Fig. 4.25d), and B12 (Fig. 4.25e). Again, instabilities in the sub-horizontal boreholes (BEZ-B8 and B12) were more severe than those in the inclined borehole (BEZ-B11) with notch-like formation in the former and surficial flaking in the latter. Instabilities were also diametrically-opposed (and concentrated where bedding was tangential to the borehole wall), commenced a distance from the collar, and intensified in severity with greater distance from the borehole collar. With time, borehole instabilities increased in width.

In most of the boreholes, the mini-sonic probe travelled along the top of the borehole (when facing the borehole) with the exception of BEZ-B10 and B13 where the probe travelled along the right wall (when facing the niche face). Again, directional-dependency in the seismic data was seen in the sub-horizontal boreholes as reductions were only seen in the normalised amplitudes (Fig. 4.25a). In BEZ-B8 (Fig. 4.25a), a plateau in the normalised amplitude was reached between 0.6m and 0.7m distance from the collar. Logging in BEZ-B12 was problematic due to the borehole instabilities, which adversely affected sensor coupling at depths greater than 1.2m (Fig. 4.25e). In all the other boreholes, plateaus in the normalised amplitudes and velocities were reached at nearly the same borehole length. In BEZ-B9 (Fig. 4.25b) and B10 (Fig. 4.25c), plateaus in both the normalised amplitudes and velocities were reached between 0.5m to 0.6m. In BEZ-B11 (Fig. 4.25d), the plateau was found near 0.6m. In BEZ-B13 (Fig. 4.25f), three plateaus were seen. The first occurred between 0.5m and 1.4m: the first 0.5m consisted of the concrete floor. The second plateau occurred between 1.4m and 2.2m while the last plateau consisted of the remaining borehole length.

Again the field data from each borehole were integrated and similar findings to the southern vertical plane were indicated. The zone of IF1 fracturing coincided with the lowest seismic wave amplitudes and diametrically-opposed borehole instabilities began near seismic wave amplitude and velocity plateaus. Integration of the field data with the modelling data showed that IF1 fracturing coincided with stress ratios of zero to 0.1 while seismic wave amplitude and velocity plateaus coincided with stress ratios of 0.05 to 0.2. The numerical results obtained from the isotropic and anisotropic simulations also differed little with the exception of BEZ-B10, B11, and B13. Above the crown, stress ratios differed between 0.3m and 1.5m from the borehole collar. Below the invert and in the east upper wall, stress ratios between the two simulations deviated after a distance of 0.5-0.6m.

Interestingly, the stress ratios at BEZ-B13 (below the invert) also showed a two-step pattern that coincided roughly with a similar pattern in the seismic wave data (Fig. 4.25f). In the first 1-1.5m of the borehole, little fracturing was mapped but P-wave normalised amplitudes and velocities were the lowest while the S-wave signal strength was poor. Between 1.4-2.2m, several fractures were mapped in the drillcore and seen in the younger DOPTV images (and these are mostly likely associated with a possible tectonic shear) but the seismic wave amplitudes and velocities increased rather than decreased. This is due to the timing of the seismic data acquisition, which coincided with the older DOPTV images where these fractures were not seen. From 2.2m depth, the seismic data again increased.

Around the northern cross-section, the perturbed zone was about 0.6-0.7m in extent. In the western portion of the niche, the boundary of the perturbed zone coincided with stress ratios of 0.1 to 0.2. Above the crown, the rock mass appeared to be perturbed with seismic wave velocities and ratios of 0.05 to 0.1. The most perturbed zones corresponded with the inclined borehole in the upper east wall and below the invert where seismic wave parameters and stress ratios were lowest in values.

4.5.4 Horizontal Borehole Plane Ahead of the Face

The final plane of post-excavation boreholes consisted of three boreholes along a horizontal plane in the final niche face (Fig. 4.8). BEZ-B18 was drilled roughly 1.4m west of BEZ-B3 (drilled in the pre-excavation stage) while BEZ-B19 was drilled about 1.3m east of BEZ-B3. Both BEZ-B18 and B19 have a

nominal length of 2.5m whereas the unexcavated length of BEZ-B3 is about 3m. The three sub-horizontal boreholes drilled in the face intersect bedding at 45°. Figures 4.26a to 4.26c summarise the field and model data integration of the horizontal borehole plane ahead of the face.

Fractures identified in the drillcore maps and DOPTV images total 15 in the post-excitation boreholes (BEZ-B18 and B19). BEZ-B3 was not included here as the drillcore was mapped prior to the niche excavation. Two fractures were tectonic and four were IF1 fractures. All IF1 fractures were bedding-parallel and half were found in the first 20cm (Fig. 4.8).

Again diametrically-opposed borehole instabilities in both BEZ-B18 (Fig. 4.26a) and B19 (Fig. 4.26c) were found a distance from the collar (1.6-1.7m). Instabilities were seen in BEZ-B3 (Fig. 4.26b) from the collar but these occurred prior to the completion of the niche (see Chapter 5). Unlike the other boreholes, the instabilities in the face were not concentrated where bedding was tangent to the borehole walls (Fig. 4.10). This suggested that the instabilities may provide indications of the formation stress state. Although promising, there was insufficient information in the field data to constrain the stress state around the niche in this thesis.

The travel path of the probe in the seismic measurements was along the right borehole wall (when facing the niche face) in BEZ-B18 and B3 but along the left wall in BEZ-B19. Seismic wave amplitudes and velocities reached plateaus at similar borehole lengths in all three boreholes: between 0.6m and 0.8m in BEZ-B18 (Fig. 4.26a), near 6.2m in BEZ-B3 (Fig. 4.26b) with the collar at roughly 5.1m, and between 0.6m and 0.7m in BEZ-B19 (Fig. 4.26c).

Again IF1 fractures coincided with regions of lowest seismic wave amplitudes and velocities. This corresponded with a stress ratio range of zero to 0.05. Seismic wave plateaus corresponded with stress ratios of 0.05 to 0.15 in the post-excitation boreholes and 0.15 to 0.20 in BEZ-B3. Both the P- and S-wave amplitudes increased in the younger boreholes (BEZ-B18 in Fig. 4.26a and BEZ-B19 in Fig. 4.26c)

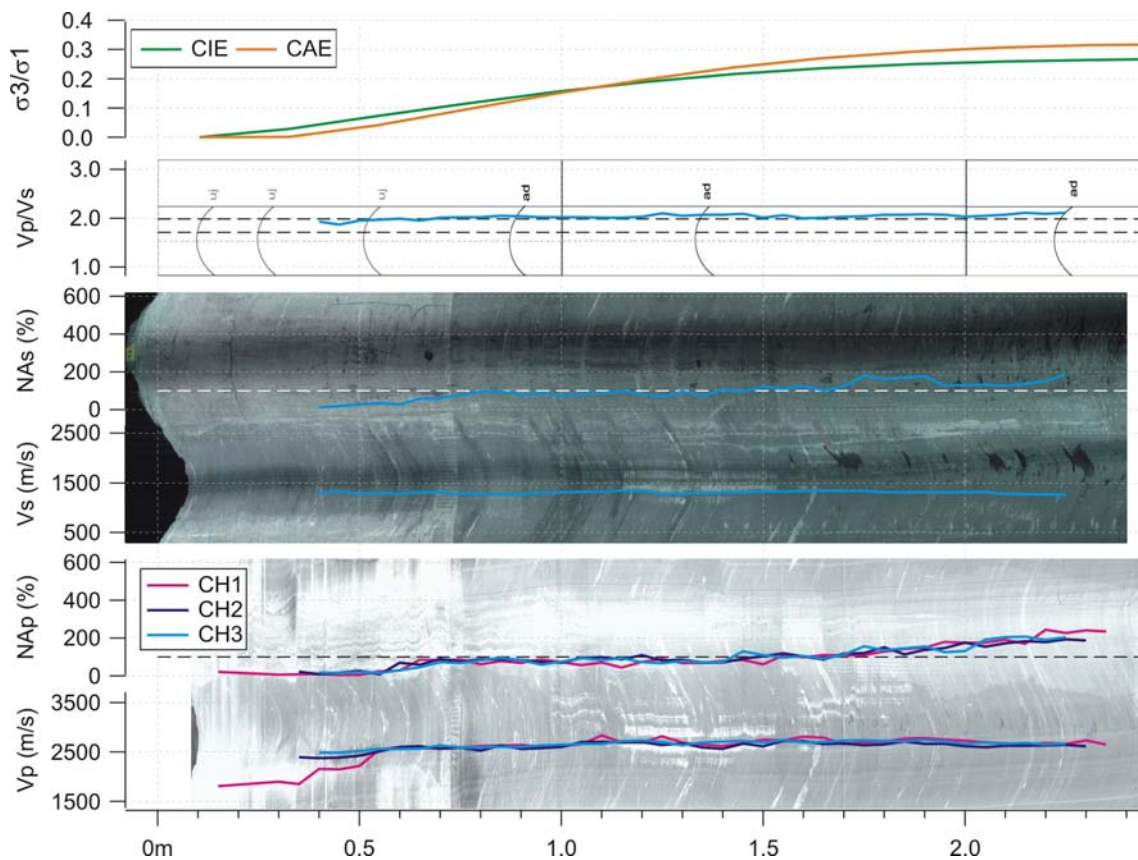


Fig. 4.26a: BEZ-B18 data integration with seismic sensors coupled to the east wall of the borehole. Refer to Fig. 4.5 for borehole location and Appendix C for enlarged drillcore maps.

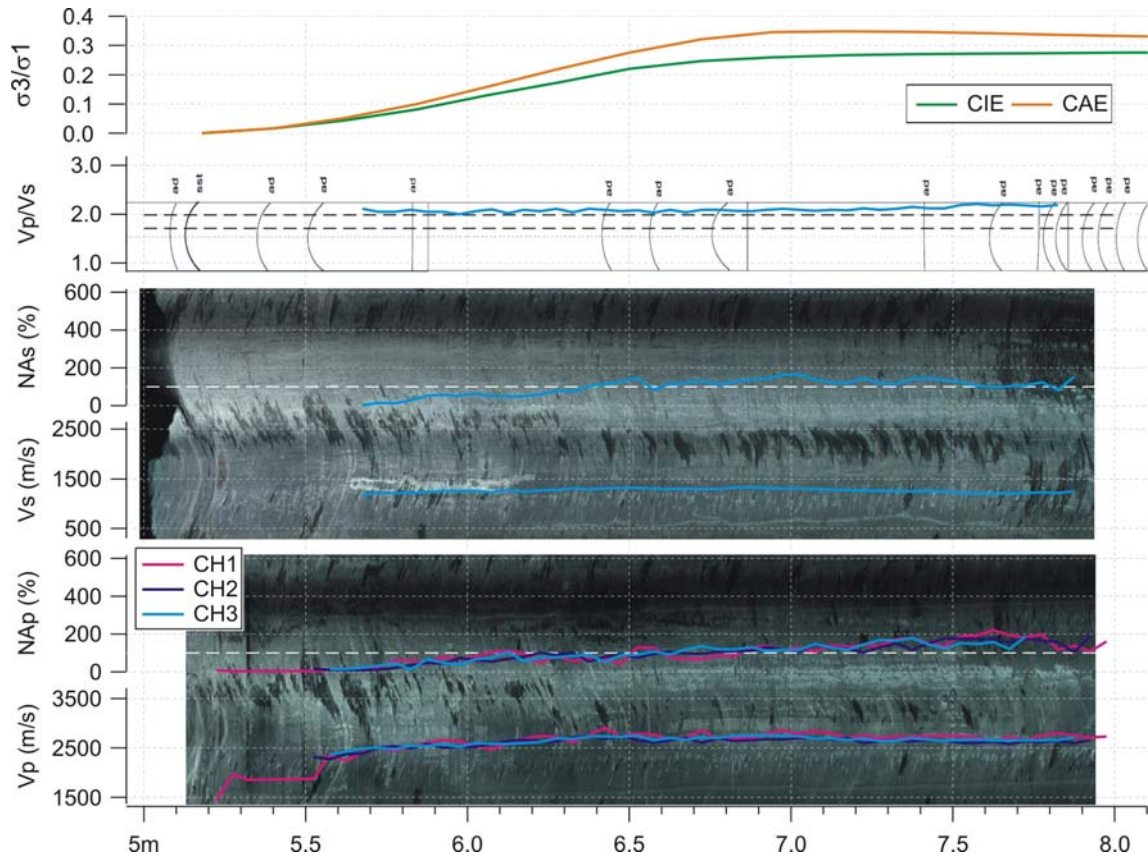


Fig. 4.26b: BEZ-B3 data integration with seismic sensors coupled to the east wall of the borehole. Refer to Fig. 4.5 for borehole location and Appendix C for enlarged drillcore maps.

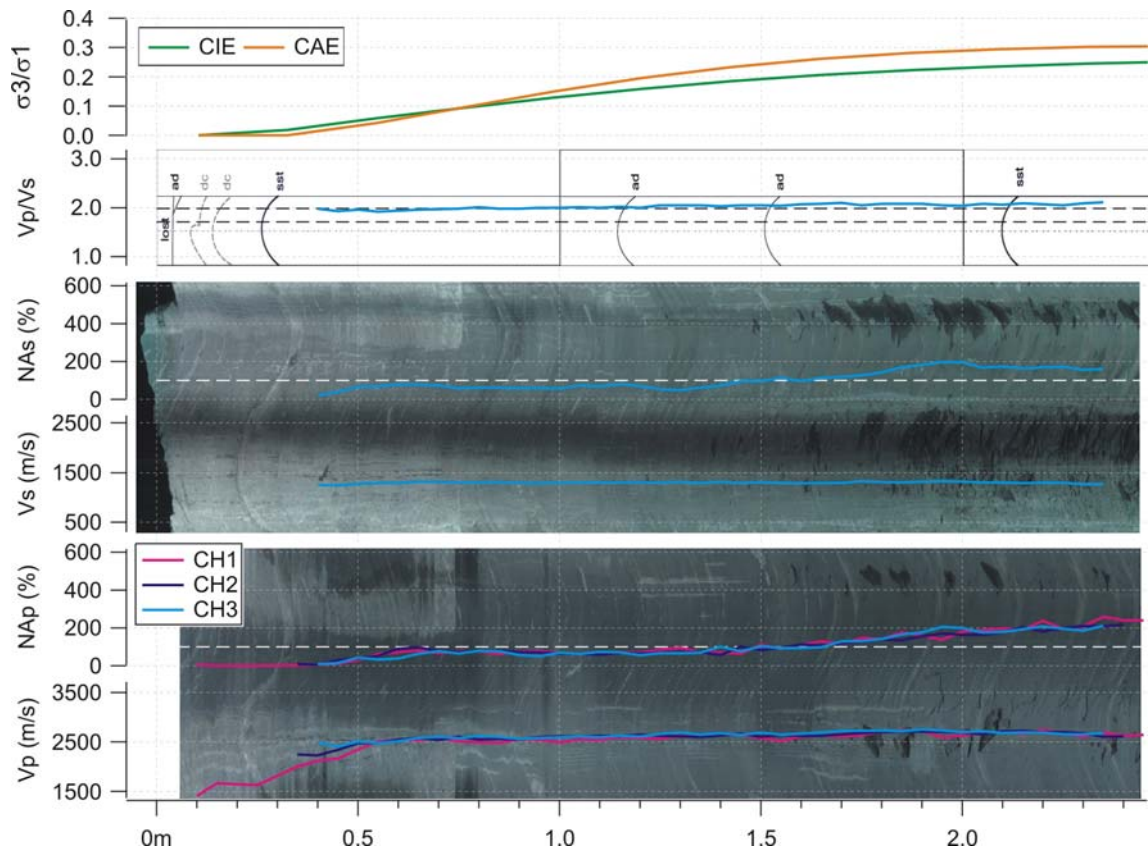


Fig. 4.26c: BEZ-B19 data integration with seismic sensors coupled to the west wall of the borehole. Refer to Fig. 4.5 for borehole location and Appendix C for enlarged drillcore maps.

at depths greater than 1.6m, which also coincided with the first visible signs of borehole damage. Stress ratios ranged between 0.2 and 0.3 at this point in both boreholes. In the older BEZ-B3, the deeper increase in amplitudes was more subtle and shallower at depths greater than 1.2m (Fig. 4.26b). This point also coincided with a slight rotation in the borehole instabilities (Fig. 4.26b) and stress ratio of nearly 0.2.

The perturbed zone ahead of the face extended about 1m near the centre to about 0.6-0.7m near the sidewalls. Stress ratios increased along the borehole lengths from 0-0.05 in regions of IF1 fracturing to 0.15-0.2, where seismic wave amplitudes and velocities plateaued, to greater than 0.2, where borehole instabilities in the younger boreholes commenced.

4.5.5 Characterising the Zone of Perturbation Around the EZ-B Niche

Integration of the borehole data indicated that the zone of perturbation around the EZ-B Niche consisted of two parts (Fig. 4.27). The inner zone averaged 20cm in thickness and consisted of macro-fracturing and the lowest seismic wave amplitudes and velocities. The outer zone consisted of increasing seismic wave amplitudes and velocities, which also corresponded roughly with where borehole instabilities intensified. The extent of the outer zone ranged from 0.5m to 0.7m around the niche cross-section and ahead of the face near the sidewalls. In the centre of the face, the extent of the outer zone was about 1m.

When the modelled stress redistribution was integrated with the field data (Fig. 4.28), decreasing stress ratios were shown to correspond with decreasing seismic wave amplitudes and velocities. As shown experimentally and numerically [39, 40, 34, 36], decreasing stress ratios imply crack propagation and therefore, strength degradation due to increasing crack-induced damage. Fig. 4.28 shows that damage in the rock mass surrounding the EZ-B Niche increased from the far- to the near-field. In this case, the lowest stress ratios corresponded with the inner macro-fractured zone. The increasing stress ratios and seismic wave amplitudes and velocities in the outer zone then implied that the damage incurred in the outer zone may be microscopic in scale.

Use of the stress ratio or spalling limit to quantify damage is applicable in regions of high deviatoric stress and low confinement (Fig. 4.20). In σ_3 - σ_1 space (Fig. 4.29), results from laboratory-scale testing of intact samples were used to estimate the strength envelope of the Opalinus Clay [28, 42]. The strength criterion considered in Fig. 4.29 is Mohr-Coulomb with averaged cohesive and frictional strength components from samples tested in directions parallel with and perpendicular to bedding [28]. Four spalling limits (0.05, 0.1, 0.15, and 0.2) have also been provided in Fig. 4.29. The damage initiation threshold in Fig. 4.29 is based on seismic wave characteristics determined from true-triaxial tests [42]. Laboratory testing showed that the onset of Vs reduction coincided with the initiation of micro-cracking whereas progressive crack opening was required for the onset of Vp reduction [42]. This was attributed to the greater sensitivity of

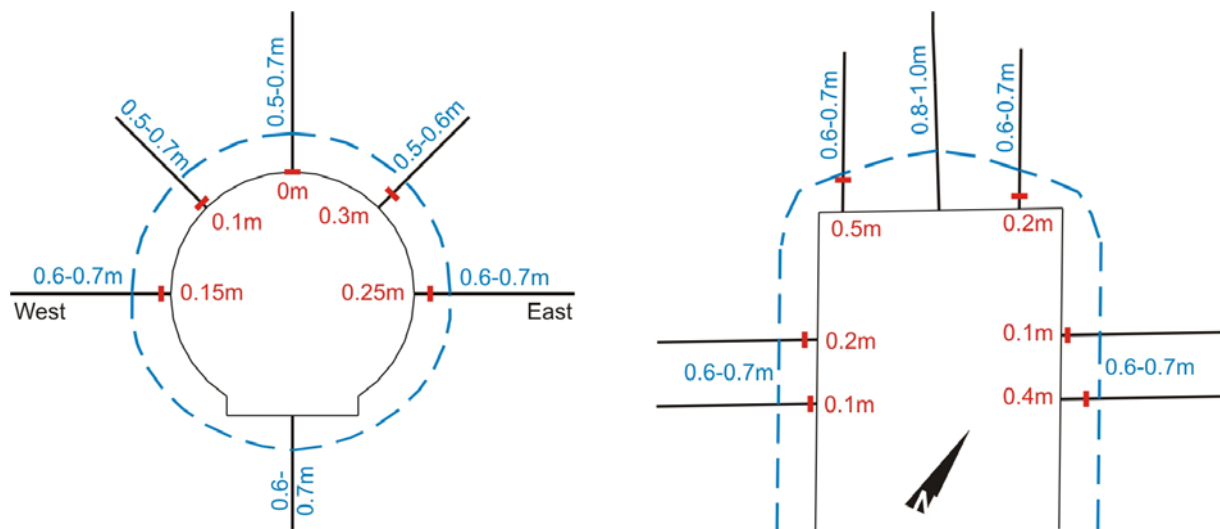


Fig. 4.27: Zone of perturbation around the niche determined from the integration of borehole data (blue). The zone of induced fracturing (IF) is shown in red.

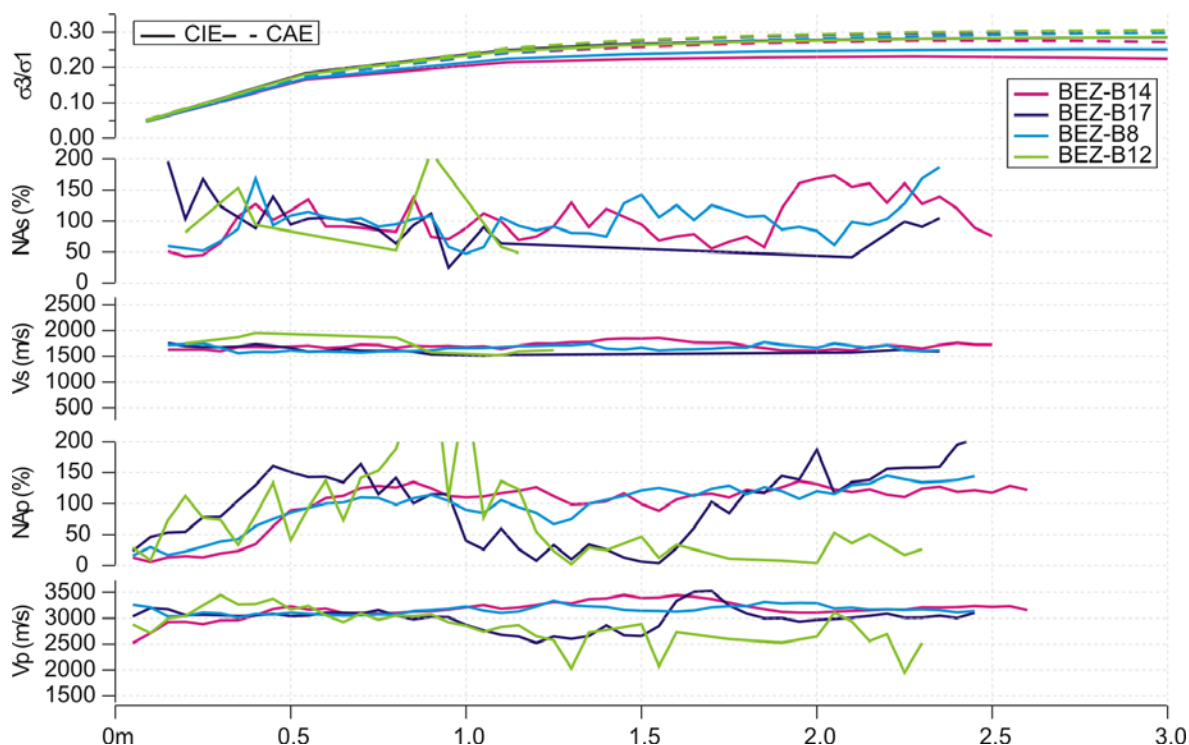


Fig. 4.28a: Bedding-parallel borehole integration of seismic data with modelled stress ratios (refer to Fig. 4.5 for borehole locations).

Vs to initial flat micro-cracking that resulted in opening parallel with the direction of the particle movement of the shear waves [42]. In contrast, such opening directions had little effect on compressional waves propagating in the same direction as particle motion was perpendicular to the direction of crack opening [42]. At confining stresses less than 15MPa, volumetric strain reversal occurred near the same stress levels as the Vp reduction [43]. In samples with bedding 45° to the loading direction, Vs reversal

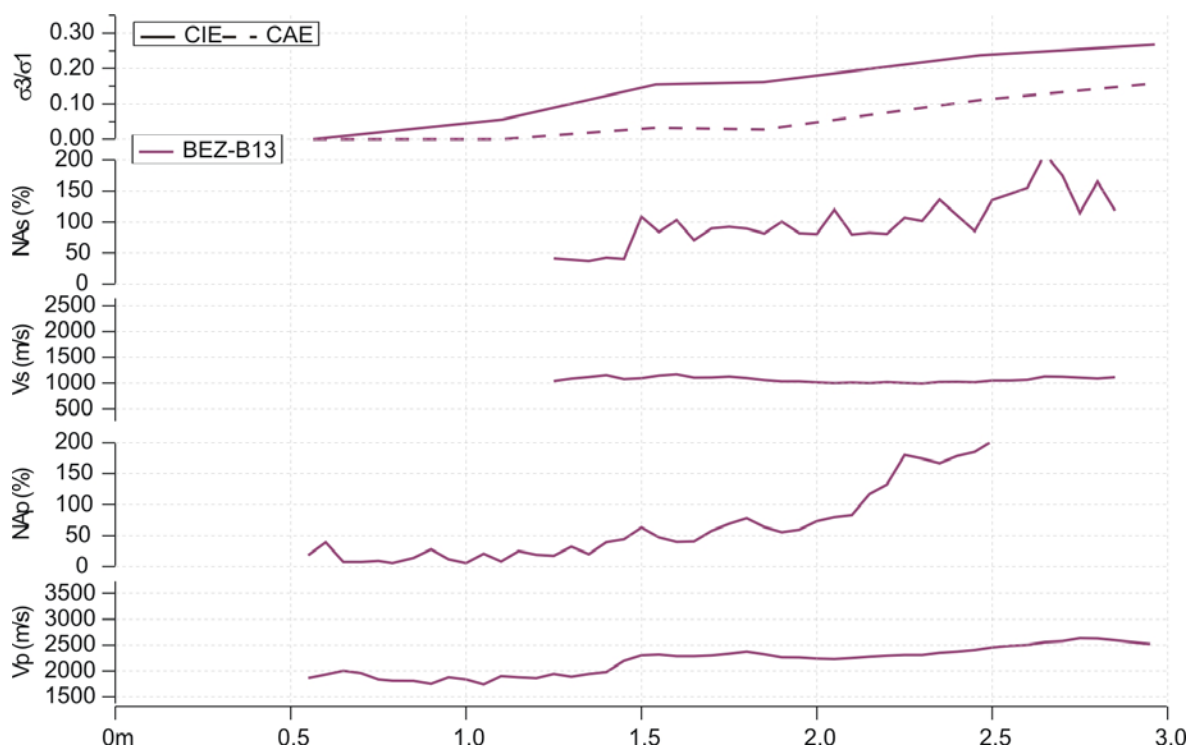


Fig. 4.28b: Bedding-perpendicular borehole integration of seismic data with modelled stress ratios (refer to Fig. 4.5 for borehole locations).

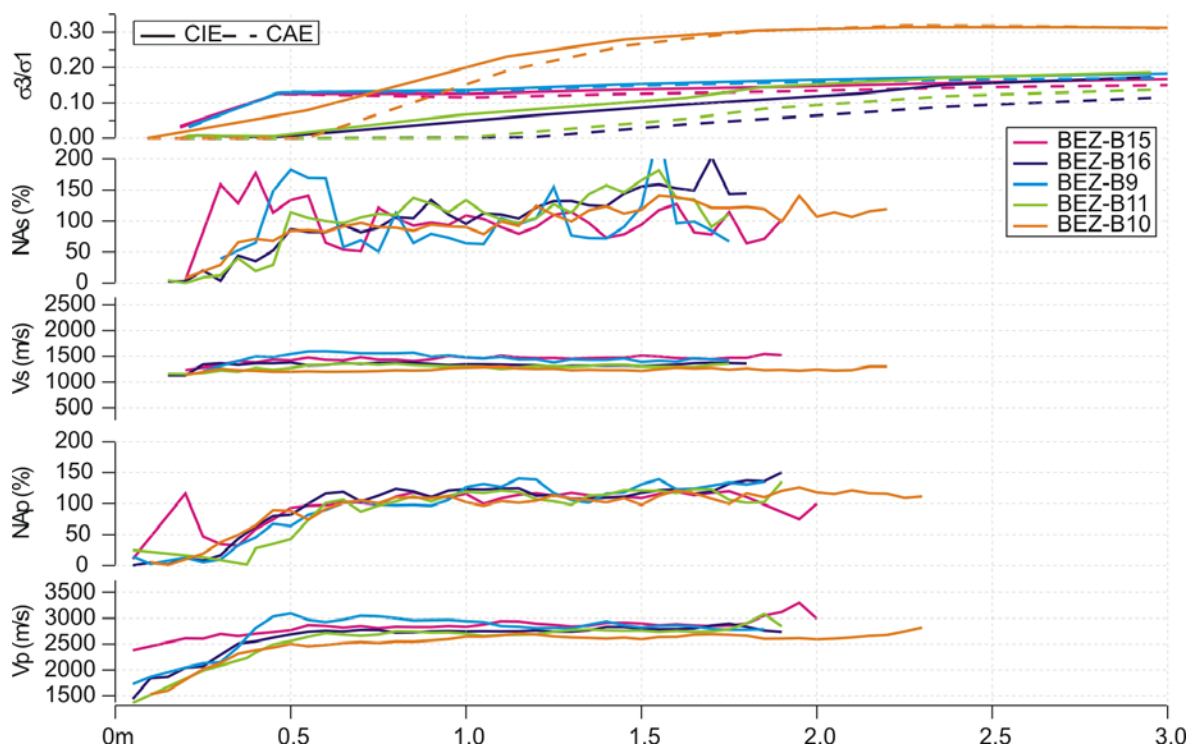


Fig. 4.28c: Bedding-45° borehole (upper walls and crown) integration of seismic data with modelled stress ratios (refer to Fig. 4.5 for borehole locations).

occurred at 60% of peak strength and V_p reversal occurred at 70% [42]. In samples with bedding orthogonal to the loading direction, V_s reversal occurred at 50% and V_p reversal occurred at 60% [42]. In comparison, Zhang and Rothfuchs [43] found that volumetric strain reversal occurred at 70% at bedding-parallel loading directions and 96% at bedding-perpendicular loading directions. Thus, the lower V_s reversal stress level coincides with the crack initiation threshold (Fig. 4.29) while the higher V_p reversal

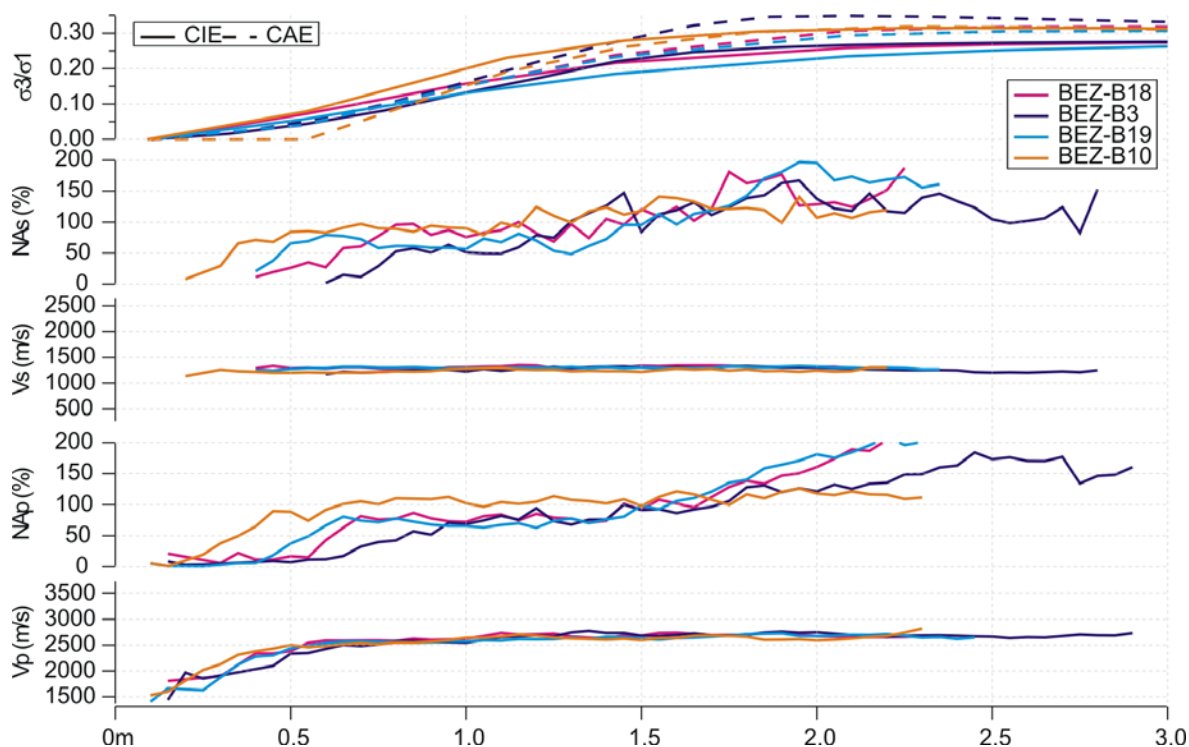


Fig. 4.28d: Bedding-45° borehole (face and crown) integration of seismic data with modelled stress ratios (refer to Fig. 4.5 for borehole locations).

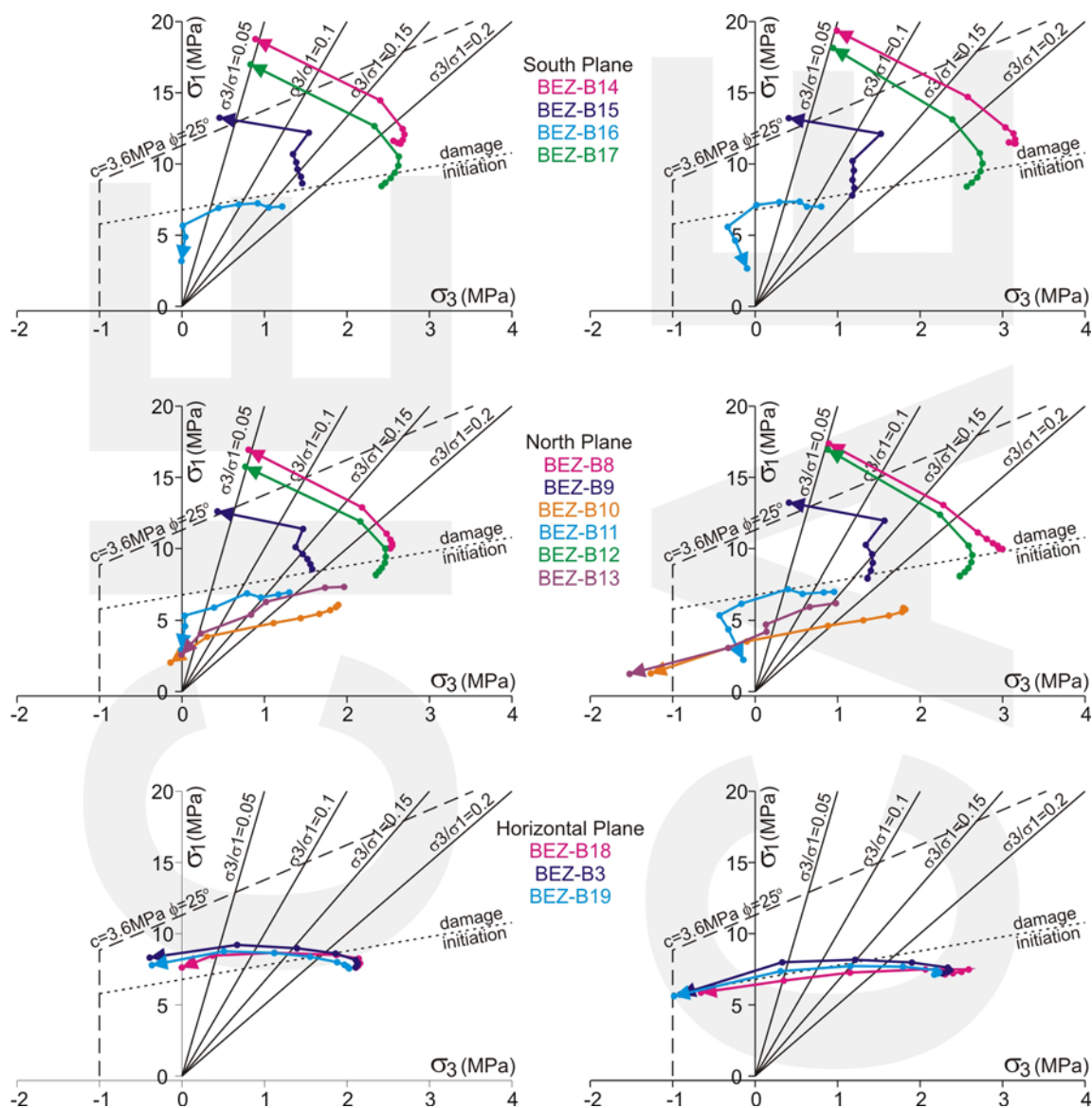


Fig. 4.29: Stress redistributions plotted along each borehole in the three borehole planes. Results from the isotropic model (CIE) are shown in the left and results from the transverse isotropic model are shown in the right (CAE). For borehole locations, refer to Fig. 4.5 and for locations of the borehole planes, refer to Fig. 4.8.

and/or volumetric strain reversal stress level coincides with the crack interaction threshold. Stress levels between these two thresholds lead to the generation and propagation of local micro-cracks while high stress levels are required for the formation of macro-cracks (via propagation and connection of micro-cracks) [44].

Stresses along the borehole centrelines from both CIE and CAE numerical simulations were plotted against the estimated strength envelope in Fig. 4.29. Around the EZ-B Niche in both CIE and CAE simulations, the rock mass in the sidewalls and upper west wall were found to be the most susceptible to failure in spalling. In these regions, stress levels exceeded the crack initiation threshold while unloading progressed towards lower values of the spalling limit as the niche boundary was approached: thus, indicating increasing damage. Interestingly, a spalling limit of 0.05 was just reached at the borehole collars. As previous experimental studies [39, 40] have shown, stable crack growth increases significantly when the spalling limit is less than 0.05 (Fig. 4.22). Hence, a significant zone of macro-fracturing around the niche did not seem to be likely. Ahead of the face at the end of the niche excavation, spalling failure was less obvious as the stress redistribution suggested possible transitional behaviour. This is examined further in Chapter 5.

According to the seismic data (Fig. 4.28), the greatest damage around the niche was incurred below the invert despite the limited number of macro-fractures mapped (Fig. 4.25f). The rock mass below the invert coincided with low deviatoric stress and low confinement (Fig. 4.29). Similarly, the rock mass above the crown (BEZ-B10) and in the upper east wall (BEZ-B11 and B16) also coincided with low deviatoric stress and low confinement (Fig. 4.29). However, damage as inferred from the P-wave amplitudes in these boreholes differed little from the data measured in the high deviatoric stress and low confinement regions (i.e. sub-horizontal boreholes in the sidewalls and upper west wall). This discrepancy may be related to the roof anchors installed during the excavation (see Section 4.2 and Fig. 4.5). Structurally with respect to bedding, the borehole in the crown (BEZ-B10) was similar to those in the face (BEZ-B18, B3, and B19) as indicated by the similarity in the trends of the P-wave and S-wave velocities in Fig. 4.28. However, the trends in the seismic wave amplitudes in BEZ-B10 (Fig. 4.28) were in better agreement with those from the diagonal boreholes (BEZ-B9, B11, B15, and B16), all of which are located within the umbrella-like support provided by the roof anchors (Fig. 4.5).

The intact rock anisotropy (due to bedding) is speculated to affect only the low deviatoric stress and low confinement regions as illustrated in (Fig. 4.28) where the stress ratios along boreholes located in the high deviatoric and low confinement regions differed little between the CIE and CAE simulations. This is notably demonstrated in the displacement vectors of the object points located near the niche floor such as those at object point 4 in the circular arrays (Fig. 4.16) and object point 503 in the face (Fig. 4.18). The relatively large displacements, roughly perpendicular to bedding, measured in the lower west wall (object point 4) and lower face (object point 503) indicated uplift of the invert orthogonal to the bedding and/or SSE bedding-parallel shears.

4.6 Conclusions

Excavation-induced perturbations lead to modifications of flow and transport properties through strength degradation of the rock mass in the vicinity of an underground opening. At the Mont Terri Rock Laboratory, previous investigations have shown permeabilities can increase up to five orders of magnitude in the EDZ/EdZ. In the context of geological waste repositories, understanding the impact of the degraded zone on hydraulic properties necessitates confident characterisation of the excavation-induced perturbed zone. Consideration of an overconsolidated argillaceous host rock, such as the Opalinus Clay at the Mont Terri Rock Laboratory, adds mechanical complexities as these materials are inherently transitional and rarely isotropic.

In the recent excavation of the EZ-B Niche at the Rock Laboratory, excavation-induced perturbations were characterised by integrating borehole data from field measurements (i.e. drillcore mapping, digital optical televiewer imaging, and seismic measurements) and numerical modelling. Fracture mapping from drillcores and televiewer images revealed few macroscopic induced fractures that could be attributed to the niche construction. Integration of the borehole data indicated that the zone of perturbation around the niche consisted of two parts. The inner macro-fractured zone (averaging 20cm in thickness) coincided with the lowest seismic wave amplitudes and velocities. The outer zone consisted of increasing seismic wave amplitudes and velocities and also corresponded roughly with where borehole instabilities intensified. The extent of the outer zone ranged from 0.5m to 0.7m around the niche cross-section and ahead of the face near the sidewalls. A larger zone of 1m was detected in the centre of the face.

Stress analyses from numerical simulations indicated that the rock mass in the sidewalls and upper west wall of the niche would be the most susceptible to failure in spalling. In these regions, stress levels exceeded the crack initiation threshold while unloading progressed towards lower values of the spalling limit as the niche boundary was approached. This decrease in stress ratios corresponded with decreasing seismic wave amplitudes and velocities. Decreasing stress ratios imply crack propagation and therefore, strength degradation as a result of increasing crack-induced damage. The lowest stress ratios corresponded with the inner macro-fractured zone while stress ratios increased along with seismic wave amplitudes and velocities in the outer zone. The latter suggested that damage in the outer zone may be microscopic in

scale. Stress ratios near the borehole collars were not considerably less than a spalling limit of 0.05 suggesting the zone of macro-fracturing around the niche would not necessarily be significant.

Damage in the crown, invert, and upper east walls were attributed to modes affected by low deviatoric stress and low confinement. In the case of the EZ-B Niche, intact rock anisotropy (due to bedding) may be most influential in these stress regimes. This is most notably demonstrated in the displacement vectors of the object points located in the lower west wall and lower face. Relatively large displacements were measured in a direction roughly perpendicular to bedding and thus, indicating uplift of the invert orthogonal to the bedding and/or SSE bedding-parallel shears. Seismic data indicated the greatest damage was incurred in the borehole drilled in the invert. Damage in the rock mass above the crown and in the upper walls may not have been fully developed as roof anchors were installed during the niche excavation.

References

- [1] Tsang C-F, Bernier F, Davies C. Geohydromechanical processes in the Excavation Damaged Zone in crystalline rock, rock salt, and indurated and plastic clays-in the context of radioactive waste disposal. *International Journal of Rock Mechanics & Mining Sciences* 2005;42:109-125.
- [2] Bluemling P, Bernier F, Lebon P, Martin CD. The excavation damaged zone in clay formations time-dependent behaviour and influence on performance assessment. *Physics and Chemistry of the Earth* 2007;32:588-599.
- [3] Rejeb A, Ben Slimane K, Cabrera JM, Matry JM, Savoye S. Excavation damaged zones in the argillaceous Tournemire site: Characterisation and failure mechanisms. In: *Clays in Natural & Engineered Barriers for Radioactive Waste Confinement, Abstracts*. 2007. pp.533-534.
- [4] Matry JM, Savoye S, Cabrera J. Desaturation and structure relationships around drifts excavated in the well-compacted Tournemire's argillite (Aveyron, France). *Engineering Geology* 2007;90:1-16.
- [5] Armand G, Wileveau Y, Morel J, Cruchaudet M, Rebours H. Excavation damaged zone (EDZ) in the Meute Haute Marne underground research laboratory. In: e Sousa LR, Grossmann CON, editors. 11th Congress of the International Society for Rock Mechanics: The second half century of rock mechanics. Lisbon: Taylor & Francis/Balkema; 2007.
- [6] Nussbaum C, Wileveau Y, Bossart P, Moeri A, Armand G. Why are the geometries of the EDZ fracture networks different in the Mont Terri and Meuse/Haute-Marne rock laboratories? Structural approach. In: *Clays in Natural & Engineered Barriers for Radioactive Waste Confinement, Abstracts*. 2007. pp.151-152.
- [7] Mertens J, Bastiaens W, Dehandschutter B. Characterisation of induced discontinuities in the Boom Clay around the underground excavations (URF, Mol, Belgium). *Applied Clay Science* 2004;26:413-428.
- [8] Bossart P, Meier PM, Moeri A, Trick T, Mayor J-C. Geological and hydraulic characterisation of the excavation disturbed zone in the Opalinus Clay of the Mont Terri Rock Laboratory. *Engineering Geology* 2002;66:19-38.
- [9] Martin CD, Lanyon GW, Bluemling P, Mayor J-C. The excavation disturbed zone around a test tunnel in the Opalinus Clay. In: Hammah R, Bawden W, Curran J, Telesnicki M, editors. *Mining and Tunnelling Innovation and Opportunity*. Vol 2. Toronto: University of Toronto Press; 2002. pp.1581-1588.
- [10] Bath A, Gautschi A. Geological setting and sample locations. In: Pearson FJ, Arcos D, Bath A, Boisson J-Y, Fernandez AM, Gaebler H-E, Gaucher E, Gautschi A, Griffault L, Hernan P, Waber HN, editors. *Reports of the Federal Office for Water and Geology, Geology Series*. 2003. pp.30-35.
- [11] Homberg C, Bergerat F, Philippe Y, Lacombe O, Angelier J. Structural inheritance and cenozoic stress fields in the Jura fold-and-thrust belt (France). *Tectonophysics* 2005;357:137-158.

- [12] Nussbaum C, Bossart P, Burrus F, Badertscher N, Meier O, Nold A. Excavation of Gallery04: general documentation, deformation measurements and geological surveys. Unpublished Mont Terri Technical Note, 2005. 87pp.
- [13] Bossart P, Wermeille S. The stress field in the Mont Terri region data compilation. In: Heitzmann p, Tripet J-P, editors. Reports of the Federal Office for Water and Geology, Geology Series. 2003. pp.65-92.
- [14] Nussbaum C, Bossart P, von Ruetten J, Meier O, Badertscher N. EZ-B experiment: small-scale mapping of tectonic and artificial (EDZ) fractures of the EZ-B niche. Unpublished Mont Terri Technical Note, 2005. 23pp.
- [15] Gaucher EC, Fernandez AM, Waber HN. Rock and mineral characterisation of the Opalinus Clay Formation. In: Pearson FJ, Arcos D, Bath A, Boisson J-Y, Fernandez AM, Gaebler H-E, Gaucher E, Gautschi A, Griffault L, Hernan P, Waber HN, editors. Reports of the Federal Office for Water and Geology, Geology Series. 2003. pp.281-303.
- [16] Yong S, Loew S, Fidelibus C, Frank E, Lemy F, Schuster K. Induced fracturing in the Opalinus Clay: an integrated field experiment. In: Leung CF, Zhou YX, editors. Rock mechanics in underground construction. Singapore: World Scientific; 2006. CD-Rom. 9pp.
- [17] Haimson B. Micromechanisms of borehole instability leading to breakouts in rocks. *International Journal of Rock Mechanics & Mining Sciences* 2007;44:157-173.
- [18] Okland D, Cook JM. Bedding-related borehole instability in high-angle wells. In: Holt R, editor. *Proceedings of the SPE/ISRM Rock Mechanics in Petroleum Industry (Eurock98)*. Vol 1. Trondheim; 1998. pp.413-422.
- [19] Schuster K, Alheid H-J, Boeddener D. Seismic investigation of the excavation damaged zone in Opalinus Clay. *Engineering Geology* 2001;61:189-197.
- [20] Schuster K, Alheid H-J. Results gained from seismic in-situ measurements in the Opalinus Clay at the Mont Terri rock laboratory. In: *Clays in Natural & Engineered Barriers for Radioactive Waste Confinement, Abstracts*. 2007. pp.137-138.
- [21] Schubnel A, Benson PM, Thompson BD, Hazzard JF, Young RP. Quantifying damage, saturation and anisotropy in cracked rocks by inverting elastic wave velocities. *Pure and Applied Geophysics* 2006;163:947-973.
- [22] Leucci G, De Giorgi L. Experimental studies on the effects of fracture on the P and S wave velocity propagation in sedimentary rock ("Calcarenite del Salento"). *Engineering Geology* 2006;84:130-142.
- [23] Meglis IL, Chow T, Martin CD, Young RP. Assessing in situ microcrack damage using ultrasonic velocity tomography. *International Journal of Rock Mechanics & Mining Sciences* 2005;42:25-34.
- [24] Klose CD, Loew S, Giese R, Borm G. Spatial predictions of geological rock mass properties based on in-situ interpretations of multi-dimensional seismic data. *Engineering Geology* 2007;93:99-116.
- [25] Lemy F, Yong S, Schulz T. Assessment of laser-based displacement mapping in an underground opening. In: Eberhardt E, Stead D, Morrison T, editors. *Rock Mechanics Meeting Society's Challenges and Demands*. Vol. 1. Vancouver: Taylor & Francis; 2007. pp.85-92.
- [26] Schulz T, Lemy F, Yong S. Laser scanning technology for rock engineering applications. In: *Proceedings of the 7th Conference on Optical 3-D Measurement Techniques*. Vienna;2005.
- [27] Itasca Consulting Group Inc. *Fast Lagrangian Analysis of Continua in 3 Dimensions*, version 3.0. Itasca Consulting Group Inc. 2005.
- [28] Bock H. RA experiment rock mechanics analyses and synthesis: data report on rock mechanics. Unpublished Mont Terri Technical Report, 2001. 52pp.
- [29] Bieniawski ZT. Mechanism of brittle fracture of rock, Part I. *International Journal of Rock Mechanics and Mining Sciences* 1967;4:395-405.

- [30] Martin CD. The strength of massive Lac du Bonnet Granite around underground openings. PhD thesis, University of Manitoba, 1993. 300pp.
- [31] Eberhardt E. Brittle rock fracture and progressive damage in uniaxial compression. PhD thesis, University of Saskatchewan, 1998. 334pp.
- [32] Diederichs MS. Instability of hard rockmasses: the role of tensile damage and relaxation. PhD thesis, University of Waterloo, 1999. 617pp.
- [33] Eberhardt E, Stead D, Stimpson B, Read RS. Identifying crack initiation and propagation thresholds in brittle rock. *Canadian Geotechnical Journal* 1998;35:222-233.
- [34] Diederichs MS, Kaiser PK, Eberhardt E. Damage initiation and propagation in hard rock during tunnelling and the influence of near-face stress rotation. *International Journal of Rock Mechanics & Mining Sciences* 2004;41:785-812.
- [35] Martin CD. Seventeenth Canadian geotechnical colloquium: The effect of cohesion loss and stress path on brittle rock strength. *Canadian Geotechnical Journal* 1997;34:698-725.
- [36] Diederichs MS. The 2003 Canadian geotechnical colloquium: Mechanistic interpretation and practical application of damage and spalling prediction criteria for deep tunnelling. *Canadian Geotechnical Journal* 2007;44:1082-1116.
- [37] Read RS, Chandler NA, Dzik EJ. In situ strength criteria for tunnel design in highly-stressed rock masses. *International Journal of Rock Mechanics & Mining Sciences* 1998;35:261-278.
- [38] Diederichs MS. Rock fracture and collapse under low confinement conditions. *Rock Mechanics and Rock Engineering* 2003;36:339-381.
- [39] Hoek E. Brittle failure of rock. In: Stagg KG, Zienkiewicz OC, editors. *Rock Mechanics in Engineering Practice*. London: John Wiley & Sons; 1968. pp.99-124.
- [40] Hoek E, Bieniawski ZT. Brittle fracture propagation in rock under compression. *International Journal of Fracture Mechanics* 1965;1:137-155.
- [41] Nussbaum C, Meier O, Badertscher N, Bossart P. Drilling campaigns of Phase 10 drilling and field mapping of drillcores including photo documentation. Unpublished Mont Terri Technical Note, 2005. 22pp.
- [42] Popp T, Salzer, K. Anisotropy of seismic and mechanical properties of Opalinus Clay during triaxial deformation in a multi-anvil apparatus. *Physics and Chemistry of the Earth* 2007;32:879-888.
- [43] Naumann M, Hunsche U, Schulze O. Experimental investigations on anisotropy in dilatancy, failure and creep of Opalinus Clay. *Physics and Chemistry of the Earth* 2007;32:889-895.
- [44] Zhang C-L, Rothfuchs T. Damage and sealing of clay rocks detected by permeability measurements. In: *Proceedings of the 3rd International Clay Meeting*. Lille; in press.

Chapter 5

Rock Mass Response Ahead of an Advancing Face

Abstract

At the Mont Terri Rock Laboratory, little is known of the response in the immediate vicinity ahead of an advancing tunnel face. Past investigations have focused on the study of excavation-induced perturbations around the tunnel cross-section. In this chapter, the rock mass ahead of an advancing short test tunnel was investigated by integrating borehole data collected before, during, and after the construction of the EZ-B Niche. As field evidence for macro-damage was absent or limited, stress ratios from numerical simulations were incorporated in the field data integration and shown to provide a good indication of rock damage (as inferred from the seismic measurements) related to spalling-related failure. The bedding-parallel shears mapped in the EZ-B Niche were found to influence the seismic parameters derived from borehole logging as these tectonic structures would provide a preferred source for stress relief in response to the against dip niche advance. Lower seismic velocities and amplitudes found near the bedding-parallel shears suggested local relaxation of the surrounding rock mass near the shears. As the advancing niche face progressively reduced the kinematic constraint of the bedding-parallel shears, both elastic and plastic deformations along the shears were allowed. Damage ahead of the niche face most likely accumulated progressively as the formerly compressed volume of rock was unloaded during the subsequent excavation rounds. As a consequence, the spalling limit is first reached and then exceeded. In this investigation, consideration of both rock mass anisotropy (i.e. the bedding-parallel shears) and geometry (i.e. distance from a previously stressed volume of rock) were necessary to understand both the state and extent of damage ahead of the niche face.

5.1 Introduction

The construction of a tunnel may lead to degradation of the surrounding rock mass. As a result, rock mass transport properties may be altered and tunnel stability may be compromised. Safety assessment of geological nuclear waste storage facilities necessitates an understanding of the processes leading to rock mass disturbance and damage induced by tunnel excavation. While many have focused on excavation-induced perturbations around the tunnel cross-section, few have considered the development of perturbations ahead of an advancing tunnel. Degradation of the rock mass ahead of the advancing face may in turn influence the development of the perturbed zone around the tunnel cross-section: for example, asymmetry in the orientation of tunnel breakouts [1, 2].

Abel and Lee [3] showed that changes in the stress state can be detected several tunnel diameters ahead of the face. In a series of laboratory-scale tunnel excavations (in acrylic, concrete, and granite), the onset of stress changes ranged from two tunnel diameters in granite to more than four tunnel diameters in acrylic. A peak in the stress redistribution ahead of the face was also seen in all cases and occurred from one tunnel diameter in granite to two tunnel diameters in acrylic. This was attributed to destressing at the unrestrained tunnel surfaces thereby leading to load transfer to the more confined rock mass ahead of the face. At the field scale, two probes installed 15.2m ahead of a crosscut (1.5m x 2.1m) in foliated gneissic rocks showed stress changes initiated more than seven tunnel diameters ahead of the advancing face with a stress peak at six to seven tunnel diameters. Absent in the laboratory studies, the field study also illustrated the influence of the foliation on the rock mass response. Tensile strain relief resulted from tunnel advance with the apparent dip of the foliation, which resulted in preferential expansion perpendicular to the foliation. From these investigations, tunnel advance was shown to result in an overall decompression ahead and to the side of the tunnel.

Read et al. [1] and Martin [2] found that the formation of v-shaped notches around a test tunnel excavated in the Lac du Bonnet granite at the AECL (Atomic Energy of Canada Limited) Underground Research Laboratory depended on changes in the stress state ahead of the tunnel face. The mine-by test tunnel was circular with a diameter of 3.5m and length of 46m. The tunnel was roughly 10° from the intermediate principal stress (σ_2) while the minimum principal stress (σ_3) was sub-vertical and the maximum principal stress (σ_1) was nearly orthogonal to the tunnel axis. V-shaped notches formed in the roof and floor of the tunnel about 0.6m behind the face. The notches were not diametrically opposed and their locations coincided with concentrations of microseismic activity, which encompassed a region of 2.4 tunnel diameters (0.4 diameters ahead of and two diameters behind the face) in size. Asymmetry in the notch formation was attributed to the offset of the tunnel axis with the direction of the intermediate principal stress, which resulted in non-symmetric stress concentrations ahead of the face [1]. Stress path analyses indicated the crack initiation threshold [4] was exceeded well ahead of the advancing face in regions where the notches formed. Thus, damage (i.e. micro-fracturing) to the rock mass initiated ahead of the face. Additionally, principal stress rotations, when stress levels exceeded crack initiation, also initiated ahead of the face with the maximum rotation in σ_3 occurring in the roof. Consequently, rock mass degradation near the tunnel perimeter may be further exacerbated. Through a numerical study, Eberhardt [5] found magnitude and directional changes in the redistributed stress field near the face differed depending on the tunnel alignment with the far-field principal stress axes. It was postulated that magnitude and directional changes in the redistributed stress field would lead to progressive accumulation of damage.

Investigations relating to nuclear waste storage in argillaceous media have also shown rock mass perturbations may initiate ahead of the face. Induced fracturing has been mapped in the tunnel face at the Meuse/Haute-Marne Underground Research Laboratory (URL) in France [6] and at the HADES Underground Research Facility (URF) in Belgium [7]. In both cases, the fracturing formed a “v” with a horizontal axis of symmetry near the mid-height of the tunnel (about 4m in diameter). At the French URL, which is located in the argillaceous Callovo- Oxfordian formation, fractures were initiated about four metres (or one tunnel diameter) ahead of the face during tunnel excavation. Fracturing was also found to be more pronounced when the tunnel axis was aligned parallel with the maximum horizontal stress. At the Belgian URF, which is located in the Boom Clay, v-shaped fracturing was mapped in the sidewalls and

face during the excavation of an 84m-long gallery (4.9m in diameter). It was postulated that fracturing formed several metres ahead of the face as numerical modelling indicated the highest stress concentrations occurred about six metres ahead of the face.

The Opalinus Clay in Switzerland is under consideration as a potential host rock for the storage of nuclear waste [8]. In the Opalinus Clay at the Mont Terri Rock Laboratory (Fig. 5.1), the zone of perturbation around the tunnel cross-section has been repeatedly investigated and consist of high-angle extensional fracturing in the sidewalls and bedding-parallel fracturing above the crown and below the invert [9, 10]. Knowledge regarding perturbations ahead of a tunnel face at Mont Terri is limited to the mine-by study of the EDB Section in Gallery98 [11, 12]. The EDB Section (Fig. 5.2) is nearly circular in cross-section with a diameter of 3.6m and length of 35m. Nine boreholes, located 7-25m from the tunnel face, were instrumented to monitor displacements (via an extensometer, sliding micrometers, and inclinometers) and pore pressures. Elastic boundary element modelling was undertaken and the largest variance between the modelled results and field data were found in the sidewalls. Much greater displacements were measured in the sidewalls than predicted in the numerical model, suggesting non-elastic behaviour around the sidewalls. This coincided with the location of observed extensional fracturing. Pore pressure sensors increased and responded rapidly as the face approached within a metre of the monitoring intervals and dropped rapidly afterwards. While the investigation at the EDB Section considered the rock mass response several metres ahead of the face, relatively little is known of the response in the immediate vicinity ahead of an advancing face. In this chapter, the rock mass immediately ahead of an advancing tunnel face is investigated by integrating borehole data collected before, during, and after the construction of a short test tunnel, the EZ-B Niche (Fig. 5.2).

5.2 Site Description

The Mont Terri Rock Laboratory is a research facility located in northern Switzerland (Fig. 5.1). The facility consists of eight niches excavated in the northwestern wall of the Security Gallery and two galleries located to the northwest (Fig. 5.2). The EZ-B Niche is located in the younger Gallery04 while the EDB Section is located in the older Gallery98.

5.2.1 Geological Setting

Mont Terri is the northernmost in a series of anticlines in the Jura Mountains, which formed during late Miocene to early Pliocene in response to late alpine folding and thrusting [13]. The anticline was formed by fault bend folding and fault propagation folding that have resulted in a number of thrust faults, such as those found in the northern limb [14]. The laboratory is located in the weakly deformed and less tectonically disturbed southern limb [15]. The in situ stress field at Mont Terri consists of a sub-vertical σ_1 inclined towards the S-SW and a sub-horizontal σ_3 inclined towards the northeast [16, 17]. Consequently,

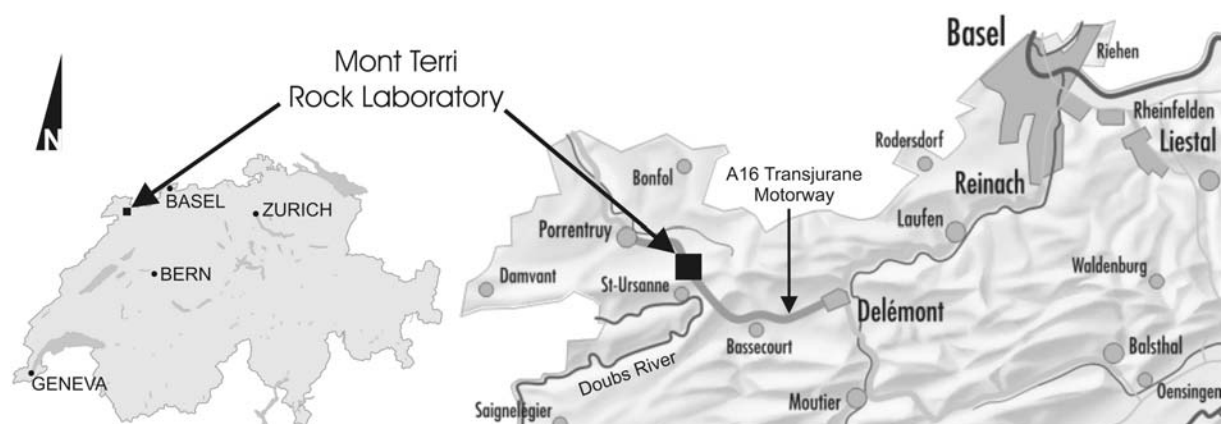


Fig. 5.1: Location of the Mont Terri Rock Laboratory in northern Switzerland (modified from www.swisstopo.ch).

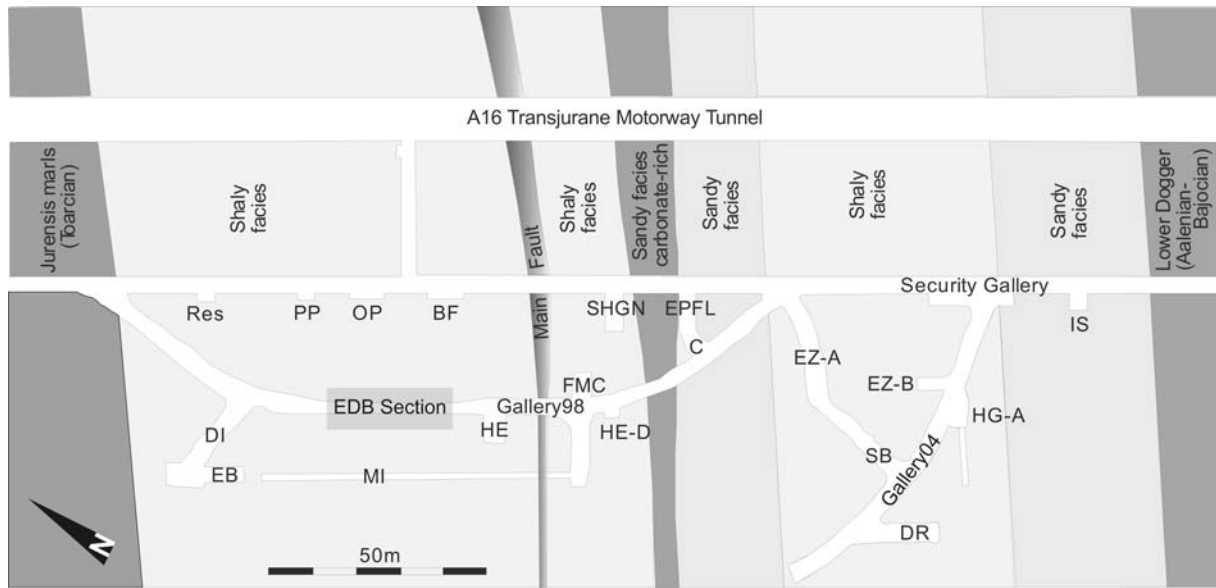


Fig. 5.2: Plan view of the Mont Terri Rock Laboratory crossing the main facies of the Opalinus Clay (after [14]).

the minimum principal stress is approximately normal to the axis of the EZ-B Niche while the intermediate is sub-parallel with an offset of about 14° (Fig. 5.3).

At the Laboratory, tectonic features consist of several thin (millimetres thick) shear zones and a larger thrust fault zone (Main Fault in Fig. 5.2) [14, 15]. The use of “shear” rather than “fault” in this chapter departs from the terminology established at the Laboratory as the former term is more descriptive of the displacement magnitude and thickness of the structures. Three sets of tectonic shears have been identified in Gallery04 [14] but only two sets intersect the EZ-B Niche [18]. The most frequently occurring is sub-parallel with bedding dipping SSE (i.e. bedding-parallel shears) [14]. SSE bedding-parallel shears are closed and sealed with calcite and clay minerals. On average, the SSE bedding-parallel shears in the niche dip 46° (ranging from 45° to 50°) towards 146° (ranging from 138° to 156°) [18] and strikes roughly perpendicular to the niche axis (Fig. 5.3). A second set mapped in isolated regions in the niche [18] consists of minor sub-horizontal shears that dip S to SW; the S-SW shears range in dip from 0° to 20° and dip direction from 132° to 186° [18]. In the niche, the S-SW set is bounded by shears belonging to the SSE set. Shear surfaces of both sets are slickensided and indicate thrusting towards the northwest [14].

The Opalinus Clay is dark grey Jurassic shale consisting of claystone and marl with intercalated sandy and calcareous layers and lenses. At Mont Terri, the formation consists of five lithostratigraphic subunits, which constitute three main facies [19]: shaly, sandy, and carbonate-rich sandy (Fig. 5.2). The major components of the shaly facies, where the EZ-B Niche is located, consist of [19]: clay minerals (58-76%), carbonates (0-28%), quartz (6-24%), feldspars (0-3%), pyrite (0-2%), and organic carbon (0-2%). Clay minerals consist mostly of illite (16-40% of total weight) and kaolinite (15-33%) followed by chlorite (4-20%) and illite/smectite mixed-layers (0-20%). The carbonate fraction is dominated by calcite at 5-28%

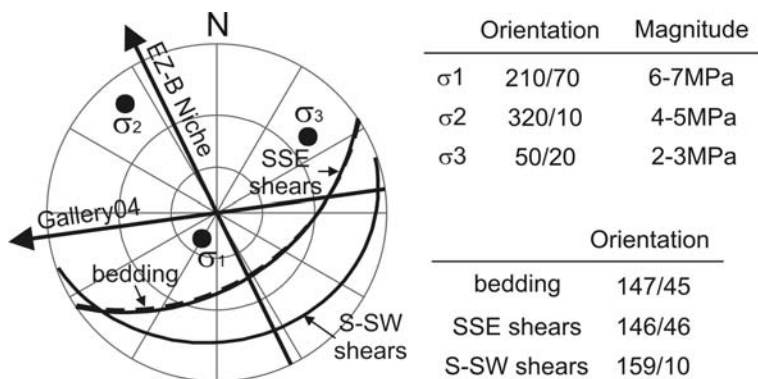


Fig. 5.3: The in situ stress field (lower hemisphere) at the Mont Terri Rock Laboratory. The orientation of the bedding and SSE shears are values averaged from geological mapping.

(total weight). Structurally, the fabric is dominated by bedding-parallel flocculation. In the niche, bedding is millimetres thick with an average dip angle of 45° (ranging from 38° to 50°) and dip direction of 147° (ranging from 140° to 155°) [16]. The niche trends sub-perpendicular to the strike of bedding (Fig. 5.3).

5.2.2 The EZ-B Niche

The EZ-B Niche is circular in cross-section with a flat floor and a diameter of 3.8m and length of 6-7m (Fig. 5.4). Construction of the EZ-B Niche and associated borehole drilling campaigns spanned a period of five months from December 2004 to April 2005 [20 or Chapter 2]. In December, an entrance to the niche with a length of 1-2m was excavated (Fig. 5.5). Fibre-reinforced shotcrete (150mm nominal thickness) was applied to the entrance surfaces and a 300mm-thick concrete floor slab was poured over the entrance invert. Four pore pressure sensors were installed near the mid-length of the niche in 20mm-diameter boreholes (BEZ-B4 to B7) in January. Three 100mm-diameter horizontal observation boreholes (BEZ-B1 to B3) with lengths of 8-9.5m were drilled in February. The remainder of the niche was excavated over a 12-day period in March with the main body (inset of Fig. 5.4) constructed in six steps (Fig. 5.5) and the invert in a single step. A pneumatic hammer was used in the construction of the niche with the exception of the entrance, where a road-header was additionally employed [18]. Due to the advantageous orientation of the niche axis with the SSE-dipping fault system and bedding, the niche required only minimal support consisting of a roof mesh, aluminium nails, and un-tensioned steel anchors (25mm diameter) grouted in place with a nominal embedment length of 0.5m. In April, 12 additional observation boreholes (BEZ-B8 to B19) with diameters of 100mm and lengths of 2-3m were drilled in three planes: two vertical planes near the mid-length of the niche and one horizontal plane near the springline.

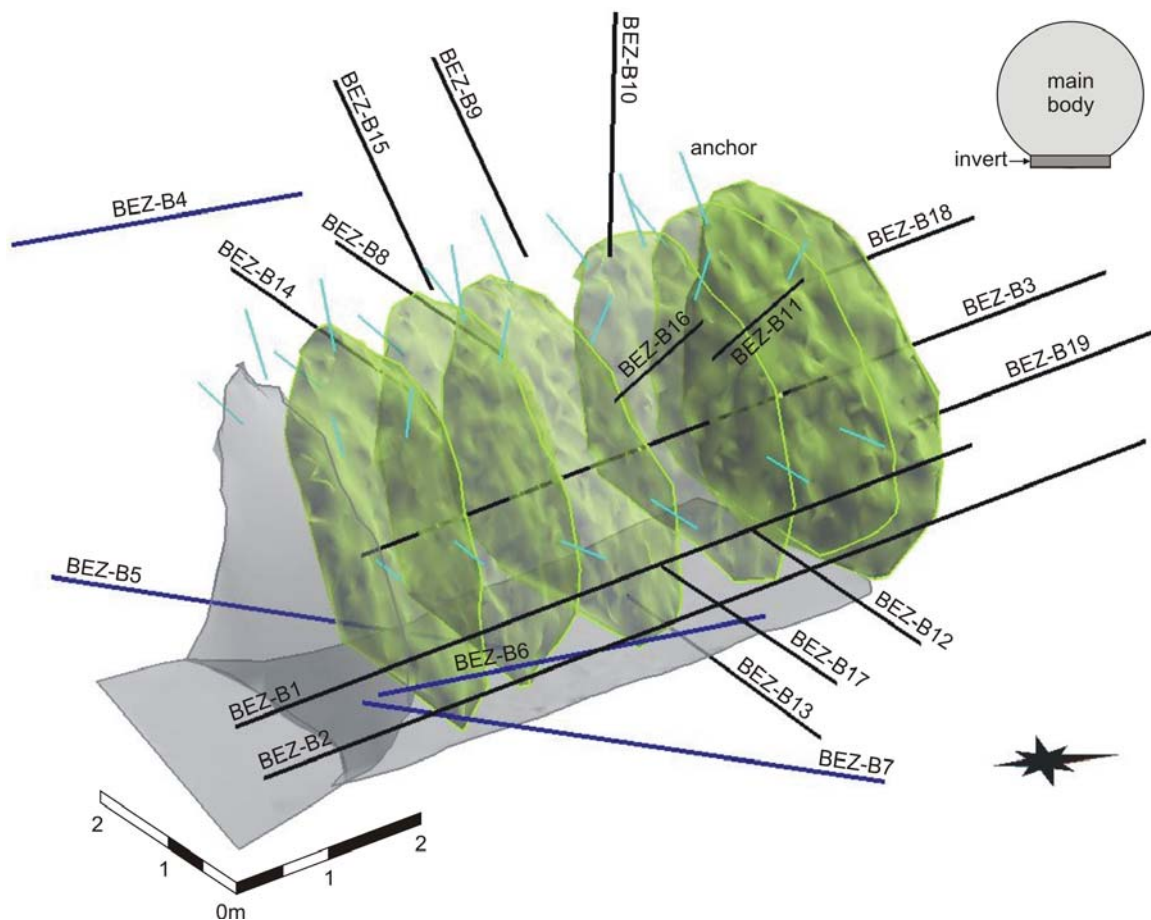


Fig. 5.4: Isometric view of the EZ-B Niche with the entrance face and the top of the concrete floor shown in grey. Interim and final faces are shown in yellow. Observation boreholes (BEZ-B1 to B3, B8 to B19) are shown in black and pore pressure sensors installed in BEZ-B4 to B7 (blue). Roof anchors are shown in light blue. A cross-sectional view of the niche is shown in the inset.

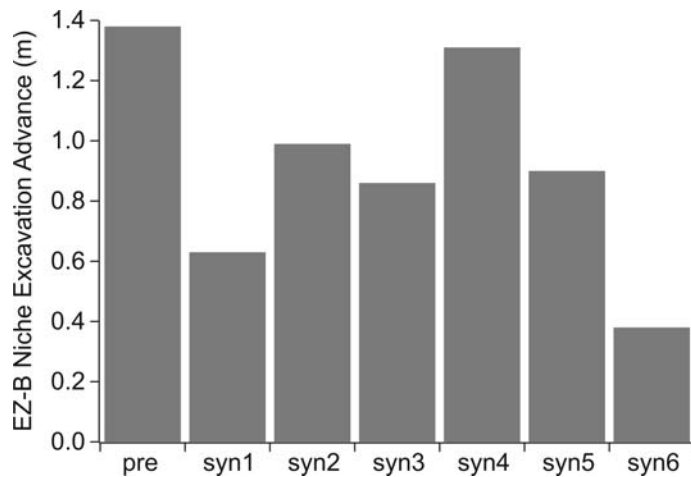


Fig. 5.5: Step sizes of the EZ-B Niche excavation.

This chapter examines the rock mass response ahead of the advancing niche face by following the data obtained from BEZ-B3 (near the centre of the face) as the borehole was shortened to its current length of roughly three metres (Fig. 5.4). Data from the post-excavation boreholes in the face (BEZ-B18 and B19) will also be considered but only one point in time will be considered in this case. The rock mass response elsewhere in the niche was considered in Chapter 4.

5.3 Field and Model Data Integration

Understanding the rock mass response ahead of the niche face required integration of the data collected in the field during the construction of the EZ-B Niche and results obtained from three-dimensional numerical modelling. The field campaign consisted of three stages [20]. The pre-excavation stage (December, 2004 to February, 2005) covered the period when the entrance was excavated, the first three observation boreholes (BEZ-B1 to B3) were drilled and logged, and the entrance surfaces and drillcores were mapped. In the syn-excavation stage (March, 2005), the last 5.1m of the niche was excavated with the boreholes logged at the end of each excavation step. The niche surfaces at the end of each step were also scanned optically with a panoramic laser scanner [21]. From these scans, the niche geometry and the location and geometry of the tectonic shears were established (Appendices A and B). The post-excavation stage started in April with the drilling and data logging of the last 12 observation boreholes (BEZ-B8 to B19) and repeat measurements in the older boreholes. Although repeat measurements as recent as October 2007 continue to be collected, only the first three post-excavation borehole logging campaigns (April, June, and November in 2005) are considered in this chapter. Due to constraints in manpower, not all boreholes were logged in every post-excavation campaign nor did the campaigns involve the same boreholes.

5.3.1 Field Data

The field data considered in this chapter included drillcore mapping, digital optical televiewer (DOPTV) imaging, and single-hole seismic measurements. The data considered were collected from boreholes (BEZ-B3, B18, and B19) drilled in the niche face (Fig. 5.6).

In the drillcores obtained from these boreholes, four types of structures have been mapped by field geologists (Fig. 5.7): bedding-parallel shears (sst), excavation-induced unloading joints (uj), dessication cracks (dc), and artificial discontinuities (ad). Dessication cracks have been attributed to drying and are non-persistent thin features. Artificial discontinuities have been attributed to drillcore extraction and handling.

Imaging of the borehole walls involved the Robertson Geologging Digital Optical Televiewer (Fig. 5.8). The probe consists of a downward-looking video camera, a lighting ring, and a hyperboloidal mirror upon which the image is reflected [22]. Consequently, a 360-degree view of the borehole wall is obtained at each sampling interval. The boreholes were imaged at the maximum resolution of half a degree and at a sample interval of 1mm. Fracture identification in the DOPTV images was thereby limited to those with aperture

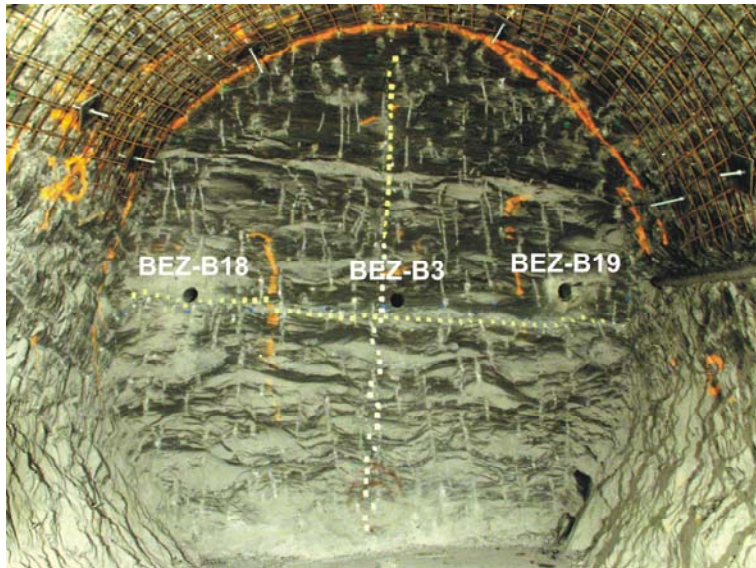


Fig. 5.6: Boreholes drilled into the face of the EZ-B Niche.

sufficiently large enough to be resolved by the chosen sampling setting. The probe was centralised with customised rigid aluminium collars and the logging speed ranged from 0.5m/min to 1m/min.

A mini-sonic probe (Fig. 5.9) from BGR (Federal Institute for Geosciences and Natural Resources) was used in the single-hole seismic measurements. The probe with a maximum sampling frequency of 10MHz consists of four piezo-electric transducers, one as a seismic source and three as receivers, spaced 10cm apart [23]. The larger the separation between the source and receiver, the greater the depth of seismic wave penetration. For the BGR mini-sonic probe, a penetration depth of 1-2cm has been determined from finite difference modelling (Schuster, pers. comm.). As a result, channel 1 is most affected by the borehole EDZ/EdZ (Excavation Damaged Zone/Excavation Disturbed Zone) while channel 3 is least affected. Coupling of the probe was achieved pneumatically and travel times were measured at intervals of 5-10cm. The P-wave and S-wave velocities and respective amplitudes were derived from first-arrival phases. Uncertainties involved in processing the seismic measurements are roughly $\pm 9\%$ for channel 1 P-wave velocities, $\pm 3\%$ for channel 3 P-wave velocities, and 4% for channel 3 S-wave velocities: i.e. $\pm 0.5\mu\text{s}$ to $\pm 1.5\mu\text{s}$ for the onsets of P-wave first arrivals and $\pm 1\mu\text{s}$ to $\pm 4\mu\text{s}$ for the S-waves [24]. A more detailed description of the equipment, logging method, and data processing is found in Schuster et al. [23] and Schuster and Alheid [24].

5.3.2 Numerical Modelling

Numerical modelling was carried out with FLAC3D (Fast Lagrangian Analysis of Continua in 3 Dimensions), version 3.00-308 [25]. Two elastic continuum models were simulated with each model

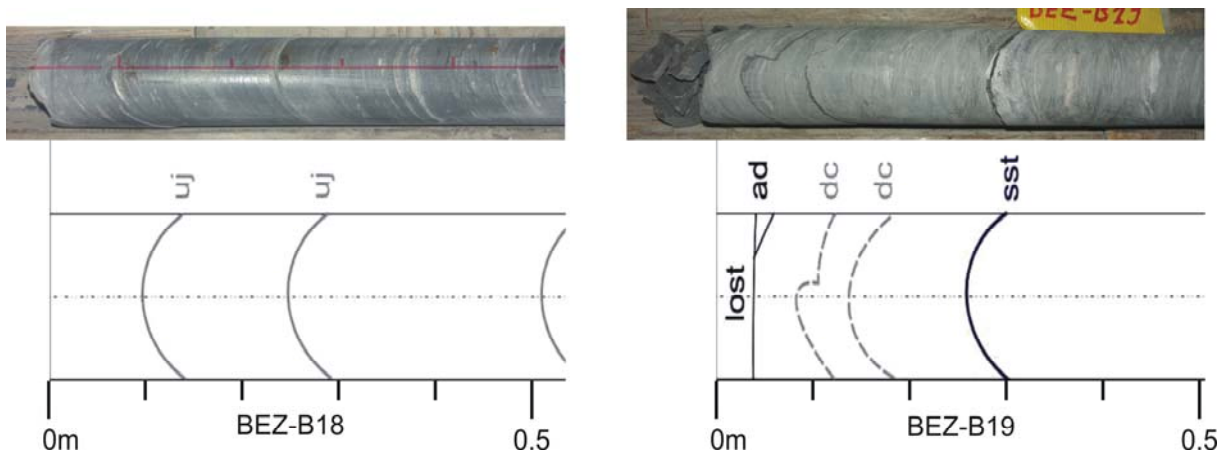


Fig. 5.7: Structures mapped in the EZ-B drillcores with corresponding photographs: artificial discontinuities (ad), dessiccation cracks (dc), unloading joints (uj), and tectonic shears (sst).

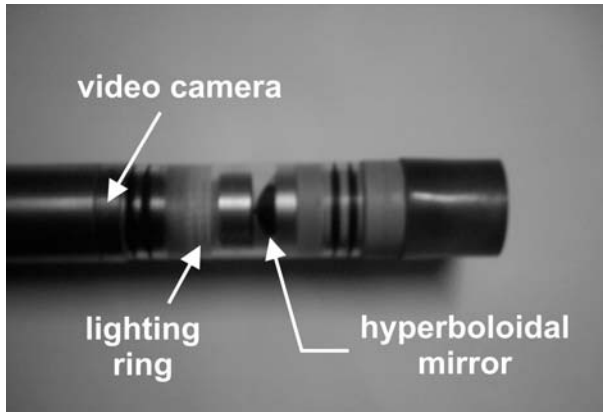


Fig. 5.8: The Robertson Geologging Digital Optical Televiewer (DOPTV) used to image the borehole walls.

requiring three days (Intel Pentium 4 3.2GHz processor and 3GB RAM) for completion. The grid (Fig. 5.10) consisted of 391,620 zones graded radially outwards from the EZ-B Niche. A volume 65m wide, 77m long, and 65m high (five to eight tunnel diameters) was modelled. The external boundaries were fixed in all three directions and the initial stress shown in Fig. 5.3 was implemented. The simulation involved the excavation of three openings: Gallery04, the HG-A and EZ-B Niches. Gallery04 was simplified to a straight alignment (69m long) and excavated full-face in 33 steps. The HG-A Niche excavation was simulated in three steps with the last step including the entrance of the EZ-B Niche to match the as-built sequence [26]. The EZ-B Niche was excavated in seven steps with the main body excavated in the first six steps and the invert in the seventh step (Fig. 5.4). Two sets of material properties were considered in the stress analysis. In the first, elastic isotropic (CIE) properties (Tab. 5.1) were implemented in accordance with Bock [27]. The second set (Tab. 5.1) consisted of a transverse isotropic matrix (CAE) with the plane of transverse isotropy dipping 45° towards 147° (to match bedding). The model data considered in this chapter consists of stress ratios (between σ_3 and σ_1) calculated at the centreline of where each borehole would be located in the numerical simulations. Similar to the approach taken in Chapter 4, the results from the numerical modelling thereby supplements the field data interpretation by providing an indication of the degree of damage.

5.3.3 Data Integration

Integration of the field data is illustrated in Fig. 5.11 through consideration of the data collected in BEZ-B3 during the pre-excavation stage. Fig. 5.11 incorporates the positions of the niche face and bedding-parallel shears with the drillcore map, DOPTV image, and derived seismic parameters. The position of the niche face and intersecting bedding-parallel shears are shown in the top where a longitudinal section from a three-dimensional visualisation (see Appendices A and B) of BEZ-B3 intersecting the niche is shown. The borehole collar coincided with the face of the niche in each excavation step; thus, the collar moves with the niche advance. The blue spheres indicate where tectonic structures were mapped in the drillcore. The stress ratios (or spalling limits) along the borehole from the numerical models are plotted below. The

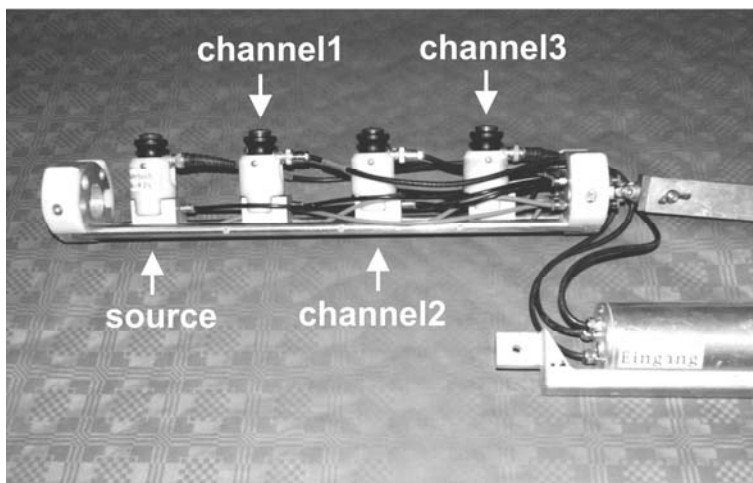


Fig. 5.9: The BGR mini-sonic probe used in the single-hole seismic measurements.

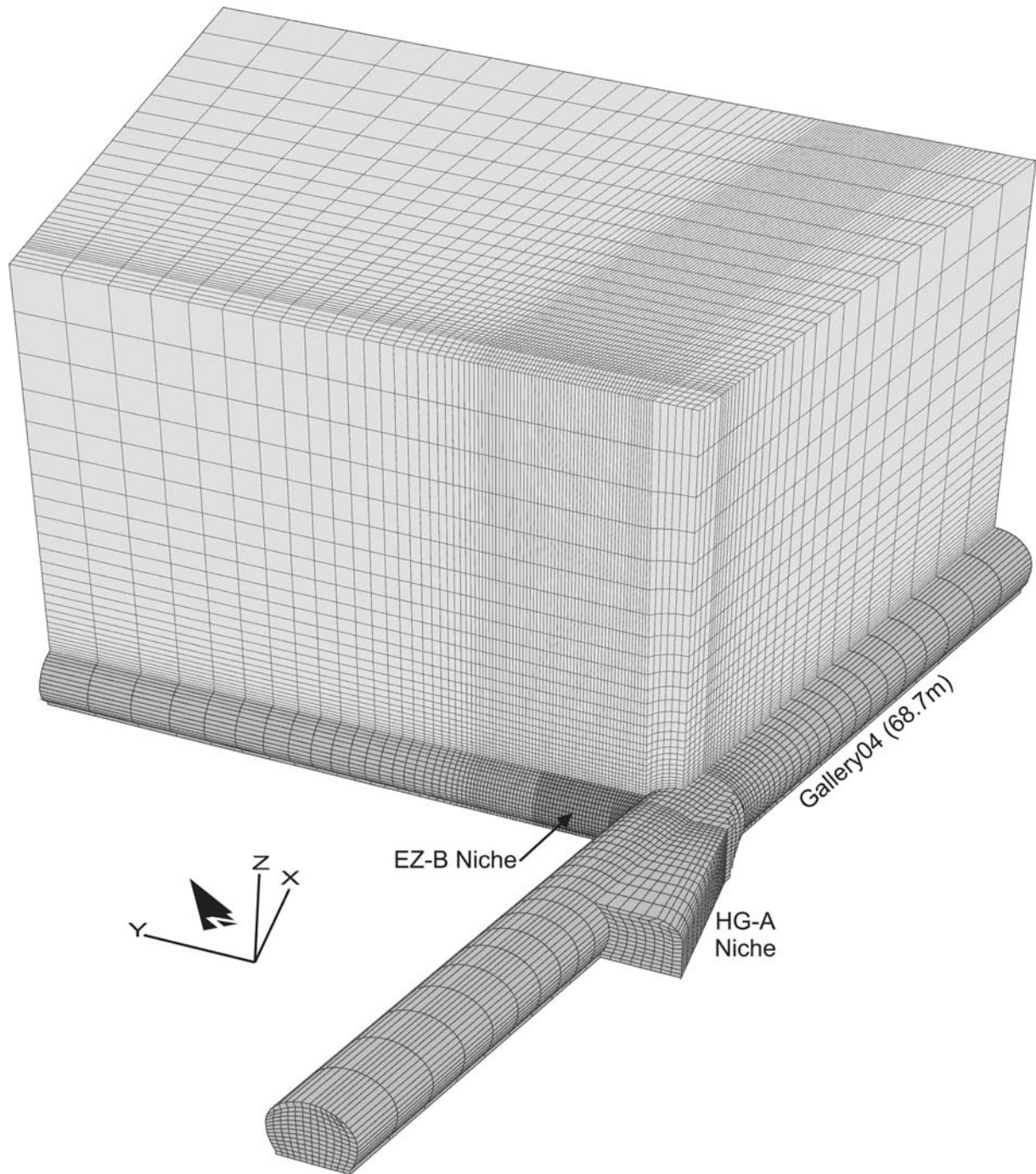


Fig. 5.10: Excavations simulated in the continuum model (looking northeast).

Tab. 5.1: Material properties used in the elastic anisotropic continuum model (after [27]).

	Isotropic	Anisotropic
E(parallel bedding)	6 GPa	10 GPa
E(perpendicular bedding)		4 GPa
G(perpendicular bedding)	1.2 GPa	1.2 GPa
ν (parallel bedding)	0.27	0.33
ν (perpendicular bedding)		0.24

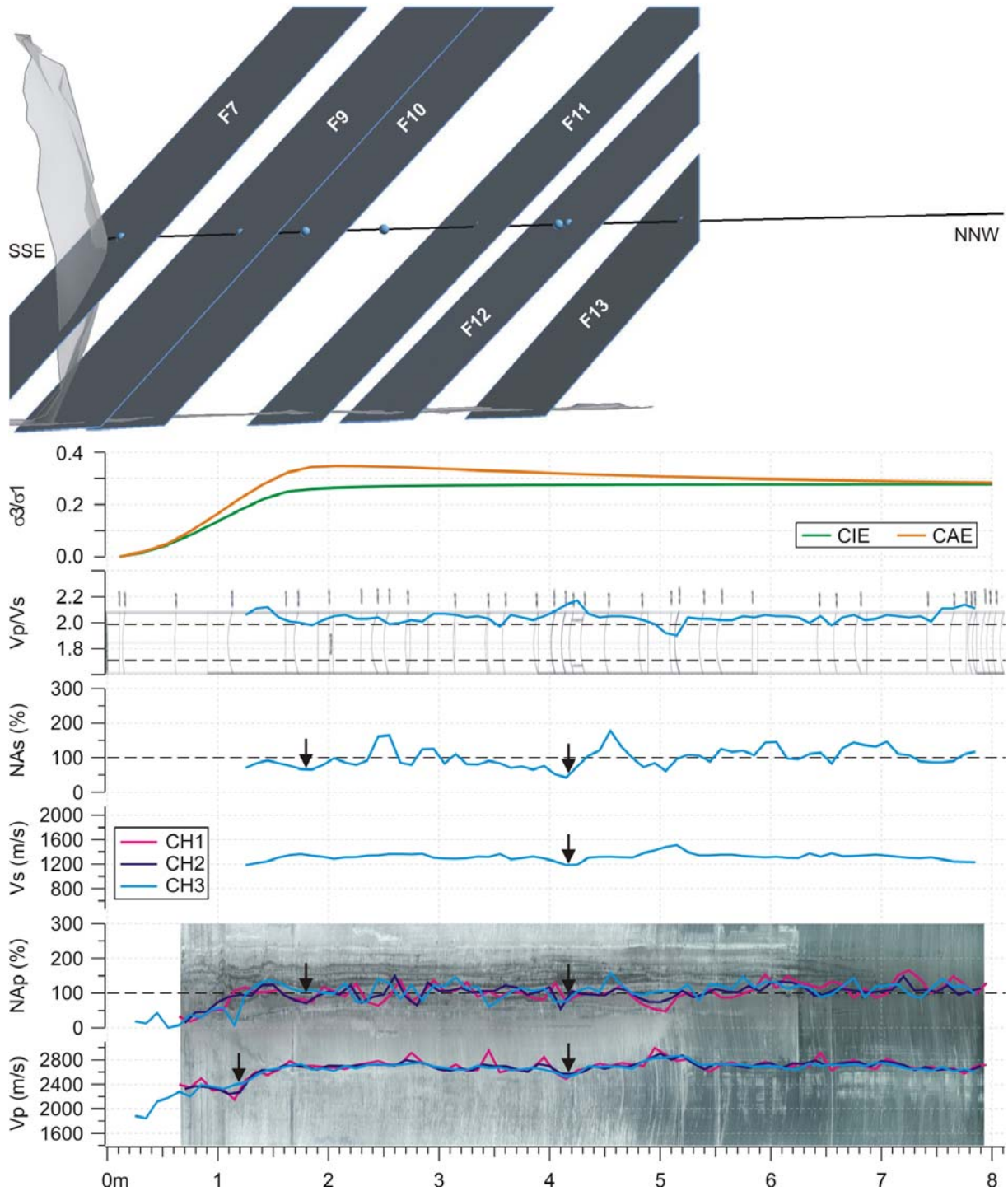


Fig. 5.11: Pre-excitation stage integration of drillcore mapping, DOPTV imaging, and seismic parameters derived from logging BEZ-B3 along the east borehole wall. Intersections of mapped bedding-parallel shears with BEZ-B3 and the niche entrance face are shown in the longitudinal-section (top). Enlarged drillcore maps can be found in Appendix C.

V_p/V_s ratio is plotted over the drillcore map along with two reference ratios. The higher ratio ($V_p/V_s = 2.0$) represents the Poisson's ratio ($\nu = 0.33$ [27]) determined from laboratory testing with loading parallel with bedding. The lower ratio ($V_p/V_s = 1.7$) was determined from bedding-perpendicular loading (with $\nu = 0.24$ [27]). Below this are plots of the shear wave (S-wave) and compression wave (P-wave) amplitudes and velocities. Due to difficulty in picking the first S-wave arrivals and interference from the borehole EDZ/EdZ [23], only channel 3 data were considered for parameters associated with S-waves. Both the P-wave and S-wave amplitudes were normalised by the average of each respective channel (in accordance

with Schuster et al. [23]). This was a necessary step to enable comparison between the channels as attenuation increased rapidly with increasing distance between the source and receiver. The P-wave velocities and amplitudes overlay the DOPTV image, which has been rotated so that the horizontal centreline of the image coincides roughly with the travel path of the mini-sonic probe. In the case of BEZ-B3 and in all the field campaigns, the travel path of the probe was along the east borehole wall.

5.4 Data Analysis and Interpretation

Data interpretation in this chapter has been organised according to the three stages of the field investigation (Chapter 2 or [20]). The purpose of the pre-excitation stage was to set benchmarks for the field data. Consequently, the seismic data obtained in the syn- and post-excitation stages have been compared with those obtained in the pre-excitation stage. In this case, only channel 3 data is considered as it is the least affected by the borehole EDZ/EdZ.

5.4.1 Before the EZ-B Niche Excavation

In the pre-excitation stage, the 1-2m long EZ-B Niche entrance was excavated and borehole, BEZ-B3, was subsequently drilled near the centre of the entrance face (Fig. 5.4). Most of the structures identified in the BEZ-B3 drillcores were artificial discontinuities or “ad” (see Appendix C for enlarged figures of the drillcore maps) and 77% of these were oriented sub-parallel with bedding. The other structure identified in the drillcores was tectonic in nature (and belonged to the SSE bedding-parallel set) and constituted 17% of structures mapped. In general, the bedding-parallel shears intersected the borehole near seismic amplitude and velocity troughs (arrows in Fig. 5.11), such as F12, thereby suggesting local damage.

Experimental studies [28, 29] have shown that stable crack growth increases significantly when the spalling limit falls below 0.05 (see Chapter 4 for a more detailed explanation). However, no induced fractures were mapped in the drillcore [18] despite stress ratios falling below 0.05 in the first 50cm of the borehole (Fig. 5.11) and spalling-type failure (Fig. 5.12) indicated in both CIE and CAE simulations. The stress redistribution plotted along BEZ-B3 in both simulations for the pre-excitation stage indicated that the damage initiation threshold (see Chapter 4 for definition of the strength envelope) was well exceeded for the first time after the niche entrance was excavated (Fig. 5.12). Seismic wave amplitudes and velocities were seen to increase along with the stress ratios (Fig. 5.11) suggesting damage increased towards the borehole collar or niche entrance face (in the direction of the arrowheads in Fig. 5.12). The end of the arrow for GA4 in Fig. 5.12 coincides approximately with the collar of BEZ-B3 at the niche entrance face. In the subsequent simulated excavation rounds (Fig. 5.13) in Fig. 5.12, the arrow head ends at the advancing niche face as BEZ-B3 was shortened.

As no induced fractures were mapped, the extent of the entrance excavation-induced perturbation was determined from the seismic parameters. The depth where the parameters reached a plateau was chosen as the boundary of the perturbed zone. In the pre-excitation stage, perturbations extended as far as 1.4m to 1.5m ahead of the entrance face (Fig. 5.11). Interestingly, this occurred near the intersection of F9 with the borehole. The tectonic shears, F7 and F9, near the borehole collar may have affected the size of EDZ/EdZ ahead of the niche face as these shears bounded a low and relatively uniform seismic wave amplitude and velocity zone in the first 1-1.2m. It is speculated that deformation may have occurred at these shears as they were least kinematically constrained. Since F9 intersected the entrance face near the invert, the maximum stress trajectory (see Chapter 3, Section 3.6) would have been inclined more with the dip of the shear and thus, minimising any clamping effect. In Chapter 4, the rock mass in the lower part of the niche was shown to have displaced in a direction that was sub-perpendicular to the bedding and/or bedding-parallel shear. In addition to stress-induced damage, uplift of the lower part of the niche, with little kinematic constraint on F7 and F9, could have also led to micro-scale induced damage that may have been bound between the tectonic shears.

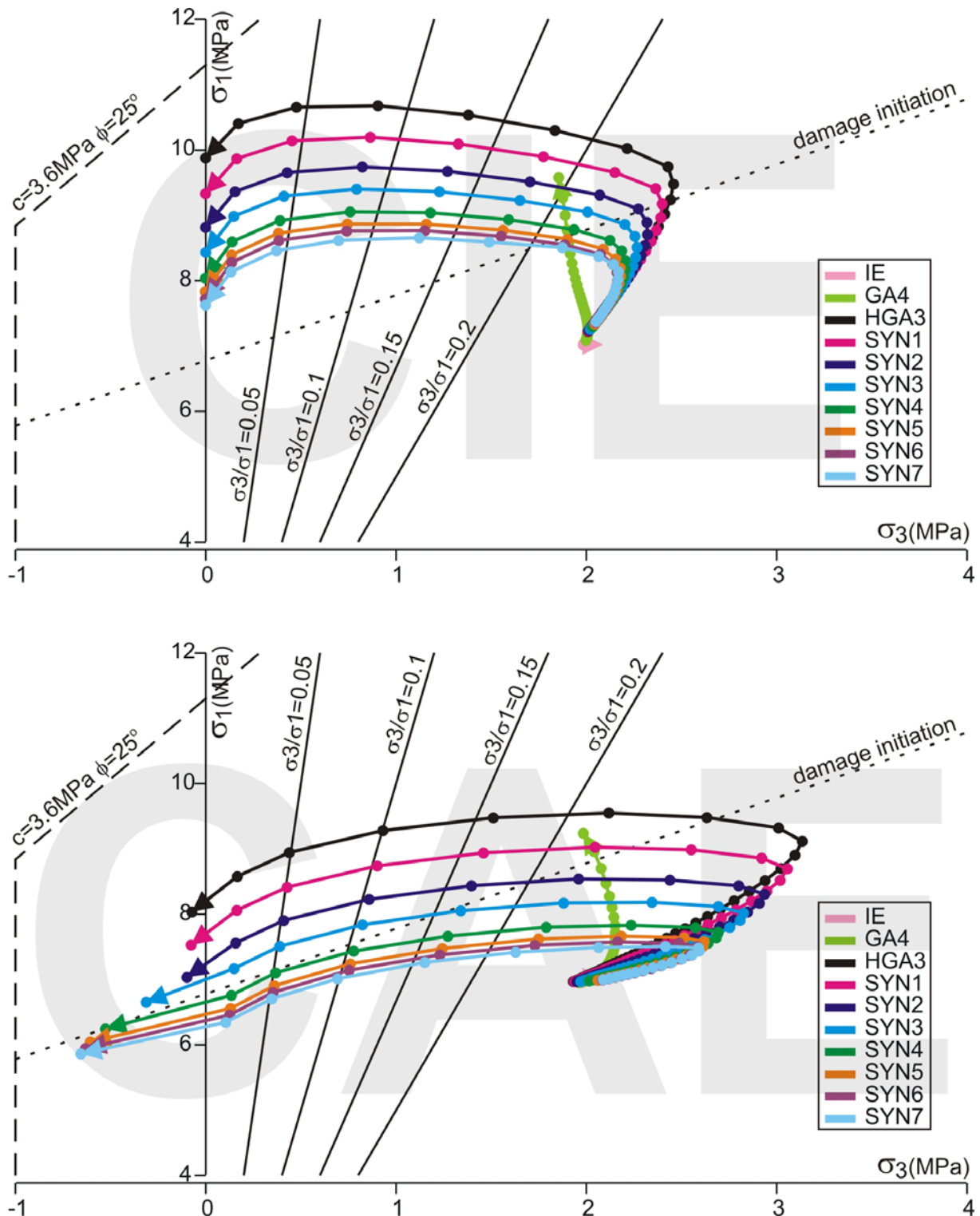


Fig. 5.12: Simulated stress redistributions plotted along BEZ-B3 for key steps in the excavation sequence. Results from the isotropic model (CIE) are shown in the top and results from the transverse isotropic model are shown in the bottom (CAE). Refer to Fig. 5.4 for borehole locations and Fig. 5.13 for the excavation steps.

5.4.2 During the EZ-B Niche Excavation

The syn-excavation stage began 23 to 24 days after BEZ-B3 was drilled. The main body (Fig. 5.4) of the niche was excavated in six steps and the invert was excavated in the last and seventh step. The excavation rounds for the main body ranged roughly from 40cm to 130cm (Fig. 5.5). In Syn1, the first 65cm was

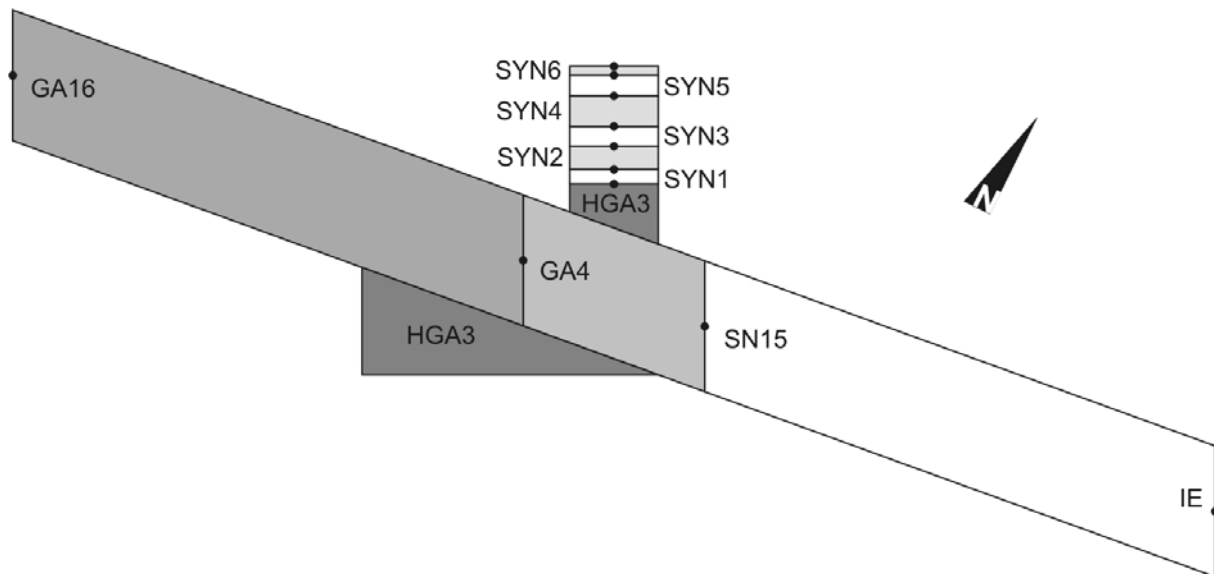


Fig. 5.13: Key excavation steps in the numerical simulations where data were analysed. The pre-excavation stage is represented by HGA3 while the syn-excavation stage is represented by the six excavation rounds (SYN1 to SYN6).

completed in two days with the excavation of a smaller niche (“mini niche”) near the centre of the face in the first day (Fig. 5.14). The second round (Syn2) of 1m was completed two days after Syn1. Syn3 to Syn6 were completed consecutively with a 12-hour stoppage between each round. Syn3 and Syn5 entailed nearly the same volume of excavated rock with an 85cm-advance in the former and 90cm in the latter. The largest round (of roughly 1.3m) was excavated in Syn4 due to a wedge failure that occurred in the upper half of the advancing face. The instability has been attributed to the intersection of a steeper dipping shear plane (FA in Fig. 5.15), which has only been mapped in the face of Syn3 (see Appendix B for the original geological maps) [18]. The smallest round of about 40cm was excavated in Syn6.

With little field evidence of macro-damage in the form of induced fracturing during the syn-excavation stage, the zone of induced perturbation was identified by using the seismic parameters. Seismic wave amplitudes and velocities were lowest in the first 10-70cm of the shortening BEZ-B3 and increased until benchmark levels were reached (Figures 5.16, 5.17, 5.18, 5.19, 5.20, and 5.21). The increasing seismic parameters (in the direction of the niche advance) coincided with increasing stress ratios in each of the syn-excavation rounds (Figures 5.16, 5.17, 5.18, 5.19, 5.20, and 5.21). Numerical simulations showed that the rock mass ahead of the advancing niche face was susceptible to spalling failure (Fig. 5.12), suggesting that the degree of damage (as inferred from the seismic data) increased as the stress ratio decreased.



Fig. 5.14: Excavation of the “Mini niche” in the centre of the entrance face.

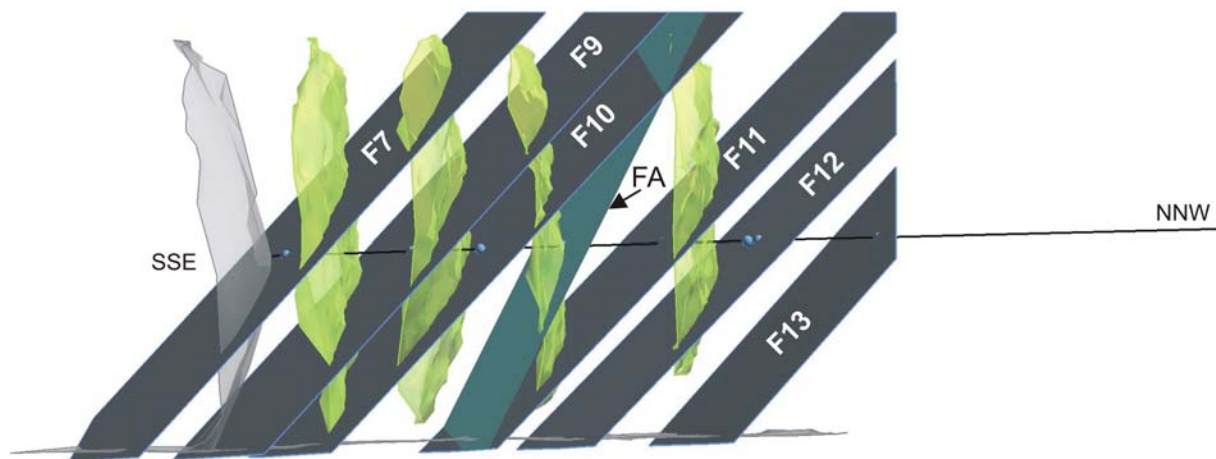


Fig. 5.15: Location of the steeper-dipping shear, FA, between the faces of Syn3 and Syn4.

Damage ahead of the advancing face was most likely microscopic in scale and possibly aligned with bedding and/or the tectonic shears as these structures provided the paths of least resistance.

The extent of the perturbed zone ahead of the niche face was determined by comparing the repeat seismic measurements with the benchmark measurements carried out in the pre-excavation stage. Due to time constraints, the entire borehole in Syn1 (Fig. 5.16) and Syn2 (Fig. 5.17) was not logged in the seismic investigation. However, logging was carried out until the undisturbed rock mass was reached. Integration of the borehole data in Syn1 showed almost no difference in all the seismic parameters when compared with the benchmark measurement (Fig. 5.16). The EDZ/EdZ extent in Syn2 (Fig. 5.17) and Syn3 (Fig. 5.18) were 40cm and 30 cm, respectively. From Syn4 to Syn6, the extent increased two- to three-fold (Fig. 5.22). The extent in Syn4 was roughly 1m to 1.1m (Fig. 5.19), about 1.1m to 1.3m in Syn5 (Fig. 5.20) and around 1m to 1.2m in Syn6 (Fig. 5.21). One could argue that the larger excavation step (due to the wedge failure) in Syn4 was responsible for this increase in the extent of the perturbed zone. However, the excavation round at Syn6 was the smallest and the perturbed zone was similar in extent to Syn4. Alternatively, the large jump between Syn3 and Syn4 (Fig. 5.22) could have been attributed to the zone of perturbation from the entrance excavation whereby the volume of rock up to about 3.5m from the entrance face was previously stressed to higher levels. In this case, only the rock mass ahead of the Syn4 face would have been newly disturbed from the syn-excavation rounds. This may explain the consistently larger extents indicated by the seismic parameters from Syn4 onwards. If Syn4 was used as the benchmark, the zone of perturbation in Syn5 would then be 70-90cm and 0.5-1.2m in Syn6.

Possible influences of the tectonic shears on the extent of the EDZ/EdZ as the face advanced were best observed in the seismic parameters obtained in Syn1, Syn4, Syn5, and Syn6. In Syn1, the influence of F7 and F9 from the entrance excavation (pre-excavation stage) was still seen (Fig. 5.14). In Syn4, F12 appeared to divide the perturbed zone into two regions with the lowest amplitudes and velocities forming a flatter step-like trend towards the collar while amplitudes and velocities increased at a relatively constant slope until respective plateaus were reached in the undisturbed rock mass (Fig. 5.19). Reductions in seismic wave amplitudes and velocities near F13, which intersected the final niche face near the centre, were also first seen in Syn4. In Syn5 (Fig. 5.20), further reductions, most notably in the seismic wave amplitudes, were seen near F13. The influence of F13 on the perturbed zone continued in Syn6 (Fig. 5.21) with the formation of step-like structures in the seismic wave amplitude and velocity profiles. These observations suggested that the tectonic shears might have influenced the development of the perturbed zone ahead of the face. Unloading of the rock mass closest to the advancing face could have been exacerbated by the bedding-parallel shears, which would introduce stress heterogeneities. Advance of the niche against dip would have led to the progressive reduction of kinematic constraint on the bedding-parallel shears thereby leading to elastic and possibly plastic deformations along the shears. As the EZ-B Niche is relatively short with possibly half the niche affected by the zone of perturbation from the entrance excavation, it is difficult at the moment to draw robust conclusions on the effect of the tectonic

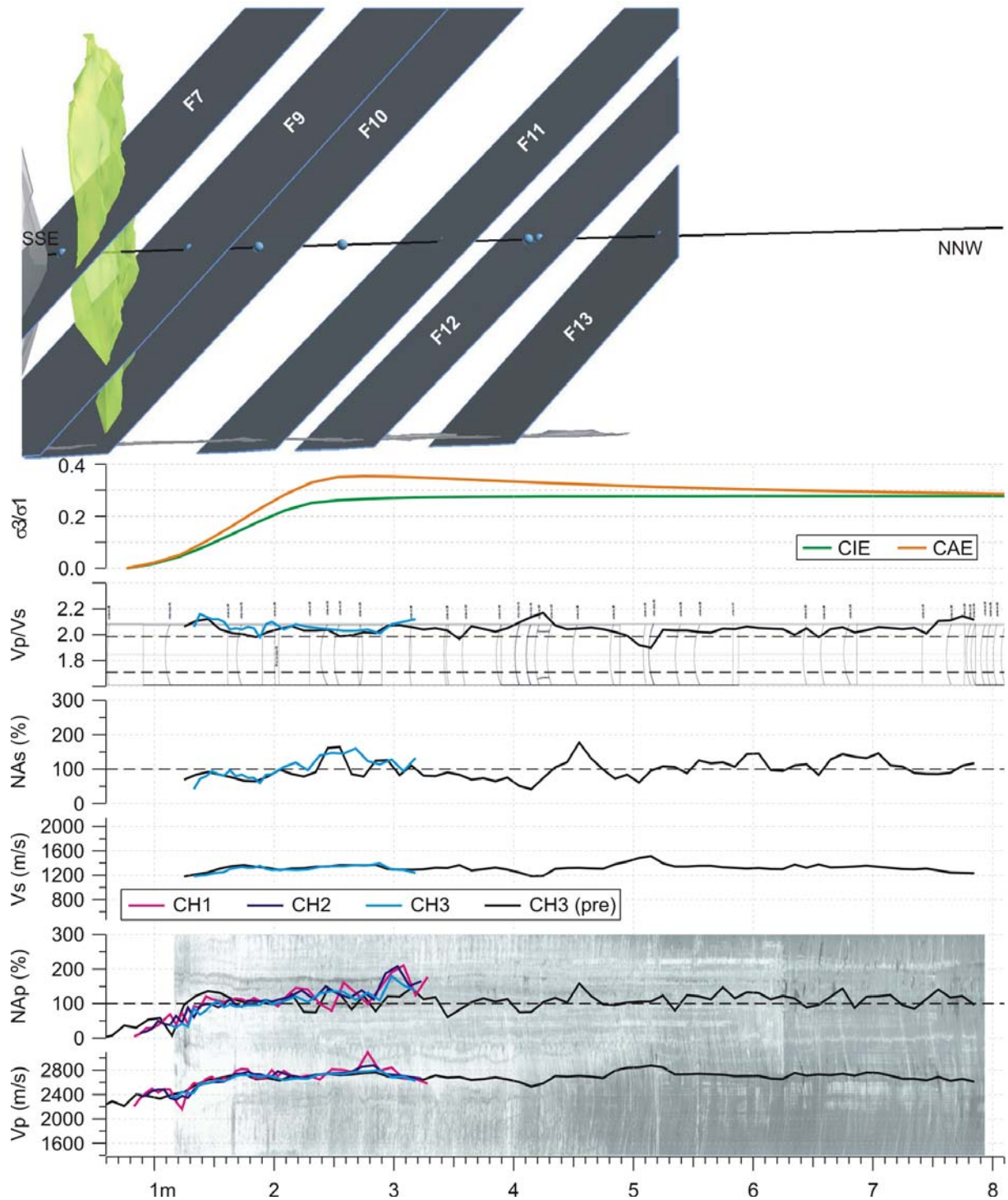


Fig. 5.16: Syn1 integration of field and model data from BEZ-B3. Intersections of mapped bedding-parallel shears with BEZ-B3 and the advancing niche face are shown in the longitudinal-section (top). Enlarged drillcore maps can be found in Appendix C.

shears on excavation-induced perturbations ahead of the advancing niche face. In future work, an investigation carried out in a longer tunnel is required to gain a more comprehensive understanding of the influence of the tectonic shears on the EDZ/EdZ ahead of the face.

5.4.3 After the EZ-B Niche Excavation

In the post-excavation stage, two additional boreholes (BEZ-B18 and B19) were drilled in the face (Fig. 5.4). BEZ-B18 is located near the west wall and about 1.5m from BEZ-B3. BEZ-B19 is slightly closer to

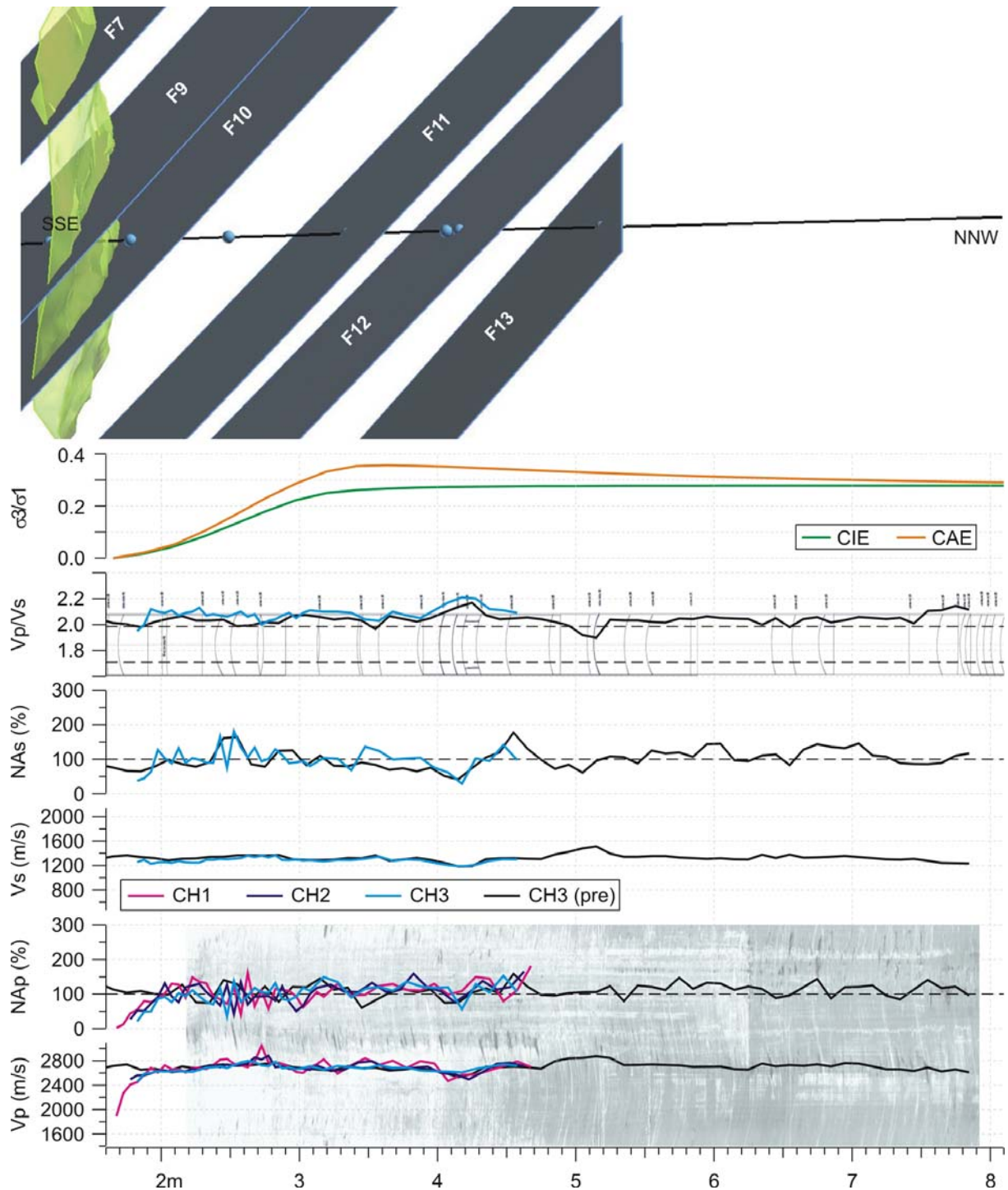


Fig. 5.17: Syn2 integration of field and model data from BEZ-B3. Intersections of mapped bedding-parallel shears with BEZ-B3 and the advancing niche face are shown in the longitudinal-section (top). Enlarged drillcore maps can be found in Appendix C.

BEZ-B3 (about 1.2m) but located near the east niche wall. The first three seismic post-excitation measurement campaigns considered in this thesis were carried out 25 to 33 days after Syn6 (PostA), 88 to 91 days after Syn6 (PostB), and 257 to 264 days after Syn6 (PostC). Data from all three measurement campaigns were only available from BEZ-B3 at the time of writing. As a result, a comparison of the data obtained from all three boreholes was only possible for the first campaign, PostA.

The lowest velocities and amplitudes in PostA were again found in the first 50-70cm (BEZ-B18 in Fig. 5.23, BEZ-B3 in Fig. 5.24, and BEZ-B19 in Fig. 5.25). Diametrically-opposed borehole instability was also

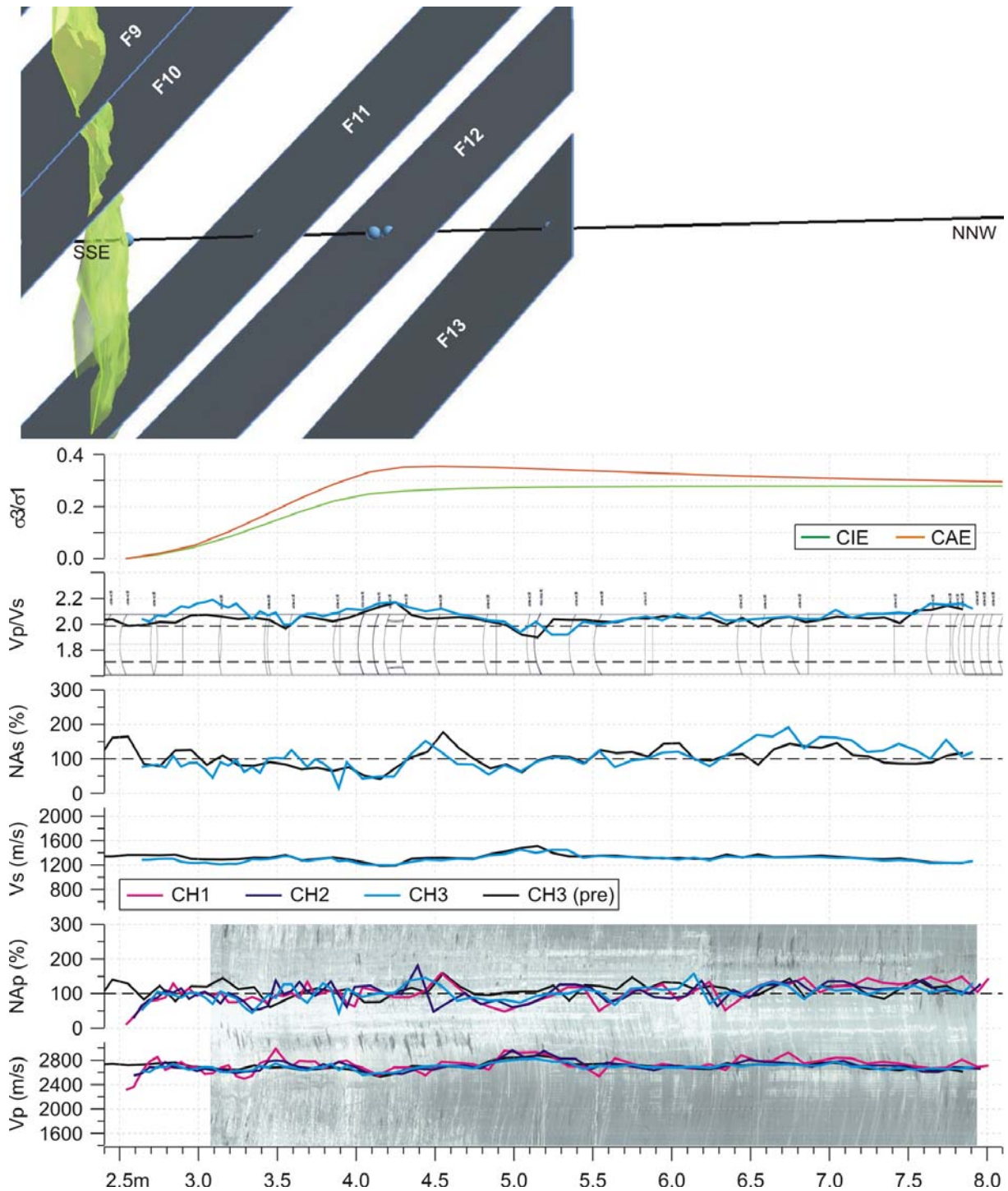


Fig. 5.18: Syn3 integration of field and model data from BEZ-B3. Intersections of mapped bedding-parallel shears with BEZ-B3 and the advancing niche face are shown in the longitudinal-section (top). Enlarged drillcore maps can be found in Appendix C.

observed in the DOPTV images of BEZ-B18 (Fig. 5.23) and B19 (Fig. 5.25) but at greater depths (1.6-1.7m). Instabilities in BEZ-B18 appeared to be less developed than those in BEZ-B19. Borehole instabilities in BEZ-B3 (Fig. 5.24) were also visible but these first appeared in Syn1 (Fig. 5.16) where the instabilities formed thin flakes that exposed new surfaces at roughly 5.7m depth. Humidity trapped at depth in the borehole would likely lead to degradation of the borehole walls but this would have equally affected the entire borehole perimeter. Presently, the cause of these borehole instabilities is unknown. One could argue the instabilities represent incipient breakouts in which case they would provide information

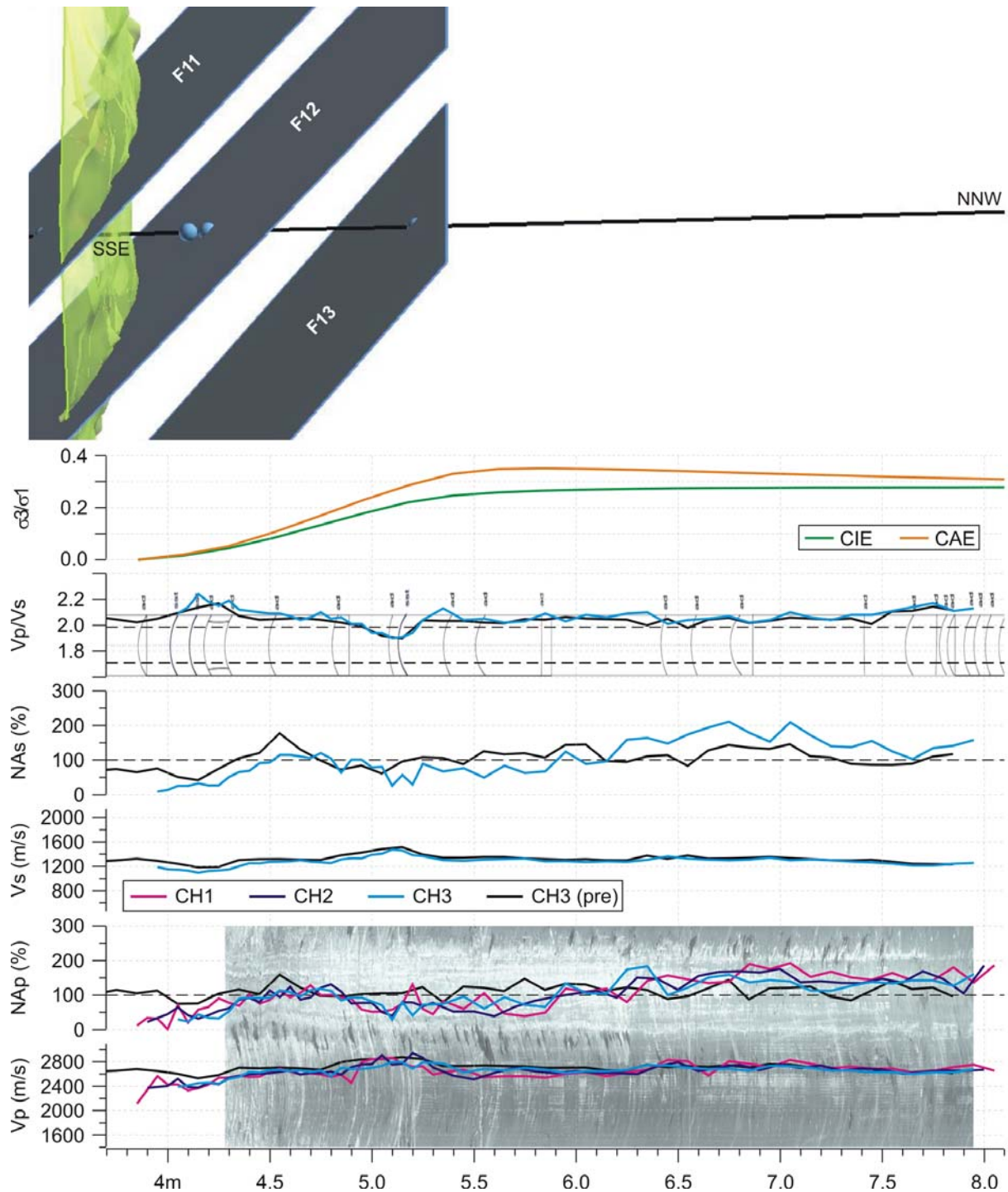


Fig. 5.19: Syn4 integration of field and model data from BEZ-B3. Intersections of mapped bedding-parallel shears with BEZ-B3 and the advancing niche face are shown in the longitudinal-section (top). Enlarged drillcore maps can be found in Appendix C.

regarding the stress state in the rock mass. However, without a rigorous numerical examination and precise geometrical information, this notion remains speculative.

The onset of borehole instabilities in BEZ-B18 and B19 coincided with an increase in the normalised P- and S-wave amplitudes. Similar increases were also seen in the amplitudes of BEZ-B3 during the syn-excavation stage (Fig. 5.22). The relative increase in amplitudes from the borehole collar to the terminus may be indicative of decreasing relaxation-related rock mass damage. Integration of the seismic parameters derived from channel 1 indicated little difference between the three boreholes in PostA (Fig. 5.26). However, channels 2 and 3 data indicated slightly lower velocities and amplitudes in the near-face

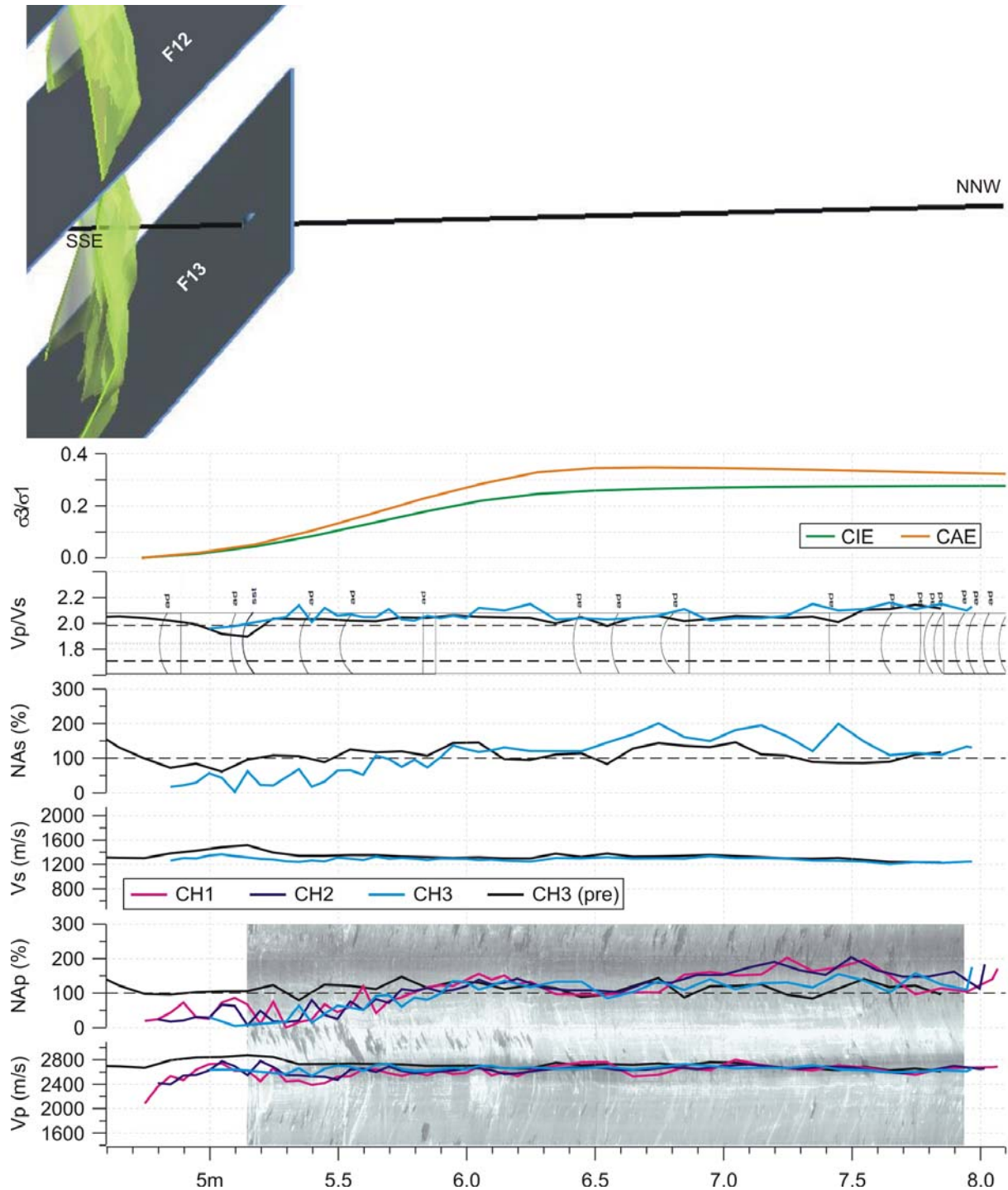


Fig. 5.20: Syn5 integration of field and model data from BEZ-B3. Intersections of mapped bedding-parallel shears with BEZ-B3 and the advancing niche face are shown in the longitudinal-section (top). Enlarged drillcore maps can be found in Appendix C.

perturbed zone in BEZ-B3 and to greater depth by about plus or minus 0.3m suggesting a larger zone of perturbation in the niche centre.

Seismic parameters derived from all the post-excavation measurement campaigns in BEZ-B3 were also compared with those obtained at Syn6 (Fig. 5.27). While some local variations were seen, overall little change was seen along the entire borehole length. Hence, the extent of the perturbed zone ahead of the niche face appeared to have changed little within a time span of eight to nine months.

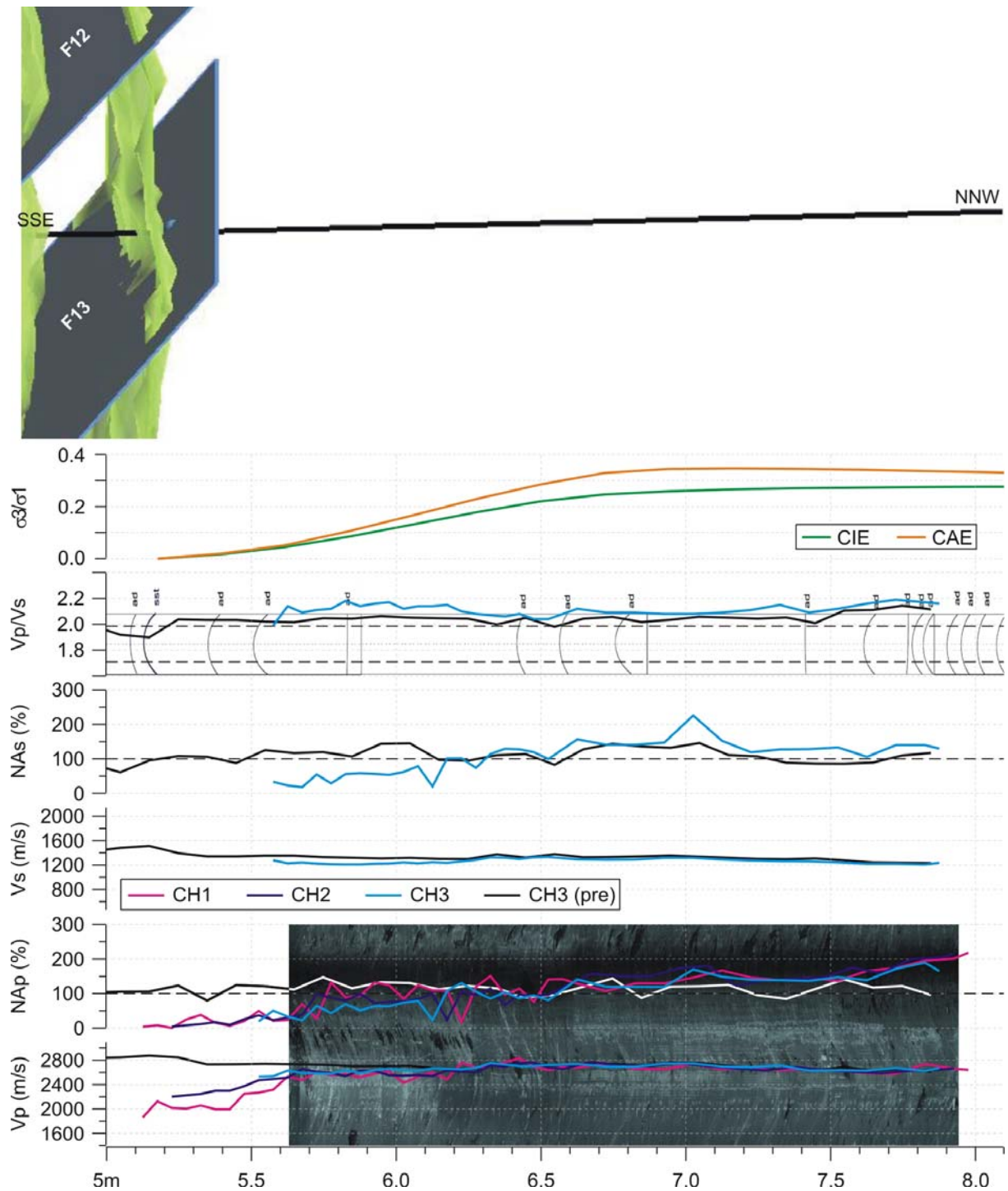


Fig. 5.21: Syn6 integration of field and model data from BEZ-B3. Intersections of mapped bedding-parallel shears with BEZ-B3 and the advancing niche face are shown in the longitudinal-section (top). Enlarged drillcore maps can be found in Appendix C.

5.5 Conclusions

In this chapter, the rock mass ahead of an advancing short test tunnel at the Mont Terri Rock Laboratory was investigated by integrating borehole field data with stress ratios that were determined from numerical simulations. Bedding in the Opalinus Clay at Mont Terri is well developed and a pronounced feature that has resulted in anisotropy in the intact elastic modulus and Poisson's ratio (as determined from laboratory testing). An added complexity in the Opalinus Clay at Mont Terri is the occurrence of thin tectonic shears: most notably the set sub-parallel with bedding. The bedding-parallel shears were found to influence

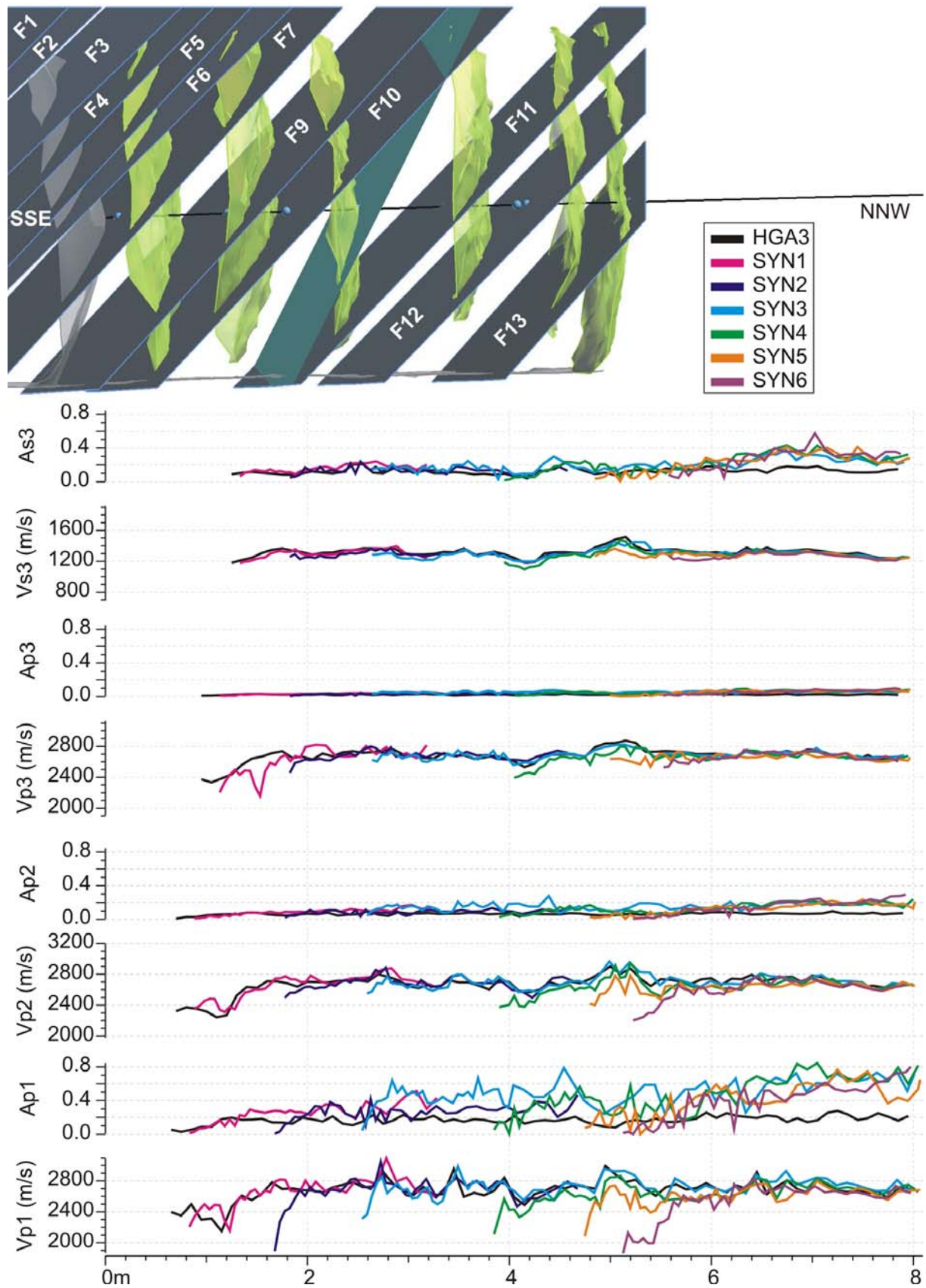


Fig. 5.22: Seismic parameters derived from the syn-excitation measurements made along the east borehole wall of BEZ-B3 include: P-wave velocities (V_p) and amplitudes (A_p) for all three channels (1 to 3) and S-wave velocities (V_s) and amplitudes (A_s) for channel 3. Profiles corresponding to the pre-excitation stage (HGA3) are also included.

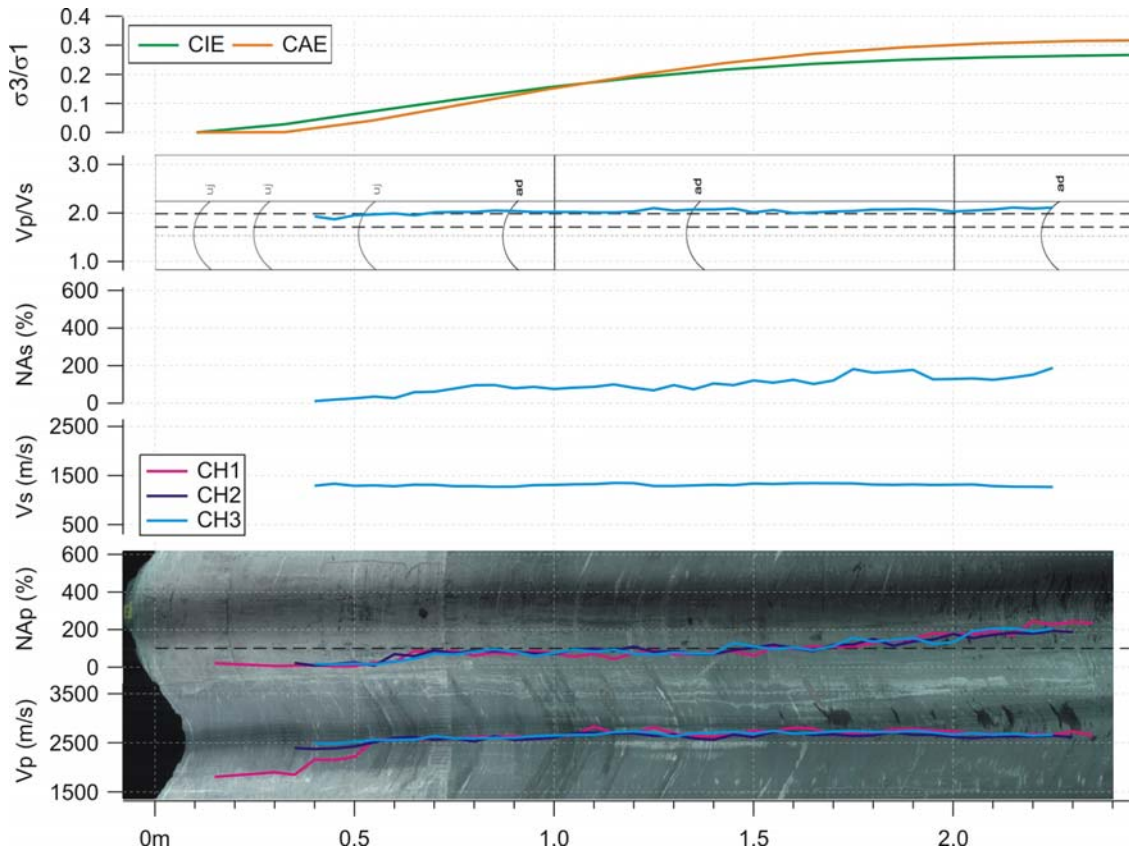


Fig. 5.23: BEZ-B18 PostA integration of drillcore mapping, DOPTV imaging, and seismic parameters derived from measurements made along the east borehole wall.

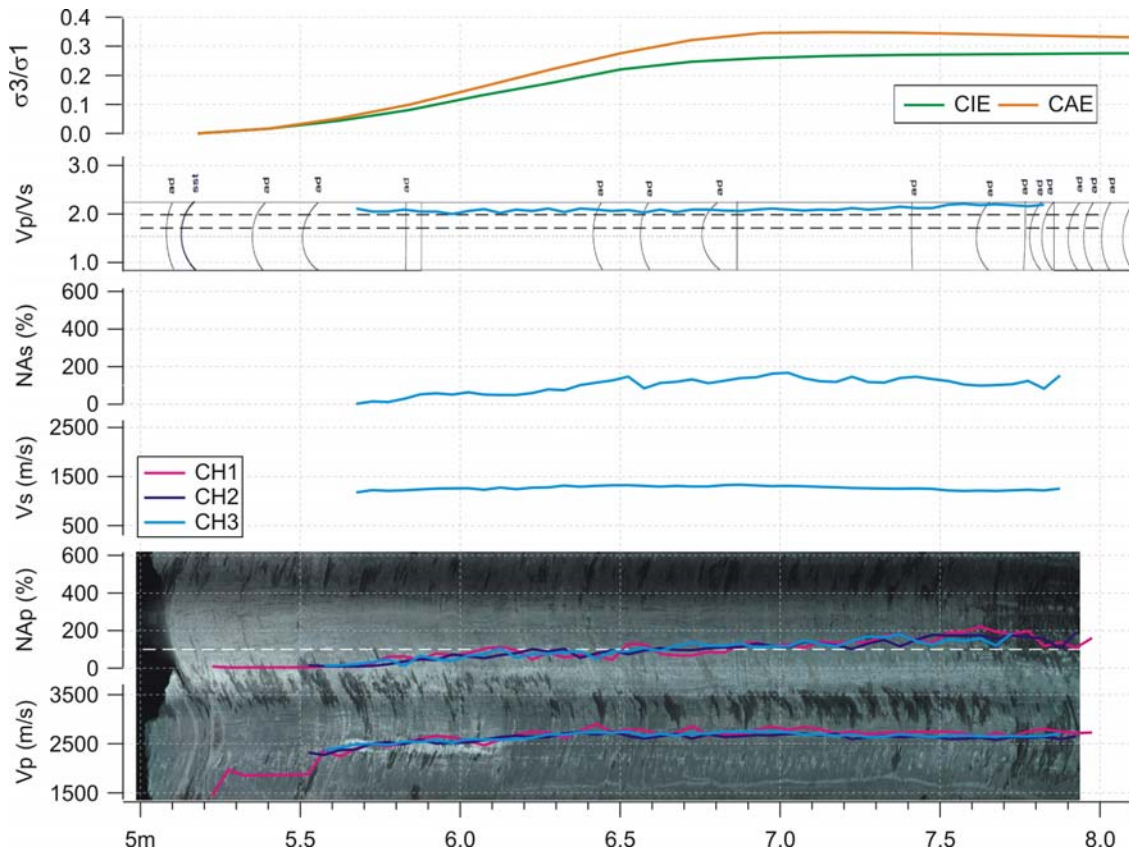


Fig. 5.24: BEZ-B3 PostA integration of drillcore mapping, DOPTV imaging, and seismic parameters derived from measurements made along the east borehole wall.

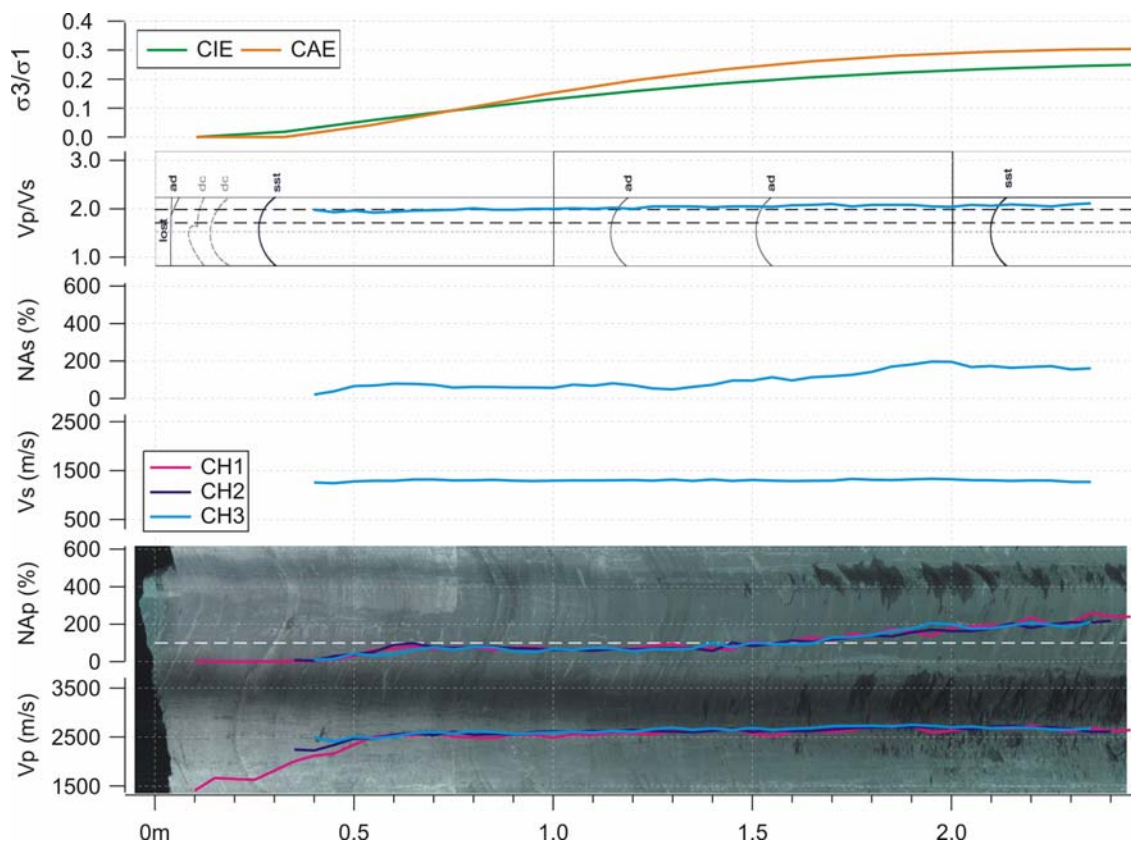


Fig. 5.25: BEZ-B19 PostA integration of drillcore mapping, DOPTV imaging, and seismic parameters derived from measurements made along the west borehole wall.

the seismic parameters derived from borehole logging. The shears would provide a preferred source for stress relief when a tunnel is advanced against dip, as is the case in the EZ-B Niche. Lower seismic velocities and amplitudes found near the bedding-parallel shears suggested local relaxation of the surrounding rock mass near the shears. As the advancing niche face progressively reduced the kinematic constraint of the bedding-parallel shears, elastic and possibly plastic deformations along the shears were allowed. Damage ahead of the niche face may have accumulated progressively as the formerly compressed volume of rock was unloaded during the excavation sequence. Stress ratios coincided with the damage inferred from the seismic measurements and hence, provided a good indication of the damage related to spalling failure.

Results from this investigation exemplified the need to consider the rock mass anisotropy in addition to the rock matrix anisotropy if the process of damage is to be understood when both play a role. In the case of the advancing EZ-B Niche face (with EDZ/EdZ extents that ranged from 0.3m to 1.5m), consideration of the bedding-parallel shears and distance from a previously stressed volume of rock were necessary to understand both the state and extent of damage ahead of the niche face. Strength and deformation properties of the bedding-parallel shears mapped in this investigation are unknown and need to be determined in future investigations. Future work also needs to consider a longer tunnel if a better understanding of the influence of the tectonic shears on the EDZ/EdZ ahead of an advancing face is to be gained.

The potential in utilising seismic measurements not only for characterisation but also for understanding the damage processes was also demonstrated in this chapter. In the case of the EZ-B Niche, where field evidence for macro-damage was absent or limited, the seismic data provided a means for identifying smaller-scale damage. Due to the difficulty of drillcore mapping in a rock with well-developed bedding planes, such as the Opalinus Clay at Mont Terri, seismic measurements may also prove to be a useful tool in the identification of induced fractures. In this regard, the optical televiewer is only a powerful tool for identifying sufficiently opened fractures (such as those seen in Chapter 4).

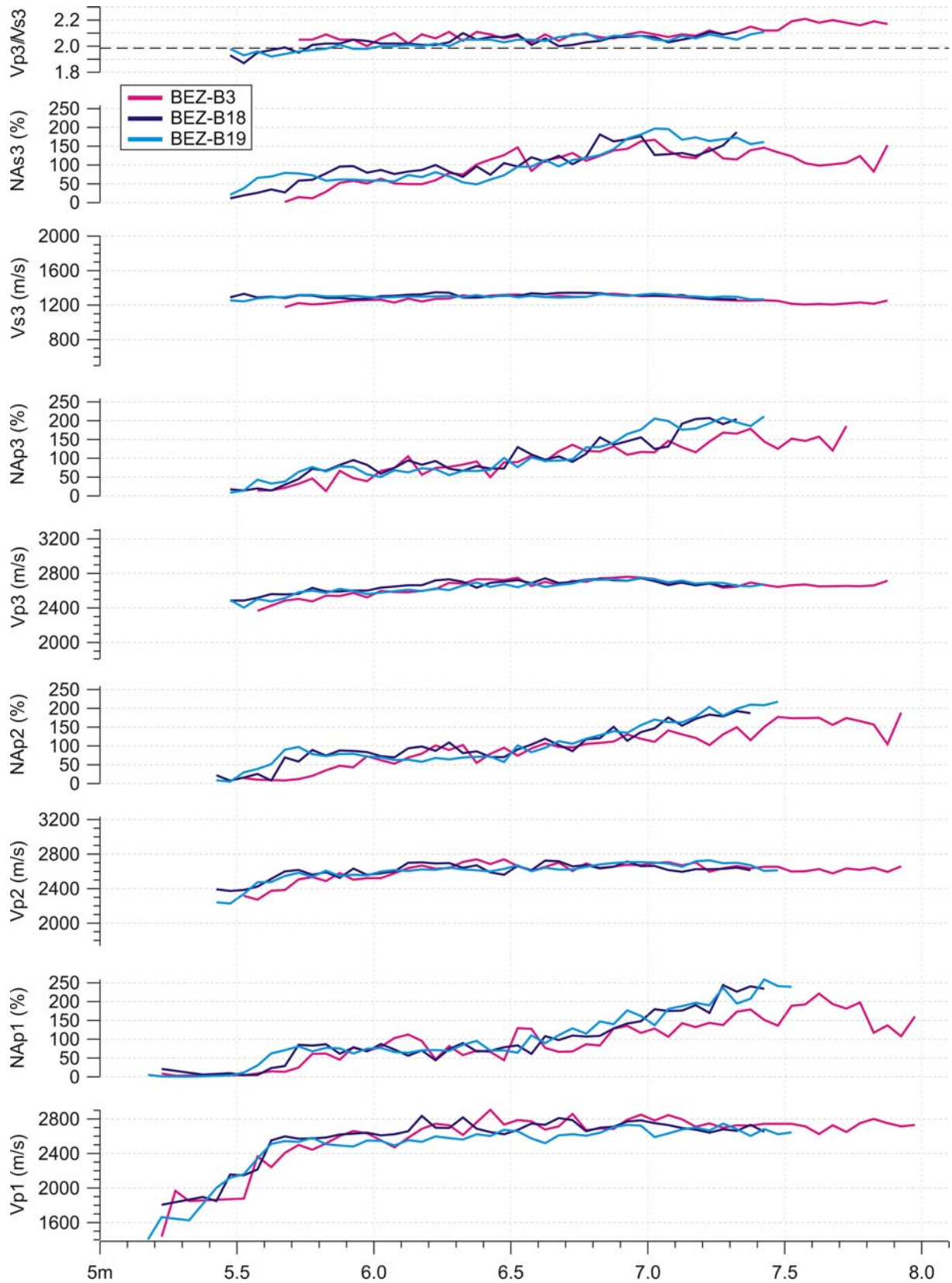


Fig. 5.26: Seismic parameters derived from post-excavation measurements in BEZ-B3, B18, and B19 include: P-wave velocities (V_p) and normalised amplitudes (NAp) for all three channels (1 to 3) and S-wave velocities (V_s) and normalised amplitudes (NAs) for channel 3.

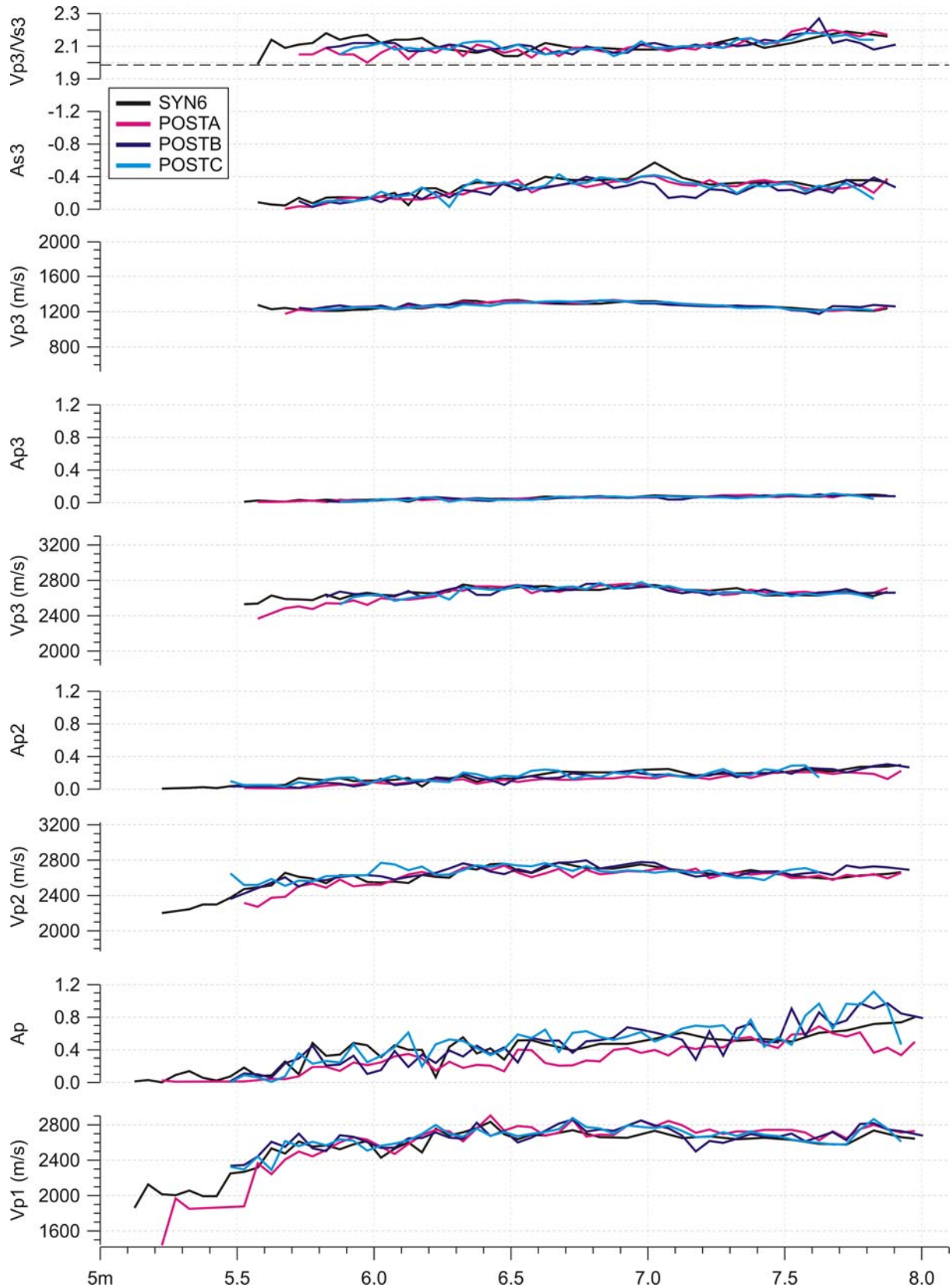


Fig. 5.27: Seismic parameters derived from post-excitation measurements made along the east borehole wall of BEZ-B3 include: P-wave velocities (V_p) and amplitudes (A_p) for all three channels (1 to 3) and S-wave velocities (V_s) and amplitudes (A_s) for channel 3. Profiles corresponding to Syn6 are included as a reference point.

References

- [1] Read R, Martin CD, Dzik EJ. Asymmetric borehole breakouts at the URL. In: Daemen JJK, Schultz RA, editors. Rock Mechanics Proceedings of the 35th U.S. Symposium. Reno: A.A. Balkema; 1995. pp.879-884.
- [2] Martin CD. Seventeenth Canadian geotechnical colloquium: The effect of cohesion loss and stress path on brittle rock strength. Canadian Geotechnical Journal 1997;34:698-725.
- [3] Abel JF, Lee FT. Stress changes ahead of an advancing tunnel. International Journal of Rock Mechanics, Mining Sciences & Geomechanical Abstracts 1973;10:673-697.
- [4] Bieniawski ZT. Mechanism of brittle fracture of rock, parts I, II, and III. International Journal of Rock Mechanics, Mining Sciences & Geomechanical Abstracts 1967;4:395-430.
- [5] Eberhardt E. Numerical modelling of three-dimensional stress rotation ahead of an advancing tunnel face. International Journal of Rock Mechanics & Mining Sciences 2001;38:499-518.
- [6] Armand G, Wileveau Y, Morel J, Cruchaudet M, Rebours H. Excavation damaged zone (EDZ) in the Meute Haute Marne underground research laboratory. In: e Sousa LR, Grossmann CON, editors. 11th Congress of the International Society for Rock Mechanics: The second half century of rock mechanics. Lisbon: Taylor & Francis/Balkema; 2007.
- [7] Mertens J, Bastiaens W, Dehandschutter B. Characterisation of induced discontinuities in the Boom Clay around the underground excavations (URF, Mol, Belgium). Applied Clay Science 2004;26:413-428.
- [8] Thury M, Bossart P. The Mont Terri rock laboratory, a new international research project in a Mesozoic shale formation, in Switzerland. Engineering Geology 1999;52:347-359.
- [9] Bossart P, Meier PM, Moeri A, Trick T, Mayor J-C. Geological and hydraulic characterisation of the excavation disturbed zone in the Opalinus Clay of the Mont Terri Rock Laboratory. Engineering Geology 2002;66:19-38.
- [10] Martin CD, Lanyon GW, Bluemling P, Mayor J-C. The excavation disturbed zone around a test tunnel in the Opalinus Clay. In: Hammah R, Bawden W, Curran J, Telesnicki M, editors. Mining and Tunnelling Innovation and Opportunity. Vol 2. Toronto: University of Toronto Press; 2002. pp.1581-1588.
- [11] Martin CD, Lanyon GW. Excavation Disturbed Zone (EDZ) in clay shale: Mont Terri. Unpublished Mont Terri Technical Report, 2004. 207pp.
- [12] Corkum AG, Martin CD. Modelling a mine-by test at the Mont Terri rock laboratory, Switzerland. International Journal of Rock Mechanics & Mining Sciences 2007;44:846-859.
- [13] Homberg C, Bergerat F, Philippe Y, Lacombe O, Angelier J. Structural inheritance and cenozoic stress fields in the Jura fold-and-thrust belt (France). Tectonophysics 2005;357:137-158.
- [14] Nussbaum C, Bossart P, Burrus F, Badertscher N, Meier O, Nold A. Excavation of Gallery04: general documentation, deformation measurements and geological surveys. Unpublished Mont Terri Technical Note, 2005. 87pp.
- [15] Bath A, Gautschi A. Geological setting and sample locations. In: Pearson FJ, Arcos D, Bath A, Boisson J-Y, Fernandez AM, Gaebler H-E, Gaucher E, Gautschi A, Griffault L, Hernan P, Waber HN, editors. Reports of the Federal Office for Water and Geology, Geology Series. 2003. pp.30-35.
- [16] Bossart P, Wermeille S. The stress field in the Mont Terri region data compilation. In: Heitzmann p, Tripet J-P, editors. Reports of the Federal Office for Water and Geology, Geology Series. 2003. pp.65-92.
- [17] Martin CD, Lanyon GW. Measurement of in-situ stress in weak rocks at Mont Terri Rock Laboratory, Switzerland. International Journal of Rock Mechanics & Mining Sciences 2003;40:1077-1088.

- [18] Nussbaum C, Bossart P, von Ruette J, Meier O, Badertscher N. EZ-B experiment: small-scale mapping of tectonic and artificial (EDZ) fractures of the EZ-B niche. Unpublished Mont Terri Technical Note, 2005. 23pp.
- [19] Gaucher EC, Fernandez AM, Waber HN. Rock and mineral characterisation of the Opalinus Clay Formation. In: Pearson FJ, Arcos D, Bath A, Boisson J-Y, Fernandez AM, Gaebler H-E, Gaucher E, Gautschi A, Griffault L, Hernan P, Waber HN, editors. Reports of the Federal Office for Water and Geology, Geology Series. 2003. pp.281-303.
- [20] Yong S, Loew S, Fidelibus C, Frank E, Lemy F, Schuster K. Induced fracturing in the Opalinus Clay: an integrated field experiment. In: Leung CF, Zhou YX, editors. Rock mechanics in underground construction. Singapore: World Scientific; 2006. CD-Rom 9pp.
- [21] Lemy F, Yong S, Schulz T. Assessment of laser-based displacement mapping in an underground opening. In: Eberhardt E, Stead D, Morrison T, editors. Rock Mechanics Meeting Society's Challenges and Demands. Vol. 1. Vancouver: Taylor & Francis; 2007. pp.85-92.
- [22] Robertson Geologging Limited. Guide to setting up and using DOPTV Digital Optical Tele-viewer, version 2. 2001.
- [23] Schuster K, Alheid H-J, Boeddener D. Seismic investigation of the excavation damaged zone in Opalinus Clay. *Engineering Geology* 2001;61:189-197.
- [24] Schuster K, Alheid H-J. Engineered Barrier (EB) experiment and geophysical characterisation of the excavation disturbed zone (ED-C) experiment: Seismic investigation of the EDZ in the EB niche. Unpublished Mont Terri Technical Report, 2002. 91pp.
- [25] Itasca Consulting Group Inc. Fast Lagrangian Analysis of Continua in 3 Dimensions, version 3.0. 2005.
- [26] Nussbaum C, Bossart P, Burrus F, Badertscher N, Meier O, Nold A. Excavation of Gallery04: general documentation, deformation measurements and geological surveys. Unpublished Mont Terri Technical Note, 2005. 87pp.
- [27] Bock H. RA experiment rock mechanics analyses and synthesis: data report on rock mechanics. Unpublished Mont Terri Technical Report, 2001. 52pp.
- [28] Hoek E. Brittle failure of rock. In: Stagg KG, Zienkiewicz OC, editors. *Rock Mechanics in Engineering Practice*. London: John Wiley & Sons; 1968. pp.99-124.
- [29] Hoek E, Bieniawski ZT. Brittle fracture propagation in rock under compression. *International Journal of Fracture Mechanics* 1965;1:137-155.

Chapter 6

Summary & Recommendations

Safety assessment of geological nuclear waste storage facilities necessitates an understanding of the processes responsible for rock mass disturbance and damage induced by tunnel excavation. Consideration of overconsolidated argillaceous host rocks for repositories such as the Opalinus Clay adds mechanical complexities as these materials are transitional and rarely isotropic. Adding to the complexity at the Mont Terri Rock Laboratory is the frequent occurrence of small-scale tectonic shears.

In this thesis, excavation-induced rock mass perturbations around a short tunnel (EZ-B Niche) were investigated. The objectives were to define the extent of perturbation, to identify the mechanisms responsible for the formation of the perturbed zone, and to identify influential factors.

This final chapter summarises the investigation methods, the interpretation approach, and the major findings. Due to the large volume of data collected and the number of individuals involved, not all the data was utilised and interpreted in this thesis. Here, the focus is on seismic wave amplitudes and velocities and visual observations. With this data, this thesis has addressed issues that have been explored by others and others such as the influence of shears that have not been considered in previous studies.

6.1 Summary of the Field Approach

As the focus of this thesis is the perturbed zone around an underground opening, a perturbed zone first had to be created. This involved the construction of the EZ-B Niche at the Mont Terri Rock Laboratory in Switzerland. To capture the most complete range in the rock mass response, the field campaign was separated into three stages: pre-excavation for the period before the main niche was excavated, syn-excavation for the period during the main niche excavation, and post-excavation for the period after the niche excavation. In the pre-excavation stage, an entrance to the niche was excavated followed by the installation of pore pressure sensors and the drilling of three observation boreholes. The target of the pre-excavation stage was to set benchmarks. The syn-excavation involved the excavation of the niche to its final length in a stepwise manner to allow for field measurements between excavation steps. The niche was only lightly supported due to its favourable orientation with the strike of bedding and a tectonic shear set that occurred sub-parallel with bedding (bedding-parallel shears). In the post-excavation stage, an additional 12 observation boreholes were drilled in three planes: a horizontal plane near the springline and two vertical planes near the middle of the niche. The purpose of this stage was to define the zone of perturbation in three dimensions and to monitor its evolution.

The volume of data collected in this investigation is large and included both borehole and surface measurements. A complete listing of the data collected can be found in Chapter 2. However, not all the data was considered in this thesis. This thesis focuses on geological maps, drillcore maps, optical televiewer images, absolute point displacements, and single-hole seismic wave parameters (velocities and amplitudes).

6.2 Summary of the Interpretation Approach

Gaining a proper understanding of the rock mass response necessitated the integration of the available data. Integration of surface and borehole data in three-dimensional space was also necessary to constrain the geometry of the niche and the boreholes (Appendix A) and the relative location of significant geological structures (Appendix B). The physical definition of the niche perturbation was determined from the integration of all available borehole data.

Numerical modelling was incorporated to identify the processes responsible for the observed perturbation. This required an examination of the changes in the stress state and the influence of relevant geological structures. Numerical modelling in three dimensions was also required as the intersection of the EZ-B Niche with the adjoining Gallery04 is also shared with the intersection of a neighbouring niche. In addition, the axis of the EZ-B Niche is not perpendicular to Gallery04 nor is it parallel with a principal stress axis. As a result, stresses are non-symmetrically redistributed as the niche advanced.

6.3 Summary of Findings

In Chapter 3, rock mass heterogeneity resulting from the inclusion of mapped tectonic shears were shown to play a dominant role in the development of induced fracturing mapped in the entrance of the niche. From geological mapping, induced fractures were found to be normal to the bedding-parallel shears in the west wall and parallel with the wall of the adjoining gallery in the east wall. The distinct difference between the two walls was the location of the sub-horizontal set of tectonic shears. In the east wall, these were located near the gallery while in the west wall, the sub-horizontal shears were found at greater depth. Numerical modelling demonstrated that the bedding-parallel shears in the west wall could displace more than those in the east wall. Mobilisation of the bedding-parallel shears in the west wall caused stress levels in the surrounding rock matrix to exceed both the deviatoric stress and spalling limits. Hence, fracturing between and normal to the bedding-parallel shears was induced. In contrast, mobilisation of the sub-horizontal shears interfered with mobilisation of the bedding-parallel shears in the east wall. As a result, induced fracturing in the east niche wall was related to mobilisation of the sub-horizontal shears. Hence, fracturing was sub-parallel with the gallery wall.

Perturbation of the rock mass surrounding the niche at the end of its excavation was examined in Chapter 4. Borehole data integration indicated that the perturbation zone consisted of two parts: 1) an inner macro-fractured zone coinciding with the lowest seismic wave amplitudes and velocities and 2) an outer zone absent of macro-fracturing but coinciding with increasing seismic wave amplitudes and velocities. The extent of the inner zone averaged 20cm while the outer zone ranged in extent from 0.5m to 0.7m around the niche cross-section and ahead of the face near the sidewalls and about 1m in the centre of the face. Stress redistributions from numerical simulations indicated that the rock mass in the sidewalls and upper west wall of the niche would be the most susceptible to failure in spalling. In these regions, stress levels exceeded the crack initiation threshold and unloaded towards lower stress ratios (i.e. spalling limits defined as ratios between the minimum and maximum principal stresses) in the direction of the niche perimeter. The lowest stress ratios corresponded with the inner macro-fractured zone while stress ratios increased along with seismic wave amplitudes and velocities in the outer zone. This suggested increasing damage (as inferred from the seismic measurements) coincided with decreasing stress ratios and hence, showed that the stress ratios provided a good indication of the damage related to spalling failure.

Damage in the crown, invert, and upper east walls around the niche cross-section were attributed to modes affected by low deviatoric stress and low confinement. In this case, damage may be more readily influenced by the intact rock anisotropy resulting from the thin and pronounced bedding. In the lower portion of the niche, relatively large displacements were measured in a direction roughly perpendicular to bedding suggesting uplift of the invert. Seismic data also indicated the greatest damage in the borehole drilled in the invert.

The rock mass response ahead of the niche face was investigated in Chapter 5 and illustrated the need to consider both the bedding-parallel shears and distance from a previously stressed volume of rock when interpreting the field data. The seismic data showed that at least half the niche was located in the perturbation zone related to the niche entrance excavation. As a result, the EDZ/EdZ extent determined from the seismic measurements in the first three syn-excavation rounds reflected this damage. Bedding-parallel shears mapped in the EZ-B Niche were also found to influence the seismic parameters derived from borehole logging. Tectonic shears provide ready avenues for stress relief when a tunnel is advanced parallel with the strike or (as in the case of the niche) against the dip of these structures. As the advancing niche face progressively reduced the kinematic constraint of the bedding-parallel shears, both elastic and plastic deformations along the shears were allowed. Damage ahead of the niche face most likely accumulated progressively as the formerly compressed volume of rock was unloaded during the subsequent excavation rounds.

6.4 Assessment of Field Methods

Characterisation of the rock mass perturbation surrounding the EZ-B Niche in this thesis primarily involved data derived from field observations and measurements. Successful acquisition and use of the field data for this purpose was not achieved equally. This section provides a brief assessment of the field methods used in this investigation.

Fracture mapping from drillcore is a subjective matter and challenging when dealing with thinly bedded overconsolidated argillaceous rock. Integration of the drillcore maps with digital images acquired from the optical televiewer illustrated these difficulties in interpretation. For example, some open structures identified in the televiewer images were mapped as structures relating to borehole drilling, drillcore extraction, and/or handling. Such discrepancies would suggest the information from the drillcore maps should be considered with caution. The optical televiewer is also not without limitations, as fracture mapping was found to be successful only for fractures with sufficient apertures to be resolved by the instrument. In addition, logging in argillaceous media requires adequate ventilation to minimise the degradation caused by trapped humidity.

The borehole instabilities observed around the EZ-B Niche presented interesting insights to the rock mass response. However, the extent of the instabilities cannot be determined from an optical televiewer.

Acquiring the extent of these instabilities requires an instrument capable of capturing the quantitative changes in the topography of the borehole wall (e.g. acoustic televiewer, caliper).

The seismic measurements carried out in this study illustrated the potential of this method in investigating rock mass damage. However, it is unclear how far the method can be taken regarding field-scale investigations.

Geodetic displacement monitoring in the niche also illustrated the potential of this method. With this method, absolute magnitudes and directions are determined thereby allowing for the exact isolation of problematic locations. However, care must be taken when installing the bolts used for the monitoring targets. In the case of the EZ-B experiment, bolts anchored sub-parallel with bedding were particularly problematic and often required a number of installation attempts.

6.5 Future Work

A large volume of data remains to be processed and the insights gained from this additional information may enhance the interpretation presented in this thesis. In particular, a large amount of seismic data (i.e. cross-hole and tunnel surface) taken from the niche sidewalls and the final face has not yet been processed. A panoramic laser scanner was also utilised for monitoring the displacements of the niche surfaces. The dataset acquired from the laser scanner is also large and much of it has not yet been examined. Most of the analysis to date focuses on the final niche face (see Lemy et al., 2007). Pore pressure data was also not analysed in this thesis as poro-elastic modelling would be required. Spectral gamma logging was also carried out in all the boreholes at the end of the niche excavation but the data acquired has not yet been processed. These measurements should be evaluated and interpreted within the framework proposed in this thesis.

This thesis illustrated a predominant influence of the tectonic shears on excavation perturbation, induced fracturing, and in providing an avenue for preferential stress relieving. Since most of the past material testing at the Mont Terri Rock Laboratory has focused on the matrix anisotropy, little is known regarding material and strength properties of the tectonic shears that have been mapped throughout the research facility. Accounting for the tectonic shears requires both strength (e.g. peak and residual cohesive and frictional components) and stiffness (i.e. normal and shear) properties. The modelling presented in Chapter 3 demonstrated that the tectonic shears needed to be considered when assessing excavation disturbances. The influence of the tectonic shears was also supported by the field observations made ahead of the advancing niche face in Chapter 5. In this case, a longer tunnel would be required to gain a better understanding of the influence of the tectonic shears on the EDZ/EdZ ahead of an advancing face.

A better definition of the in situ rock mass properties in terms of strength and deformation properties is also needed for a proper interpretation of field observations and understanding of the rock mass response. Developing field testing methods for ascertaining rock mass strength and deformation properties may prove to be invaluable in overconsolidated argillaceous media as they are particularly susceptible to sample disturbance. Such tests should include instrumented plate load tests, shear tests, and ideally, large-scale compression tests. Disturbance incurred during drilling and sample extraction may produce irreversible damage that would adversely affect the material and strength properties determined in the laboratory.

Finally, coupled processes (e.g. hydro-mechanical) have not been considered in this thesis, which has been limited to a mechanical treatment of the data. Future work should properly incorporate relevant coupled processes.

Bibliography

- Abel JF, Lee FT. Stress changes ahead of an advancing tunnel. *International Journal of Rock Mechanics, Mining Sciences & Geomechanical Abstracts* 1973;10:673-697.
- Armand G, Wileveau Y, Morel J, Cruchaudet M, Rebours H. Excavation damaged zone (EDZ) in the Meute Haute Marne underground research laboratory. In: e Sousa LR, Grossmann CON, editors. 11th Congress of the International Society for Rock Mechanics: The second half century of rock mechanics. Lisbon: Taylor & Francis/Balkema; 2007.
- Barton NR. A model study of rock-joint deformation. *International Journal of Rock Mechanics & Mining Sciences* 1972;9:579-602.
- Bath A, Gautschi A. Geological setting and sample locations. In: Pearson FJ, Arcos D, Bath A, Boisson J-Y, Fernandez AM, Gaebler H-E, Gaucher E, Gautschi A, Griffault L, Hernan P, Waber HN, editors. Reports of the Federal Office for Water and Geology, Geology Series. 2003. pp.30-35.
- Bieniawski ZT. Mechanism of brittle fracture of rock, parts I, II, and III. *International Journal of Rock Mechanics, Mining Sciences & Geomechanical Abstracts* 1967;4:395-430.
- Bluemling P, Bernier F, Lebon P, Martin CD. The excavation damaged zone in clay formations time-dependent behaviour and influence on performance assessment. *Physics and Chemistry of the Earth* 2007;32:588-599.
- Bock H. RA experiment rock mechanics analyses and synthesis: data report on rock mechanics. Unpublished Mont Terri Technical Report, 2001. 52pp.
- Bossart P, Adler M. Tectonic and artificial fractures. In: Thury M, Bossart P, editors. Mont Terri Rock Laboratory: Results of the Hydrogeological, Geochemical and Geotechnical Experiments Performed in 1996 and 1997. Bern: Swiss National Hydrological and Geological Survey; 1999. pp.19-26.
- Bossart P, Wermeille S. Geological overview. In: Thury M, Bossart P, editors. Mont Terri Rock Laboratory: Results of the Hydrogeological, Geochemical and Geotechnical Experiments Performed in 1996 and 1997. Bern: Swiss National Hydrological and Geological Survey; 1999. pp.5-14.
- Bossart P, Wermeille S. The stress field in the Mont Terri region data compilation. In: Heitzmann p, Tripet J-P, editors. Reports of the Federal Office for Water and Geology, Geology Series. 2003. pp.65-92.
- Bossart P, Trick T, Meier PM, Mayor J-C. Structural and hydrogeological characterisation of the excavation-disturbed zone in the Opalinus Clay (Mont Terri Rock Project, Switzerland). *Applied Clay Science* 2004;26:429-488.
- Bossart P, Meier PM, Moeri A, Trick T, Mayor J-C. Geological and hydraulic characterisation of the excavation disturbed zone in the Opalinus Clay of the Mont Terri Rock Laboratory. *Engineering Geology* 2002;66:19-38.
- Corkum AG, Martin CD. Modelling a mine-by test at the Mont Terri rock laboratory, Switzerland. *International Journal of Rock Mechanics & Mining Sciences* 2007;44:846-859.
- Diederichs MS. Instability of hard rockmasses: the role of tensile damage and relaxation. PhD thesis, University of Waterloo, 1999. 617pp.
- Diederichs MS. Rock fracture and collapse under low confinement conditions. *Rock Mechanics and Rock Engineering* 2003;36:339-381.
- Diederichs MS. The 2003 Canadian geotechnical colloquium: Mechanistic interpretation and practical application of damage and spalling prediction criteria for deep tunnelling. *Canadian Geotechnical Journal* 2007;44:1082-1116.

Bibliography

- Diederichs MS, Kaiser PK, Eberhardt E. Damage initiation and propagation in hard rock during tunnelling and the influence of near-face stress rotation. *International Journal of Rock Mechanics & Mining Sciences* 2004;41:785-812.
- Eberhardt E. Brittle rock fracture and progressive damage in uniaxial compression. PhD thesis, University of Saskatchewan, 1998. 334pp.
- Eberhardt E. Numerical modelling of three-dimensional stress rotation ahead of an advancing tunnel face. *International Journal of Rock Mechanics & Mining Sciences* 2001;38:499-518.
- Eberhardt E, Stead D, Stimpson B, Read RS. Identifying crack initiation and propagation thresholds in brittle rock. *Canadian Geotechnical Journal* 1998;35:222-233.
- Freivogel M, Huggenberger P. Modellierung bilanzierter Profile im Gebiet Mont Terri - La Croix (Kanton Jura). In: Heitzmann p, Tripet J-P, editors. Reports of the Federal Office for Water and Geology, Geology Series. 2003. pp.7-43.
- Ganne P, Vervoort A. Characterisation of tensile damage in rock samples induced by different stress paths. *Pure Applied Geophysics* 2006;163:2153-2170.
- Gaucher EC, Fernandez AM, Waber HN. Rock and mineral characterisation of the Opalinus Clay Formation. In: Pearson FJ, Arcos D, Bath A, Boisson J-Y, Fernandez AM, Gaebler H-E, Gaucher E, Gautschi A, Griffault L, Hernan P, Waber HN, editors. Reports of the Federal Office for Water and Geology, Geology Series. 2003. pp.281-303.
- Haimson B. Micromechanisms of borehole instability leading to breakouts in rocks. *International Journal of Rock Mechanics & Mining Sciences* 2007;44:157-173.
- Hoek E. Brittle failure of rock. In: Stagg KG, Zienkiewicz OC, editors. *Rock Mechanics in Engineering Practice*. London: John Wiley & Sons; 1968. pp.99-124.
- Hoek E, Bieniawski ZT. Brittle fracture propagation in rock under compression. *International Journal of Fracture Mechanics* 1965;1:137-155.
- Hoek E, Carranza-Torres C, Corkum B. Hoek-Brown failure criterion - 2002 edition. In: Hammah r, Bawden W, Curran J, Telesnicki M, editors. *Mining and Tunnelling Innovation and Opportunity*. Vol 1. Toronto: University of Toronto Press; 2002. pp.267-273.
- Homberg C, Bergerat F, Philippe Y, Lacombe O, Angelier J. Structural inheritance and cenozoic stress fields in the Jura fold-and-thrust belt (France). *Tectonophysics* 2005;357:137-158.
- Itasca Consulting Group Inc. 3 Dimensional Distinct Element Code, version 3.0. Itasca Consulting Group Inc. 2003.
- Itasca Consulting Group Inc. Fast Lagrangian Analysis of Continua in 3 Dimensions, version 3.0. Itasca Consulting Group Inc. 2005.
- Jaeger JC. Shear failure of anisotropic rocks. *Geological Magazine* 1960;97:65-72.
- Kaiser PK, Yazici S, Maloney S. Mining-induced stress change and consequences of stress path on excavation stability - a case study. *International Journal of Rock Mechanics & Mining Sciences* 2001;38:167-180.
- Kaiser PK, Diederichs MS, Martin CD, Sharp J, Steiner W. Underground works in hard rock tunnelling and mining. In: *GeoEng2000 An International Conference on Geotechnical & Geological Engineering*. Vol 1. Melbourne: Technomic Publishing Company; 2000. pp.841-926.
- Klose CD, Loew S, Giese R, Borm G. Spatial predictions of geological rock mass properties based on in-situ interpretations of multi-dimensional seismic data. *Engineering Geology* 2007;93:99-116.
- Lemy F, Yong S, and Schulz T. A case study of monitoring tunnel wall displacement using laser scanning technology. In: Culshaw M, Reeves H, Spink T, Jefferson I, editors. *IAEG 2006 engineering geology*

Bibliography

- for tomorrow's cities. Nottingham: Geological Society of London;2006. Paper 482, CD.
- Lemy F, Yong S, Schulz T. Assessment of laser-based displacement mapping in an underground opening. In: Eberhardt E, Stead D, Morrison T, editors. *Rock Mechanics Meeting Society's Challenges and Demands*. Vol. 1. Vancouver: Taylor & Francis; 2007. pp.85-92.
- Leucci G, De Giorgi L. Experimental studies on the effects of fracture on the P and S wave velocity propagation in sedimentary rock ("Calcarene del Salento"). *Engineering Geology* 2006;84:130-142.
- Marinos P, Hoek E. GSI: a geologically friendly tool for rock mass strength estimation. In: *Proceedings of GeoEng 2000*, Melbourne, 2000. 19pp.
- Martin CD. The strength of massive Lac du Bonnet Granite around underground openings. PhD thesis, University of Manitoba, 1993. 300pp.
- Martin CD. Seventeenth Canadian geotechnical colloquium: The effect of cohesion loss and stress path on brittle rock strength. *Canadian Geotechnical Journal* 1997;34:698-725.
- Martin CD, Lanyon GW. Measurement of in-situ stress in weak rocks at Mont Terri Rock Laboratory, Switzerland. *International Journal of Rock Mechanics & Mining Sciences* 2003;40:1077-1088.
- Martin CD, Lanyon GW. Excavation Disturbed Zone (EDZ) in clay shale: Mont Terri. Unpublished Mont Terri Technical Report, 2004. 207pp.
- Martin CD, Lanyon GW, Bluemling P, Mayor J-C. The excavation disturbed zone around a test tunnel in the Opalinus Clay. In: Hammah R, Bawden W, Curran J, Telesnicki M, editors. *Mining and Tunnelling Innovation and Opportunity*. Vol 2. Toronto: University of Toronto Press; 2002. pp.1581-1588.
- Matry JM, Savoye S, Cabrera J. Desaturation and structure relationships around drifts excavated in the well-compacted Tournemire's argillite (Aveyron, France). *Engineering Geology* 2007;90:1-16.
- Mazurek M, Elie M, Hurford A, Leu W, Gautschi A. Burial history of Opalinus Clay. In: *Clays in Natural and Engineered Barriers for Radioactive Waste Confinement*. 2002. pp.101-102.
- McLamore R, Gray KE. The mechanical behavior of anisotropic sedimentary rocks. *Journal of Engineering for Industry* 1967;89:62-73.
- Meglis IL, Chow T, Martin CD, Young RP. Assessing in situ microcrack damage using ultrasonic velocity tomography. *International Journal of Rock Mechanics & Mining Sciences* 2005;42:25-34.
- Mertens J, Bastiaens W, Dehandschutter B. Characterisation of induced discontinuities in the Boom Clay around the underground excavations (URF, Mol, Belgium). *Applied Clay Science* 2004;26:413-428.
- Naumann M, Hunsche U, Schulze O. Experimental investigations on anisotropy in dilatancy, failure and creep of Opalinus Clay. *Physics and Chemistry of the Earth* 2007;32:889-895.
- Nussbaum C, Meier O, Badertscher N, Bossart P. Drilling campaigns of Phase 10 drilling and field mapping of drillcores including photo documentation. Unpublished Mont Terri Technical Note, 2005. 22pp.
- Nussbaum C, Bossart P, Zingg A, Inderbitzin L, Steiger H. Géométrie et cinématique d'une zone de chevauchement („Main Fault“) recoupant les Argiles à Opalinus dans le laboratoire souterrain du Mont Terri. Unpublished Mont Terri Technical Report, 2001. 28pp.
- Nussbaum C, Bossart P, Burrus F, Jeannin PY, Graf A. Survey and documentation of the Start Niche excavation. Unpublished Mont Terri Technical Note, 2004. 26pp.
- Nussbaum C, Bossart P, von Ruetze J, Meier O, Badertscher N. EZ-B experiment: small-scale mapping of tectonic and artificial (EDZ) fractures of the EZ-B niche. Unpublished Mont Terri Technical Note, 2005. 23pp.

Bibliography

- Nussbaum C, Wileveau Y, Bossart P, Moeri A, Armand G. Why are the geometries of the EDZ fracture networks different in the Mont Terri and Meuse/Haute-Marne rock laboratories? Structural approach. In: Clays in Natural & Engineered Barriers for Radioactive Waste Confinement, Abstracts. 2007. pp.151-152.
- Nussbaum C, Bossart P, Mayoraz J, Niederhauser B, Steiger H, Zingg A. Engineered barrier experiment structural mapping of artificial fractures and tectonic features of the EB niche. Unpublished Mont Terri Technical Note, 2002. 12pp.
- Nussbaum C, Bossart P, Burrus F, Badertscher N, Meier O, Nold A. Excavation of Gallery04: general documentation, deformation measurements and geological surveys. Unpublished Mont Terri Technical Note, 2005. 87pp.
- Okland D, Cook JM. Bedding-related borehole instability in high-angle wells. In: Holt R, editor. Proceedings of the SPE/ISRM Rock Mechanics in Petroleum Industry (Eurock98). Vol 1. Trondheim; 1998. pp.413-422.
- Popp T, Salzer, K. Anisotropy of seismic and mechanical properties of Opalinus Clay during triaxial deformation in a multi-anvil apparatus. Physics and Chemistry of the Earth 2007;32:879-888.
- Read R, Martin CD, Dzik EJ. Asymmetric borehole breakouts at the URL. In: Daemen JJK, Schultz RA, editors. Rock Mechanics Proceedings of the 35th U.S. Symposium. Reno: A.A. Balkema; 1995. pp.879-884.
- Read RS, Chandler NA, Dzik EJ. In situ strength criteria for tunnel design in highly-stressed rock masses. International Journal of Rock Mechanics & Mining Sciences 1998;35:261-278.
- Rejeb A, Ben Slimane K, Cabrera JM, Matry JM, Savoye S. Excavation damaged zones in the argillaceous Tournemire site: Characterisation and failure mechanisms. In: Clays in Natural & Engineered Barriers for Radioactive Waste Confinement, Abstracts. 2007. pp.533-534.
- Robertson Geologging Limited. Guide to setting up and using DOPTV Digital Optical Tele-viewer, version 2. 2001.
- Rocscience Inc. Phase2 version 6.0 - finite element analysis for excavations and slopes. www.rocscience.com 2005.
- Schubnel A, Benson PM, Thompson BD, Hazzard JF, Young RP. Quantifying damage, saturation and anisotropy in cracked rocks by inverting elastic wave velocities. Pure and Applied Geophysics 2006;163:947-973.
- Schulz T, Lemy F, Yong S. Laser scanning technology for rock engineering applications. In: Proceedings of the 7th Conference on Optical 3-D Measurement Techniques. Vienna;2005.
- Schuster K, Alheid H-J. Results gained from seismic in-situ measurements in the Opalinus Clay at the Mont Terri rock laboratory. In: Clays in Natural & Engineered Barriers for Radioactive Waste Confinement, Abstracts. 2007. pp.137-138.
- Schuster K, Alheid H-J, Boeddener D. Seismic investigation of the excavation damaged zone in Opalinus Clay. Engineering Geology 2001;61:189-197.
- Thury M, Bossart P. The Mont Terri rock laboratory, a new international research project in a Mesozoic shale formation, in Switzerland. Engineering Geology 1999;52:347-359.
- Tien YM, Kuo MC, Juang CH. An experimental investigation of the failure mechanism of simulated transversely isotropic rocks. International Journal of Rock Mechanics & Mining Sciences 2006;43:1163-1181.
- Tsang C-F, Bernier F, Davies C. Geohydromechanical processes in the Excavation Damaged Zone in crystalline rock, rock salt, and indurated and plastic clays-in the context of radioactive waste disposal. International Journal of Rock Mechanics & Mining Sciences 2005;42:109-125.

Bibliography

- Ustaszewski K, Schmid SM. Control of preexisting faults on geometry and kinematics in the northernmost part of the Jura fold-and-thrust belt. *Tectonics* 2006;25. 26pp.
- Wermeille S, Bossart P. Paleohydrological study on the surroundings of the Mont Terri Rock Laboratory. Unpublished Mont Terri Technical Report, 1999. 22pp.
- Yong S, Loew S, Fidelibus C, Frank E, Lemy F, Schuster K. Induced fracturing in the Opalinus Clay: an integrated field experiment. In: Leung CF, Zhou YX, editors. *Rock mechanics in underground construction*. Singapore: World Scientific; 2006. CD-Rom. 9pp.
- Zhang C-L, Rothfuchs T. Damage and sealing of clay rocks detected by permeability measurements. In: *Proceedings of the 3rd International Clay Meeting*. Lille; in press.

Appendix A

Constraining the Geometry

A.1 Niche Surfaces

A panoramic laser scanner was used primarily for assessing its potential in monitoring surface displacements (see Lemy et al., 2006 in the Bibliography). However, data from the laser scanner also provided valuable geometrical information. As a result, the various surfaces of the EZ-B Niche in this thesis were defined with the laser scanner data in a three-step procedure. The scanner decomposes the surface into a number of points (such as the point clouds in Fig. A1) and acquires the x-, y-, z-coordinates of each point. The Swiss Projection System was chosen as the reference coordinate system in this thesis.

Since the volume of data acquired by the scanner is large, the first step is a reduction of the point cloud by isolating the surface of interest (Fig. A2). For clarity, only the floor and the faces of the niche were defined. The second step involved delineating the outline of each surface. This was a manual process, which required rotating the point cloud several times to ensure the outlines were properly selected (left figure of Fig. A2). The last step involved a random sampling of the points in the isolated point cloud (right figure of Fig. A2). The sampling was carried out using Matlab via a reduction factor. The reduction factor used in this thesis is 0.001, which represents 1% of the number of points isolated in the first step.

A.2 Boreholes and Roof Anchors

The boreholes were located based on information from surveyors, the drilling logs, and various borehole logging campaigns. The collars were located according to the coordinates provided by the surveyors. The terminus of each borehole was projected based on the lengths and inclinations indicated in the drilling logs and cross-checked with logging lengths from the various borehole measurements (e.g. seismic, televiwer, and spectral gamma). The inclinations were also cross-checked with a 1-2m long level.

The changing collar position of BEZ-B3 (the borehole drilled near the centre of the face) was determined from the point clouds.

The 24 roof anchors installed in the EZ-B Niche were also located according to their scanned positions in the point clouds. The embedded end of each anchor was projected from its scanned protrusion.

A.3 Integration

The individual elements of the niche construction was then assembled and integrated in GOCAD (Fig. A3). This then established the working platform for analysis of geometrical relationships.

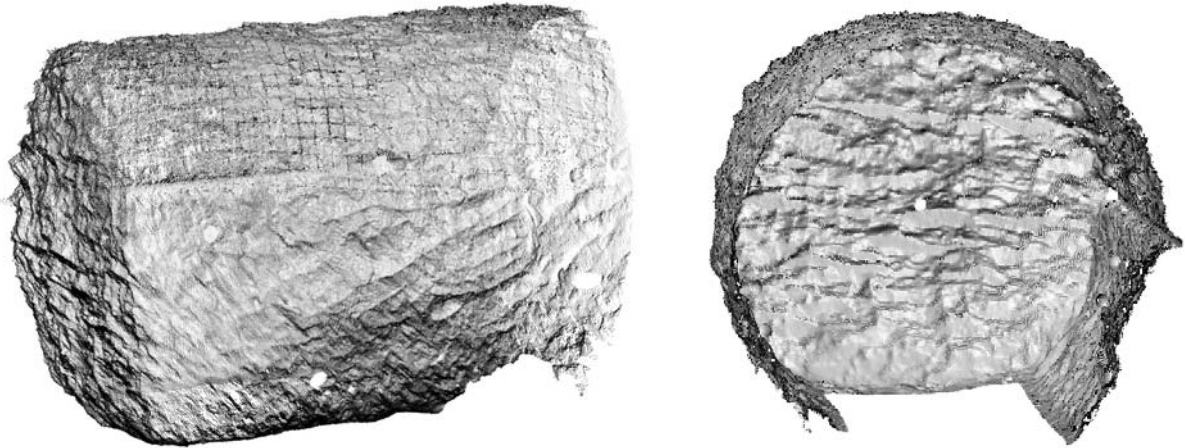


Fig. A1: Point clouds of the EZ-B Niche acquired from the laser scanner at the end of the niche construction. A view from inside the rock mass is shown in the left and a view looking at the final niche face is shown in the right.

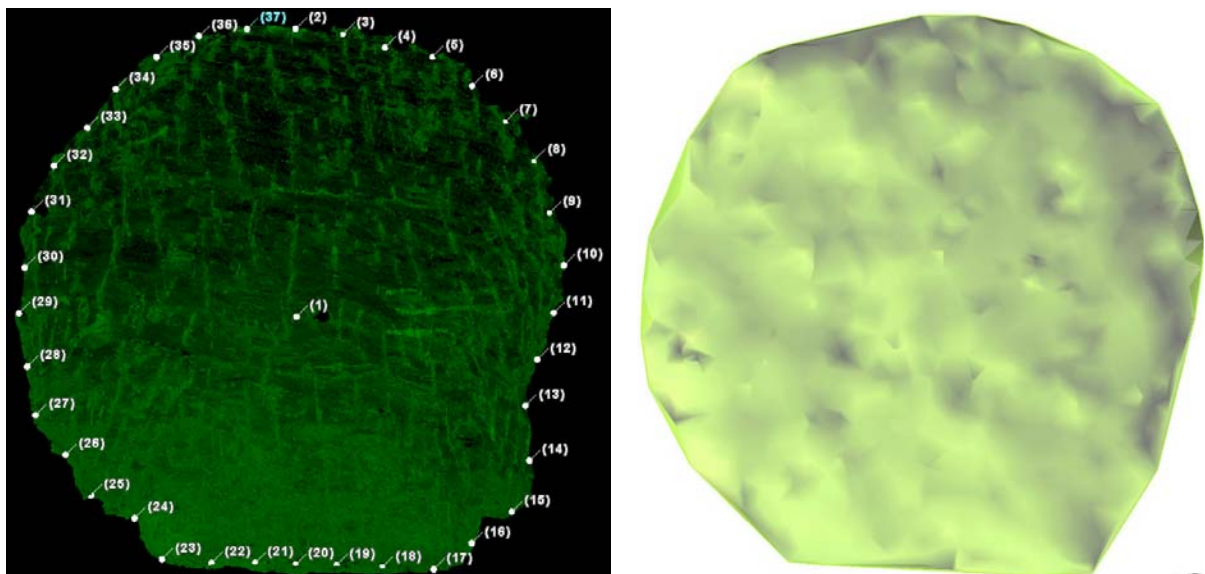


Fig. A2: Isolation of the niche face from the first syn-excavation step. The laser scanner point cloud is shown in the left and the corresponding sampled surface rendering is shown in the right.

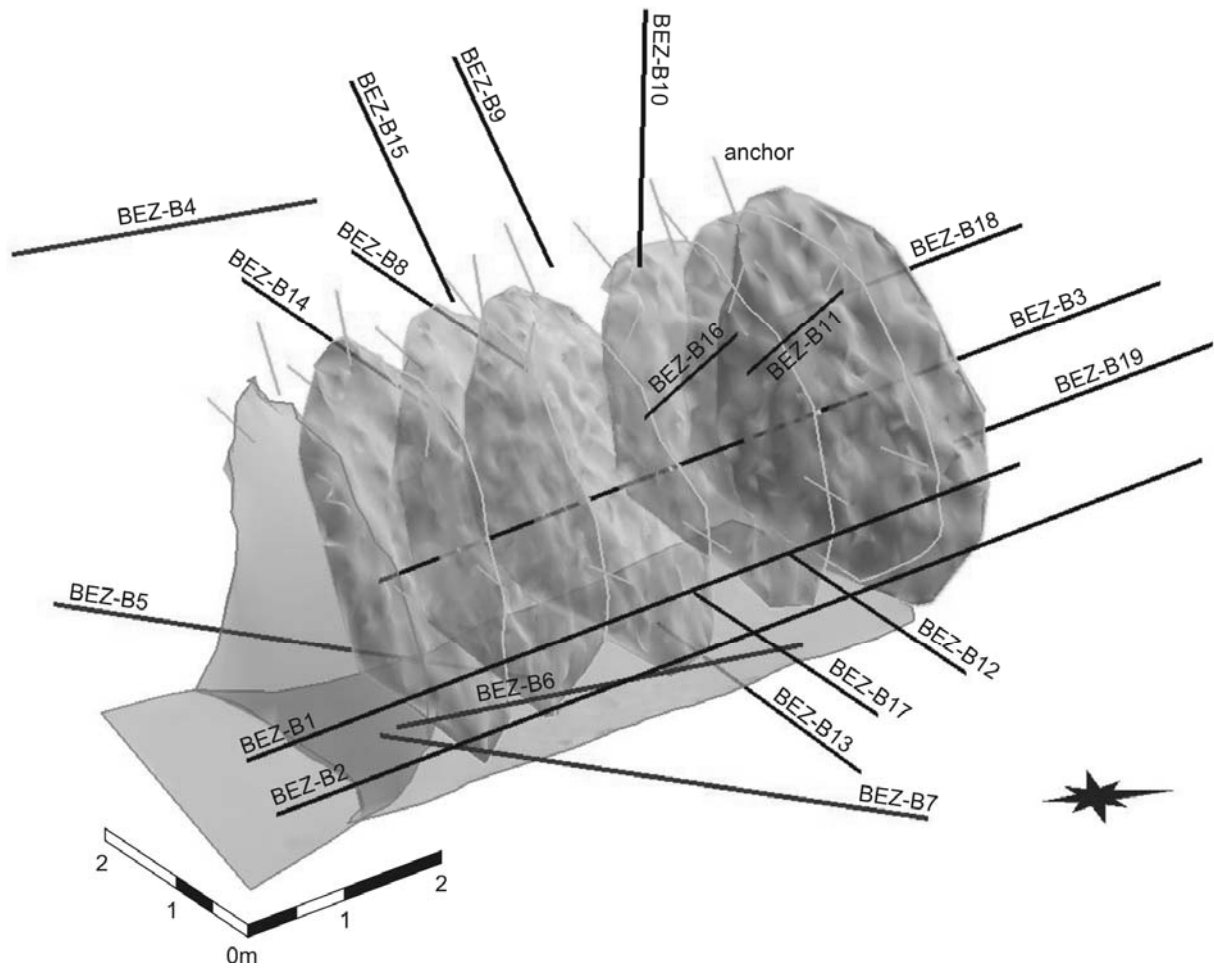


Fig. A3: The integrated geometrical relationships between the different elements of the EZ-B Niche construction.

Appendix B

Locating Tectonic Shears

B.1 Geological Maps

The tectonic shears mapped in the EZ-B Niche belonged to two sets. The most prominent set dips sub-parallel with the bedding towards SSE (foliation shears). The second set is sub-horizontal (dipping S-SW) and has been mapped in isolation. Maps of the EZ-B Niche provided by the site geologists are shown in Fig. B1 for the west niche wall, Fig. B2 for the east niche wall, Fig. B3 for the faces and invert, and Fig. B4 for the roof.

B.2 Laser Scanner

To incorporate the tectonic shears in the GOCAD model, the laser scanner was used to locate the mapped tectonic shears. With the geological maps as guidance, points along the faults were picked in the laser scanner point clouds.

B.3 Integration into the GOCAD model

Points representing the tectonic shears were then reduced to one plane via a least squares method. These planes were then integrated into the GOCAD model and cross-checked with the tectonic shear planes mapped in the drillcore (Figures B6 and B7). All the mapped drillcore structures were also integrated into the GOCAD model (see Chapter 4).

Geological and structural mapping of the EZ-B niche: left-hand (WSW) side wall

Mapping by Geotechnical Institute Ltd, St-Ursanne (C. Nussbaum & P. Bossart) - March 2005 -

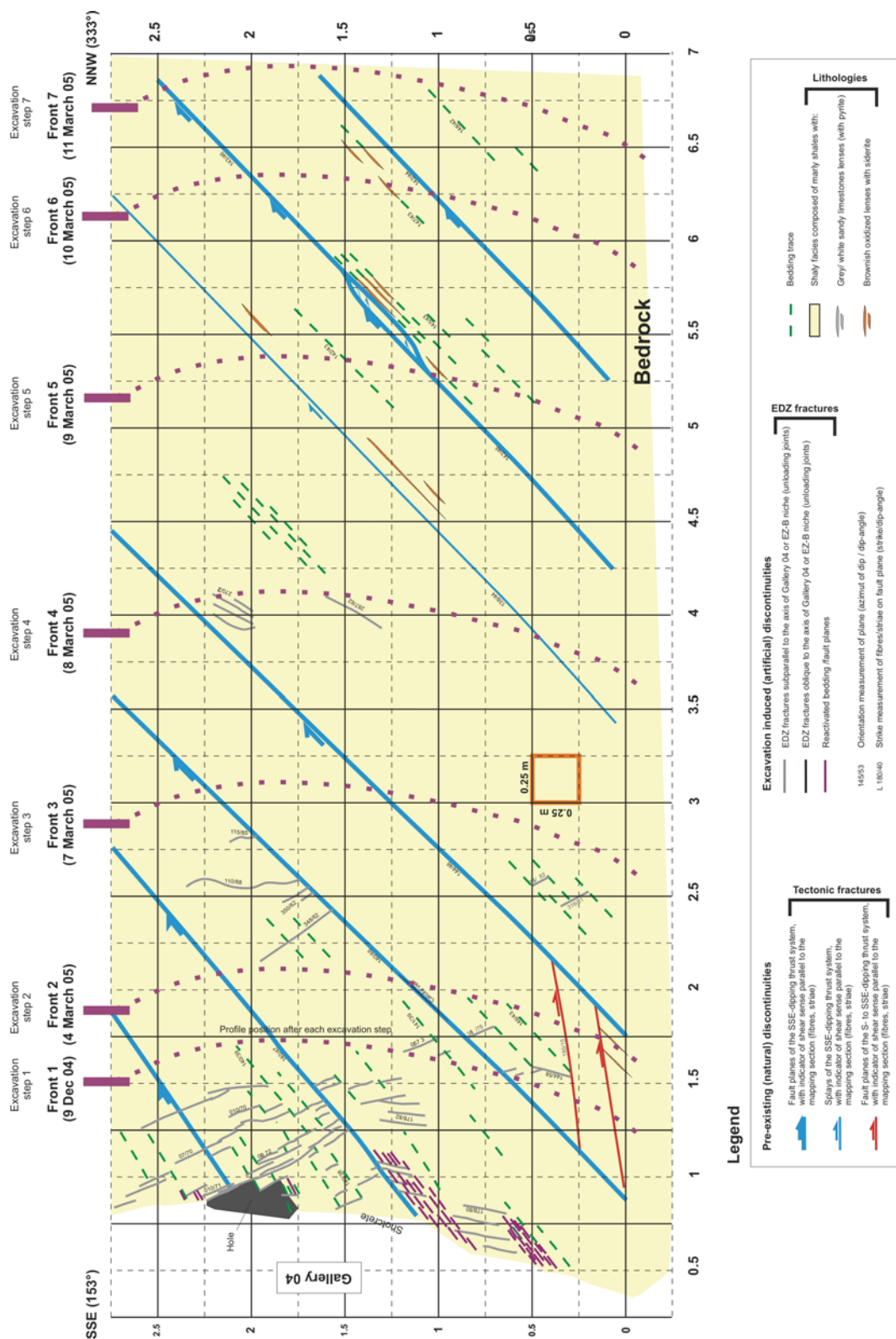


Fig. B1: Geological map of the west niche wall (after Nussbaum et al., 2006).

Geological and structural mapping of the EZ-B niche: right-hand (ENE) side wall

Mapping by Geotechnical Institute Ltd, St-Ursanne (C. Nussbaum & P. Bossart) - March 2005 -

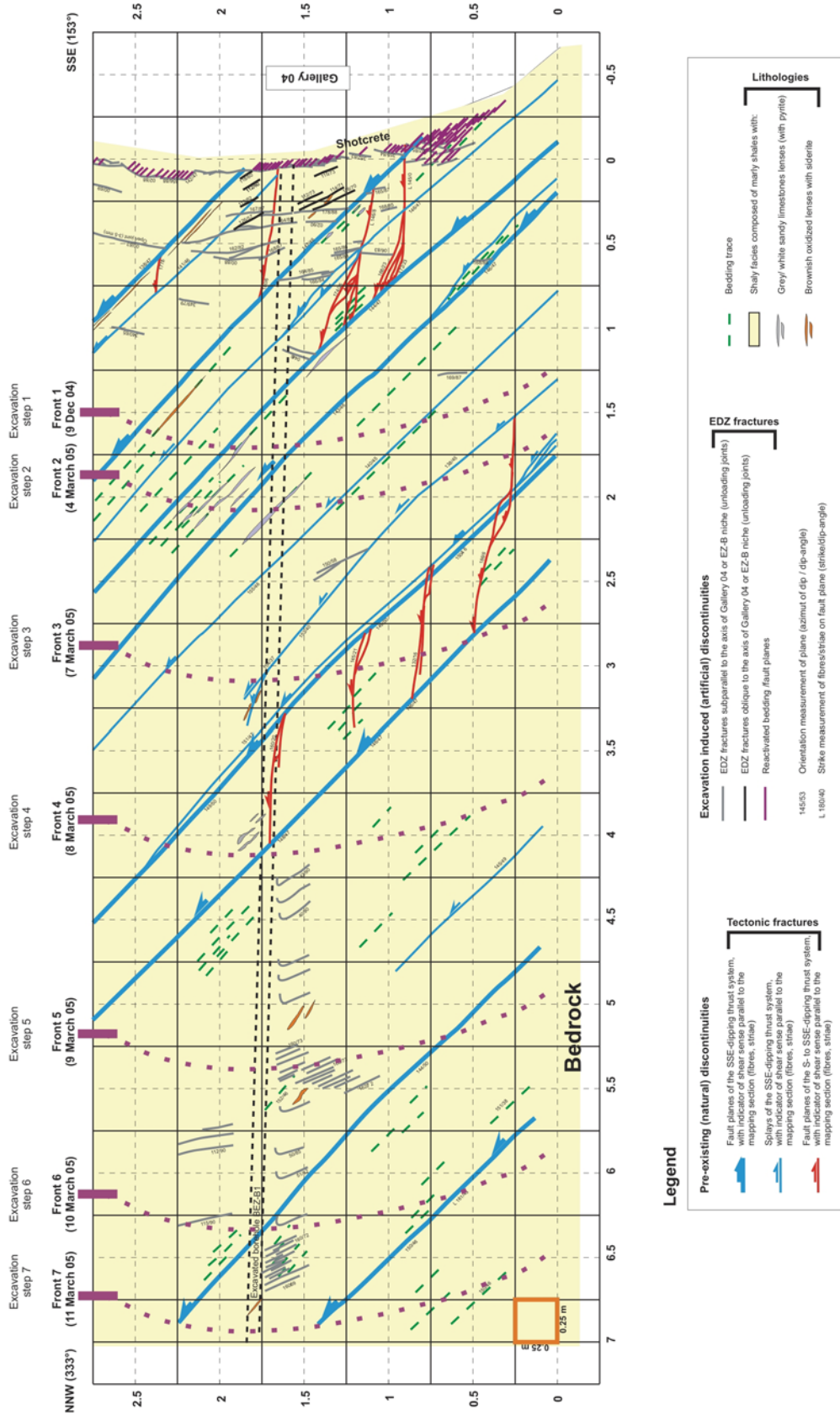


Fig. B2: Geological map of the east niche wall (after Nussbaum et al., 2006).

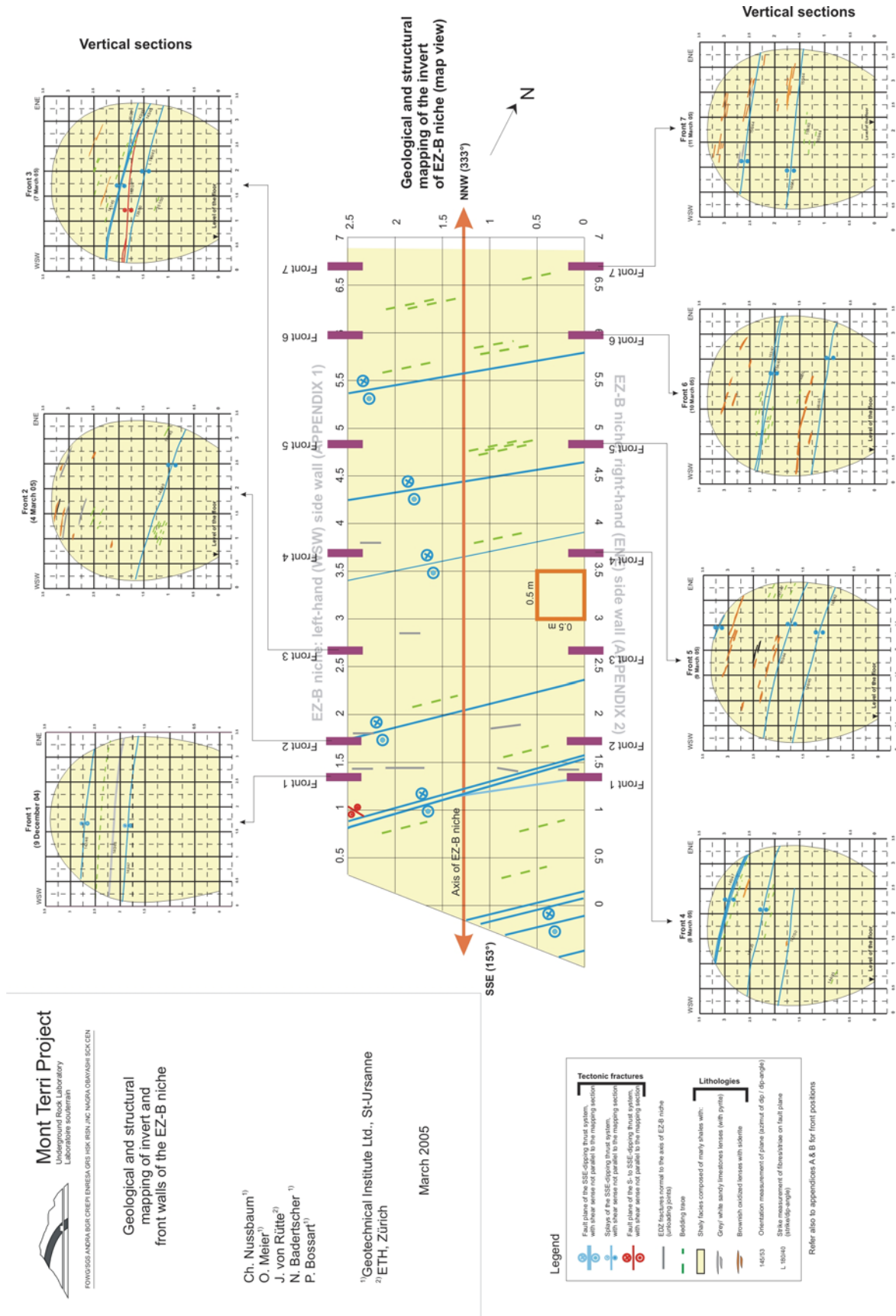


Fig. B3: Geological maps of the niche faces and invert (after Nussbaum et al., 2006).

Geological and structural mapping of the ceiling of the EZ-B niche

Mapping by Geotechnical Institute Ltd, St-Ursanne (C. Nussbaum & P. Bossart) - May 2005 -

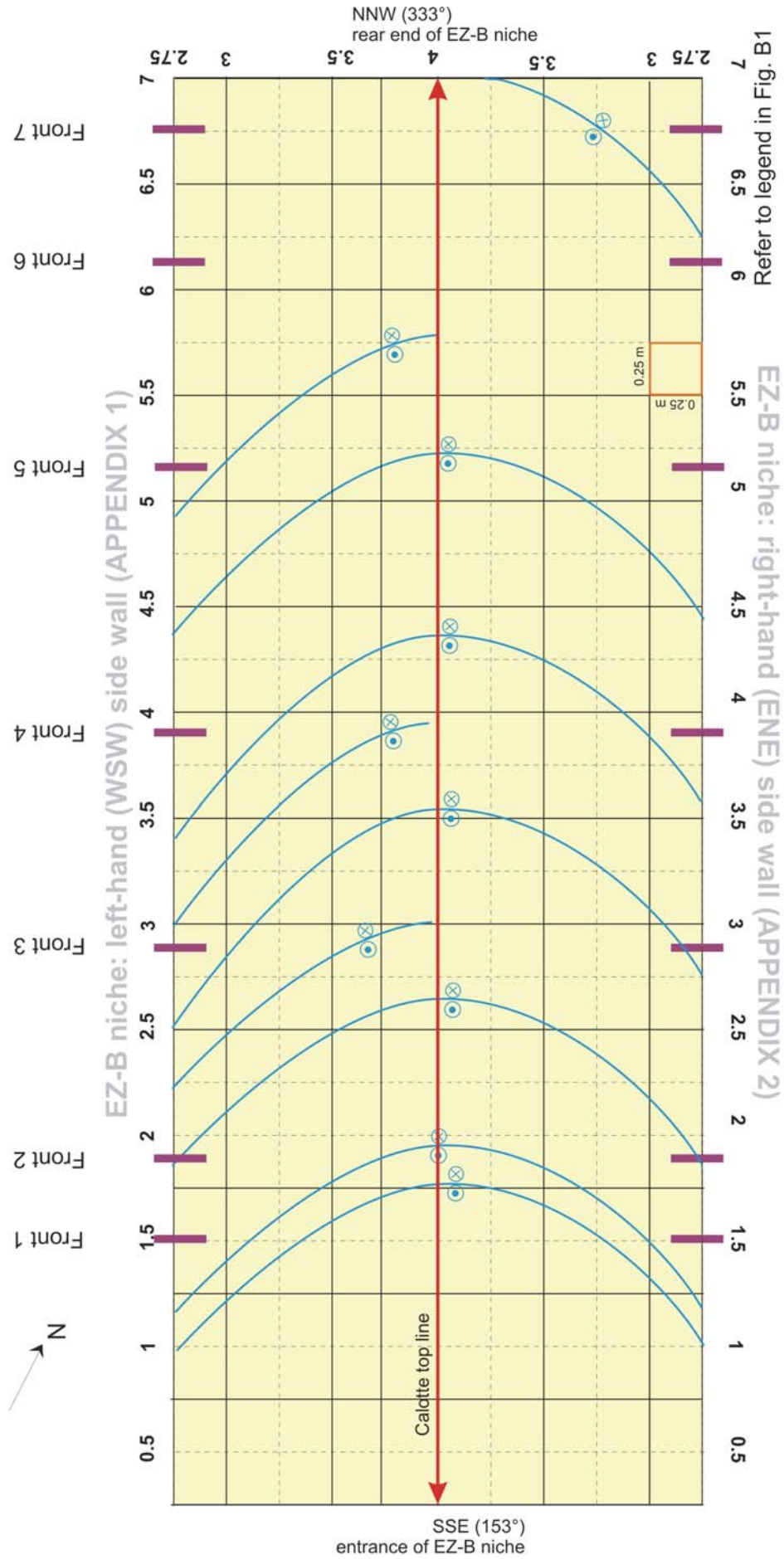


Fig. B4: Geological map of the niche roof (after Nussbaum et al., 2006).

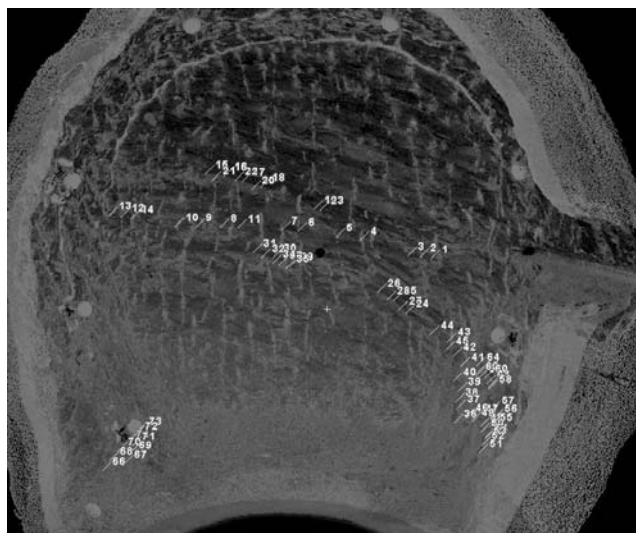
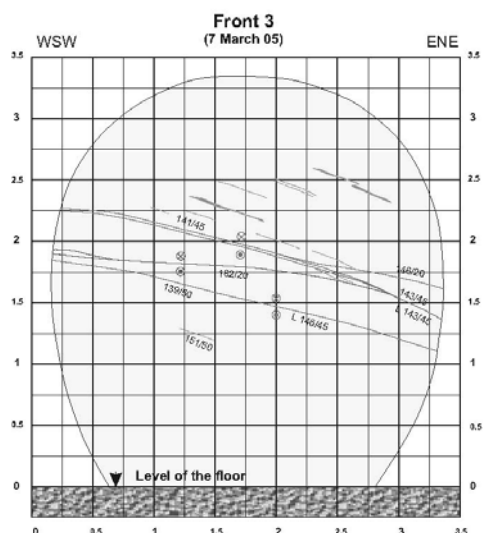


Fig. B5: Location of tectonic shears F9, F10, and F10A in the laser scanner point cloud (right) with the geological maps (left) as guidance.

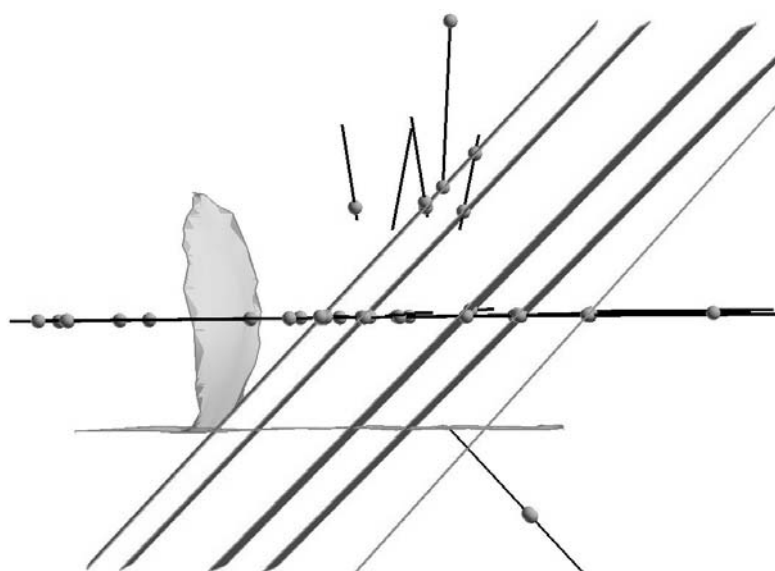


Fig. B6: Comparison of the bedding-parallel shears with the locations of shear planes (spheres) mapped in the strike of the bedding-parallel shears.

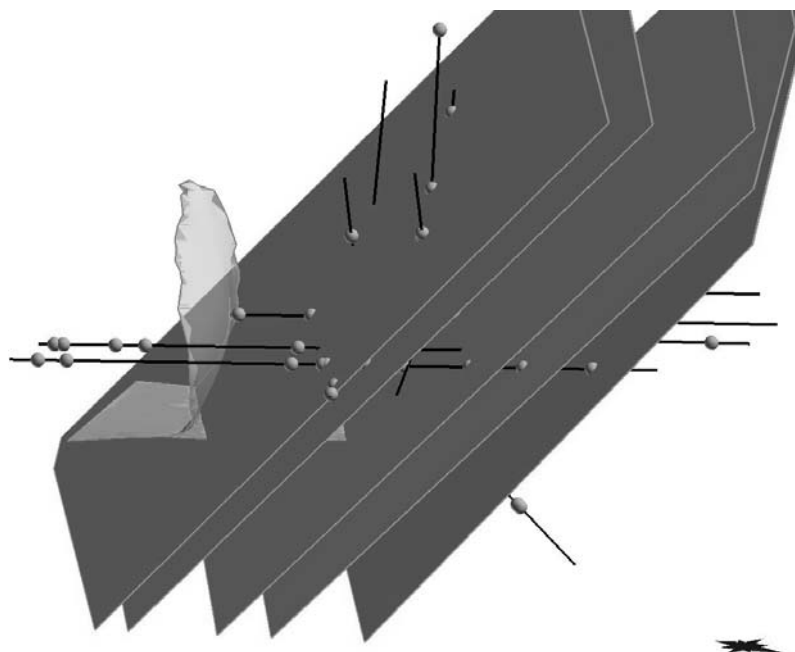


Fig. B7: Comparison of the bedding-parallel shears with the locations of shear planes (spheres) mapped in the drillcore. Viewed isometrically from the top and the northeast.

Appendix C Drillcore Maps

A total of 19 boreholes were drilled in the EZ-B Experiment (Fig. C1). Pore pressure sensors were installed in four (BEZ-B4 to B7), which were 20mm-diameter in diameter and drilled destructively. The remaining boreholes (BEZ-B1 to B3 and B8 to B19) were 100mm in diameter and used for data collection (see Chapter 2 or Yong et al., 2006). The larger observation boreholes were drilled with either a double-core or triple-core barrel. Each drillcore was mapped by geologists on extraction from the drill stem and the digitised maps are shown in the figures below.

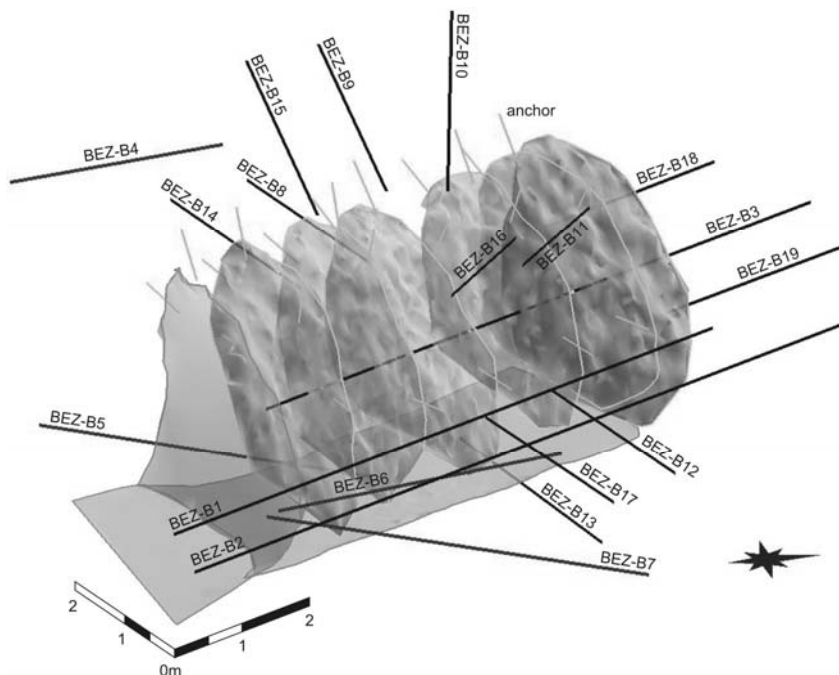


Fig. C1: Layout of the boreholes drilled in the EZ-B Experiment.

Appendix C: Drillcore Maps

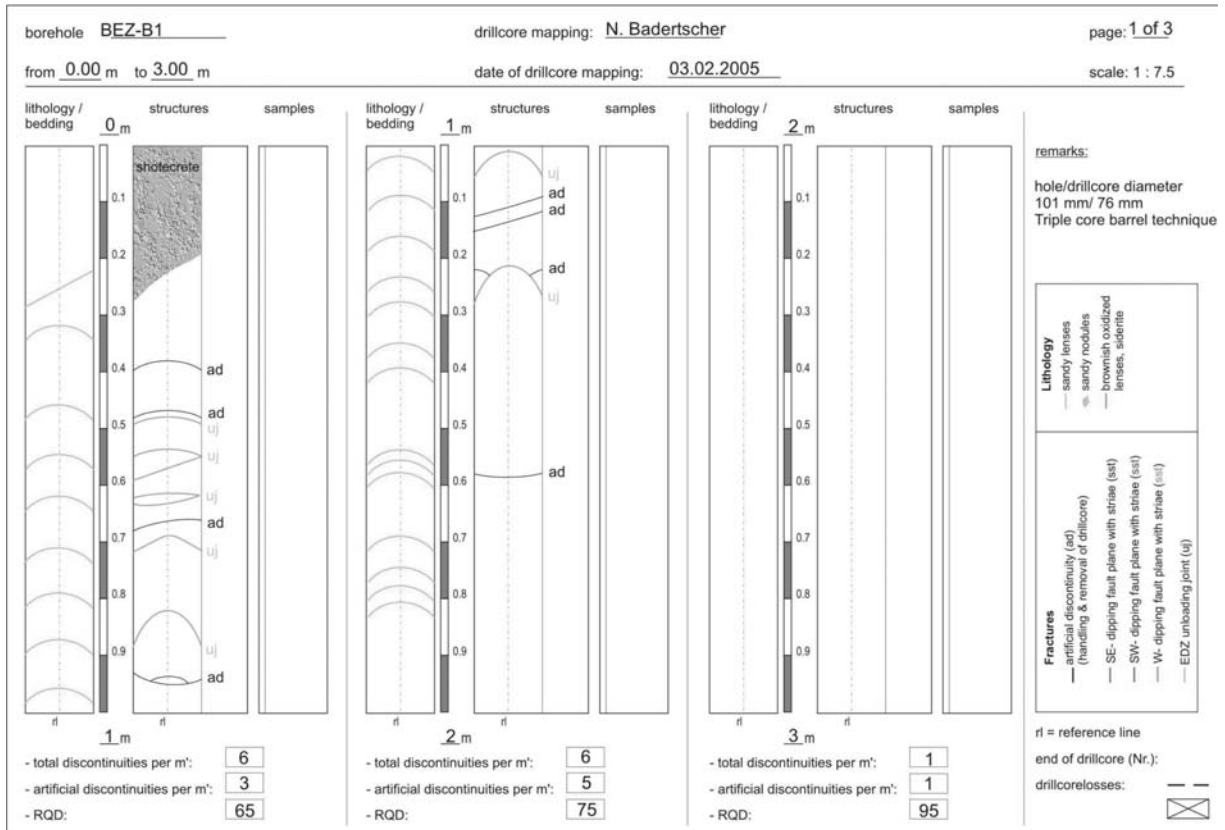


Fig. C2a: Drillcore map of BEZ-B1 (Nussbaum et al., 2005). Refer to Fig. C1 for borehole location.

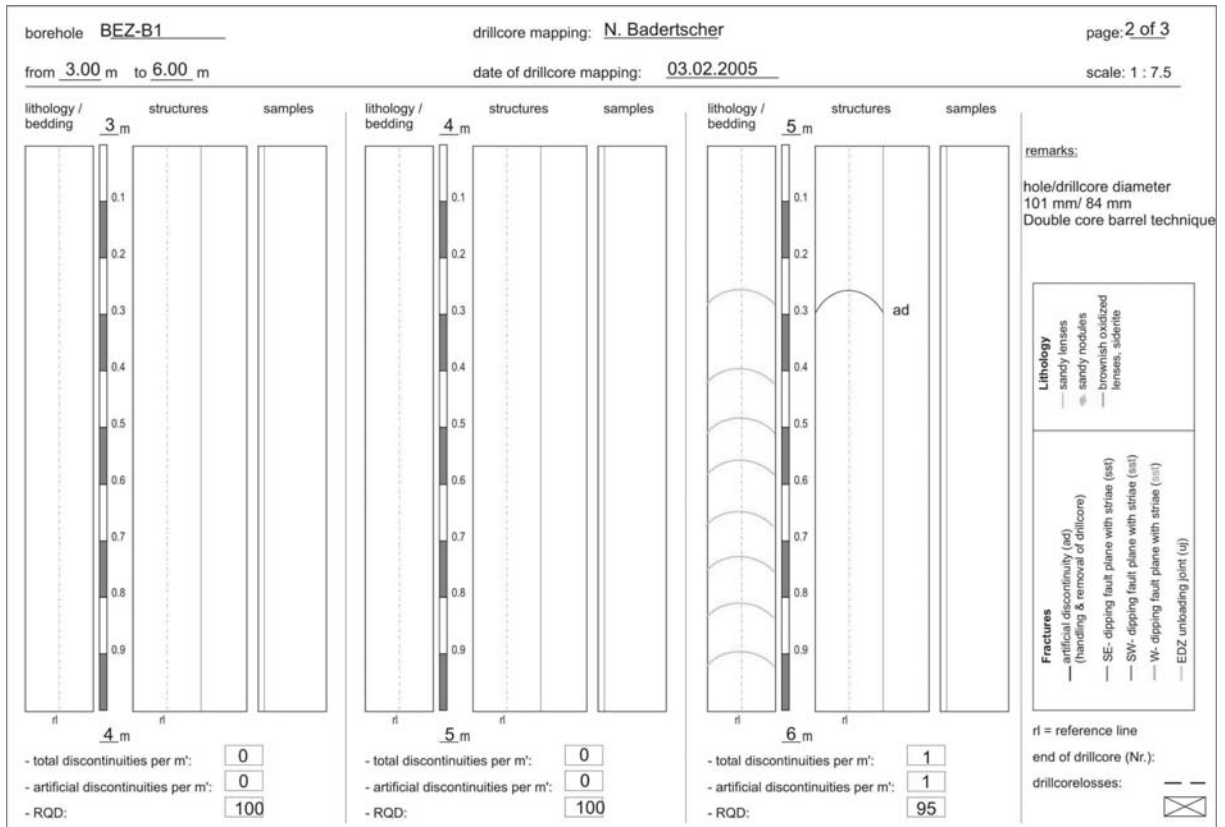


Fig. C2b: Continuation of BEZ-B1 drillcore map (Nussbaum et al., 2005).

Appendix C: Drillcore Maps

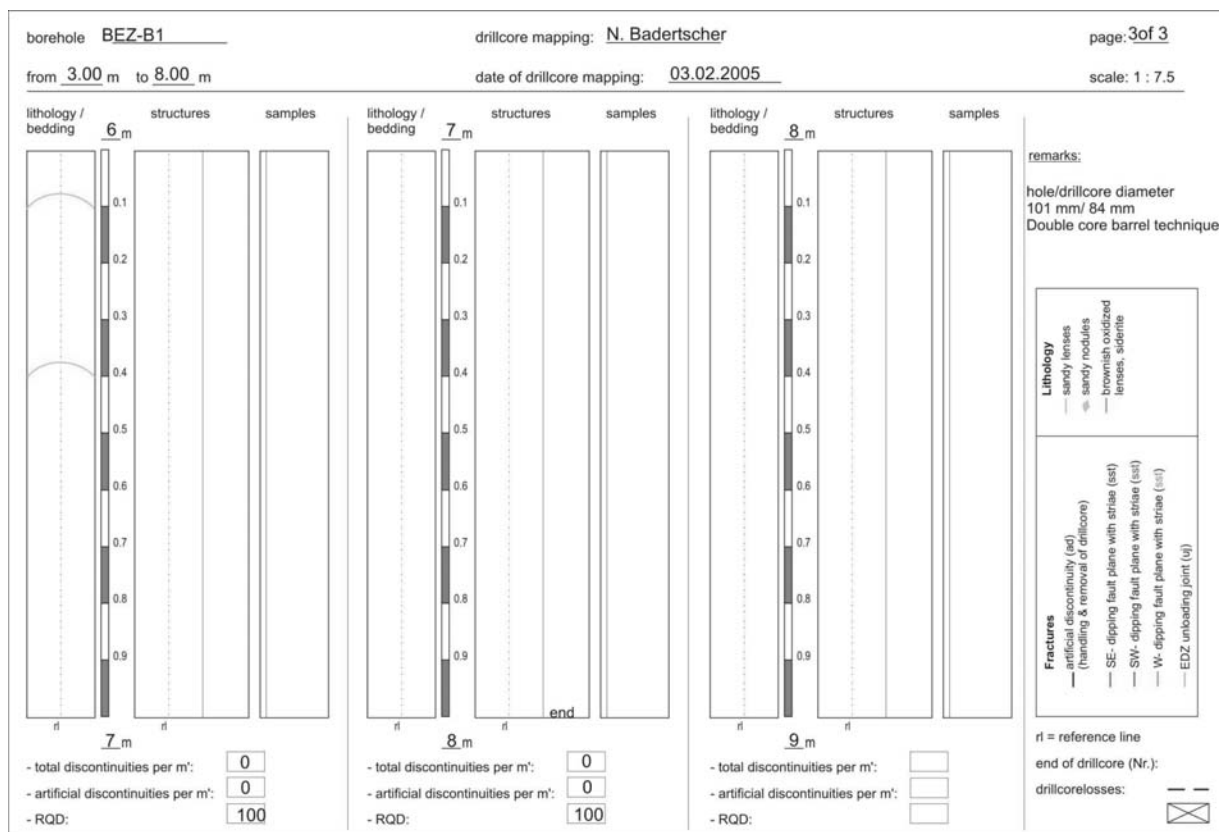


Fig. C2c: Continuation of BEZ-B1 drillcore map (Nussbaum et al., 2005).

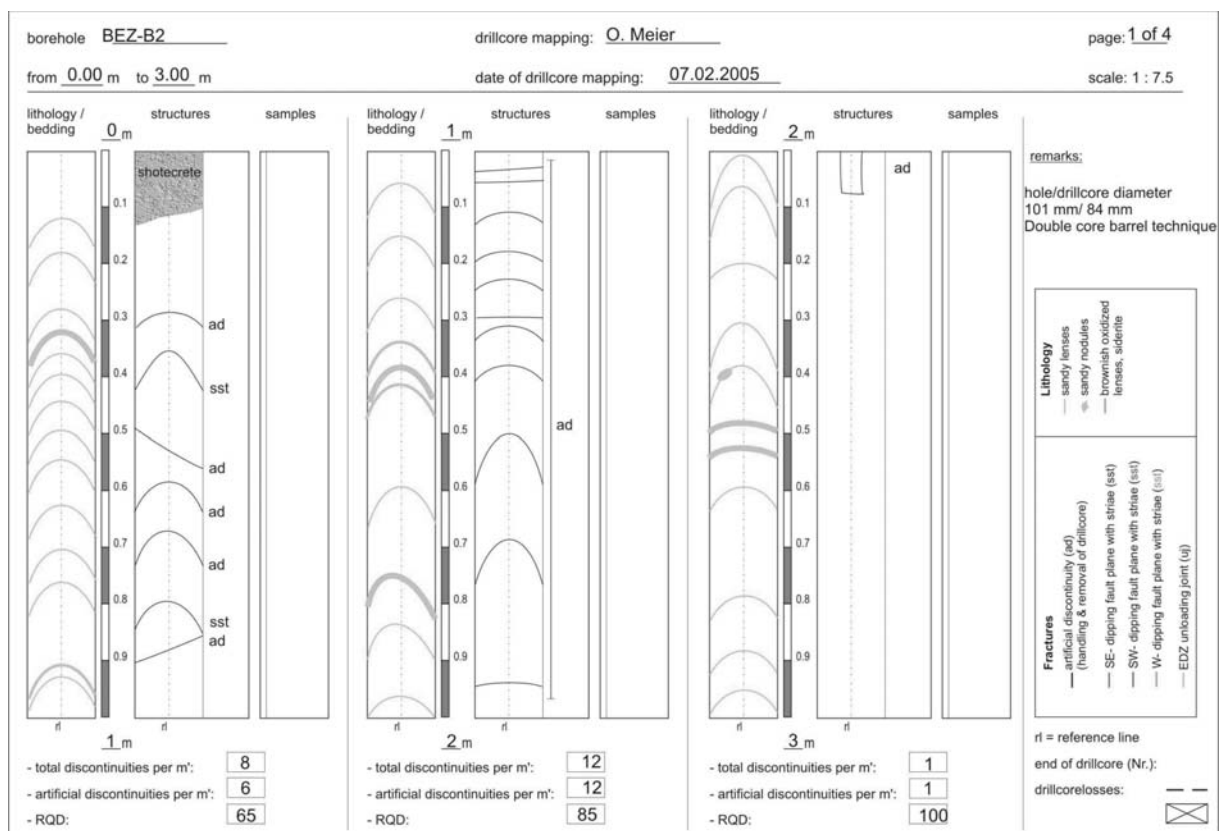


Fig. C3a: Drillcore map of BEZ-B2 (Nussbaum et al., 2005). Refer to Fig. C1 for borehole location.

Appendix C: Drillcore Maps

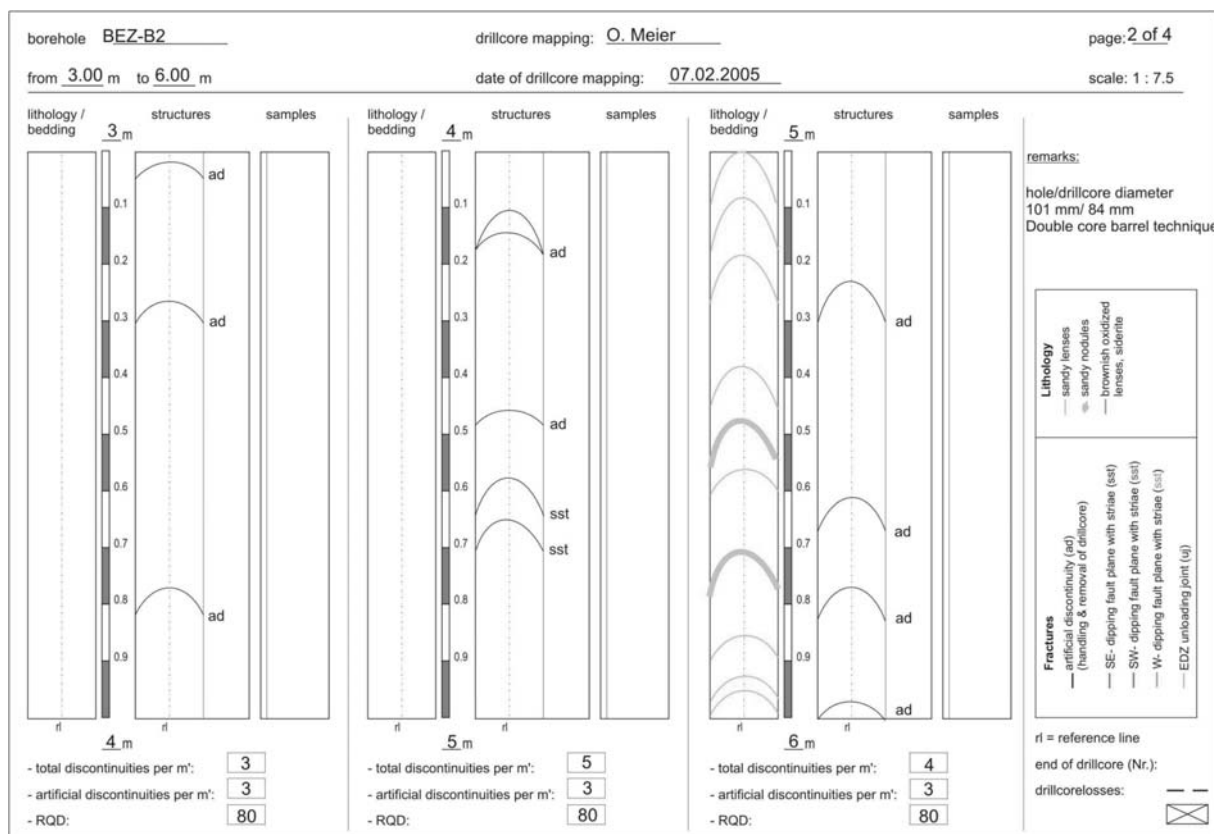


Fig. C3b: Continuation of BEZ-B2 drillcore map (Nussbaum et al., 2005).

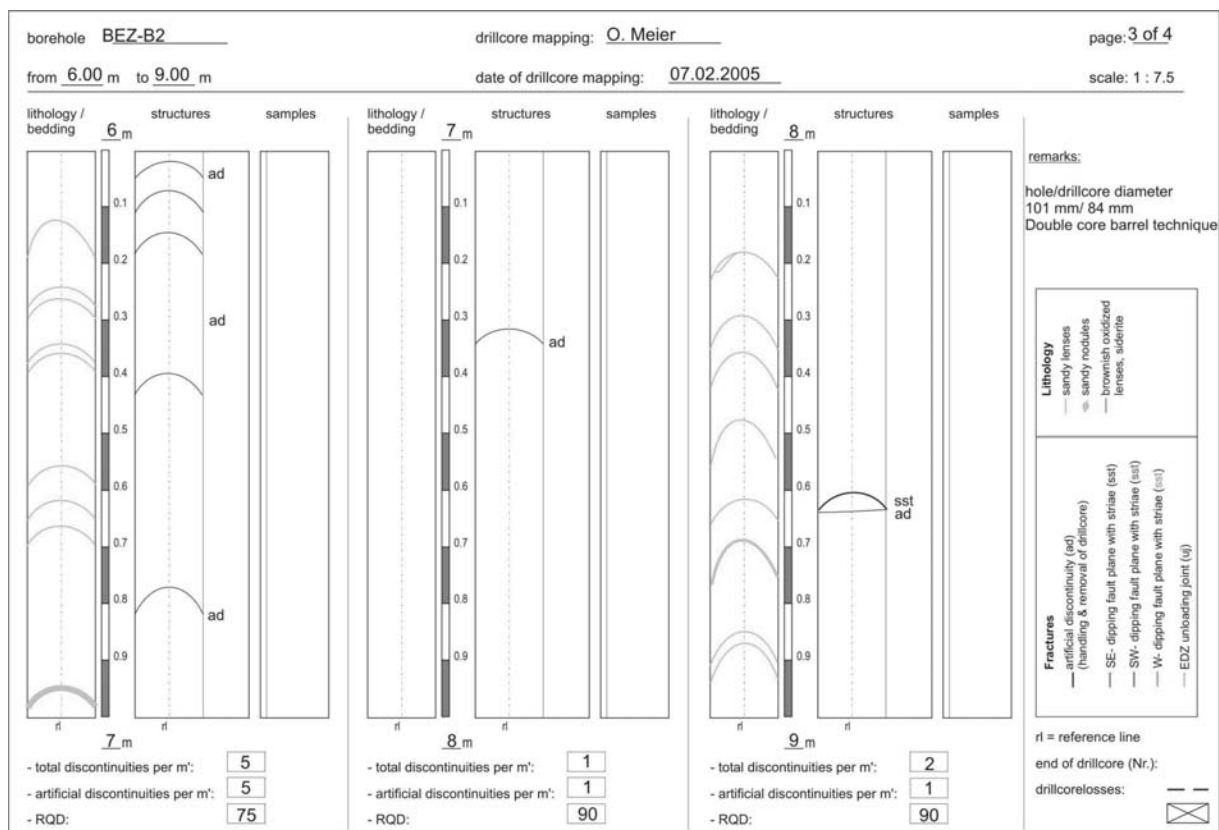


Fig. C3c: Continuation of BEZ-B2 drillcore map (Nussbaum et al., 2005).

Appendix C: Drillcore Maps

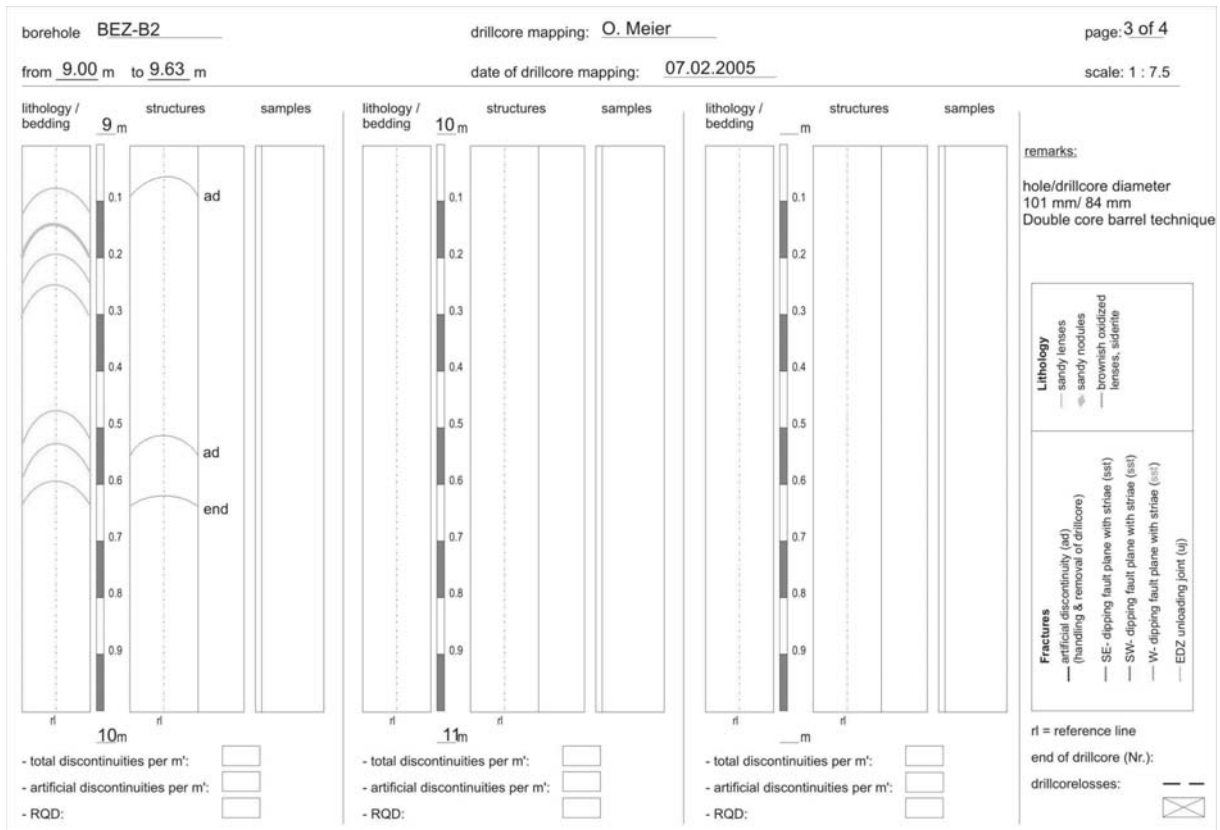


Fig. C3d: Continuation of BEZ-B2 drillcore map (Nussbaum et al., 2005).

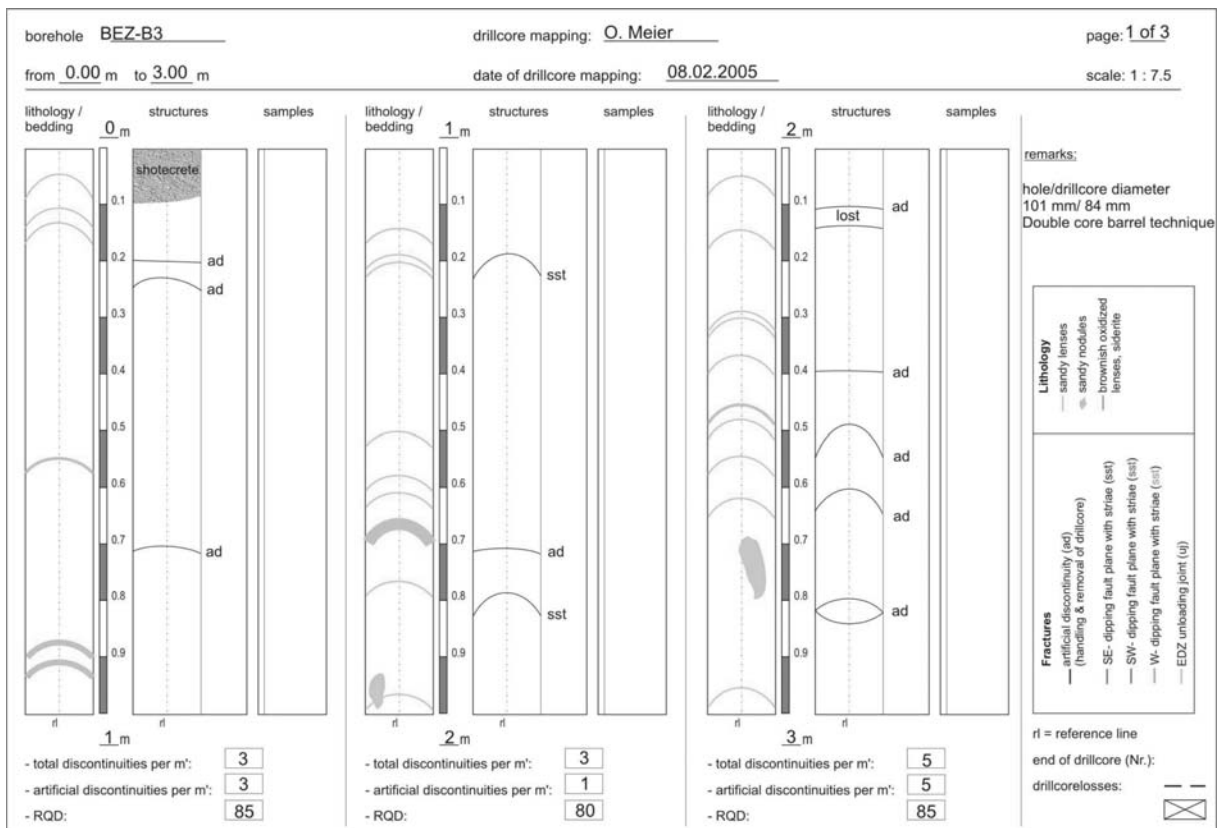


Fig. C4a: Drillcore map of BEZ-B3 (Nussbaum et al., 2005). Refer to Fig. C1 for borehole location.

Appendix C: Drillcore Maps

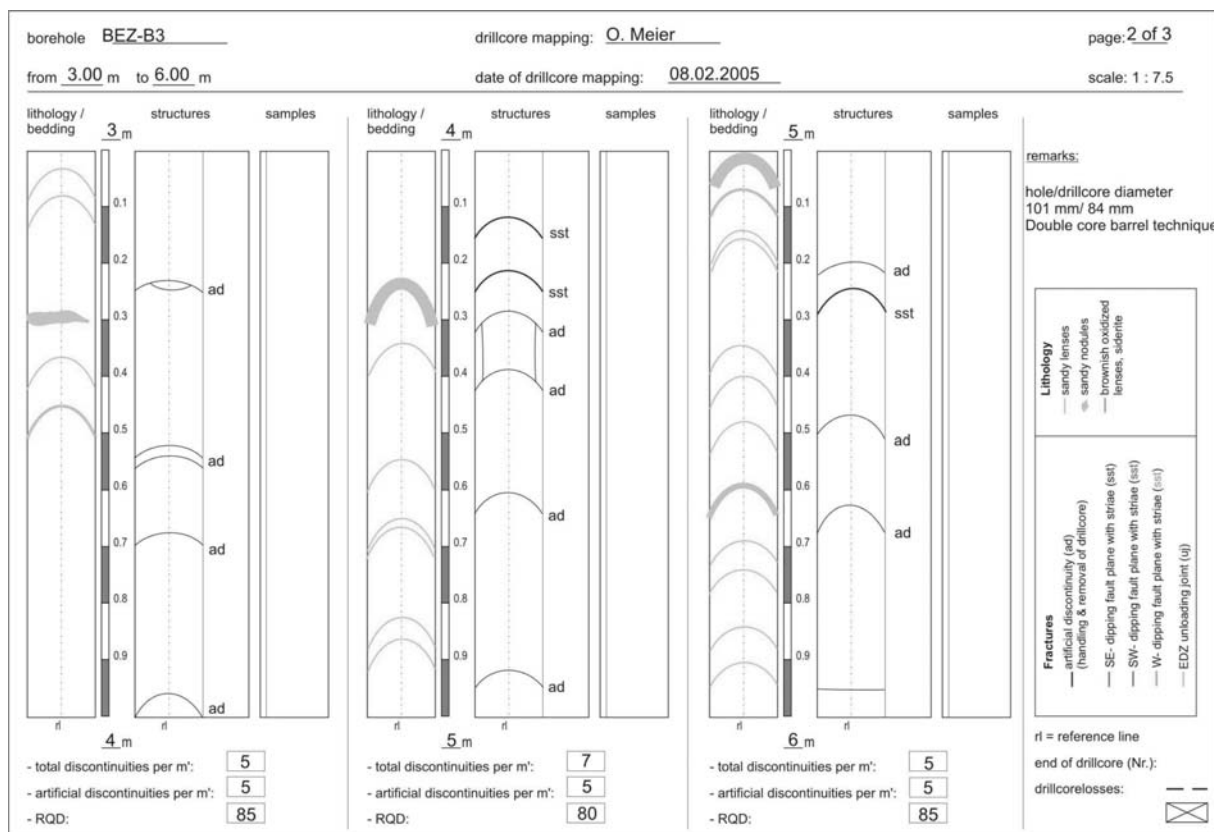


Fig. C4b: Continuation of BEZ-B3 drillcore map (Nussbaum et al., 2005).

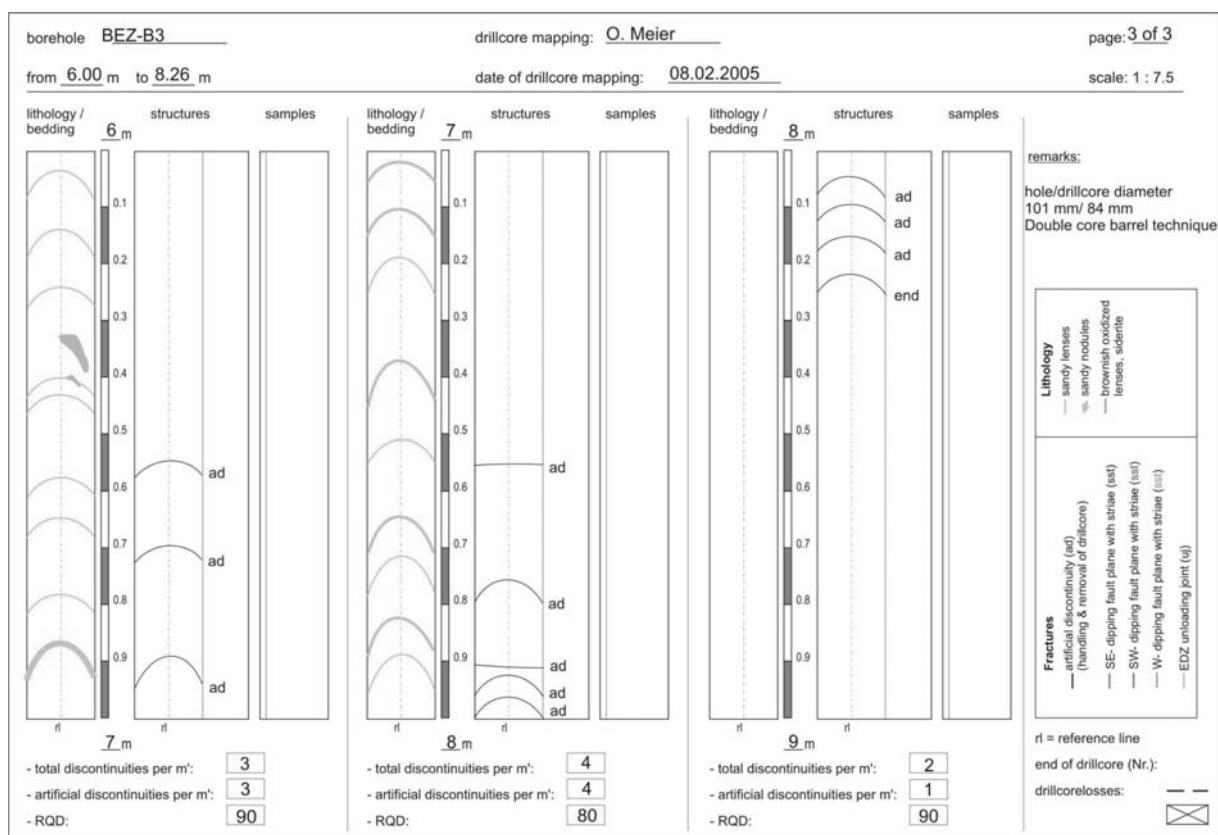


Fig. C4c: Continuation of BEZ-B3 drillcore map (Nussbaum et al., 2005).

Appendix C: Drillcore Maps

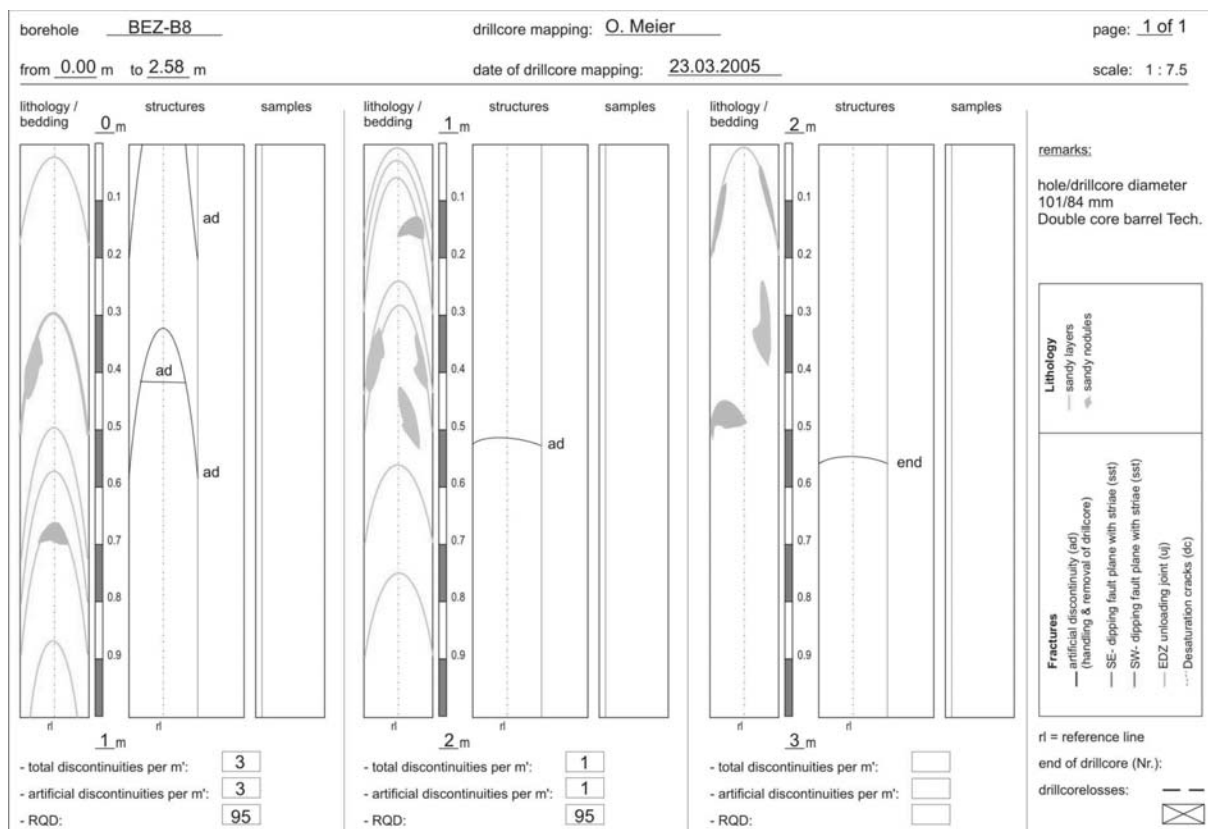


Fig. C5: Drillcore map of BEZ-B8 (Nussbaum et al., 2005). Refer to Fig. C1 for borehole location.

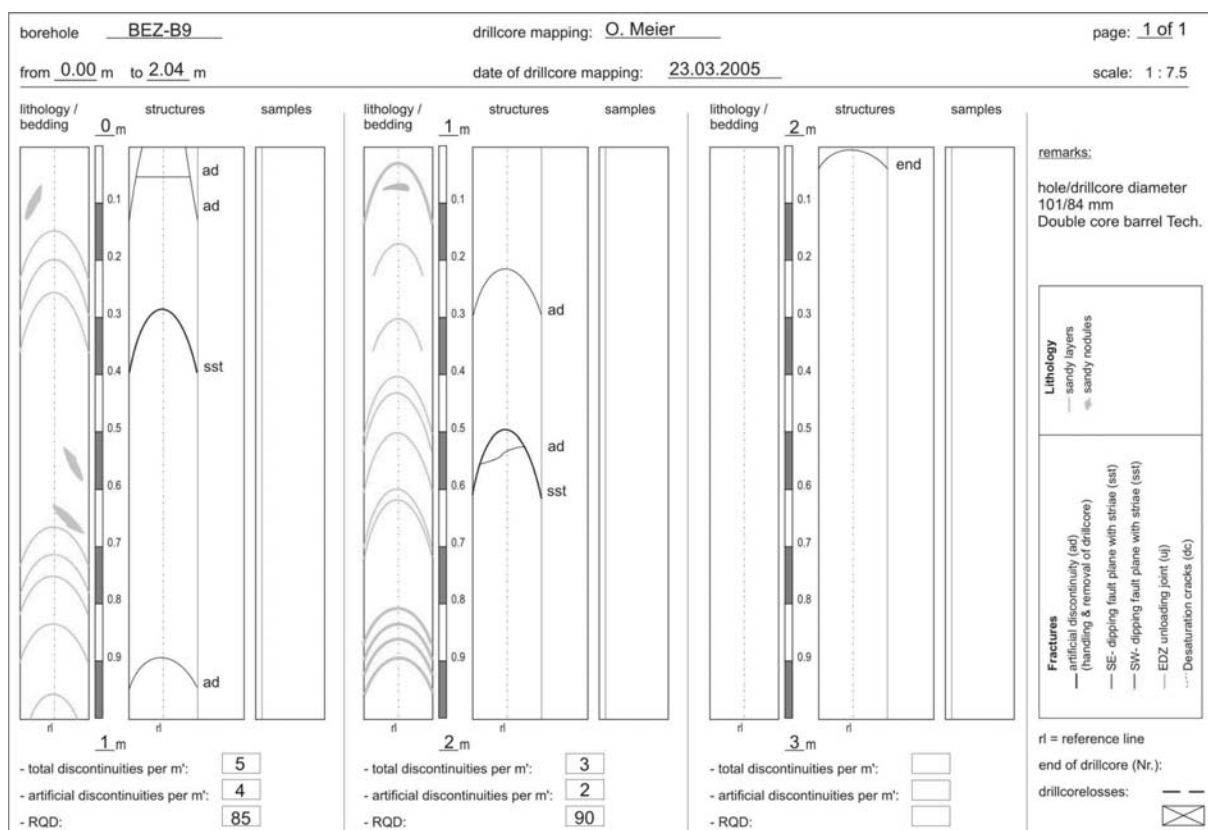


Fig. C6: Drillcore map of BEZ-B9 (Nussbaum et al., 2005). Refer to Fig. C1 for borehole location.

Appendix C: Drillcore Maps

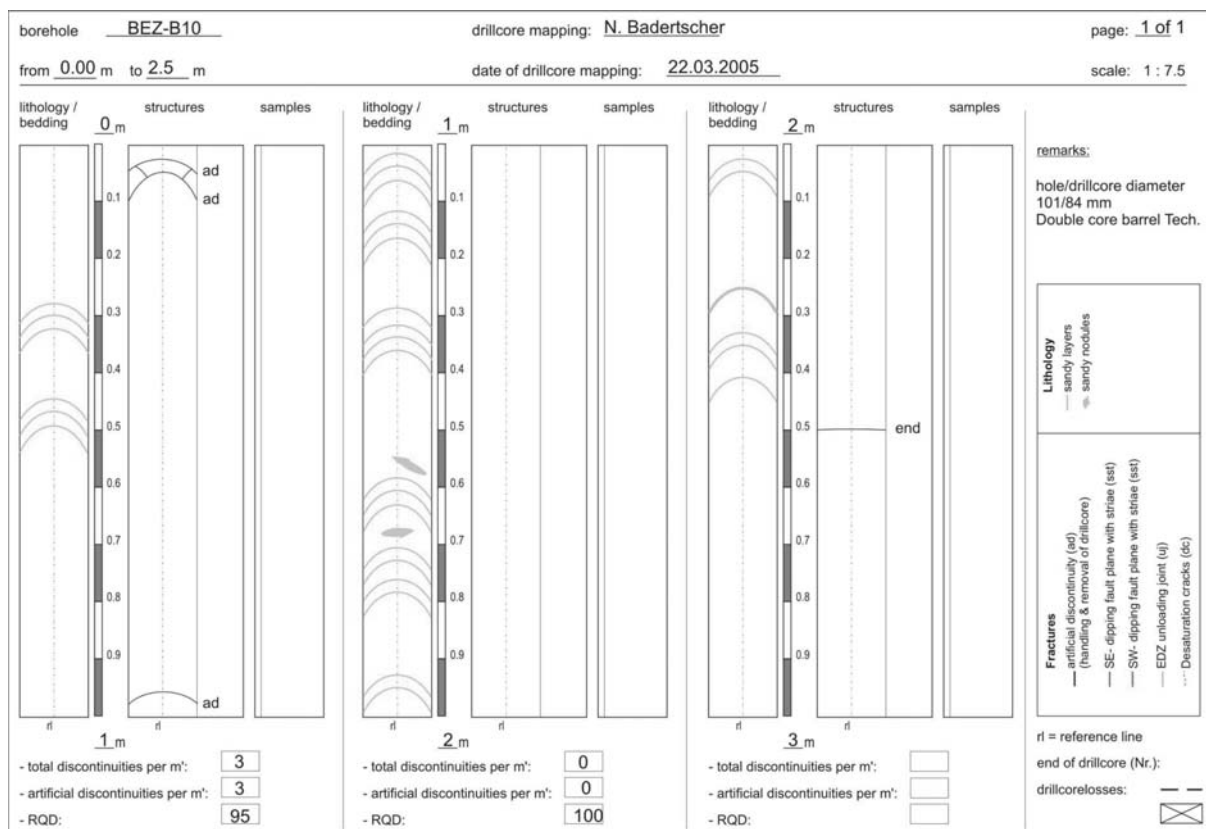


Fig. C7: Drillcore map of BEZ-B10 (Nussbaum et al., 2005). Refer to Fig. C1 for borehole location.

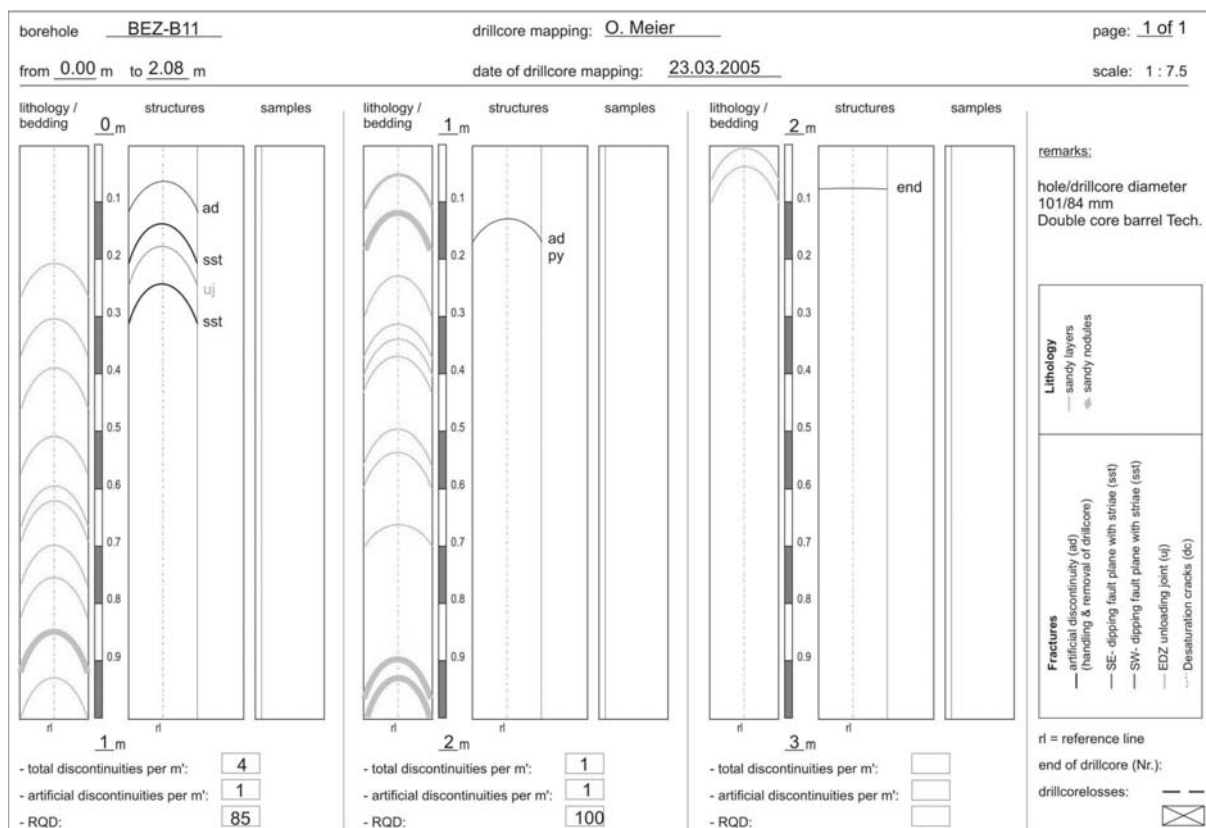


Fig. C8: Drillcore map of BEZ-B11 (Nussbaum et al., 2005). Refer to Fig. C1 for borehole location.

Appendix C: Drillcore Maps

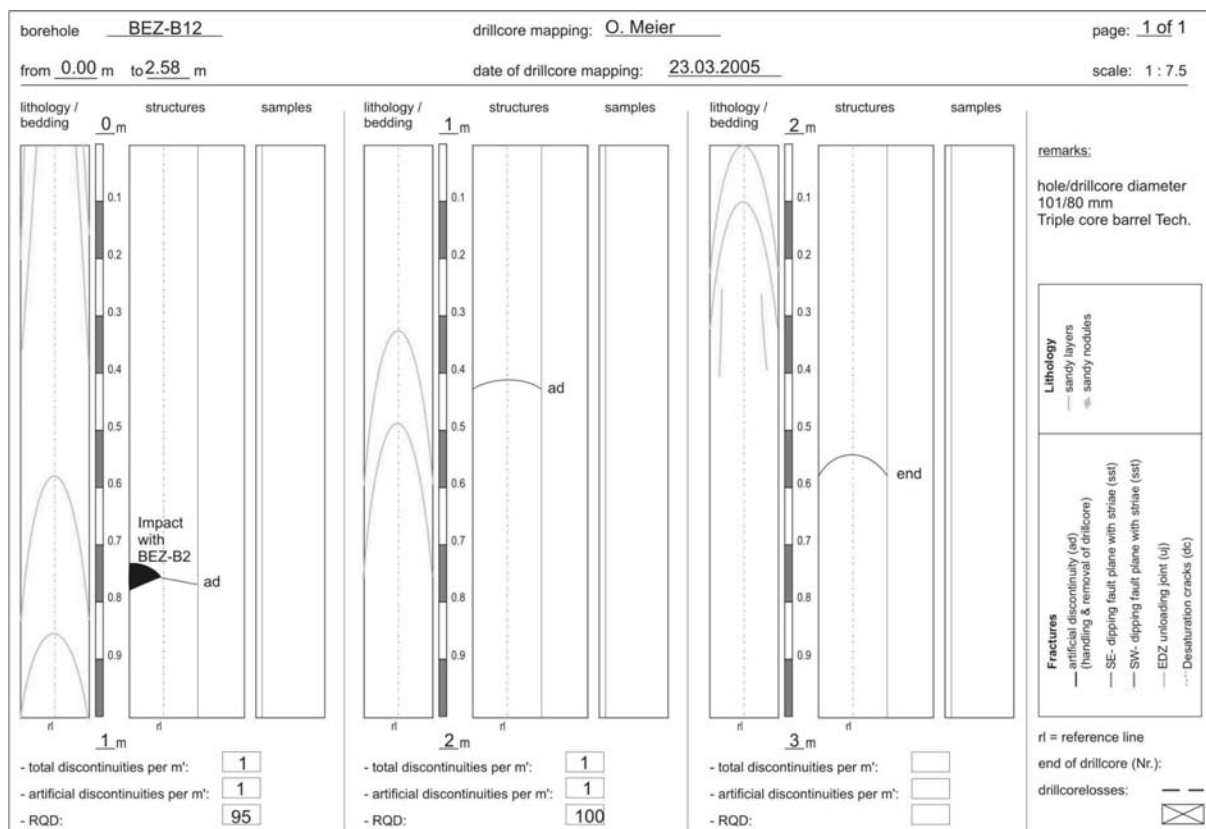


Fig. C9: Drillcore map of BEZ-B12 (Nussbaum et al., 2005). Refer to Fig. C1 for borehole location.

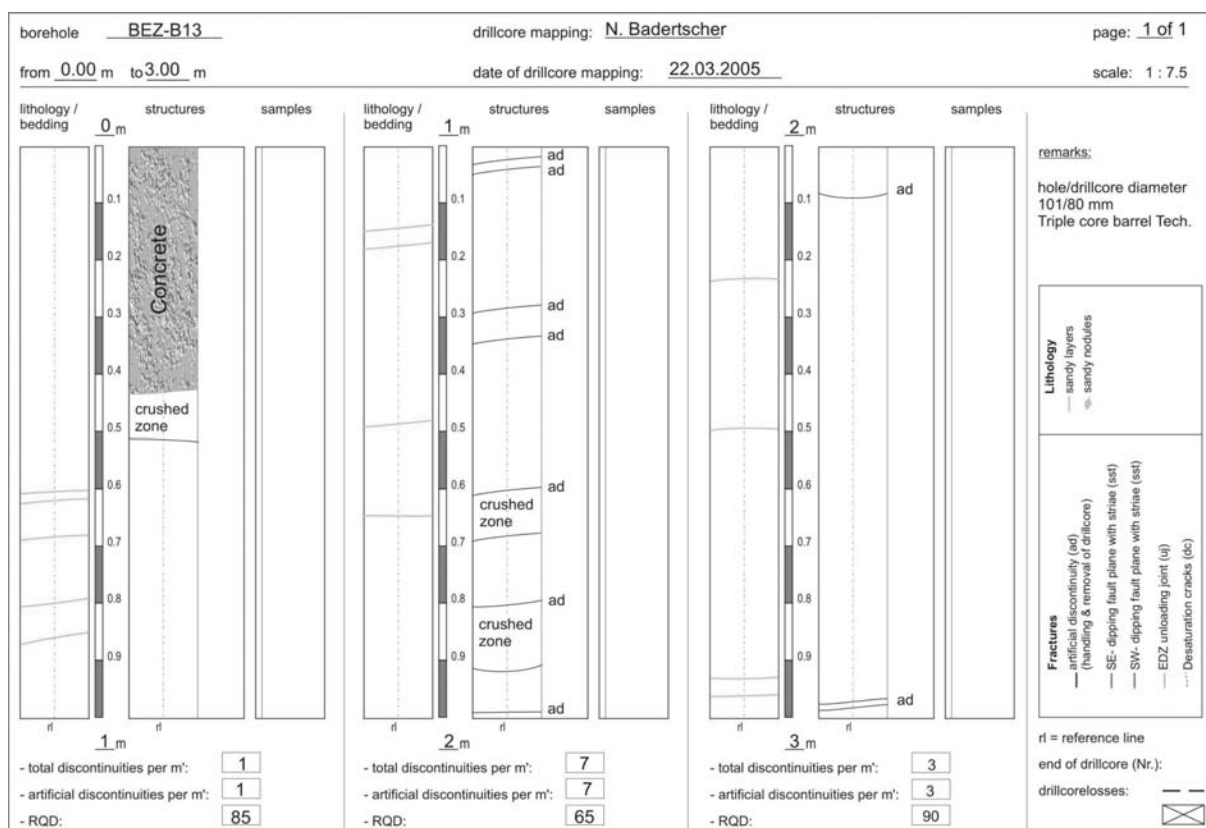


Fig. C10: Drillcore map of BEZ-B13 (Nussbaum et al., 2005). Refer to Fig. C1 for borehole location.

Appendix C: Drillcore Maps

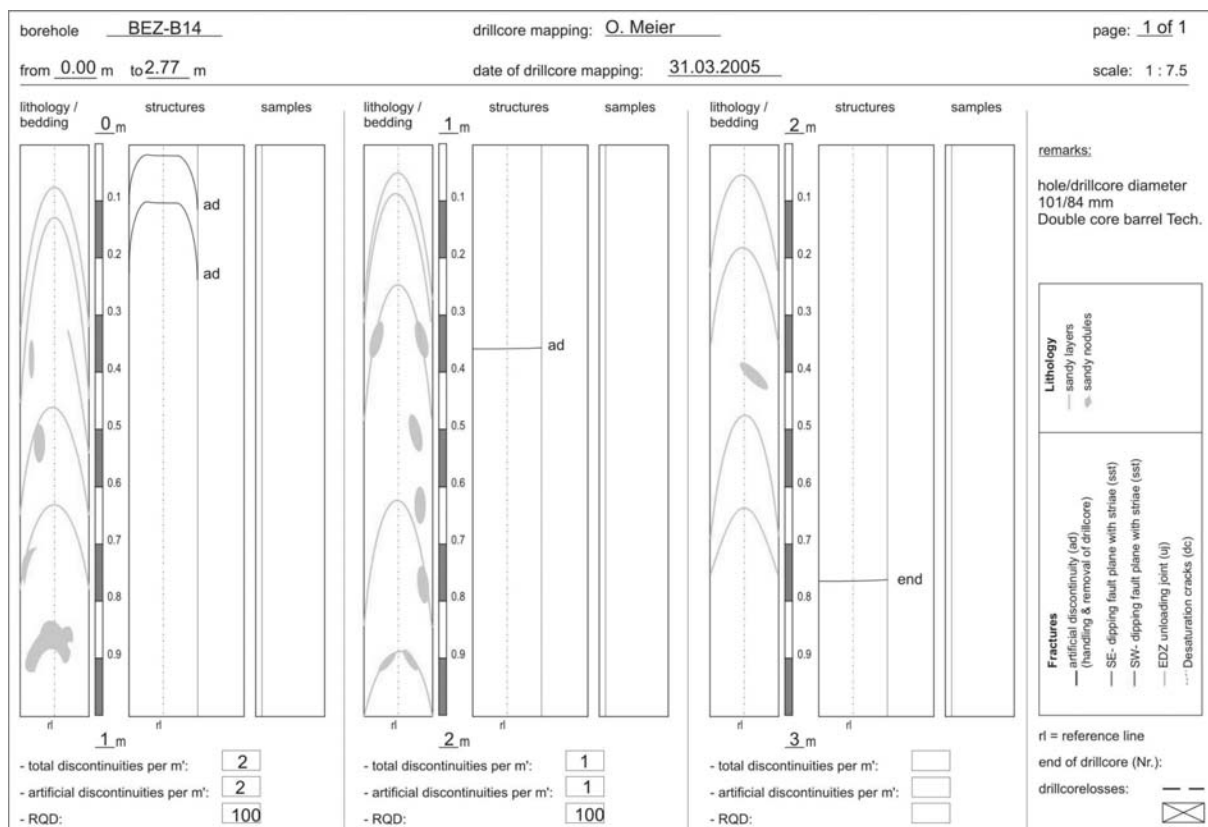


Fig. C11: Drillcore map of BEZ-B14 (Nussbaum et al., 2005). Refer to Fig. C1 for borehole location.

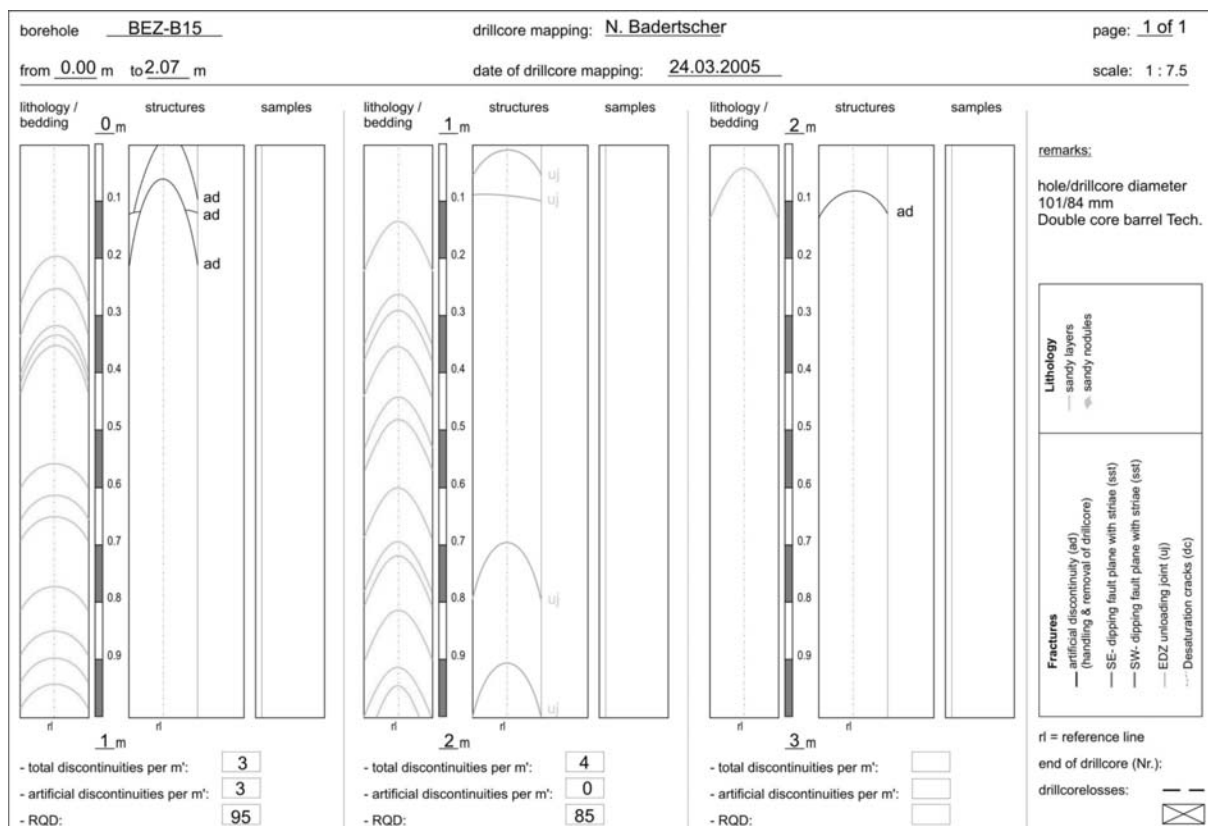


Fig. C12: Drillcore map of BEZ-B15 (Nussbaum et al., 2005). Refer to Fig. C1 for borehole location.

Appendix C: Drillcore Maps

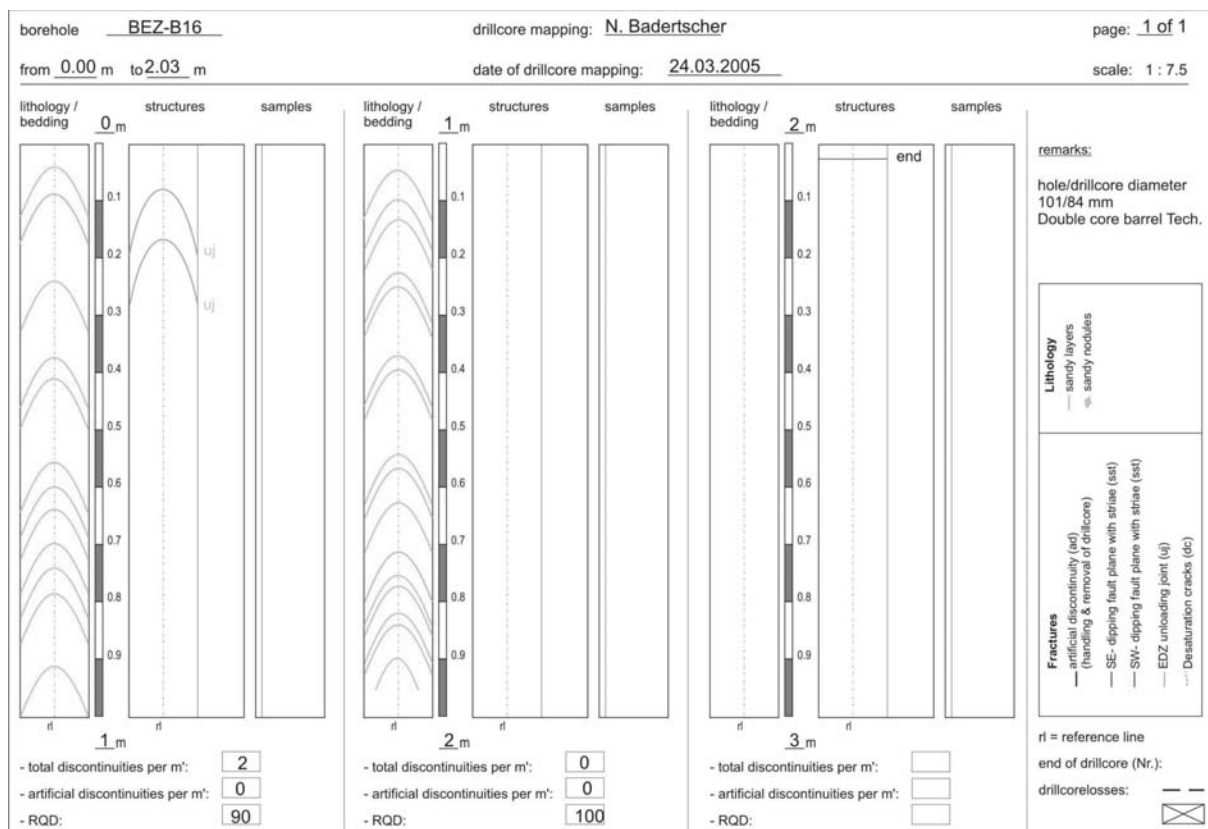


Fig. C13: Drillcore map of BEZ-B16 (Nussbaum et al., 2005). Refer to Fig. C1 for borehole location.

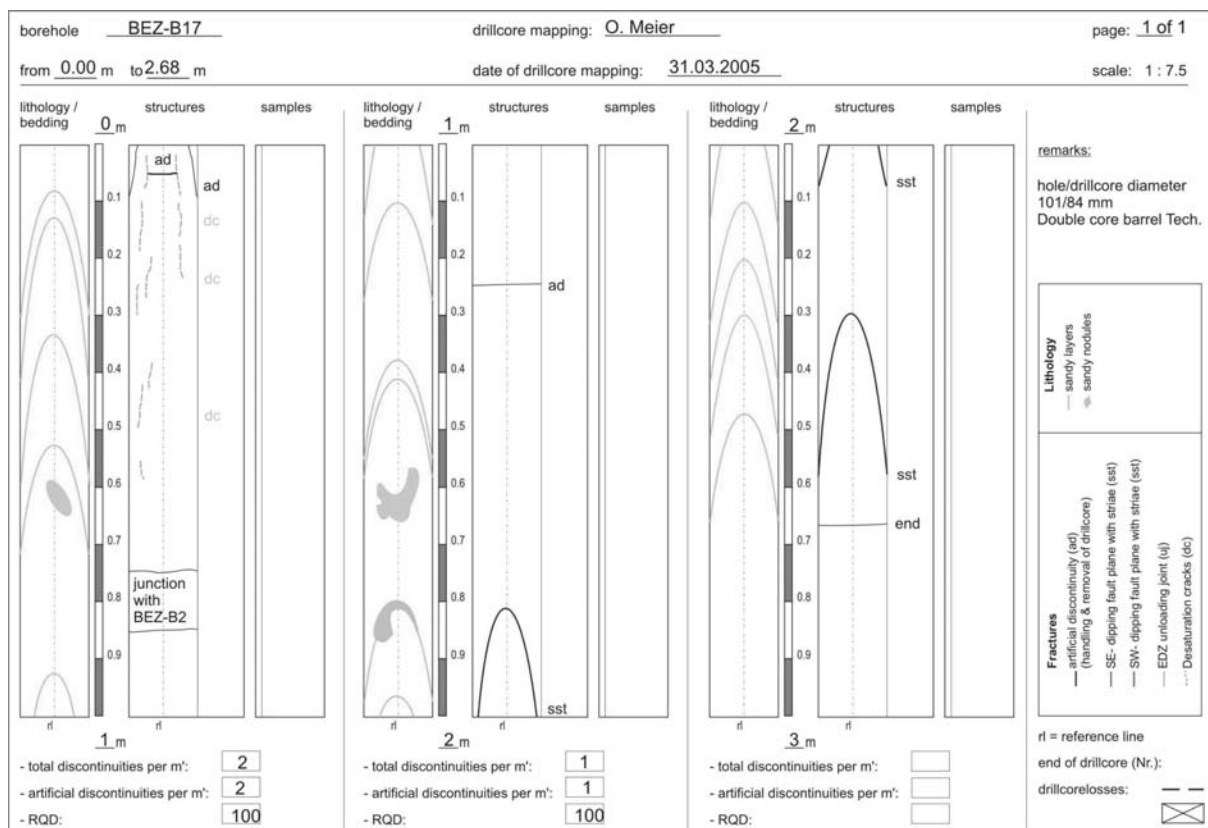


Fig. C14: Drillcore map of BEZ-B17 (Nussbaum et al., 2005). Refer to Fig. C1 for borehole location.

Appendix C: Drillcore Maps

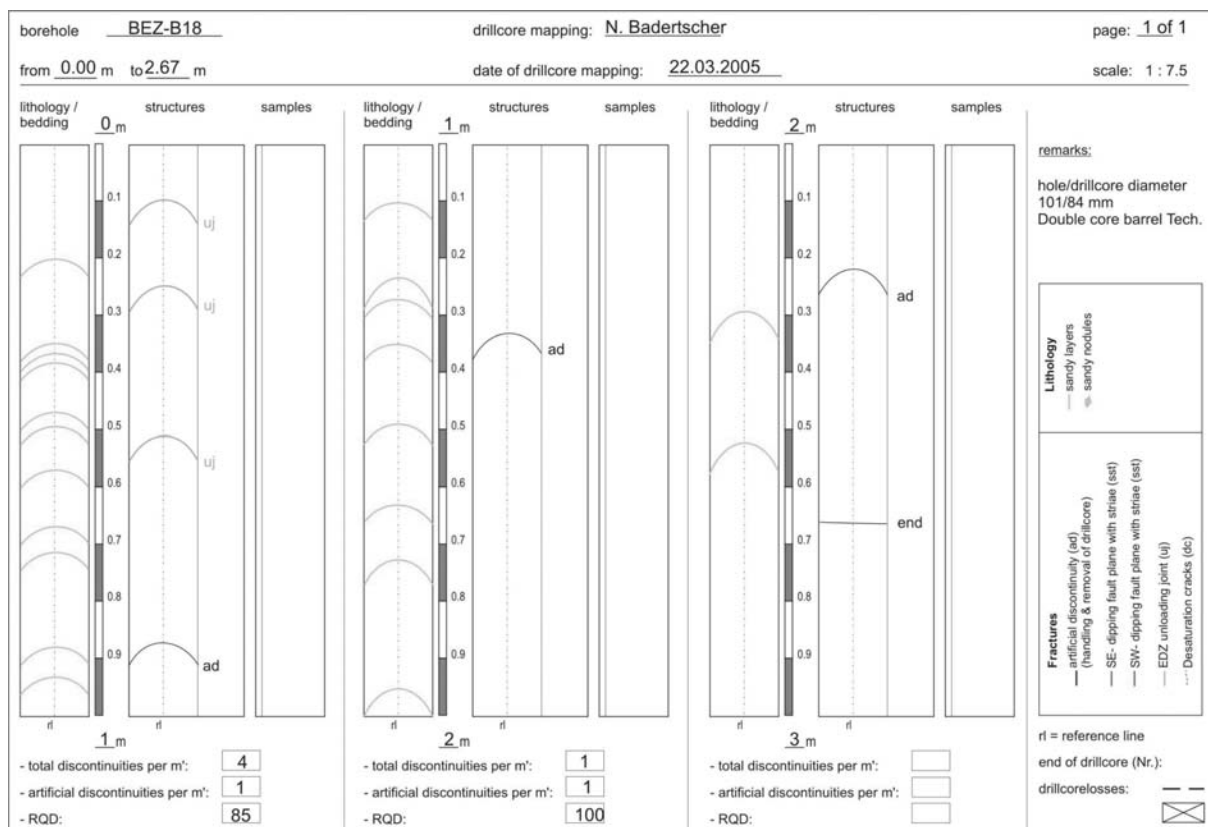


Fig. C15: Drillcore map of BEZ-B18 (Nussbaum et al., 2005). Refer to Fig. C1 for borehole location.

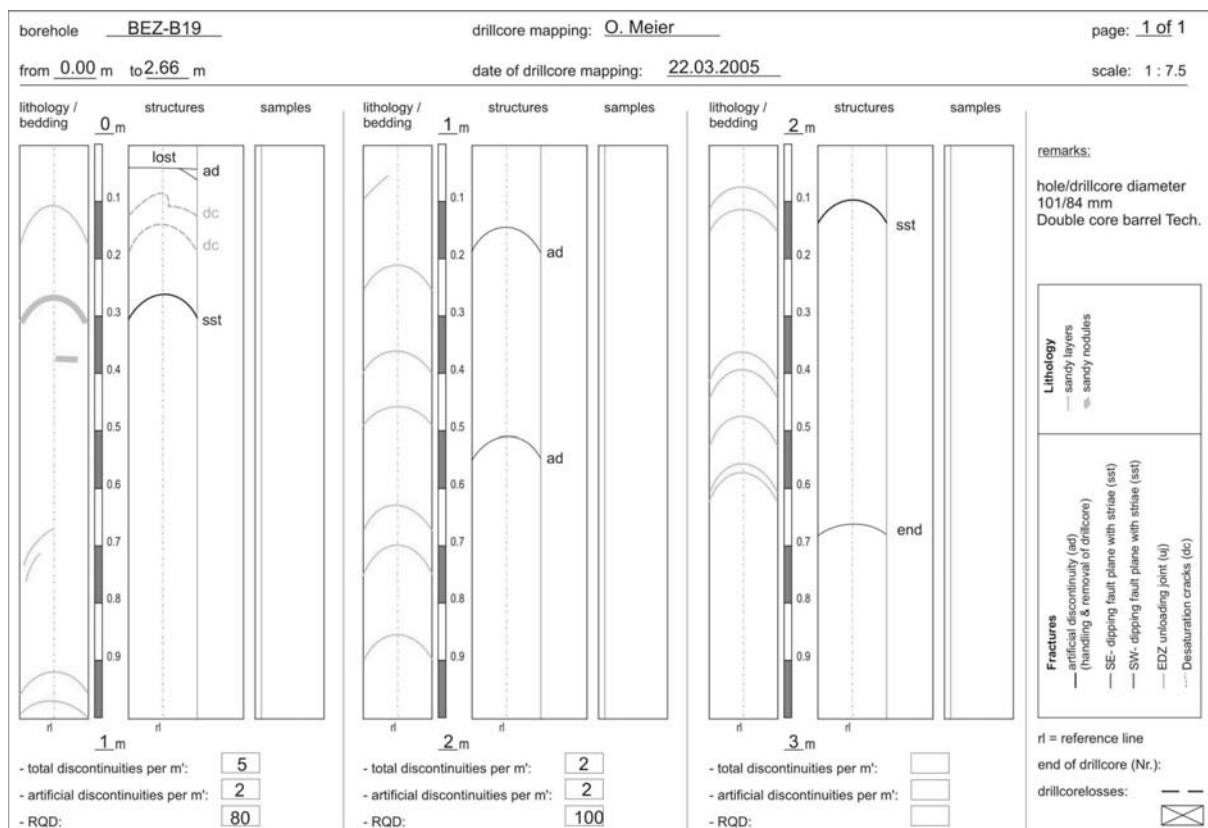


Fig. C16: Drillcore map of BEZ-B19 (Nussbaum et al., 2005). Refer to Fig. C1 for borehole location.

Appendix D

Pore Pressure and Atmospheric Data

Pore pressure monitoring was also integrated with temperature, relative humidity, and barometric pressure (Fig. D1). Out of the four sensors installed, BEZ-B4 (Fig. D2) responded the least the niche excavation. Although BEZ-B6 became problematic prior to the niche excavation and was not repaired until the third syn-excavation step. All the pore pressure sensors were opened during a software upgrade in March, 2006. This provided an unexpected test of the sensors and indicated the sub-atmospheric pressures were not due to instrument error (Fig. D1). As the atmospheric sensors were not installed in the niche until the end of construction, data from a nearby niche was used for the syn-excavation stage (Fig. D3). Both sources of atmospheric data are plotted in Fig. D1.

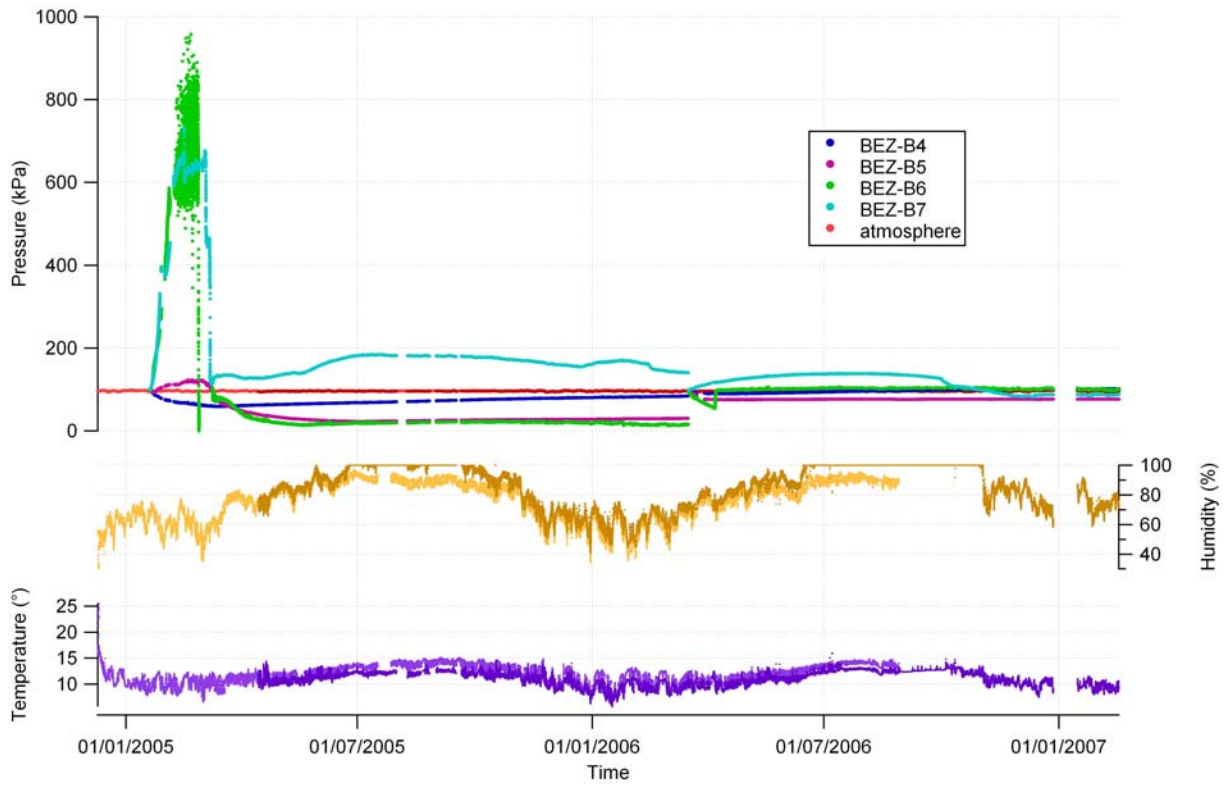


Fig. D1: Integration of the pore pressures with atmospheric data obtained from a nearby niche and from the EZ-B Niche.

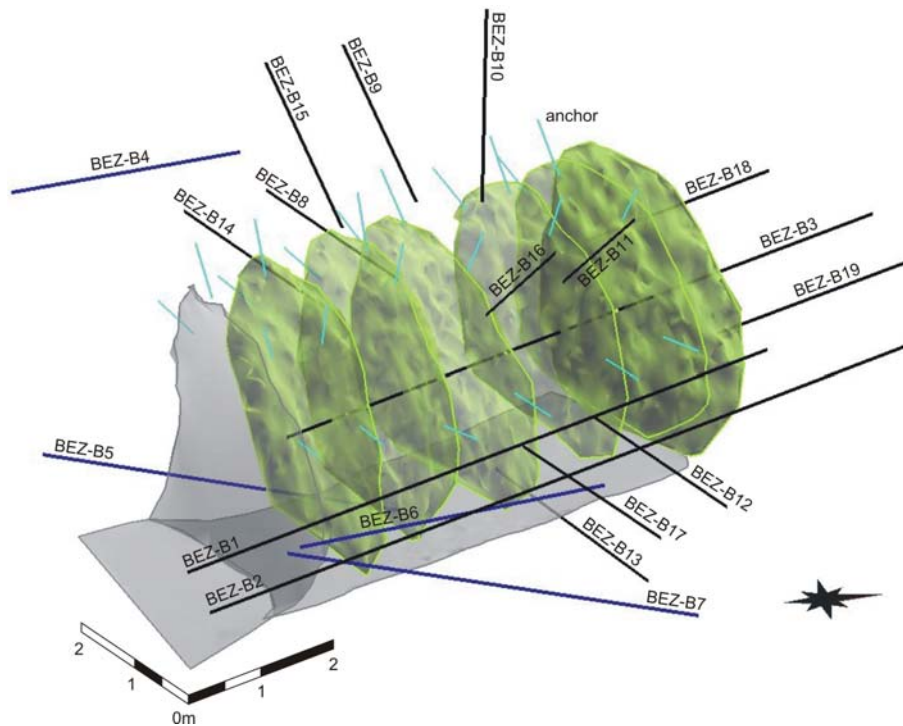


Fig. D2: Location of the boreholes (BEZ-B4 to B7) where pore pressure sensors were installed.

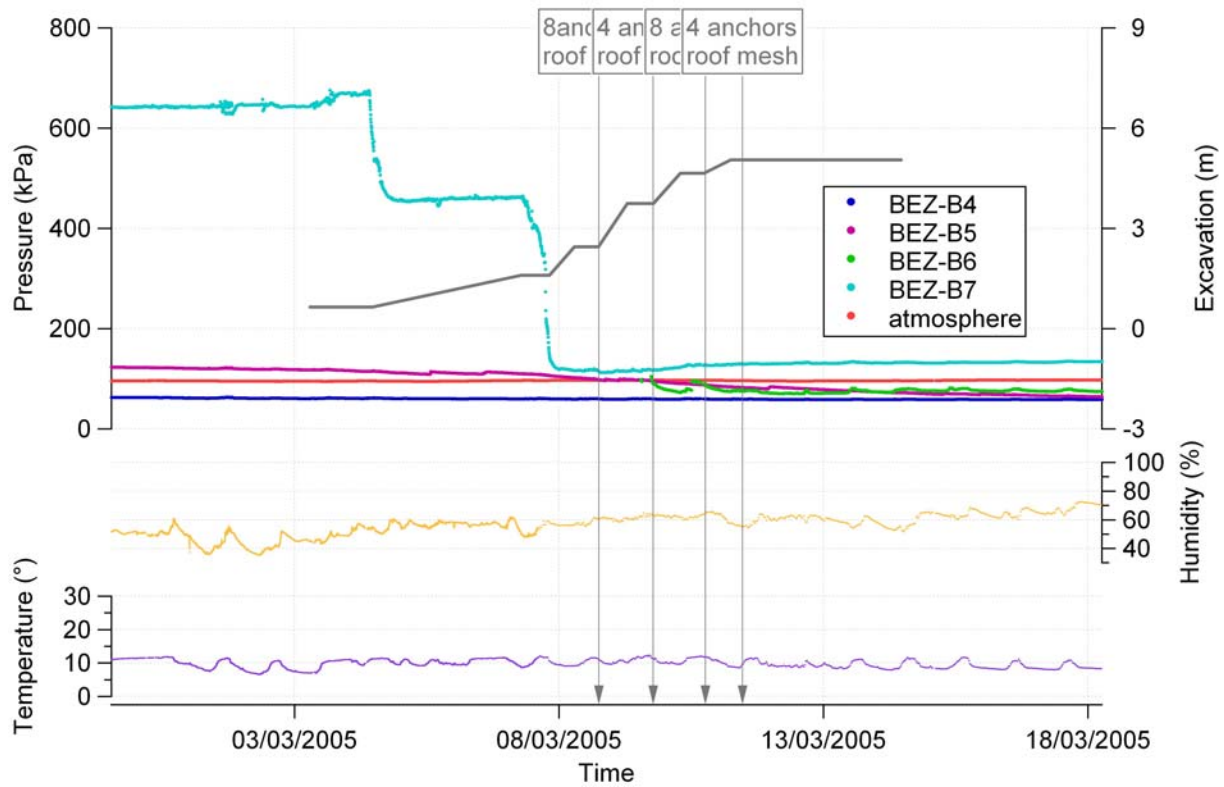


Fig. D3: Integration of the pore pressures with atmospheric data during the niche excavation.

Curriculum Vitae

Salina Yong

Education

- 2003-2007 Doctor of Sciences, Engineering Geology
ETH Zurich, Zurich, Switzerland
- 2000-2003 Master of Science in Geotechnical Engineering
University of Alberta, Edmonton, Alberta
- 1992-1997 Bachelor of Science in Civil Engineering (Co-op) with Distinction, University of Alberta,
Edmonton, Alberta

Employment

- 2003-2007 Research Assistantship, ETH Zurich, Zurich, Switzerland: PC administration for the
Chair of Engineering Geology
- 2003 Geotechnical Engineer, Thurber Engineering Limited, Calgary, Alberta: engineering
analysis (foundation design of a new petroleum plant site) & assessment (dam safety
reviews); laboratory testing; site reconnaissance.
- 2001-2002 Teaching Assistant, University of Alberta, Edmonton, Alberta: assisted in laboratory &
seminar sections of two courses (1: Introductory & Intermediary Computer Aided
Design in AutoCAD for Non-engineering Students and 2: Civil Engineering Materials);
provided private tutorials; marked assignments, laboratory reports, and exams.
- 1998-2000 Structural/Civil Engineer, Techna-West Engineering Limited., Edmonton, Alberta:
consulting engineering - design, construction supervision & inspection of structural,
geotechnical, and municipal engineering projects.
- 1996 Infrastructure Projects Coordinator (Co-op), Daishowa-Marubeni International Limited.,
Peace River, Alberta: building infrastructure inspection; restoration & maintenance
projects management & supervision; coordination of engineering capital project.
- 1995 Water Management Summer Assistant (Co-op), Parkland County, Stony Plain, Alberta:
inspection & completion of County culvert inventory; assistance in County GIS;
evaluation & inspection of subdivision proposals.
- 1994-1995 Excavation Inspector (Co-op), Northwestern Utilities Limited., Edmonton, Alberta:
material accounting for reclamation & replacement projects.